CYCLIC RESPONSE OF BEAM COLUMN JOINTS STRENGTHENED WITH SUPERELASTIC SHAPE MEMORY ALLOYS (SMAs)

BY

MUHAMMAD AJMAL

A Dissertation Presented to the
DEANSHIP OF GRADUATE STUDIES

KING FAHD UNIVERSITY OF PETROLEUM & MINERALS

DHAHRAN, SAUDI ARABIA

In Partial Fulfillment of the
Requirements for the Degree of

DOCTOR OF PHILOSOPHY

In

CIVIL ENGINEERING

MAY, 2016

KING FAHD UNIVERSITY OF PETROLEUM & MINERALS

DHAHRAN- 31261, SAUDI ARABIA

DEANSHIP OF GRADUATE STUDIES

This thesis, written by **MUHAMMAD AJMAL** under the direction of his thesis advisor and approved by his thesis committee, has been presented and accepted by the Dean of Graduate Studies, in partial fulfillment of the requirements for the degree of **DOCTOR OF PHILOSOPHY IN CIVIL ENGINEERING.**

Dr. Salah U. Al-Dulaijan
Department Chairman

Dr. Salam A. Zummo
Dean of Graduate Studies

9/ 8/16
Date

Dr. Mohammed H. Baluch
(Advisor)

Kalimur Rahman
Dr. Muhammad K. Rahman
(Co-Advisor)

Dr. Ali H. Al-Gadhib
(Member)

Dr. Ahmad Saad Al-Gahtani
(Member)

Dr. Al Farabi M. Sharif
(Member)

To my parents, wife (Aisha) and daughter (Areesha) whose utmost love, care and effort
against all odds brought me to this height of knowledge and to those who always pray for
my success in life and to those from whom I have learnt so much throughout my career
with the blessings of Almighty Allah

ACKNOWLEDGMENTS

In the name of Almighty ALLAH, the Most Beneficent and the Most Merciful

First and the foremost, I thank Allah (سبحانه و تعالى) who has bestowed health, and knowledge to complete this study. Peace and blessing of Allah be upon His holy Prophet (صلى الله عليه وسلم). I acknowledge King Fahd University of Petroleum & Minerals (KFUPM) for the support extended towards my research through its remarkable facilities and for providing me the opportunity to pursue graduate studies.

I acknowledge, with deep gratitude and appreciation, the inspiration, encouragement, valuable time and guidance given to me by Prof. M. H. Baluch, who served me as thesis advisor. This work was completed due to his guidance and personal involvement in this study. His valuable suggestions and useful discussions made this work interesting and raised my comfort and confidence level.

I am deeply indebted and grateful to Dr. Muhammad Kalimur Rahman, my co-advisor, for his extensive guidance, continuous support, and personal involvement throughout my study. I would have never accomplished this study without the valuable suggestions and the support given by him.

I am also grateful to my Committee Members, Dr. Ali H. Al-Gadhib, Dr. Ahmad Saad Al-Gahtani and Dr. Al-Farabi M. Sharif, for their constructive guidance, valuable advices and cooperation.

I would like to express my deepest gratitude to my beloved parents, my wife and my family for having faith in me and all my family members for their love, moral support, prayers and encouragement throughout my life. I would like to thanks my younger brothers Waqas and Bilal for their continuous support and help during retrofitting of specimens and testing of specimen.

I am also thankful to all my friends specially Omer Khan, Umais Khan, Mohammad Al-Huri for their support and help during testing.

I would like to thanks PRAINSA Co. for allowing us to use their lab and space for casting of beam-column joints for this study. I would like to thanks engineer Islam, Mr. Teo manager of precast units and whole team of PRAINSA Company for helping in casting of beam.

Special thanks are due to engineers Najamuddin, Syed Imran and Omer for their guidance and support during testing of beam-column joints for this study.

Special thanks to Dr. M. Al-Osta who helped in Arabic translation of Abstract of thesis.

TABLE OF CONTENTS

LIST OF TABLES

LIST OF FIGURES

LIST OF ABBREVIATIONS

ASTM: American Society for Testing and Materials

BCJ: Beam Column Joint

CEB: Comité Euro-International du Béton

CFRP: Carbon Fiber Reinforced Polymers

CPD: Concrete Plastic Damage

FEM: Finite Element Method

FRP: Fiber Reinforced Polymers

GFRP: Glass Fiber Reinforced Polymers

LVDT: Linear Variable Displacement Transducer

RC: Reinforced Concrete

SBC: Saudi Building Code

SMAs: Shape Memory Alloys

SME: Shape Memory Effect

XRF: X-Ray Fluorescence

ABSTRACT

Full Name : Muhammad Ajmal

Thesis Title : CYCLIC RESPONSE OF BEAM COLUMN JOINTS STRENGTHENED WITH SUPERELASTIC SHAPE MEMORY ALLOYS (SMAs)

Major Field : Civil Engineering (Structures)

Date of Degree : May, 2016

Recent destructive earthquake such as the Hanshin earthquake (1995) in Japan, the Kocaeli (Izmit) earthquake (1999) in Turkey, the Kashmir earthquake (2005) in Pakistan, the Sichuan earthquake (2008) in China, the Chile earthquake (2010) in Chile, the Tohoku earthquake and tsunami (2011) in Japan and the Gorkha earthquake (2015) in Nepal have shown deficiency in structures which resulted in major loss of human lives and economy. Most of these structures were poorly designed with no seismic detailing. It has been observed in many reinforced concrete structures, structural failure could be due to insufficient seismic detailing in columns, load bearing walls and beam-column joints which causes major destruction.

Reinforced concrete (RC) buildings constructed in 1980’s were designed mostly for gravity loads without seismic detailing. Such structures are extensively available worldwide in seismic prone regions. The major components of the reinforced structures which plays an important role in integrating the system and overall stability are beam-column joints (BCJs).

One of the greatest motivation for this study is to use smart material in the reinforced concrete structures. In this study, beam-column joints with lack of seismic detailing have been studied experimentally and numerically using ABAQUS FEM software. Seven specimens were tested which includes 3 control specimens and 4 retrofitted specimens using shape memory alloys (SMAs) sheets under monotonic, cyclic and reverse cyclic loading. The experimental results showed that SMAs sheets enhanced the ultimate load carrying capacity for retrofitted specimens as well as increased the residual load carrying capacity. Control cracking and reduced number of cracks were observed with the usage of SMAs sheets in the joint region as compared to the control specimens where number of cracks were more. SMAs sheets also reduced the crack widths in the joint region upon unloading which was not observed in the case of control specimens which is good sign for post rehabilitation of RC structures.

Numerical simulations were also done for control and retrofitted specimens. User-defined subroutine VUMAT was utilized to model the material behavior of SMAs sheets and elasto-plastic damage model was utilized for concrete. The load-deflection curves, stresses in SMAs sheets and cracks pattern showed good agreement with experimental results. Mechanistic model for determining the shear strength of SMAs sheet retrofitted specimen was also developed using concept of truss analogy which predicted close results to the experimental study.

ملخص الرسالة

الاسم الكامل: محمد أجمل

عنوان الرسالة: الاستجابة الدورية لعناصر التقاء الأعمدة مع الجسور والمقواه بصفائح فائقة المرونة ذات تذكر الشكل (SMAs)

التخصص: الهندسة المدنية

تاريخ الدرجة العلمية: مايو 2016

وضحت الزلازل المدمرة حديثا مثل زلزال هانشين (1995) في اليابان وزلزال كوكالي (ازميت) (1999) في تركيا وزلزال كشمير (2005) في باكستان وزلزال سيشوان (2008) في الصين وزلزال تشيلي (2010) في شيلي، وزلزال توهوكو وتسونامي (2011) في اليابان وزلزال غوركا (2015) في نيبال نقص في الهياكل الإنشائية و التي أسفرت عن خسائر كبيرة في الأرواح والاقتصاد. حيث ان اغلبية هذه الهياكل الإنشائية صممت بشكل سيئ وعدم وجود تفاصيل لمقاومة الزلازل. وقد لوحظ في العديد من المنشآت الخرسانية المسلحة، ان الانهيار الانشائي نظرا لعدم كفاية التفاصيل لمقاومة الزلازل في الأعمدة، والجدران الحاملة وعناصر التقاء الأعمدة مع الجسور والذي يسبب دمارا كبير.

تم تصميم مباني الخرسانة المسلحة (RC) والتي شيدت في عام 1980 لمقاومة الاحمال الراسية وبدون وجود تفاصيل لمقاومة الزلازل. حيث تتواجد الكثير من هذه المباني على نطاق واسع في جميع أنحاء العالم في المناطق المعرضة للزلازل. وتعتبر المكونات الرئيسية للهياكل الانشائية والتي تلعب دورا هاما في دمج النظام الانشائي والاستقرار الشامل هي عناصر التقاء الأعمدة مع الجسور (BCJs).

احدى أعظم الدوافع لهذه الدراسة هو استخدام المواد الذكية في المنشآت الخرسانية المسلحة. في هذه الدراسة، تم دراسة عناصر التقاء الأعمدة مع الجسور والتي تفتقر لوجود تفاصيل لمقاومة الزلازل عمليا وعدديا باستخدام برنامج ABAQUS FEM. تم اختبار سبعة عينات والتي تضم 3 عينات سيطرة و 4 عينات معدلة باستخدام صفائح ذات تذكر الشكل تحت الاحمال الثابتة والدورية والعكس دورية. وأظهرت النتائج التجريبية أن أوراق SMAs عززت

قدرة العينات المعدلة بالإضافة الى زيادة قدرة التحمل المتبقية. وقد تم ملاحظة ومقارنة الشقوق وعددها في نقاط اتصال العمود مع الجسر(المنطقة المشتركة) للعينات باستخدام صفائح SMAs مع عينات السيطرة حيث وجد ان عدد الشقوق أكثر في عينات السيطرة. كما خفضت صفائح SMAs عرض الشقوق في المنطقة المشتركة عند ازالة الاحمال والتي لم تلاحظ في حالة عينات السيطرة والتي تعتبر علامة جيدة لتأهيل المنشآت الخرسانية.

وقد أجريت عمليات المحاكاة العددية أيضا لعينات السيطرة والعينات المعدلة. حيث تم الاستفادة من روتين VUMATلنمذجة السلوك المادي لصفائح SMAs كما تم استخدام نموذج انهيار المرونة والدونة لنمذجة الخرسانة. وقد أظهرت نتائج منحنيات الحمل مقابل الازاحة والاجهادات لصفائح SMA ونمط الشقوق باستخدام المحاكاة العددية اتفاق جيد مع النتائج التي تم الحصول عليها من التجارب المعملية. وقد تم تطوير نموذج تحليلي لتحديد قوة القص للعينات المقواه باستخدام صفائح SMAوذلك باستخدام مفهوم قياس الجمالون حيث اعطت نتائج قريبة من النتائج التي تم الحصول عليها في الدراسة المعملية.

CHAPTER 1

INTRODUCTION

1.1 Prologue

Earthquakes are results of tectonic plates movement in earth's crust. These movements' causes ground shaking that can lead failure of structural system, collapse of building and infrastructure system. Recent destructive earthquake such as the Hanshin earthquake (1995) in Japan, the Kocaeli (Izmit) earthquake (1999) in Turkey, the Kashmir earthquake (2005) in Pakistan, the Sichuan earthquake (2008) in China, the Chile earthquake (2010) in Chile, the Tohoku earthquake and tsunami (2011) in Japan and the Gorkha earthquake (2015) in Nepal have shown deficiency in structures which resulted in major loss of human lives and economy. Most of these structures were poorly designed with no seismic detailing. It has been observed in many reinforced concrete structures, structural failure could be due to insufficient seismic detailing in columns, load bearing walls and beam-column joints which causes major destruction. Damages and collapse of non-seismic detailed structures can be seen in Figure 1.1 and Figure 1.2.

Reinforced concrete buildings constructed in 1980's were designed mostly for gravity loads without seismic detailing. Such structures are extensively available worldwide in seismic prone regions. The major components of the reinforced structures which plays an important role in integrating the system and overall stability are beam-column joints (BCJs).

Figure 1.1: Damages due to earthquake in Nepal (2015)

Figure 1.2: Damages due to earthquake in Turkey

Due to the lack of seismic detailing in BCJs of these reinforced structures there is risk of significant loss of human lives and economy during seismic events. It has been reported continuously by researcher that BCJs contribute a lot in loss of vertical load carrying capacity of gravity load designed structures because such joints were designed to resist gravity load without considering the reversal load and redistribution of load when subjected to earthquake. Exterior joints in these structures shows more damages in such an events as compared to interior BCJs because they are less confined, axial loads are less as compared to interior BCJs, torsional effect because they are far away from center of rigidity. Figure 1.3 shows typical BCJs failure during earthquake.

Figure 1.3: Typical BCJs during earthquake in Turkey (1999) Algeria and (2003)

There are two major failure mechanism in BCJs 1) shear failure and 2) end anchorage failure. The mostly observed failure mechanism of the two is shear failure which is caused by the shear stress in the joint because of resultant moments and the shear force from the member ends. These stresses can be resisted by strut and tie mechanism by providing shear reinforcement. However, majority of structures constructed prior to the seismic designed codes are lack of shear reinforcement.

1.2 Seismicity of Kingdom

The Arabian Peninsula is frequently strike by earthquake in past few years and the north, east and western border of this region is near to seismic active zone. The Arabian plate includes Yemen, some part of Iran, Syria and Gulf states strikes with the Turkish plate i.e. mountains of Anatolia and Iranian plate i.e. Zagros mountains. This strike causes movement of Arabian plate by 2 centimeters every year which causes expansion in Red Sea and movement of Arabian plate in western region.

This is near the Afar Triple Junction as shown in Figure 1.4, which includes three divergent boundaries, one tearing the African continent apart, one moving the Saudi Peninsula away from Africa, and one moving the Indian Ocean and islands away from Africa. At the triple junction, the Earth's crust is slowly being ripped apart as shown in Figure 1.5 which causes continuous earthquakes and fissures deeply.

Figure 1.4: Afar Triple Junctions

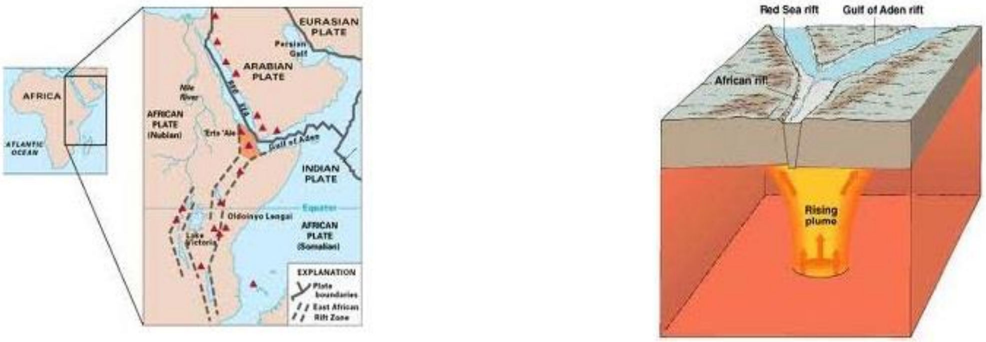

Figure 1.5: Triple Junction Ripped due to Earthquakes and Fissures

Jeddah is near the Red Sea fault which is right in the middle and rides along the Red Sea. Not too many strong earthquakes from the Red Sea fault line do much damage in Jeddah. But in late 2005, 163 earthquakes of magnitudes greater than 4 ML were recorded. The epicenter of the quake was right next to Jeddah about 70 kilometers from the coast line as shown in Figure 1.6.

Figure 1.6: Epicenter near Jeddah

The quake was only a 5.5 on the Richter scale, but it lasted for 2 minutes which is what caused all the destruction. The primary waves lasted the longest: 1 whole minute. The secondary waves and the surface waves each lasted 30 seconds.

In 2005 Saudi Geological Survey was assigned to monitor seismic activity in the region by Saudi cabinet. The Saudi Geological Survey includes the centers affiliated to King Abdul Aziz City for Science and Technology, King Saud University, King Abdul Aziz University, and King Fahd University for Petroleum and Minerals.

In 2007 Saudi Building code (SBC 301) committee decided to divide The Kingdom of Saudi Arabia into seven seismic regions as shown in Figure 1.7.

Figure 1.7: Seismic Zones of Saudi Arabia (SBC 301)

All large cities in western province which includes region 3 and 6 as well as eastern province which includes region 2 and 5 are prone to moderate earthquake. Every year population of Saudi Arabia is increasing and new cities are under development, so moderate earthquake may cause devastating damage to the human lives and economy.

1.3 Problem Statement

Recent earthquake events in moderate seismic regions of Saudi Arabia such as Otaibah, Makkah (2005), Haradh, Eastern Province (2006) , Al-Hadama, Al-Amid, Al-Qarasa and Yanbu (2009), Eastern Province (August,2010) have led to concers the safety of structures built with non-seismic detailing in Saudi Arabia. Majority of these structures are designed only for gravity and wind loads with limited lateral load resistance.

In some cases, for relatively taller buildings in Saudi Arabia the design may have considered lateral forces due to wind loads, it is still important to retrofit these structures, since higher mode effects sometimes lead to soft-story mechanisms in the mid to upper levels of the building.

This study has resulted in the development of a research collaboration between KFUPM and Istanbul Technical University (ITU) in Earthquake Engineering and it involves the study of shear deficient BCJs and strengthening of shear deficient BCJs by using superelastic shape memory alloys (SMAs) sheets.

1.4 Objective of Study

The primary goal of this study is to examine the response of typical detailed shear deficient BCJs and SMAs retrofitted BCJs under cyclic loads. The BCJs are representing the typical detailing used in Saudi Arabia. To achieve the objective of the study following tasks has been carried out.

- Testing of three shear deficient BCJs specimen under monotonic, cyclic and reversed cyclic loadings.

- Testing of four SMAs sheet retrofitted BCJs under cyclic and reversed cyclic loadings.

- Finite element simulations of shear deficient BCJs and SMAs sheet retrofitted BCJs in ABAQUS environment.

CHAPTER 2

LITERATURE REVIEW

2.1 Introduction

Beam-column joints in RC structures are pivotal section for transfer of load from beam to column. During a seismic event BCJs undergoes to large shear stresses cause by moments and shear force from the member ends. Non-seismic detailing of BCJs will not withstand these shear stresses and may cause the global failure of structures even though other structure elements are fulfilling the design requirements.

In the past few decades researchers are involved in studying the behavior of BCJs through experimental program and analytical studies. Following section will give the detail of recent studies carried out in different parts of the world.

2.2 Recent Studies on Beam-column Joints

Salloum et al. (2009) studied the seismic behavior of three half-scaled non-seismic detailed and FRP retrofitted BCJs. The specimens were without transverse reinforcement as used in old construction. Figure 2.1 shows the reinforcement detail and schematic representation of FRP beam-column joint. Figure 2.2 shows the crack pattern in control specimen and failure of CFRP repaired BCJs.

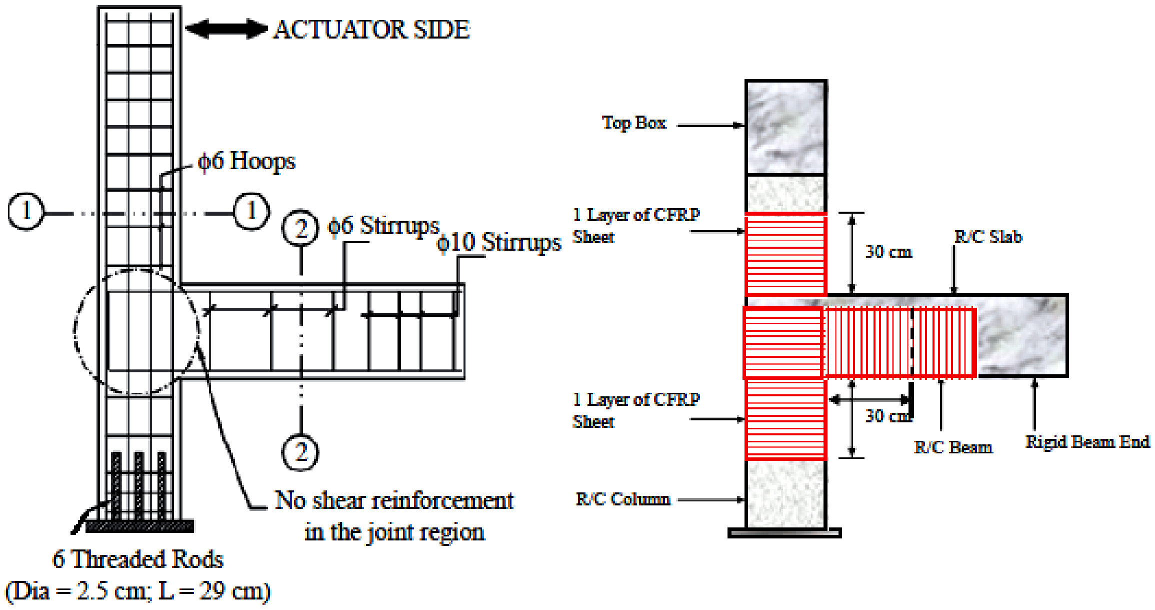

Figure 2.1: Reinforcement details and Schematic representation of FRP repaired joint (Salloum et al., 2009)

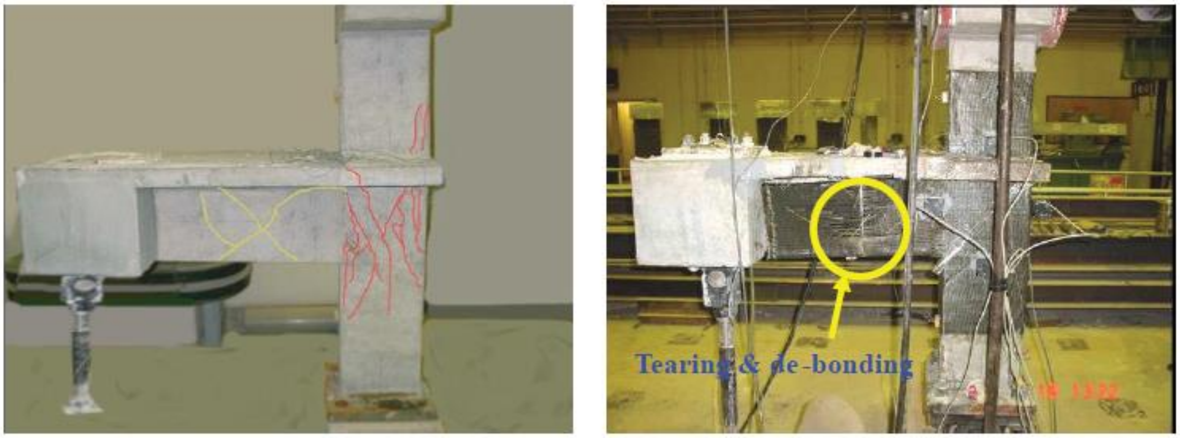

Figure 2.2: Cracks pattern in control BCJ and failure of CFRP repaired BCJ (Salloum et al., 2009)

The CFRP retrofitted BCJs showed significantly improvement in ductility. It has been observed that repaired BCJ showed 39 % more ductility as compared to control specimen whereas retrofitted specimen showed 34 % enhancement w.r.t. control specimen. Figure 2.3 shows the enhancement in ductility of repaired and retrofitted specimens as compared to control.

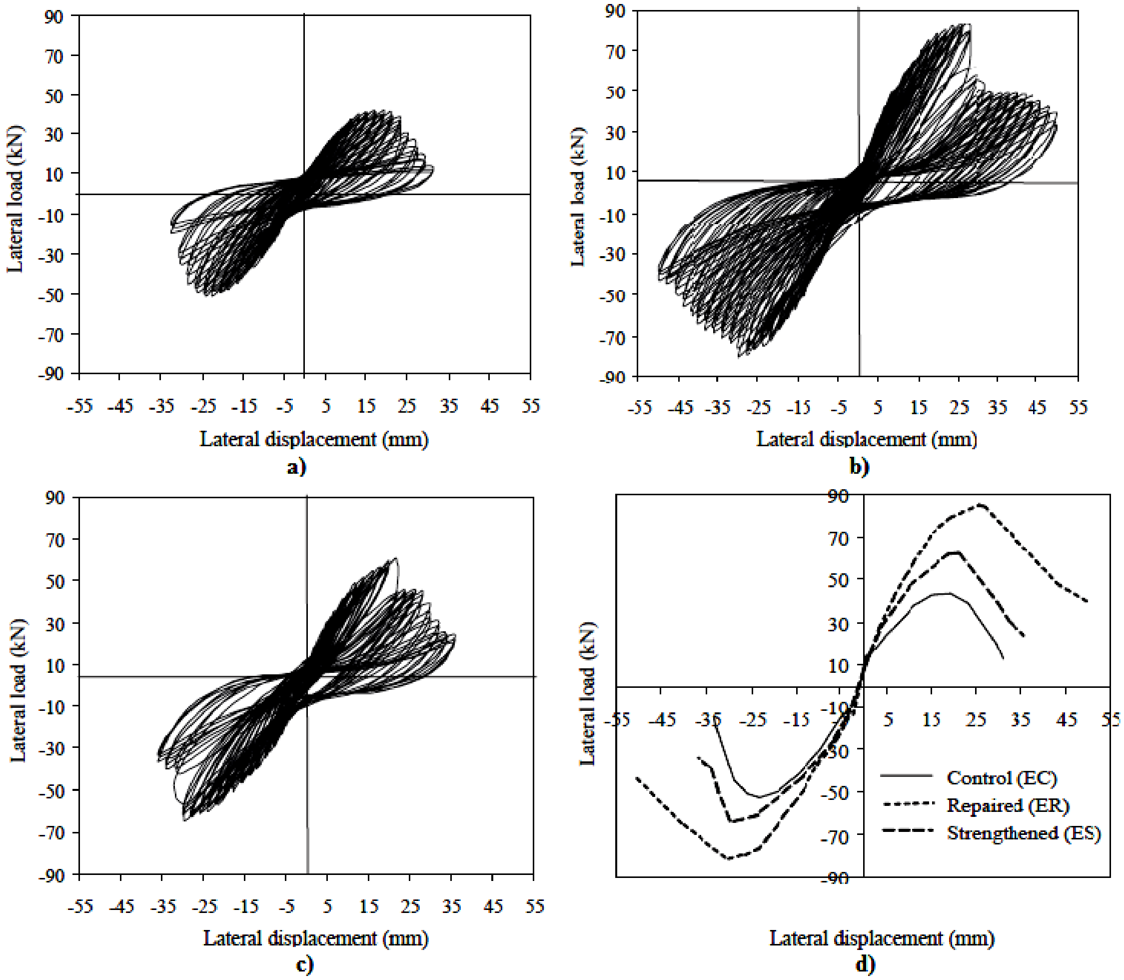

a) b) c) d)

Figure 2.3: Lateral Load-Deflection curves a) Control b) Repaired specimen c) Retrofitted specimen and d) Envelope of Hysteresis loops

Kien et al. (2010) investigated eight exterior reinforced BCJs which include non-seismic, seismic and 6 retrofitted BCJs specimens. Figure 2.4 shows the detailing of BCJs used in their studies. Kien et al. studied focus on different configuration of CFRP sheets to get useful way of enhancing the lateral load capacity and ductility of BCJs. Figure 2.5 shows the configuration used by Kien et al. for retrofitted BCJs.

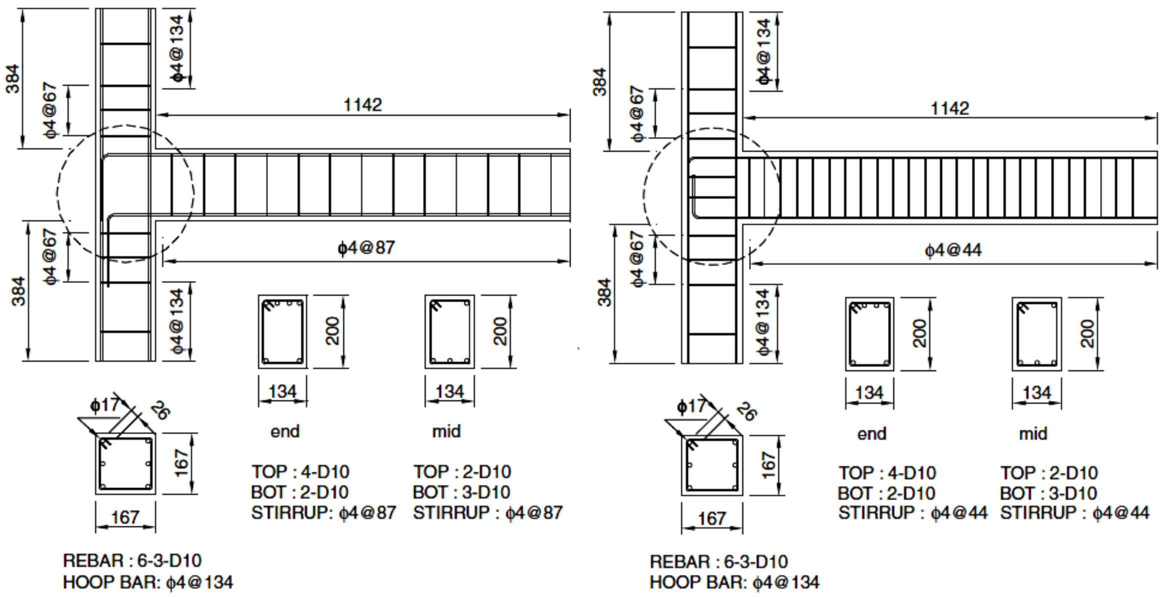

Figure 2.4: Non-seismic and Seismic detailing of BCJs (Kien et al., 2010)

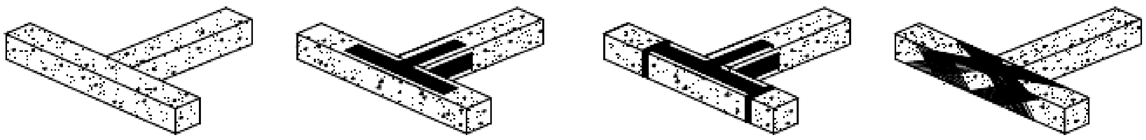

a. NS and SD b. RNS-1 c. RNS-2 d. RNS-3

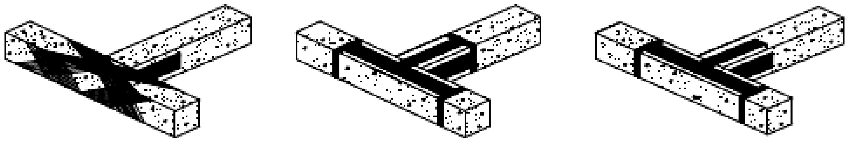

e. RNS-4 f. RNS-5 g. RNS-6

Figure 2.5: CFRP configuration retrofitted BCJs (Kien et al., 2010)

It has been observed that by the application of CFRP composites, the non-seismic BCJs got improvement in lateral strength and ductility especially with X-shaped configuration and strips on column and two sided CFRP sheets layers on beam. Figure 2.6 shows the load-displacement hysteresis envelope curves for tested specimens.

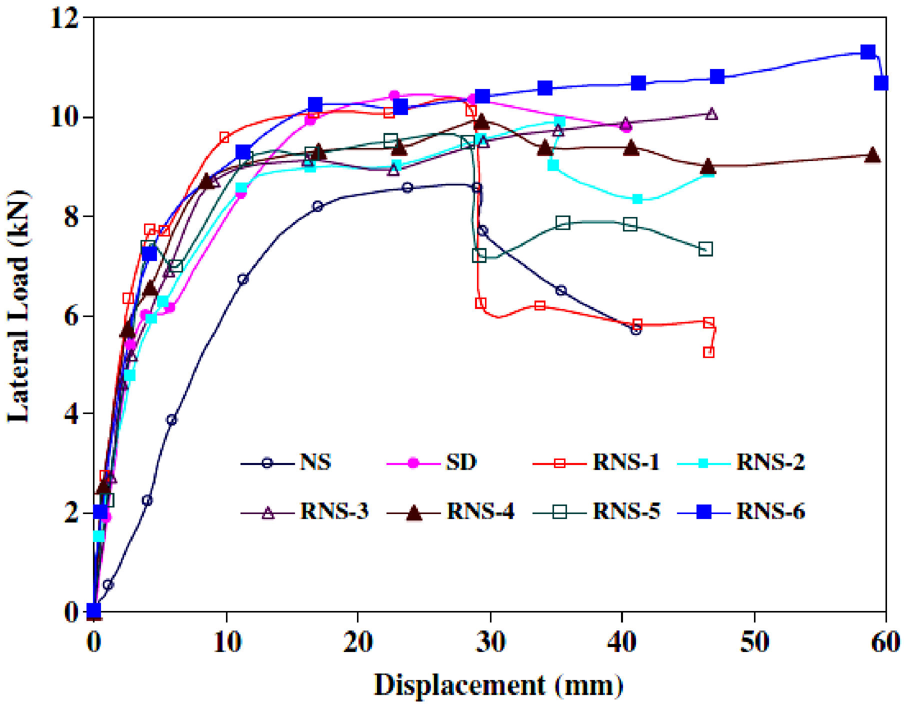

Figure 2.6: Lateral Load-Displacement Positive Hysteresis Envelope (Kien et al., 2010)

Samsal et al. (2011) studied the behavior of seismic retrofitted damage BCJ with sub-assemble of GFRP wrapping and steel jacketing under reverse cyclic loading. Their study focused on repair and retrofitting of damage beam-column joint. Figure 2.7 shows the reinforcement detailing of SP-3 (Non-ductile specimen) and schematic diagram for test setup used. First they carried out test on non-ductile BCJ and specimen were damaged significantly. Later on damaged specimen was repaired and retrofitted by hybrid scheme consist of steel plate jacket and GFRP wrap. Figure 2.8 shows the schematic diagram for retrofitted specimen SP-3R

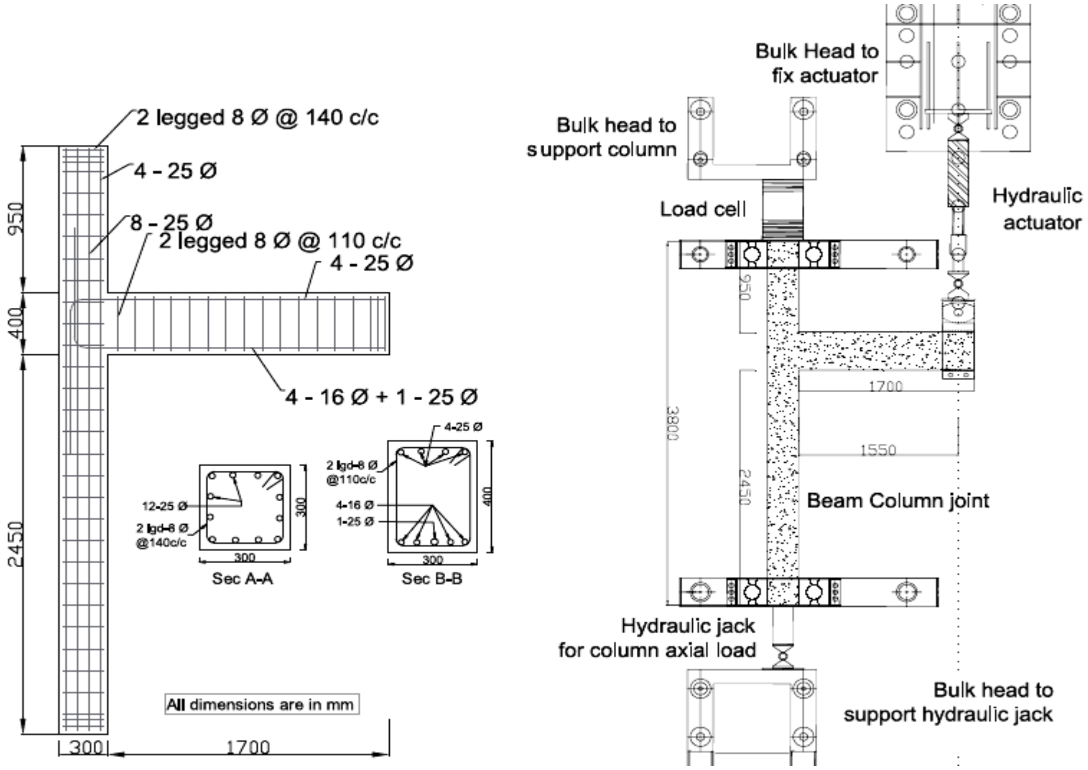

Figure 2.7: Rebar Detailing of Non-ductile SP-3 (left) and Test Setup Schematic Diagram (right) (Samsal et al., 2011)

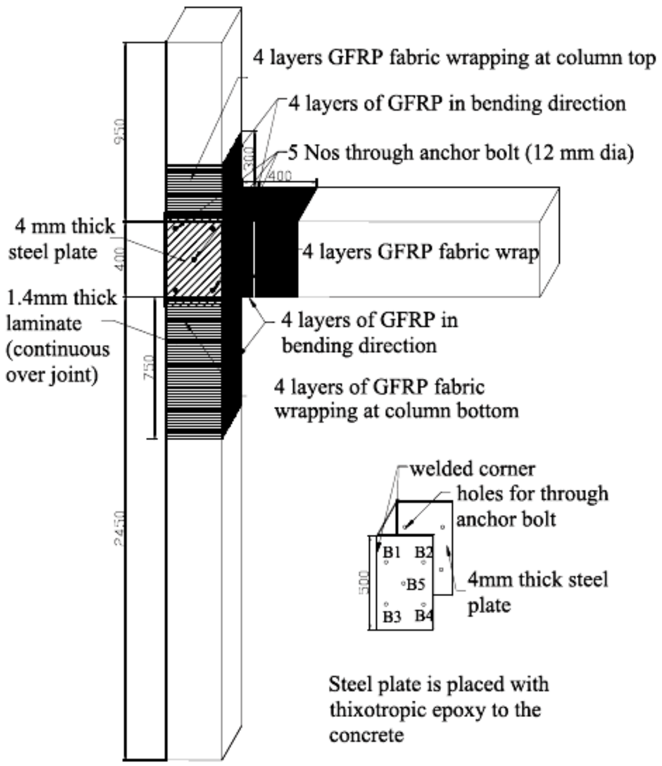

Figure 2.8: Schematic diagram for repair and retrofitted specimen SP-3R (Samsal et al., 2011)

It has been noticed that retrofitted BCJ regained original properties as well as showed more ductility as compared to non-seismic BCJ. Figure 2.9 shows the crack pattern and rupture of GFRP in control and retrofitted specimen at ultimate load. Figure 2.10 shows Load-deflection hysteresis curve for SP-3 and SP-3R

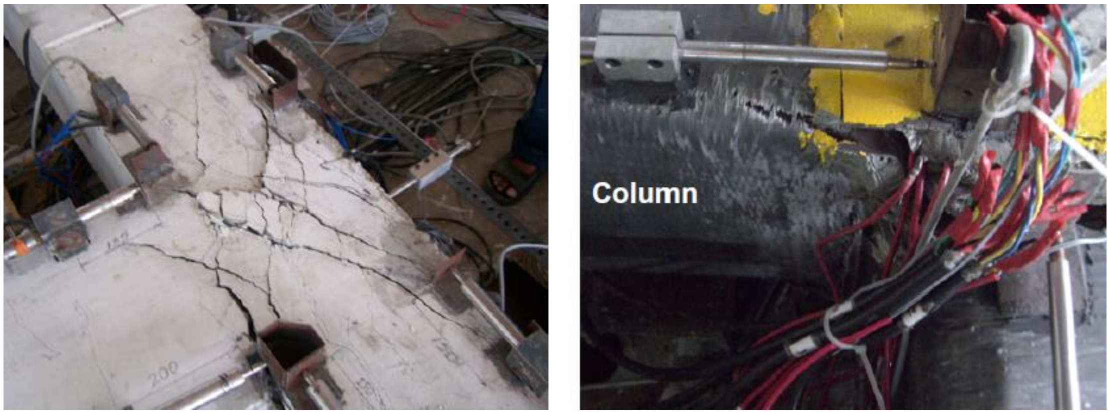

Figure 2.9: Crack Pattern for SP-3 (Left) And Rupture of GFRP at Ultimate Load for SP-3R (Right) (Samsal Et Al., 2011)

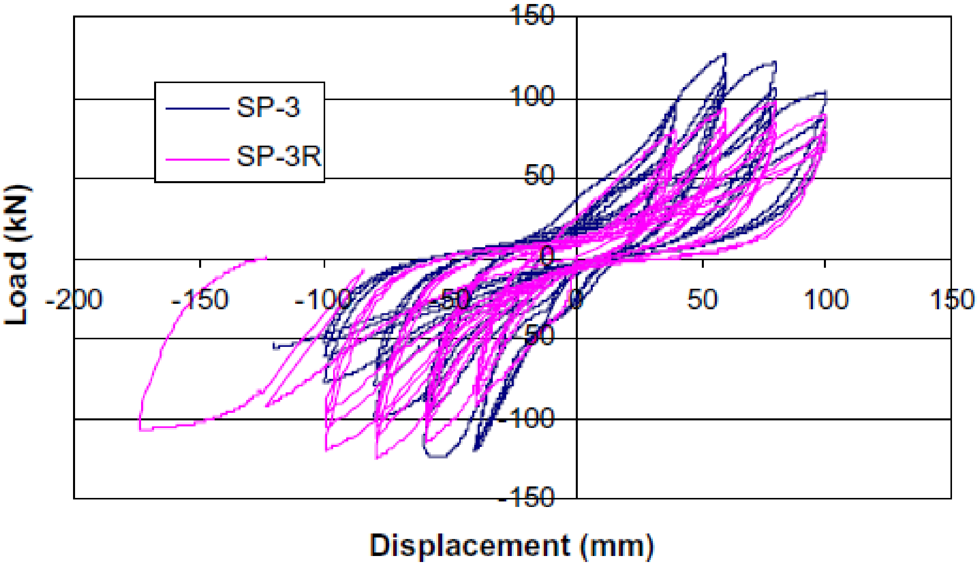

Figure 2.10: Load-Deflection Curve for Control (SP-3) and Retrofitted Specimen (SP-3R) (Samsal Et Al., 2011)

Ludovico et al. (2012) studied the experimental behavior of non-seismic full scale reinforced concrete BCJs retrofitted with FRP. Their study included one non-seismic BCJ (T_C3) and two retrofitted BCJs with light CFRP strengthening (T_FRP) and strong CFRP strengthening (T_FRP2). Figure 2.11 shows the reinforcement detailing for all specimens and test setup used in experimental program. Figure 2.12 shows the schematic diagram for retrofitted specimens.

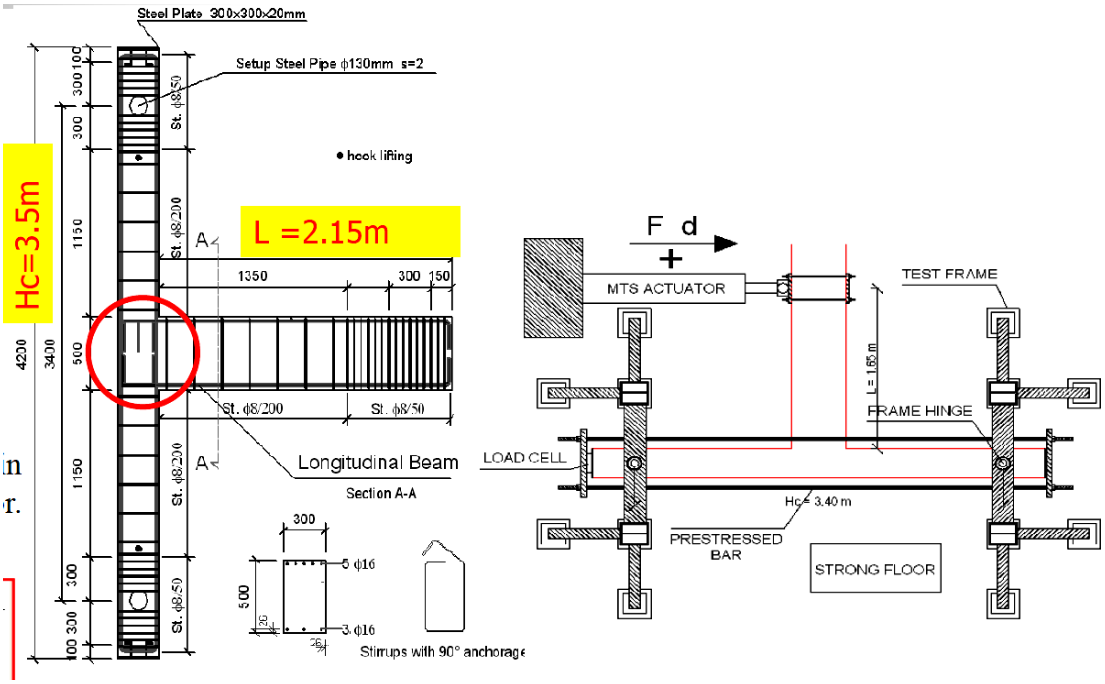

Figure 2.11: Reinforcement detail for all specimen and test setup used in experimental program (Ludovico et al., 2012)

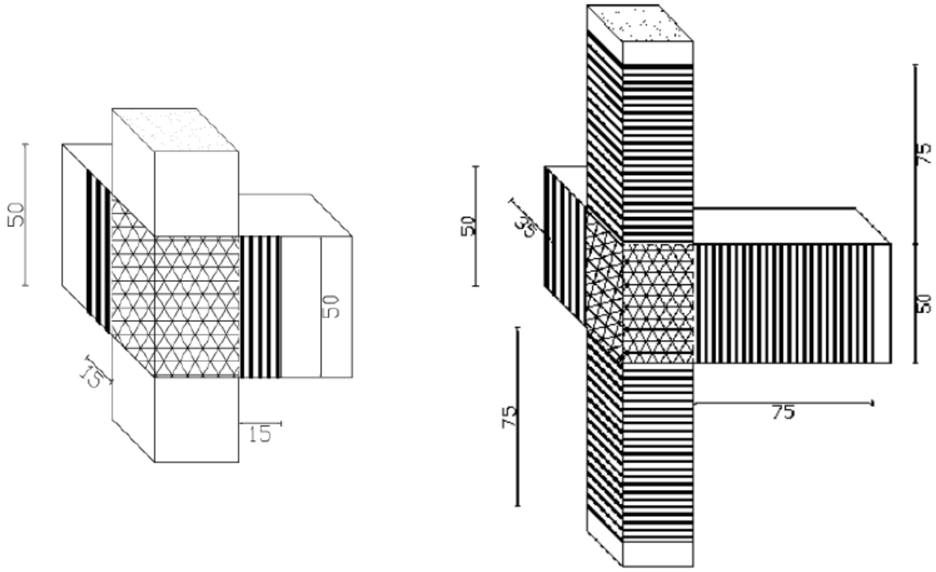

Figure 2.12: Schematic Diagram of retrofitted specimen T_FRP (left) and T_FRP2 (right) (Ludovico et al., 2012)

It has been observed that light CFRP strengthening and strong CFRP strengthening enhances the joint shear strength to 20% and 28 % as compared to control specimen. Figure 2.13 shows the hysteresis envelope of control and retrofitted specimen.

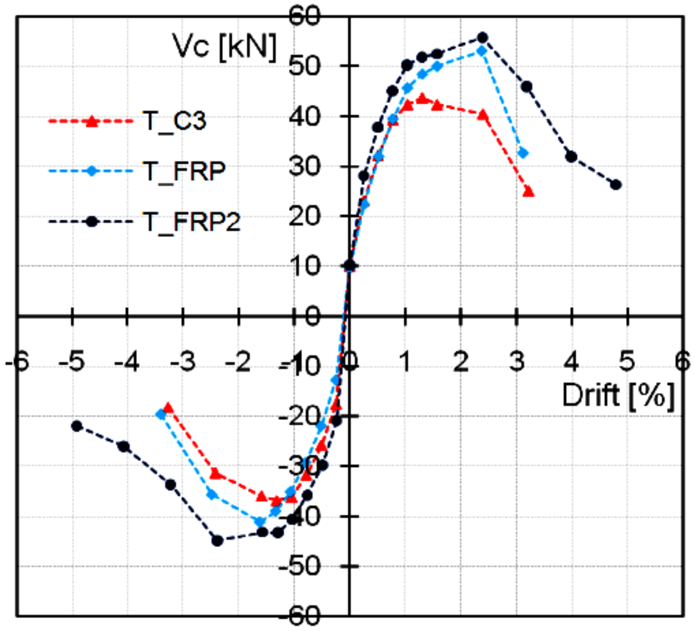

Figure 2.13: Hysteresis envelope for control and retrofitted specimen (Ludovico et al., 2012)

Jemaa et al. (2013) studied the seismic strengthening of damage BCJs using CFRP. They performed seven tests on three specimens namely JA2, JB2 and JC2. Figure 2.14 shows the reinforcement details for control specimens. First of all 3 control samples were tested under reverse cyclic loads and their seismic capacity was assessed. After that they replaced the joint core concrete of JA2, JB2 and JC2 with new high strength concrete and apply the CFRP sheets on them which were named as JA2RF, JB2RF and JC2RF. These specimens were again subjected to reverse cyclic loading and the seismic enhancement were recorded. Later on they removed the core concrete and CFRP sheets from JB2RF with new concrete which was named as JB2RF and subjected to reverse cyclic loading. It has been noticed that core concrete replacement enhances the joint capacity to 44% whereas with the application of CFRP along with new concrete the strength increased to 65 % as compared to bare specimen. Figure 2.15 shows the hysteresis envelope for control and retrofitted specimens.

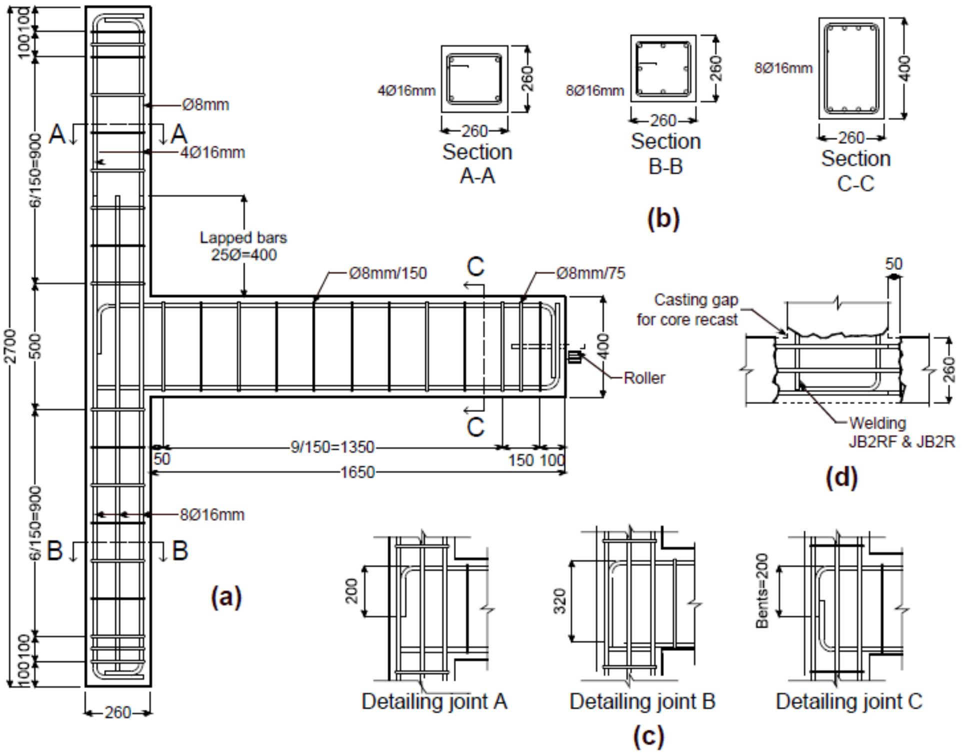

Figure 2.14: Reinforcement detail for bare specimens (Jemaa et al., 2013)

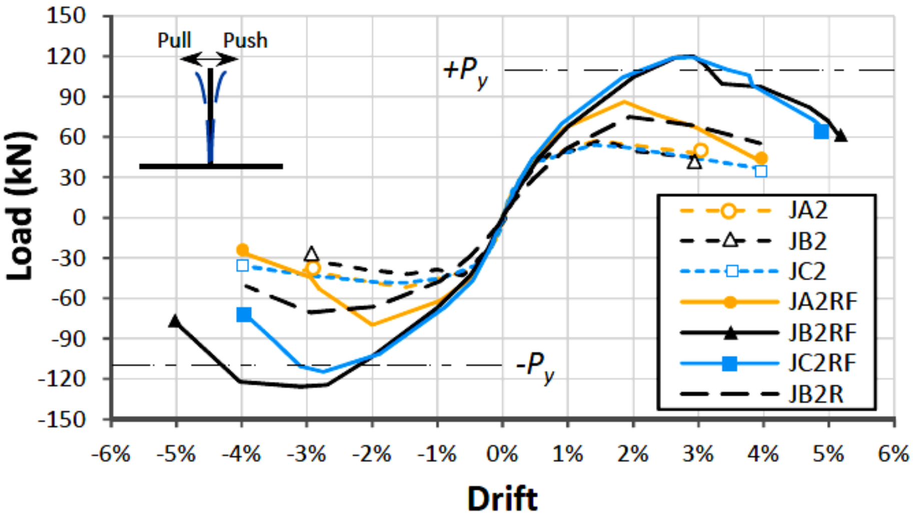

Figure 2.15: Hysteresis envelope of control and retrofitted Specimen (Jemaa et al., 2013)

Realfonzo et al. (2014) studied the cyclic behavior of reinforced concrete BCJs strengthened with FRP. They investigated the seismic behavior of 8 non-seismic detailed full scale specimens with two set of reinforcement configurations as shown in Figure 2.16. Each set contained control specimen and 3 CFRP retrofitted specimen. Out of eight damaged specimens 3 specimens were repaired and retrofitted using FRP and tested again. They studied the efficacy of different FRP retrofitting schemes and got promising results. Figure 2.17 shows the schematic diagram for retrofitting strategies used in their experimental program. All specimens were subjected to reverse cyclic loading. Figure 2.18 shows the hysteresis response and envelope of control and strengthened specimens. Figure 2.19 shows the hysteresis response and envelope of control and upgraded specimens.

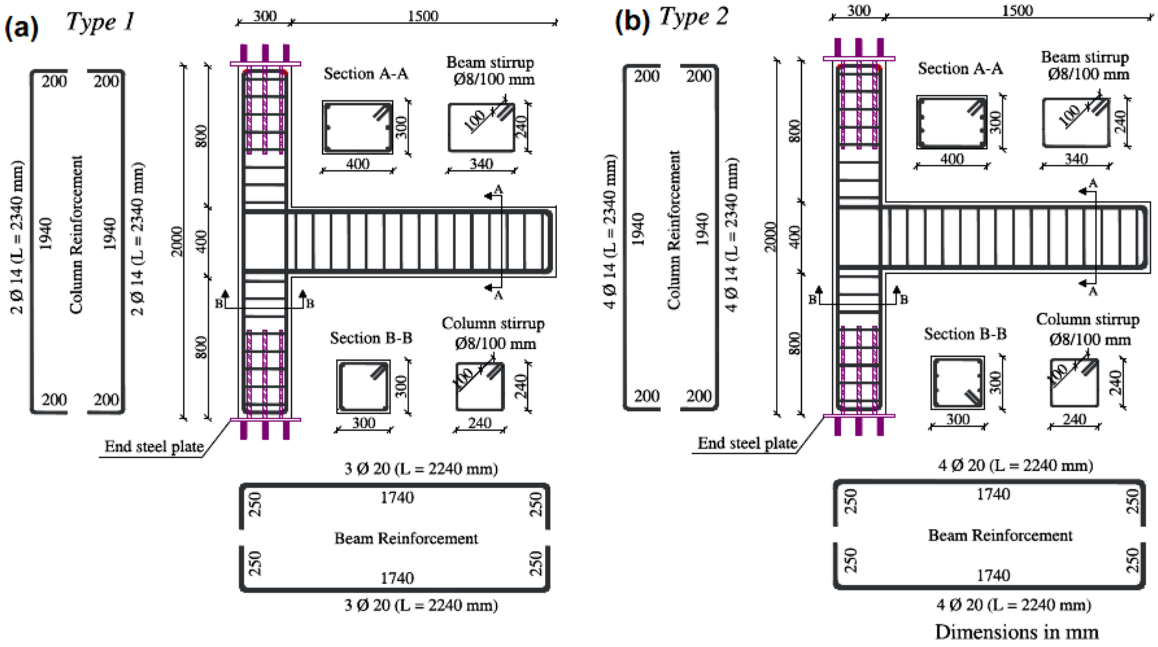

Figure 2.16: Reinforcement detailing for two sets used in experimental program (Realfonzo et al., 2014)

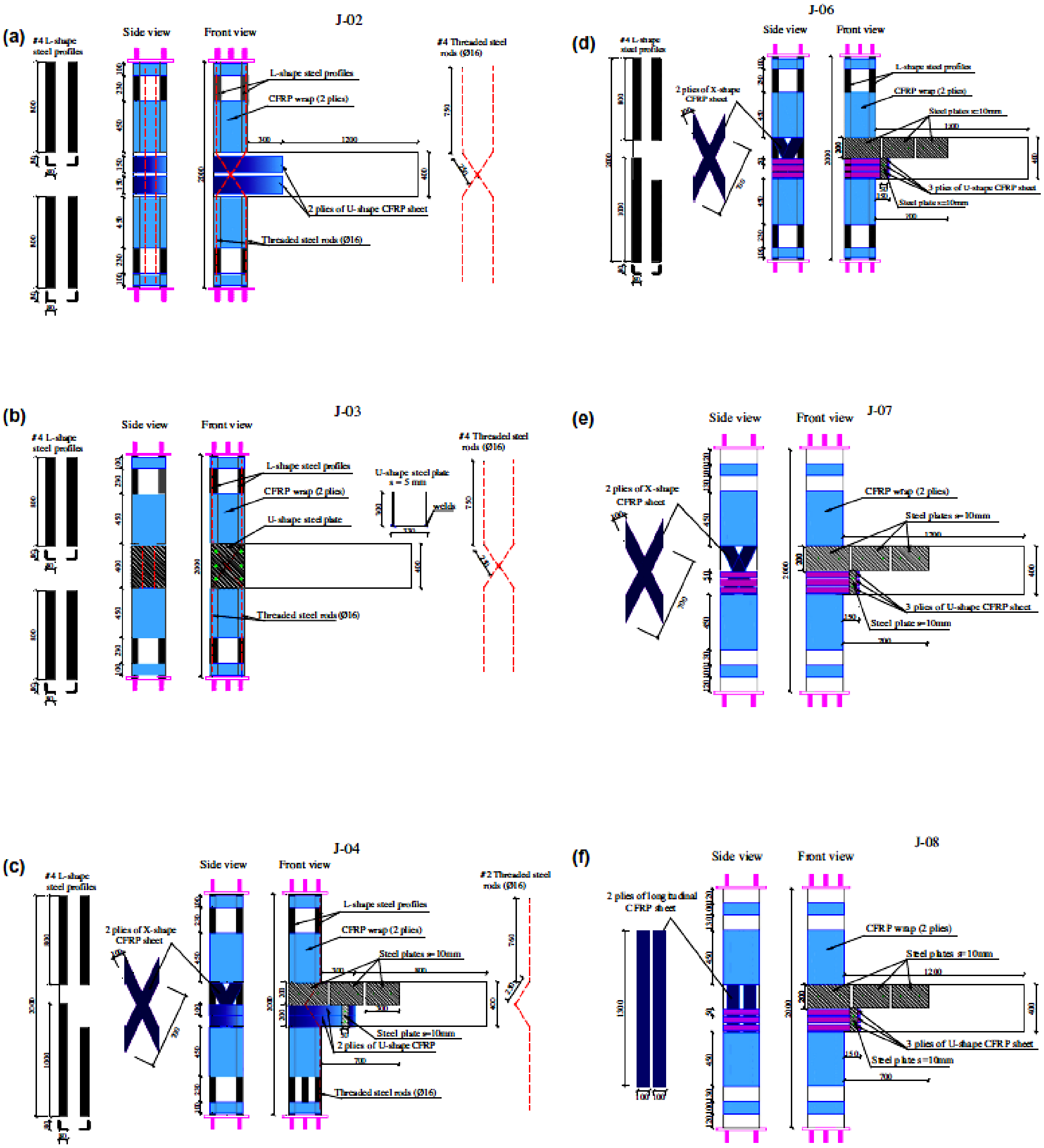

Figure 2.17: Schematic diagram for retrofitting schemes (Realfonzo et al., 2014)

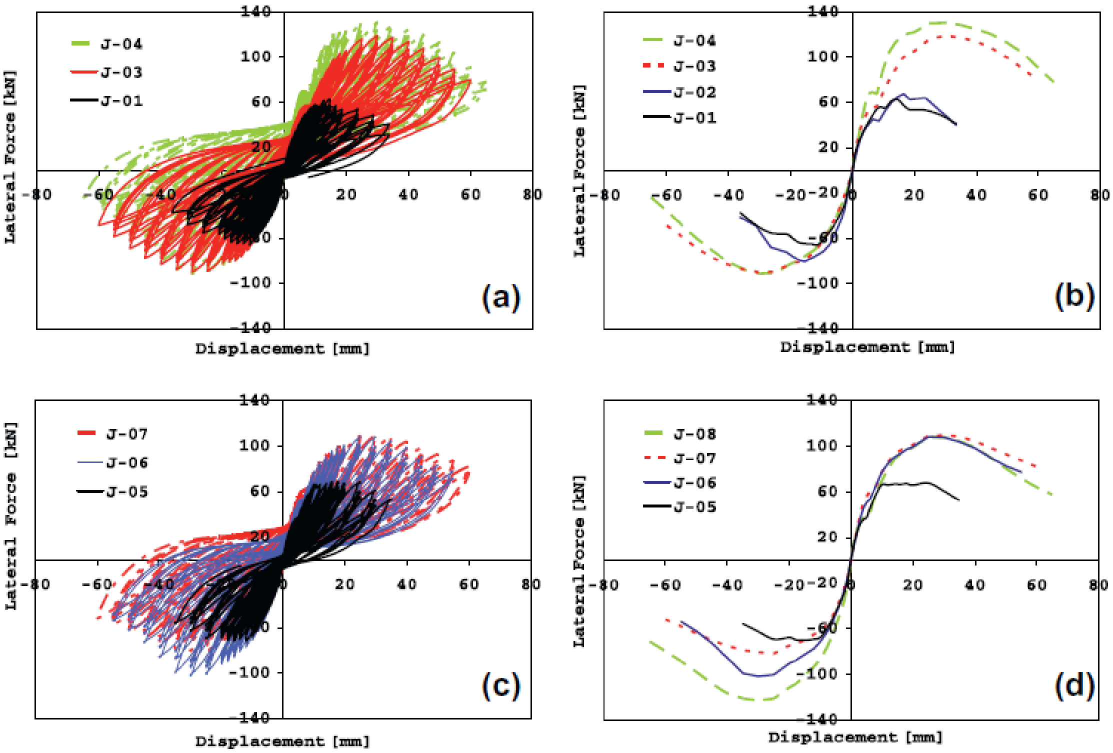

Figure 2.18: Hysteresis response and envelope of bare and strengthened Specimen (Realfonzo et al., 2014)

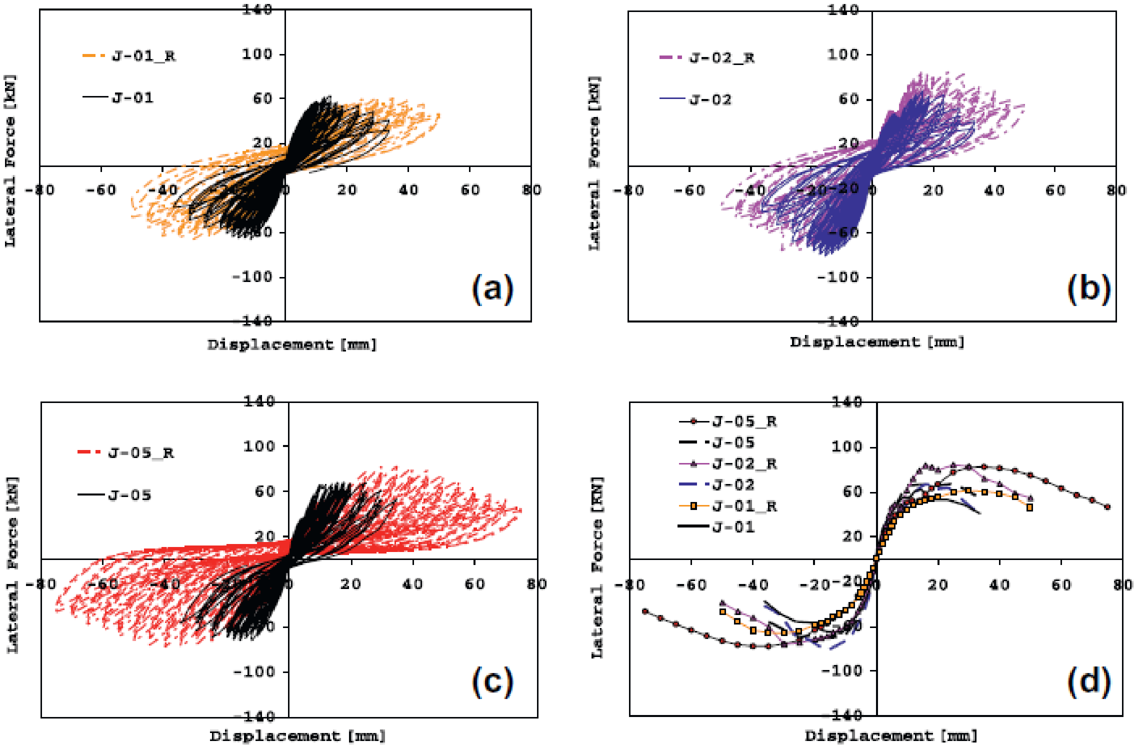

Figure 2.19: Hystersis response and envelope of control and upgrade specimens (Realfonzo et al., 2014)

Hadi and Tran (2015) evaluated the new method of strengthening of BCJs by bonding new concrete with old concrete along with FRP wraps. Four specimens which include control and three strengthened joints with different CFRP ratios were subjected to reverse cyclic loading. Figure 2.20 shows the reinforcement details and schematic diagram for testing setup. Figure 2.21 shows the schematic diagram for retrofitting strategy.

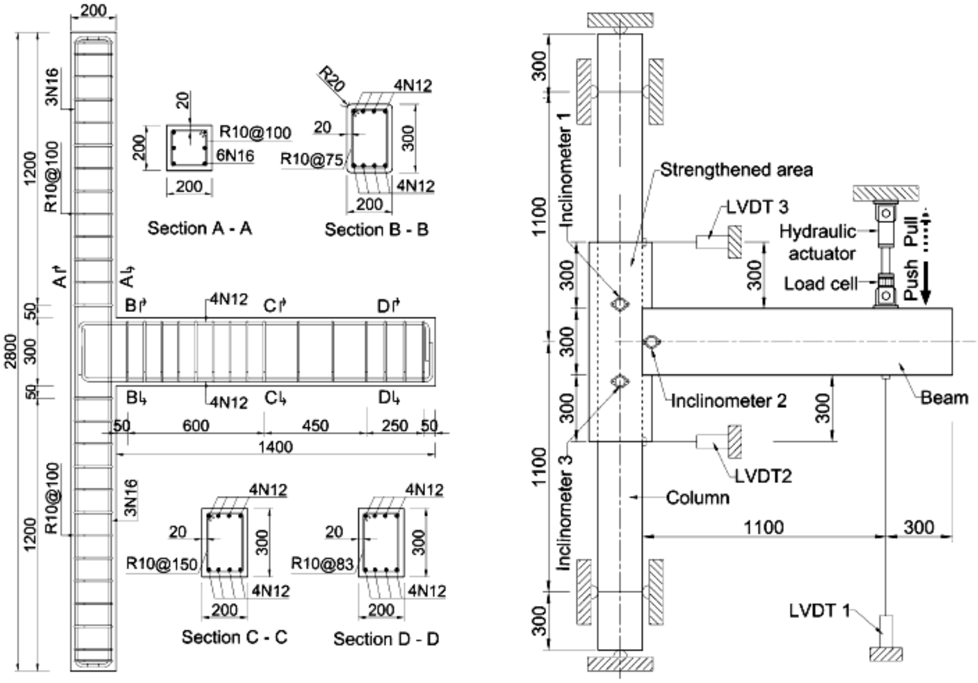

Figure 2.20: Reinforcement detailing and Schematic diagram for testing setup (Hadi and Tran, 2015)

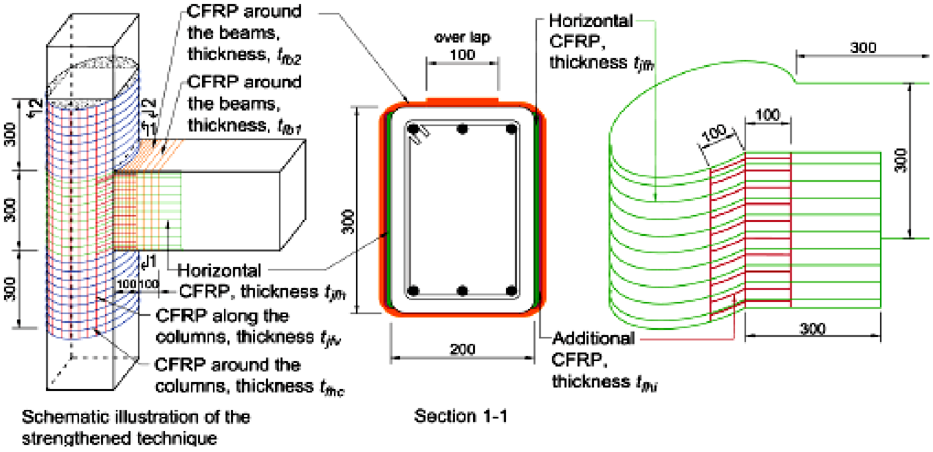

Figure 2.21: Schematic Diagram for retrofitting strategy (Hadi and Tran, 2015)

Different mode of failure, enhancement in shear strength were observed by using different CFRP wrap ratios as shown in Figure 2.22 and Figure 2.23.

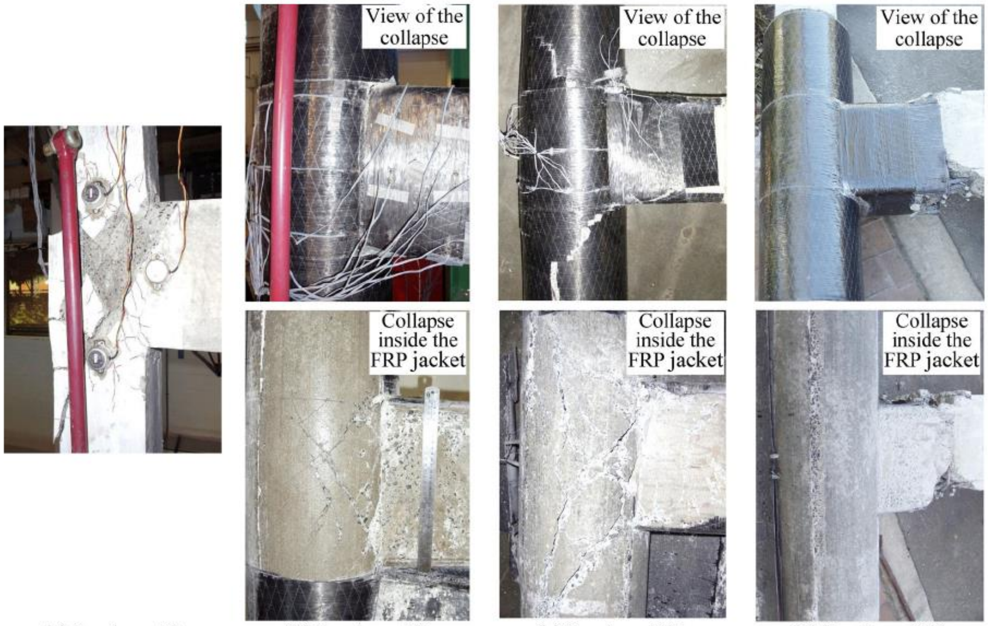

(a) Specimen T0 **(b)** Specimen TS **(c)** Specimen TS1 **(d)** Specimen TS2

Figure 2.22 : Ultimate failure of control and strengthened specimens

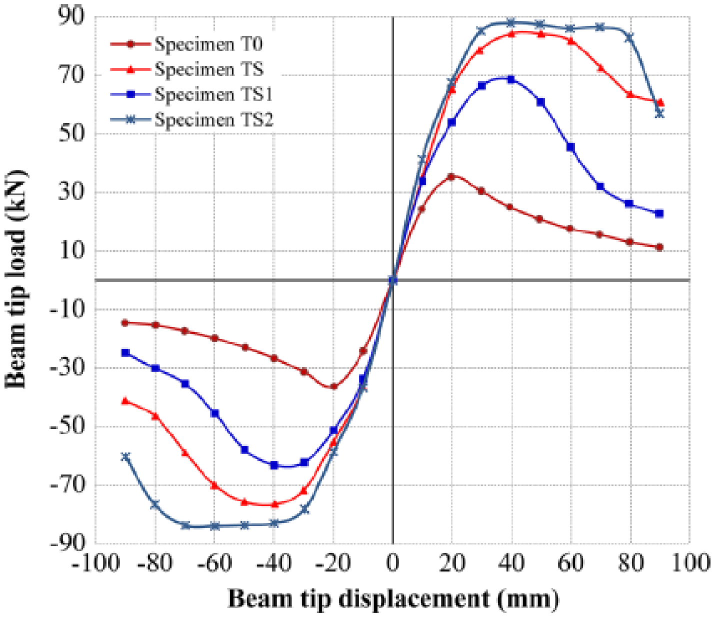

Figure 2.23: Hysteresis envelopes of control and strengthened specimens

2.3 Shape memory Alloys (SMAs)

Some class of metallic alloys have special ability to memorize their shape at low temperature can recover large deformations at low temperature on thermal activation. These alloys are named as shape memory alloys (SMAs). SMAs have shape memory effect (SME) which was first discovered by Chang and Read in 1951 in gold-cadmium (Au-CD). But this material got popularity when Buehler and Wiley discovered nickel-titanium alloy in 1961 called NiTi. The binary ratios for these alloys was 55 % to 45 %.

There are two characteristics of SMA 1) SME and 2) pseudoelasticity. SME helps in recovering large mechanically induced strains (up to 8 %) at low temperature with slightly increase in temperature whereas pseudoelasticity is the ability of material to undergo large strain during loading and recover on unloading in hysteresis loop at higher temperature. The behavior of SMA depends on the crystal structure, stress, temperature and history of material. When there is no-stress level the SMA exist in austenite phase and when there is stress condition the SMA exist in martensite phase. The crystal structure of SMA is shown Figure 2.24

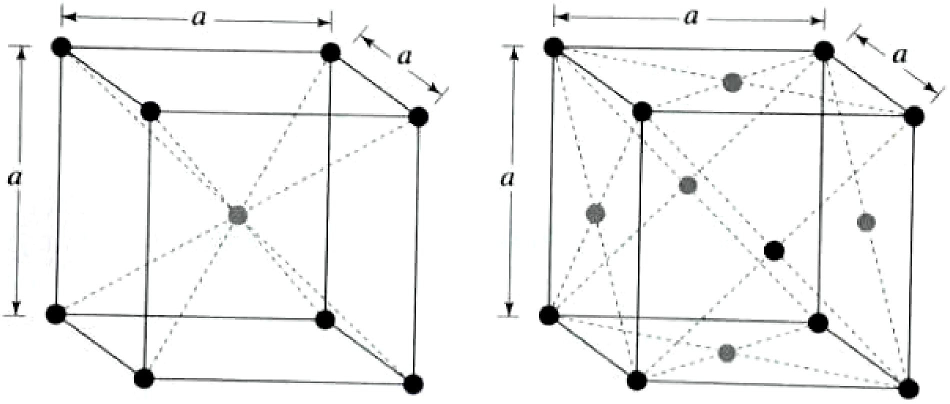

Figure 2.24: Crystal Structure of SMA Austenite (left) and Martensite (right)

There are four important temperatures related to the phase transformation occurring in SMA. The transformation temperatures are martensite start M_s, martensite finish M_f, austenite start A_s and austenite finish A_s temperatures. The temperature associated with the transformation of austenite to martensite phase are the martensite start temperature M_s, denoting the start of phase change and the martensite finish temperature M_f, denoting finish of phase change and this process is named as forward phase transformation. Similarly, the temperature associated with the transformation of martensite to austenite phase are the austenite start temperature A_s, denoting the start of phase change and the austenite finish temperature A_f, denoting finish of phase change and this process is named as reverse phase transformation. In most SMA material, $M_f < M_s < A_s < A_f$. These four temperature are determined through experiment and are also stress dependent.

The phase transformation in the SMA are induced by both temperature and mechanical stress. As this study is focused only on superelastic SMAs, so we will considered only pseudoelasticity phenomenon which is stress dependent behavior and is not triggered by temperature. A schematic diagram of the stress-strain behavior of SMA under pseudoelasticity is shown in Figure 2.25

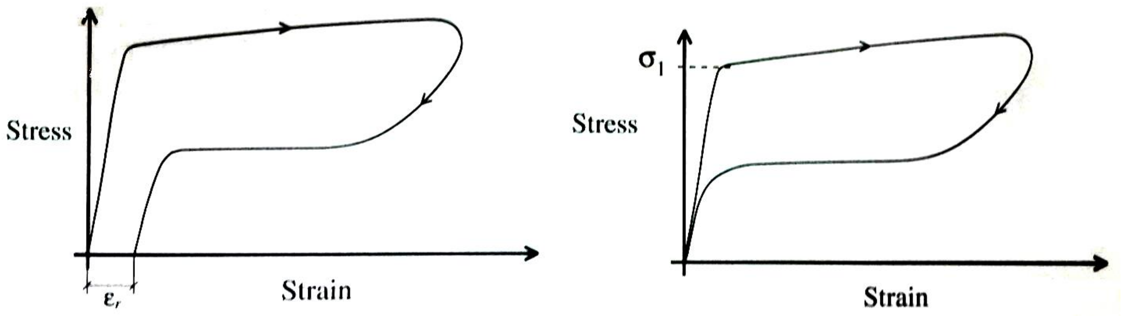

Figure 2.25: Stress-Strain behavior of superelastic SMA

Stress is applied to the SMA at a temperature above A_s, and it starts deforming elastically. When a critical stress level (σ_1) is reached the austenite phase becomes unstable and stress-induced martensite starts forming, resulting in a low stiffness region similar to the plastic deformation. This mean that the body centered cubic lattice transform in to monoclinic one, which in turns results in a macroscopic elongation. When stress is removed, the stress-induced martensite becomes unstable and transforms back in to austenite. During unloading the initial response is elastic, followed by quick recovery of strain with small change of stress, and the material transforms back to austenite phase. If the room temperature is above the austenite finish temperature A_f, the strain in the material is fully recovered. If material temperature lies between A_s and A_f than there is partial recovery of strain.

SMAs are smart and intelligent materials having potential for application as reinforcing steel in reinforced concrete smart structures. Superelastic SMAs have a unique ability to undergo large deformations under applied load, returning to a predetermined shape upon unloading. As compared to steel SMAs have a low modulus of elasticity and small hysteresis loop. This unique property of SMAs makes it amenable to use them RC structures for enhancing its ductility during seismic events.

2.3.1 Past SMAs studies in the field of Civil Engineering

DesRoches et al. (2004) evaluated the superelastic properties of NiTi SMA wires and bars under cyclic loading. They evaluated the strength, recentering ability and damping potential for wires and bars. They tested different size specimens varrying from 1.8 mm dia wire to 25.4 mm dia bar. The specimens used in their study were superelastic at normal room temperature and had very low austenite start temperature. Their study helped the future researcher to used NiTi as structural reinforcing material in concrete structures. Figure 2.26 shows the loading protocol used in their studies.

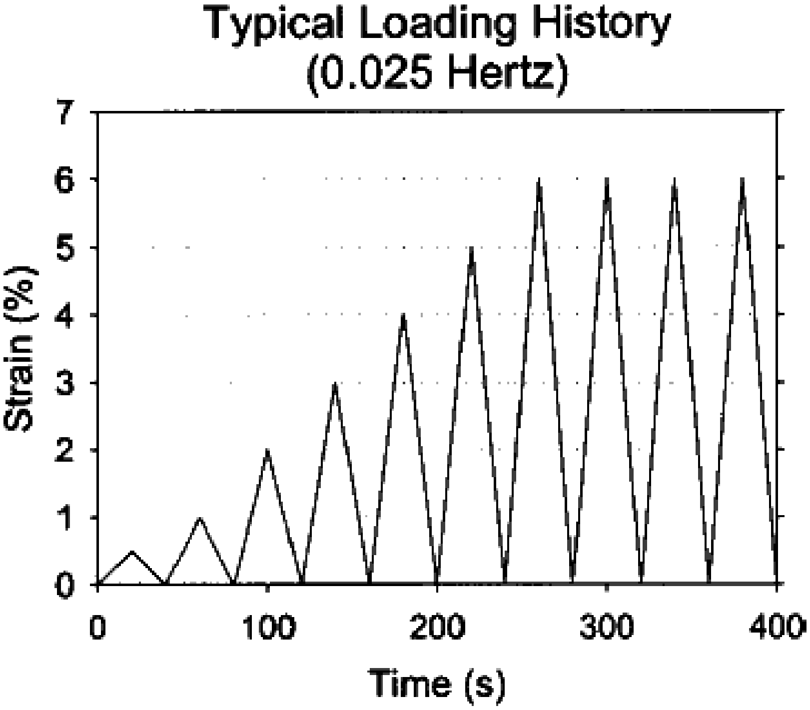

Figure 2.26: Loading Protocol for Testing (DesRoches et al., 2004)

It has been noticed that both wires and bars behaved superelastic and recovered maximam residual strain upon unloading.Also it has been observed that recentering capability is not affected by the size, but wire experiences high damping potential and strength than the SMA bars. Figure 2.27 shows the envelope of quasistatic cyclic loading.

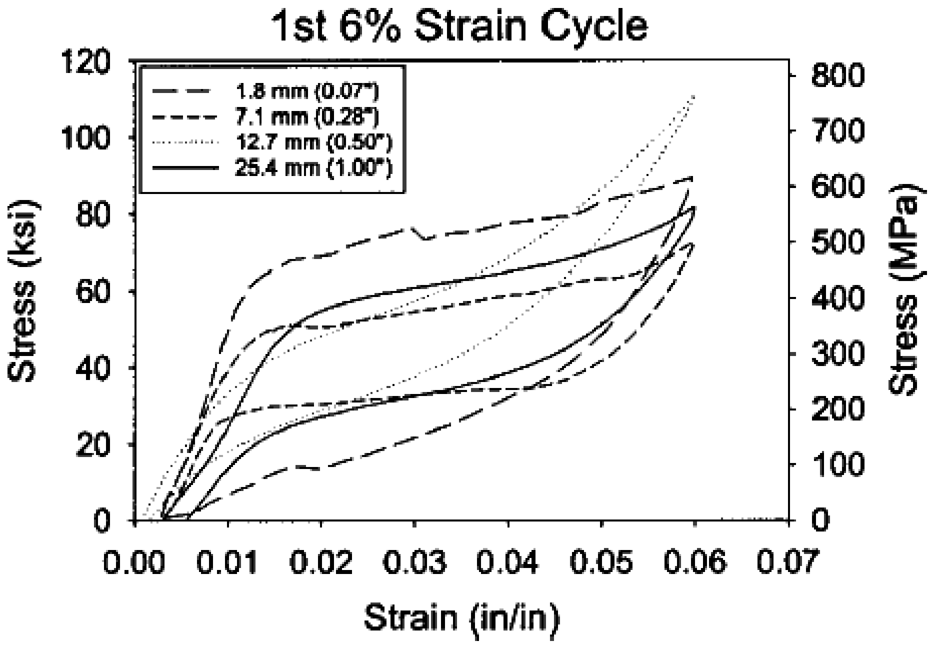

Figure 2.27: Quasistatic Cyclic Stress strain curve envelope for 1st 6% strain (DesRoches et al., 2004)

Li et al. (2006) investigated the usage of NiTi bars and wires in concrete beams. Their study focused on self-rehabilitation capacity of the structure i.e. during a seismic event the damage induced in structure can be minimized in the form of crack closure or reduction in crack width by taking the advantage of superelastic property of SMAs. They performed 3 point bending test on three RC beams which include one control (bare) specimen and two specimens with SMA stands with different configurations. Figure 2.28 shows the reinforcement detail for the 3 specimens.

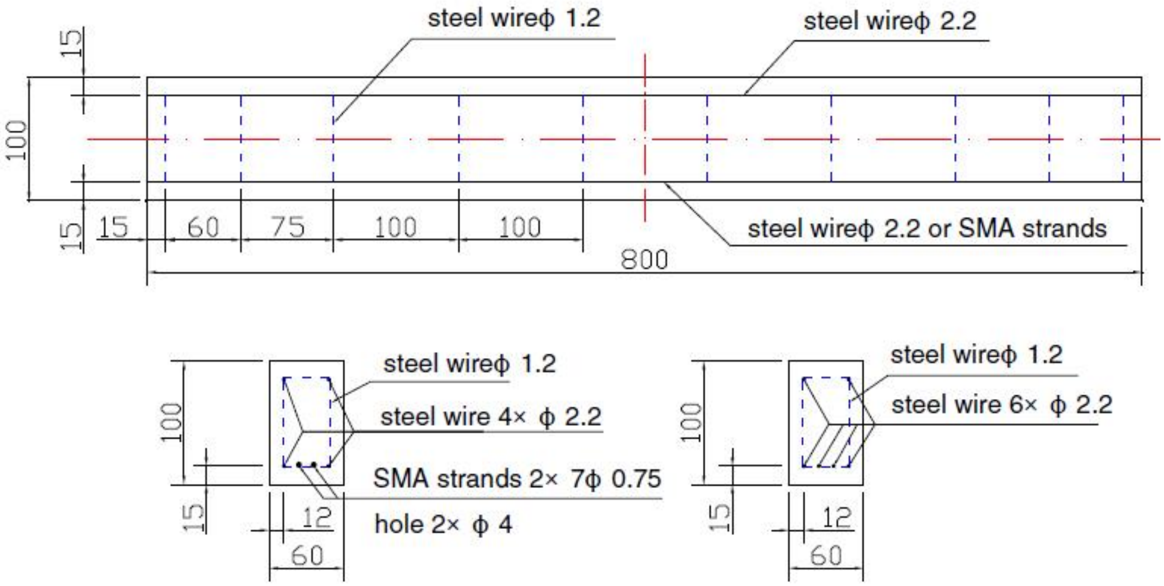

Specimen 2 Specimer 1

Specimen 3

Figure 2.28: Reinforcement detailing for specimens (Li et al., 2006)

Figure 2.29 shows the load deflection curve of specimen 1 and 2. Figure 2.30 shows the load deflection curve of specimen 3.

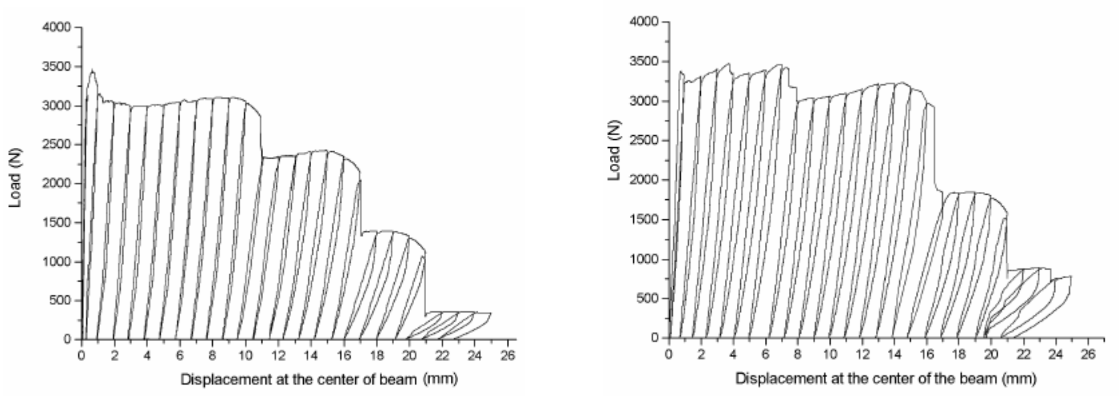

(a) Specimen 1 (b) Specimen 2

Figure 2.29: Load- Deflection curve for Specimen 1 and 2 (Li et al., 2006)

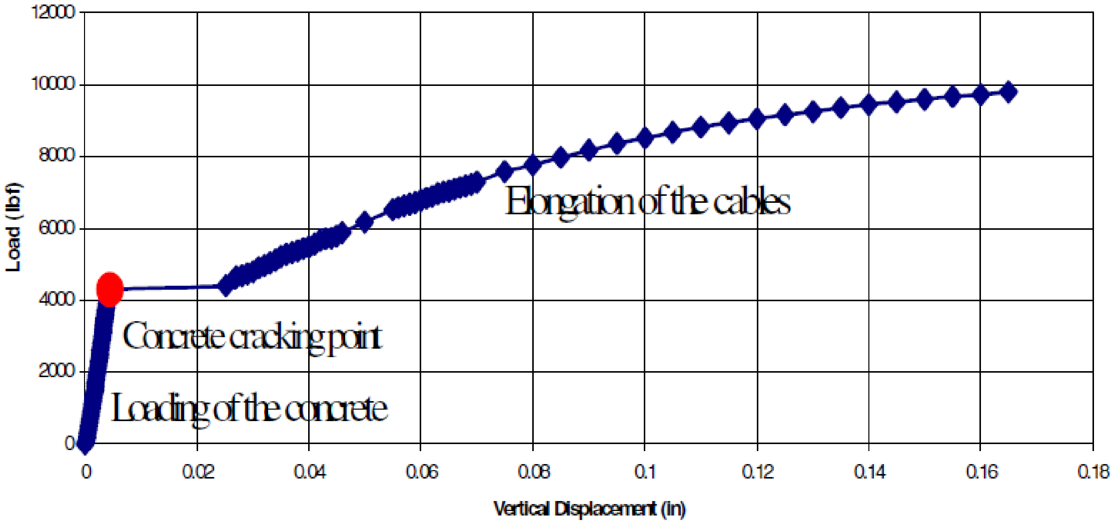

Figure 2.30: Load-deflection curve for specimen 3 (Li et al., 2006)

It has been noticed that with the usage of superelastic SMA strands with reinforcing steel in the beams, cracks width reduces upon removal of load and beams exhibits self-rehabilitation ability. Figure 2.31 shows the crack width recorded during test for specimen 1 and 2. Figure 2.32 shows the crack opening and closure during test.

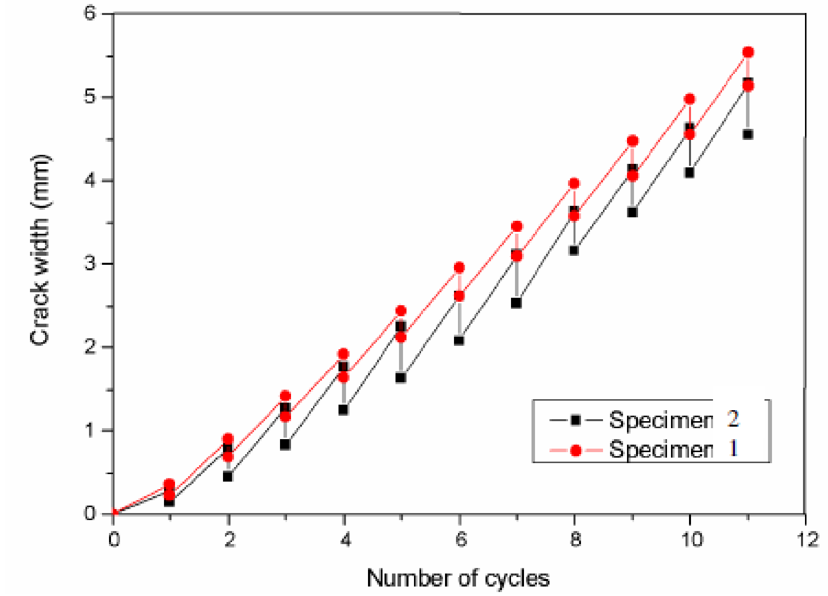

Figure 2.31: Crack width for specimens 1 and 2 (Li et al., 2006)

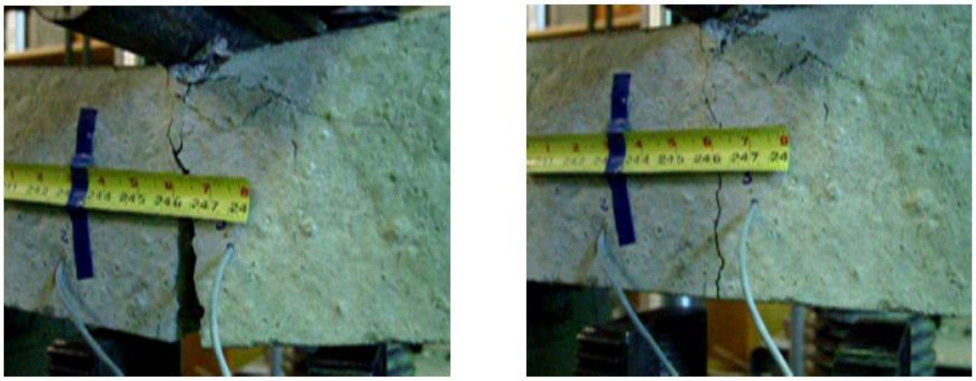

Figure 2.32: Crack opening and closure during for specimen 3 (Li et al., 2006)

Saiidi et al. (2007) studied the behavior of RC beams with SMAs. They used Nitinol as reinforcing bar in small scale concrete beams and tested them under two point loading setup. The beams were designed purely for flexural failure. To get the benefit of superelastic behavior of Nitinol and to make it cost effective and reusable they reinforced the beam externally. They varied the reinforcement ratio from 0.1 % to 0.9 %. It has been noticed that NiTi reinforced beams showed one fifth of average residual strain obtained in normal reinforced beams and stiffness of SMAs beams were comparatively less than steel beams.

Nehdi et al. (2010) studied the behavior of reinforced concrete SMA-FRP beam-column joint. They investigated the behavior of two ¾ scale BCJ. One was control specimen named as BCJ-1 whereas the second one was SMA-GFRP specimen named as BCJ-4. SMA was provided only in critical plastic hinge location only and rest was GFRP in the joint. Figure 2.33 shows the specimen details. Figure 2.34 shows the test setup used in their study.

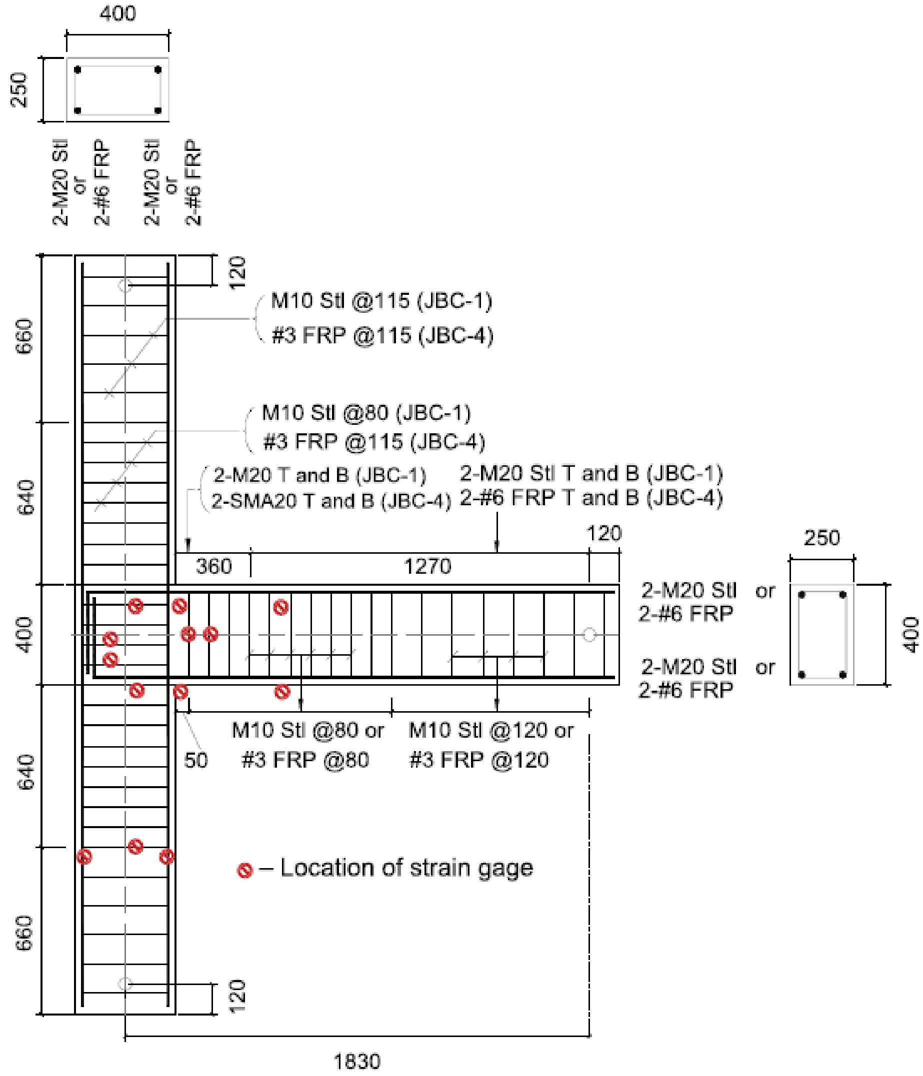

Figure 2.33: Specimens details (Nehdi et al., 2010)

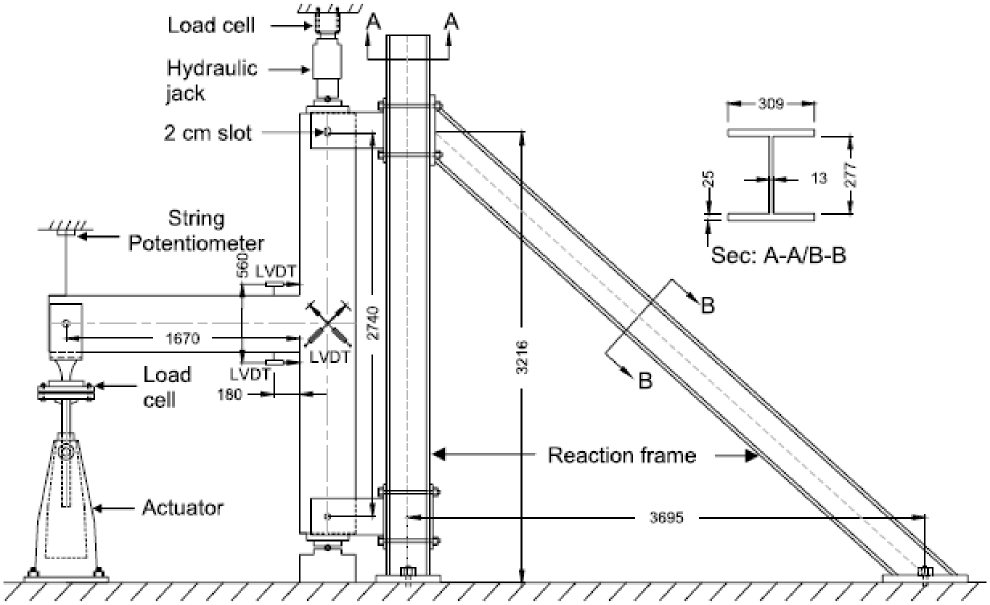

Figure 2.34: Test setup (Nehdi et al., 2010)

It has been noticed that the plastic hinge formed at the interface of beam-column joint in control reinforced concrete BCJ where as in SMA-GFRP beam-column joint it was formed at distance of ¼ of the depth of beam from column face. SMA-GFRP specimen dissipated comparable amount of energy as compared to control specimen. Moment rotation capacity of SMA-GFRP joint was found different than the normal joint because of low modulus of SMA. The residual strains in SMA bars was almost negligible whereas steel bar larger residual strains were observed. Figure 2.35 shows the hysteresis of BCJ-1 and BCJ-4. Figure 2.36 shows the moment rotation capacity. Figure 2.37 shows the crack pattern in BCJ-1 and BCJ-4.

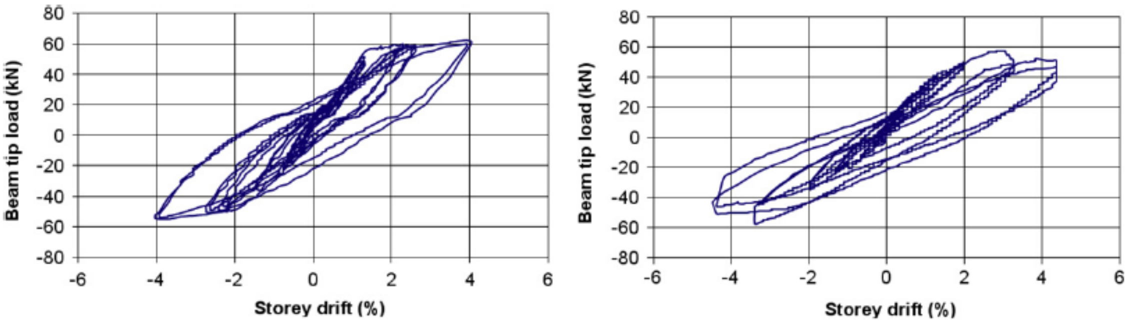

Figure 2.35: Hysteresis loop for BCJ-1 (left) and BCJ-4 (right) (Nehdi et al., 2010)

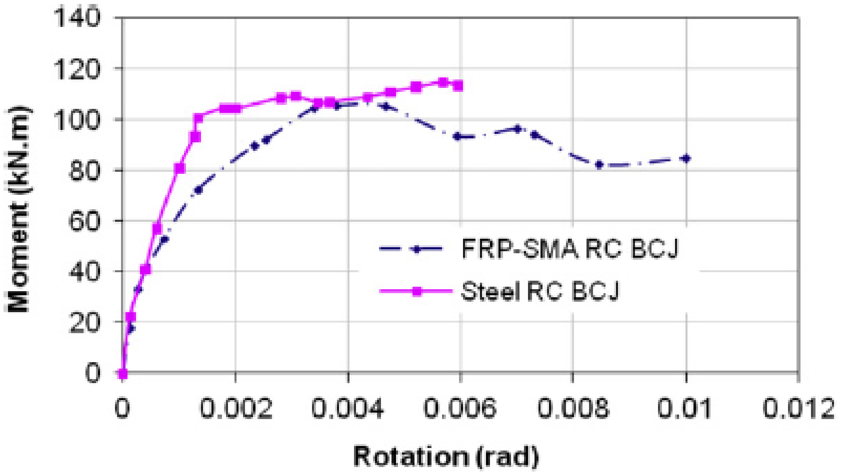

Figure 2.36: Moment-rotation capacity for BCJ-1 and BCJ-4 (Nehdi et al., 2010)

Figure 2.37: Crack pattern in BCJ-1 (left) and BCJ-4(right) (Nehdi et al., 2010)

Nehdi et al. (2011) studied the behavior of reinforced concrete SMA-reinforced beam-column joint. They investigated the behavior of two ¾ scale BCJ with SMA in joint region and remaining parts of BCJ joint were reinforced by regular steel. One was intact specimen named as BCJ-2 whereas the second one was repaired named as BCJ-4. Figure 2.38 shows the schematic diagram for reinforcement detailing for JBC-2 and JBC-3. Figure 2.39 shows the schematic diagram of test setup.

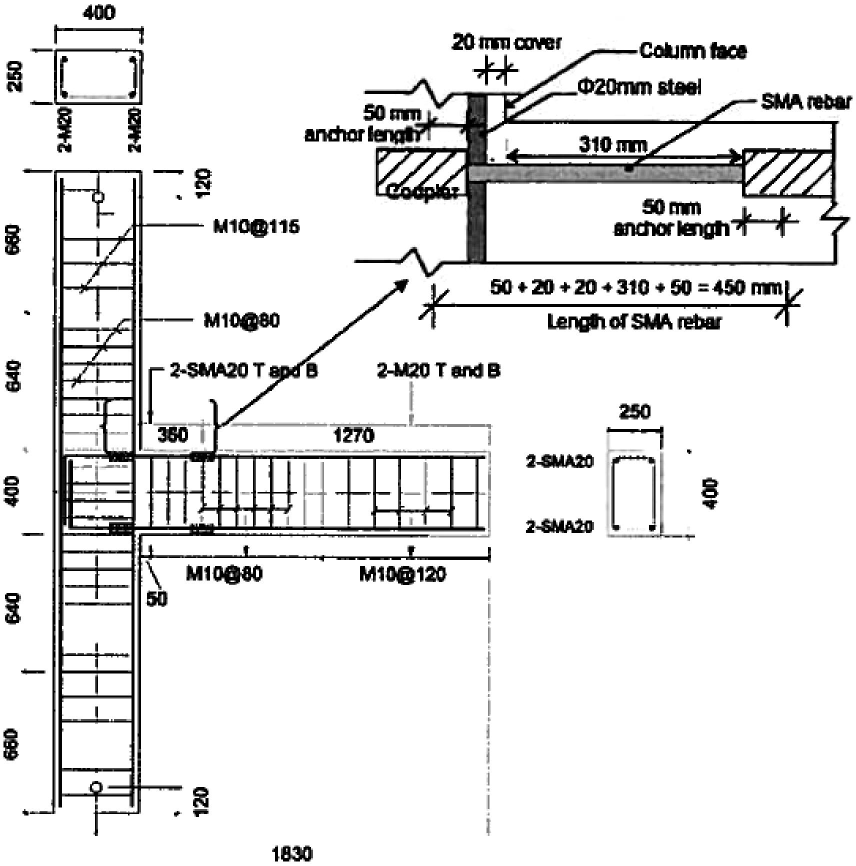

Figure 2.38: Reinforcement detailing for JBC-2 and JBC-3 (Nehdi et al., 2011)

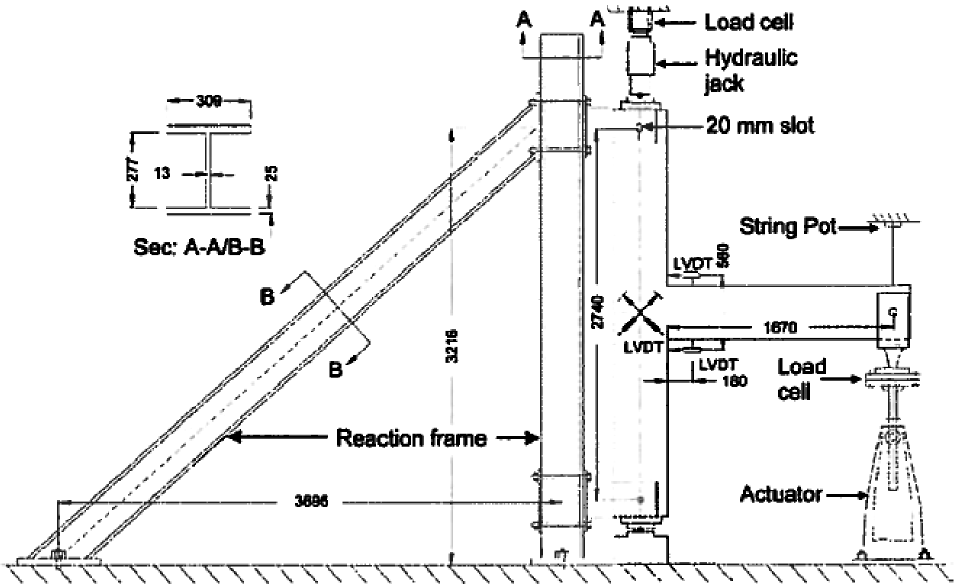

Figure 2.39: Test setup (Nehdi et al., 2011)

It has been noticed that the plastic hinge formed at the interface of beam-column joint. After failure of the specimen JBC-2 it was repaired and tested again. Also it has been noticed that the load-story drift ratio curve of repaired and control specimen was almost similar as shown in Figure 2.40.

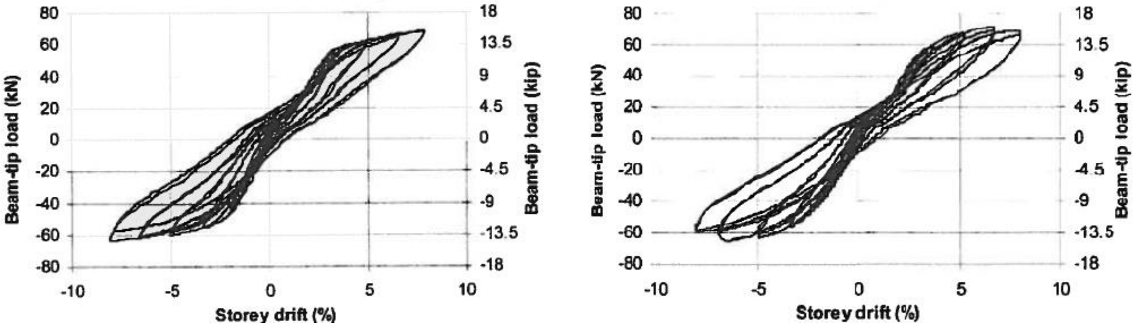

Figure 2.40: Load vs. story drift ratio for JBC-2 (left) and JBC-3 (right)

The repaired specimen dissipated equivalent amount of energy as compared to the control specimen. The SMA rebars in JBC-2 showed negligible amount of residual strain whereas in case of JBC-3 some residual strains were observed due to the repetition of loading cycles.

Abdulridha et al. (2013) studied the behavior of RC beams reinforced with superelastic SMAs. They have tested seven simply supported RC beams to get maximum moment at the midspan. The Nitinol bars were provided at critical region i.e. midspan where maximum moment was expected. The beams were subjected to monotonic, cyclic and reverse cyclic loading. Three beams were control with normal reinforcement and remaining four specimens were nitinol reinforced. The diameters of steel and nitinol bar were 11.3 mm and 12.7 mm. As it was mentioned earlier nitinol bars were used at the critical region only, so the bars were threaded and connected with couplers. Figure 2.41 shows the reinforcement detailing for the specimens used.

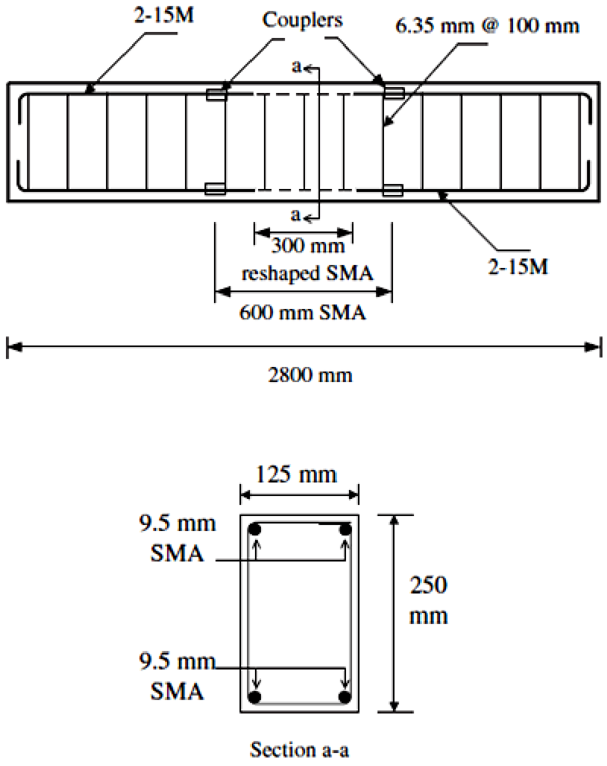

Figure 2.41: Reinforcement detailing (Abdulridha et al., 2013)

The nitinol bars were of ratio 56 % nickel to 44 % titanium. The bars were heat treated, so that superelastic effect can be achieved at normal temperature. To have failure exactly at midspan the dia of the nitinol bars were reduced to 9.5 mm at the midspan. The test setup used in their study is shown in Figure 2.42.

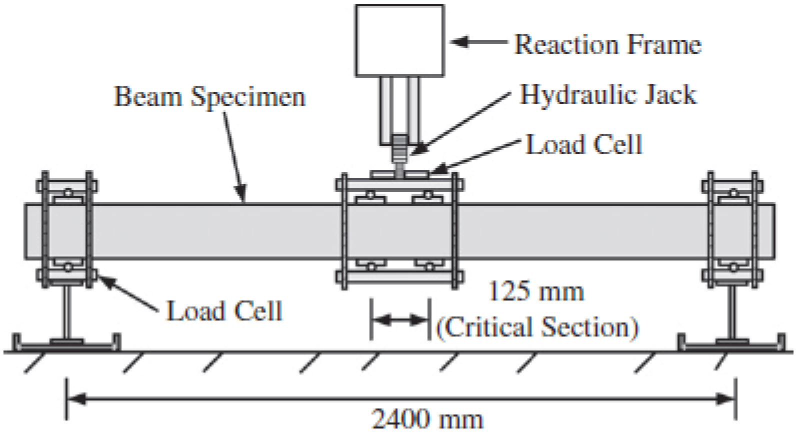

Figure 2.42: Test setup for experimental program (Abdulridha et al., 2013)

It has been observed that SMA beams showed maximum recovery of residual displacement as compared to normal reinforcement. SMA beams showed comparatively wide cracks but reduces upon unloading which can be seen in Figure 2.43.

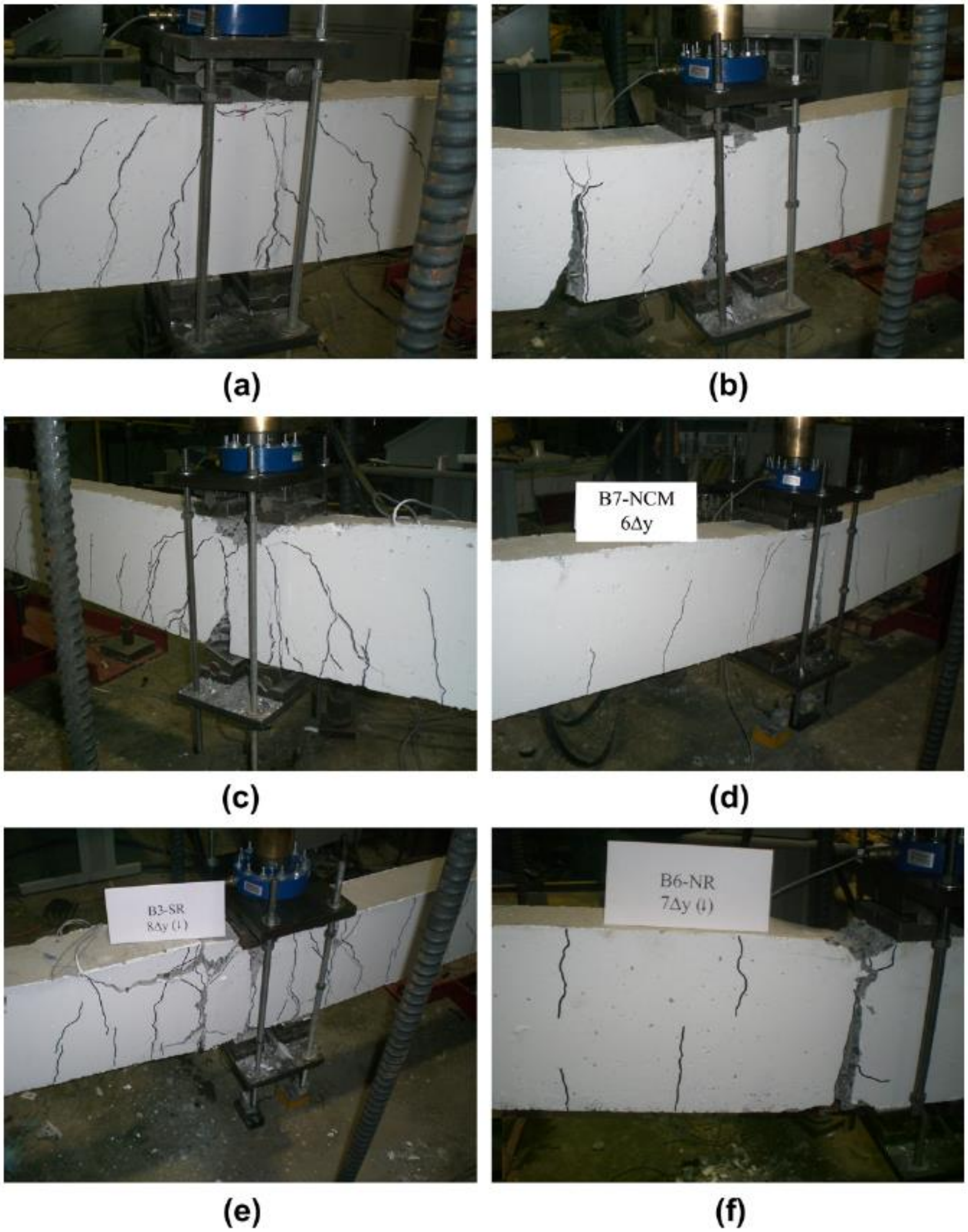

Figure 2.43: Crack pattern of test beams (Abdulridha et al., 2013)

Energy dissipation in SMA beams were lower than the normal reinforced beams. Figure 2.44 shows the load-displacement curves for monotonic loading. Figure 2.45 shows the load-displacement curves for cyclic and reverse cyclic loading.

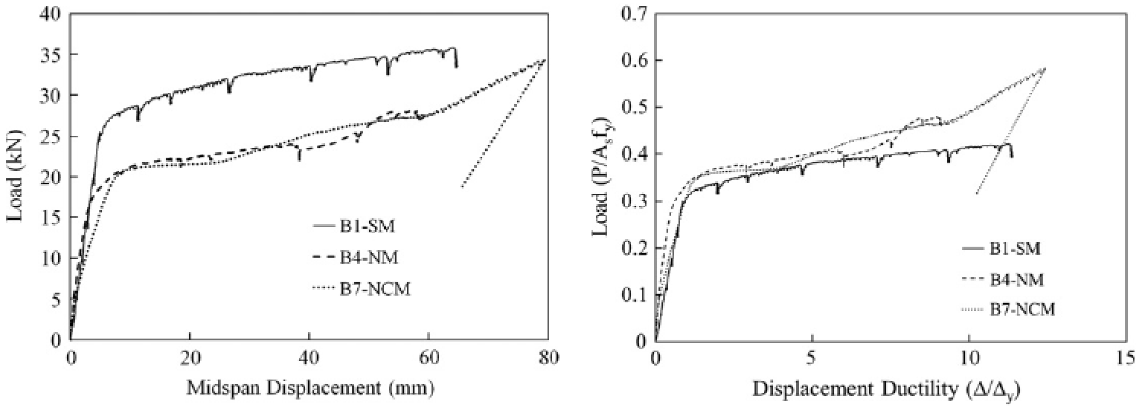

Figure 2.44: Load-displacement curve (left) and Ductility curve (right) for monotonic loading (Abdulridha et al., 2013)

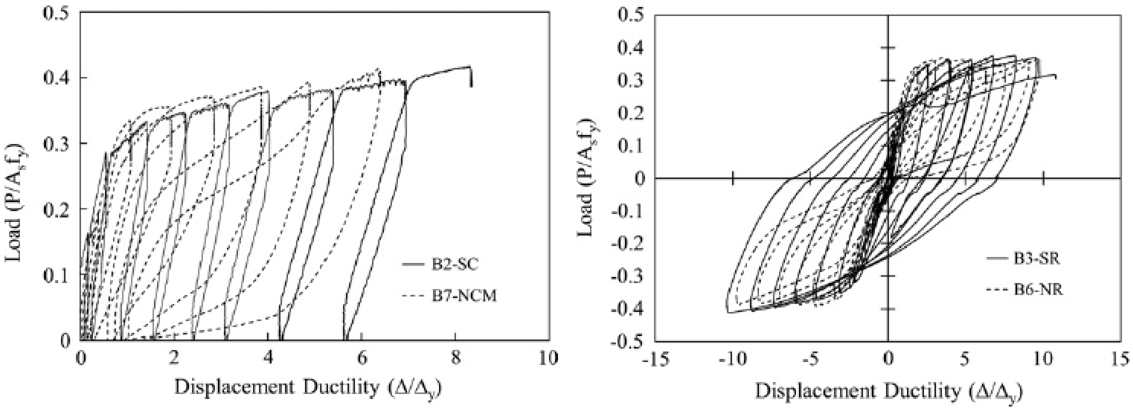

Figure 2.45: Ductility Response for cyclic (left) and reversed cyclic (right) loading (Abdulridha et al., 2013)

Zafar and Andrawes (2013, 2014) fabricated highly ductile superelastic SMA composites (100 % SMA wires and hybrid fibers of SMA and glass-FRP) and studied the cyclic behavior of composites. They also reported that SMA composite bars showed high ductility, recentering capabilities and energy dissipation as compared to the conventional FRP reinforcing bars. They used these newly developed SMA-FRP reinforcement in concrete beam and performed three point test. The experimental beam studied by Zafar and Andrawes (2013) under cyclic loading is shown in Figure 2.46. Two SMA-FRP bars were used in T-beam without any stirrups. The projection at the ends was used for anchoring the rebar. A notch was provided at the mid span to promote the crack at predefined location. The loading setup and support conditions are shown in Figure 2.47.

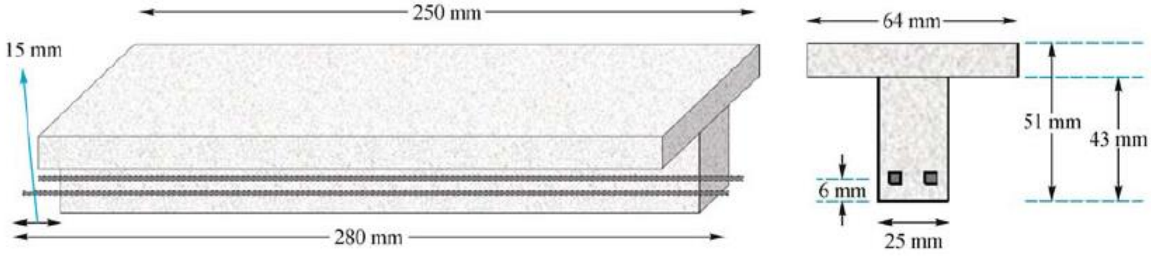

Figure 2.46: Cross sectional dimensions of T-beam tested (Zafar and Andrawes, 2013)

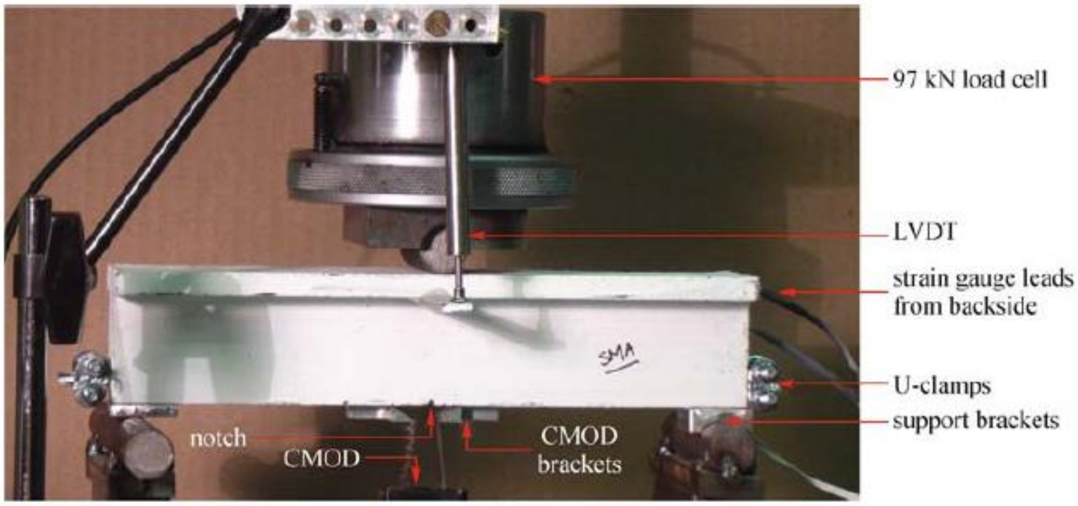

Figure 2.47: Experimental loading setup and support conditions (Zafar and Andrawes, 2013)

The beam was loaded using displacement control regime till complete failure which was shear failure. It has been observed that the SMA-FRP composite reinforcement used in RC beam enhanced the performance of member by re-centering and crack closing ability. Figure 2.48 shows the load-deflection curve of beam under different loading cycles. Figure 2.49 shows the crack mouth opening displacement for different cycles.

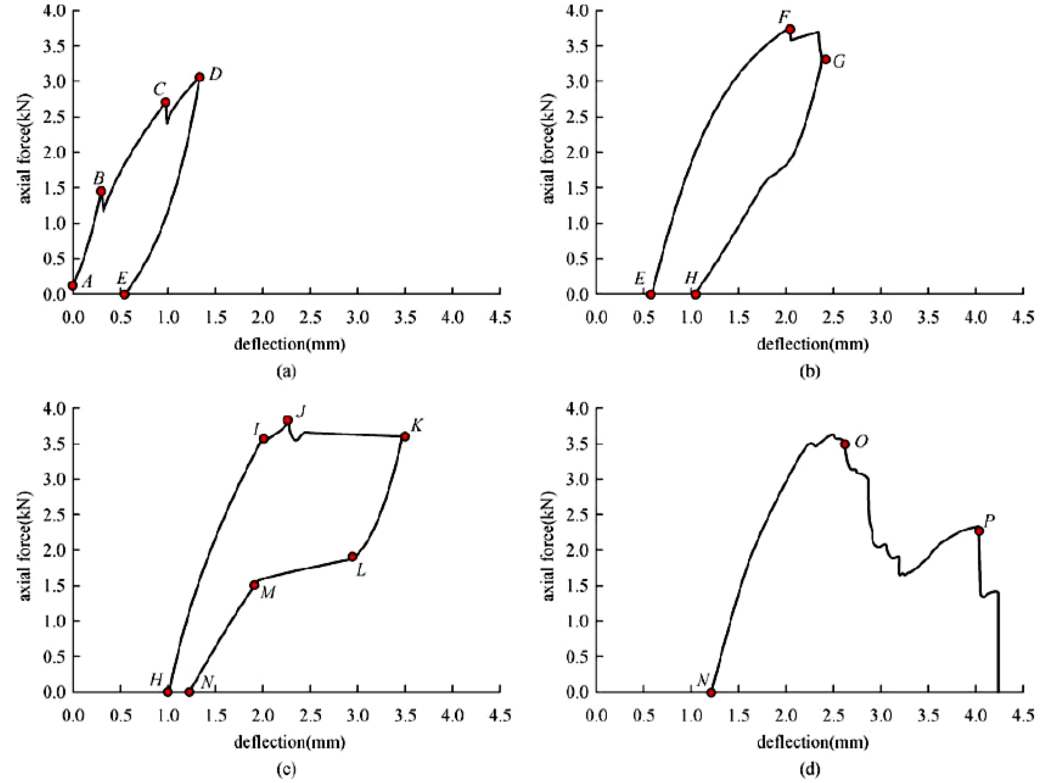

Figure 2.48: Load-deflection curves Cycles (Zafar and Andrawes, 2013)

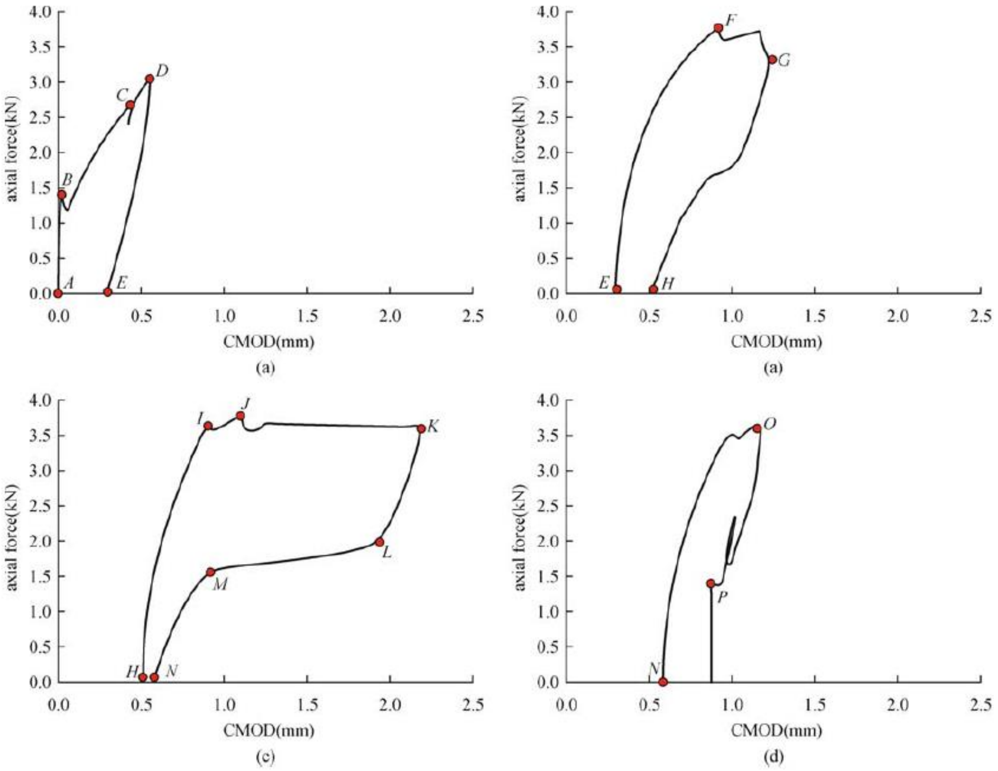

Figure 2.49: Crack opening and closing for different cycles (Zafar and Andrawes, 2013)

CHAPTER 3

MECHANISTIC MODEL FOR BEAM-COLUMN JOINTS

3.1 EXPERIMENTAL EXTERIOR BEAM COLUMN JOINTS SHEAR CAPACITY

Beam-column joint behavior is complicated and complex in nature because it consist of many interconnecting elements. Different elements from frame structure coincide at a single point. Moments, axial load and shear forces from adjoining beam elements and columns are conveyed to the joint, so it is very important to understand the response of BCJ under such loads. The load transformed from different structural components will help us in understanding the performance of BCJ.

3.1.1 Beam Loading

Suppose a point load “P” is applied at the end of beam tip. This point load “P” will create a moment at the end of beam where it is restrained. The moment will act at the interface of joint and will be given as shown in equation 3.1.

$$M_n = P \times l_p \tag{3.1}$$

Where:

M_n is the moment due to load P.

l_p is the distance from joint interface to the applied load as shown in Figure 3.1.

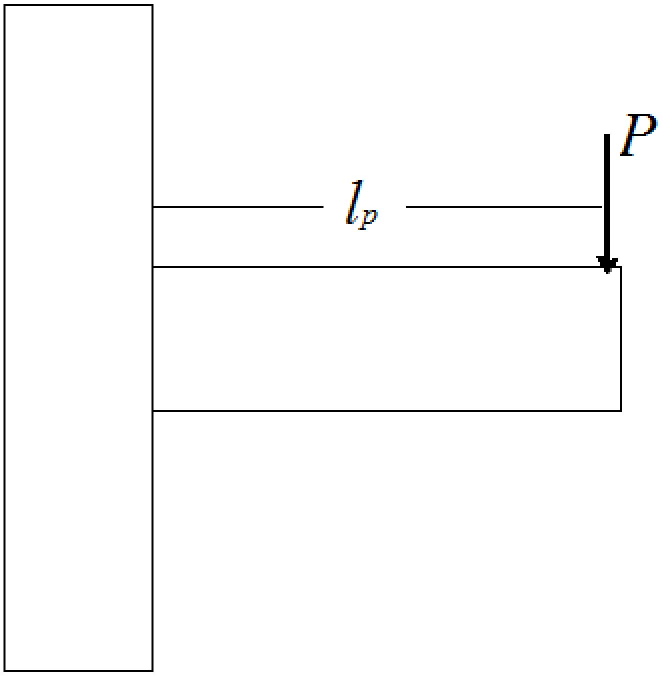

Figure 3.1: Beam Loading

3.1.2 Column Loading

It is assumed that at the inflection points in the column moment is zero and the moment in the BCJ is similar to the moment acting at the beam end, M_n. The column shear force can be obtained using equation 3.2.

$$V_c^{'} = \frac{M_n}{l_{pc}} \tag{3.2}$$

$V_c^{'}$ is the column shear force and l_{pc} is the distance between inflection points as given in Figure 3.2.

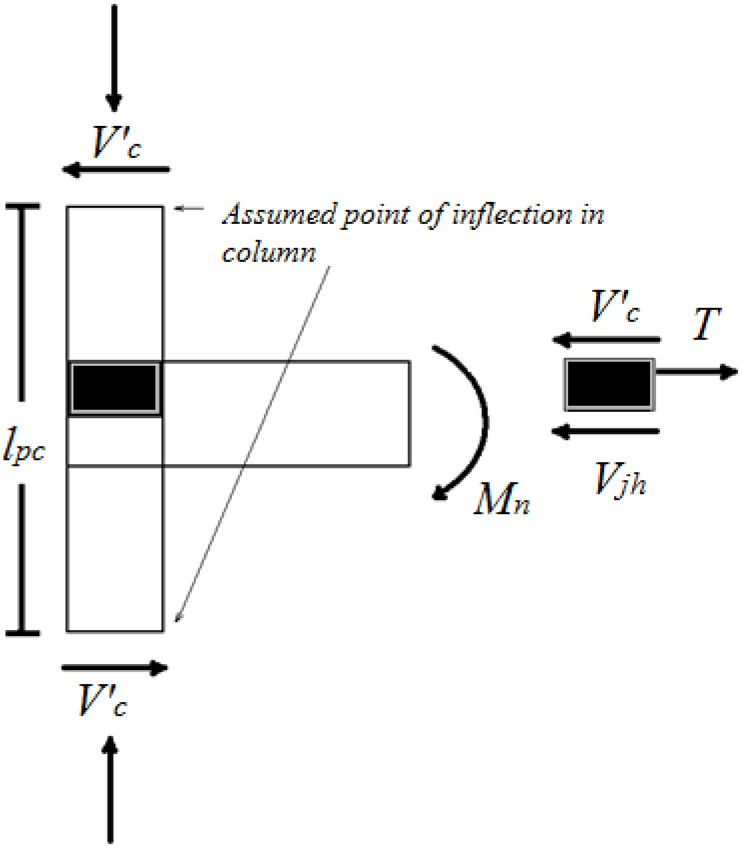

Figure 3.2: Schematic diagram for BCJs forces

Figure 3.3 shows that the joint horizontal shear force is the combine effect of column shear force and beam rebar force and can be determined by equation 3.3

$$V_{jh} = T - V_c^{'} \tag{3.3}$$

Where, T is the force in beam rebar and $V_c^{'}$ is the column shear force

The BCJ strength is the sum of forces acting in the joint as shown in Figure 3.3. From free body diagram, V_{jv} can be determined and is shown in equation 3.4.

$$V_{jv} = T^{'} + C_c^{''} + C_s^{''} - V_b \tag{3.4}$$

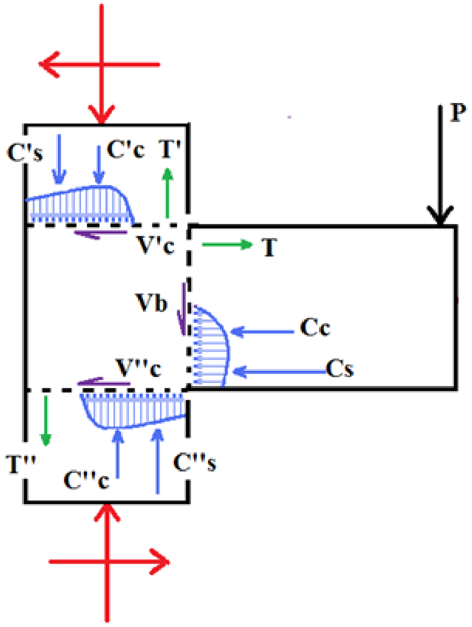

Figure 3.3: Schematic diagram for stresses in BCJs (Ahmed, 2012)

3.2 SHEAR STRENGTH OF EXTERIOR BCJs

Most of the time principal tensile stress are used to determine the shear capacity of the joints as shown in Figure 3.4

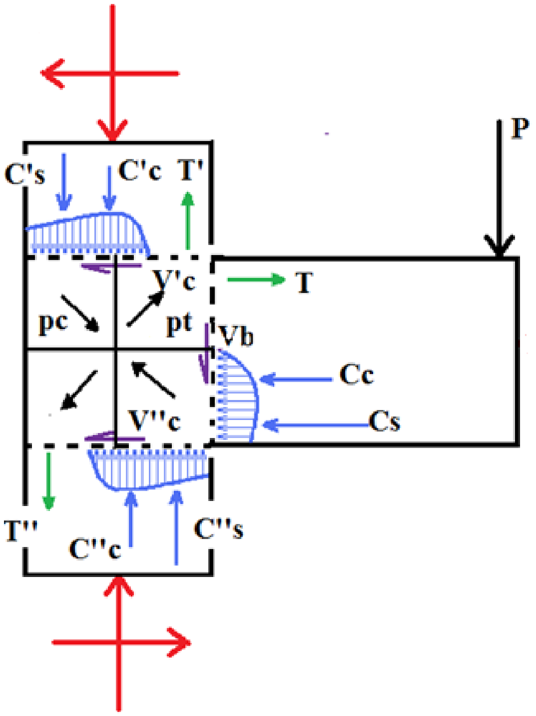

Figure 3.4: BCJs principal tensile stresses (Ahmed, 2012)

Principal tensile stresses can be obtained from Mohr's circle as shown in equation 3.5.

$$\sigma_{1,2} = \frac{\sigma_x + \sigma_y}{2} \pm \sqrt{\left(\frac{\sigma_x + \sigma_y}{2}\right)^2 + \tau_{xy}^2} \tag{3.5}$$

Where:

σ_x = The stress due to axial load (σ_a) on the column; σ_y = 0; and $\tau_{xy} = v_{jh}$, so equation 3.5 can be expressed as shown in equation 3.6.

$$\sigma_1 = \frac{-\sigma_a}{2} + \sqrt{\left(\frac{\sigma_a}{2}\right)^2 + v_{jh}^2} \tag{3.6}$$

Where:

σ_a= axial stress due to column load $\left(\frac{N}{A_g}\right)$

v_{jh}= horizontal shear stress $\left(\frac{V_{jh}}{A_j}\right)$

3.3 BEAM-COLUMN JOINT FAILURE MODE

The crack in the joint will appear if the principal tensile stress in the joint is greater of equal to the concrete tensile strength. The concrete tensile strength can be determined using equation 3.7.

$$\phi V_{nj} = 0.75\gamma\sqrt{f_c^{'}} A_j \qquad (3.7)$$

There will be a shear failure and cracks will appeared in diagonal direction. Figure 3.5 and Figure 3.6 shows the formation of diagonal cracks in push and pull direction.

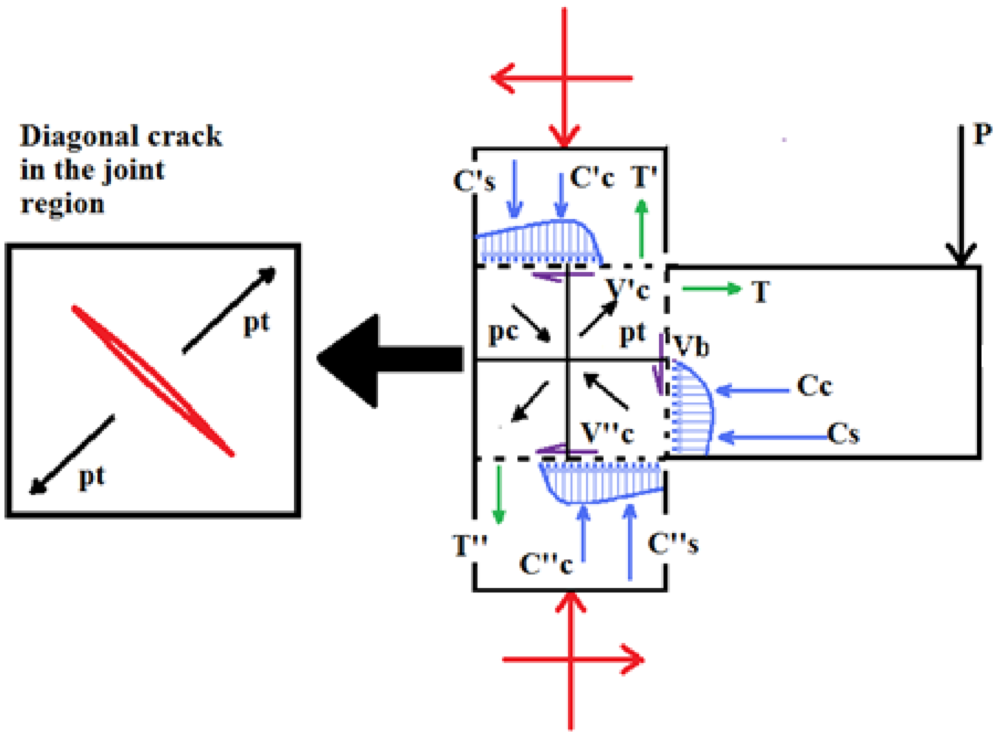

Figure 3.5: Formation of Diagonal Crack in BCJ in push direction (Ahmed, 2012)

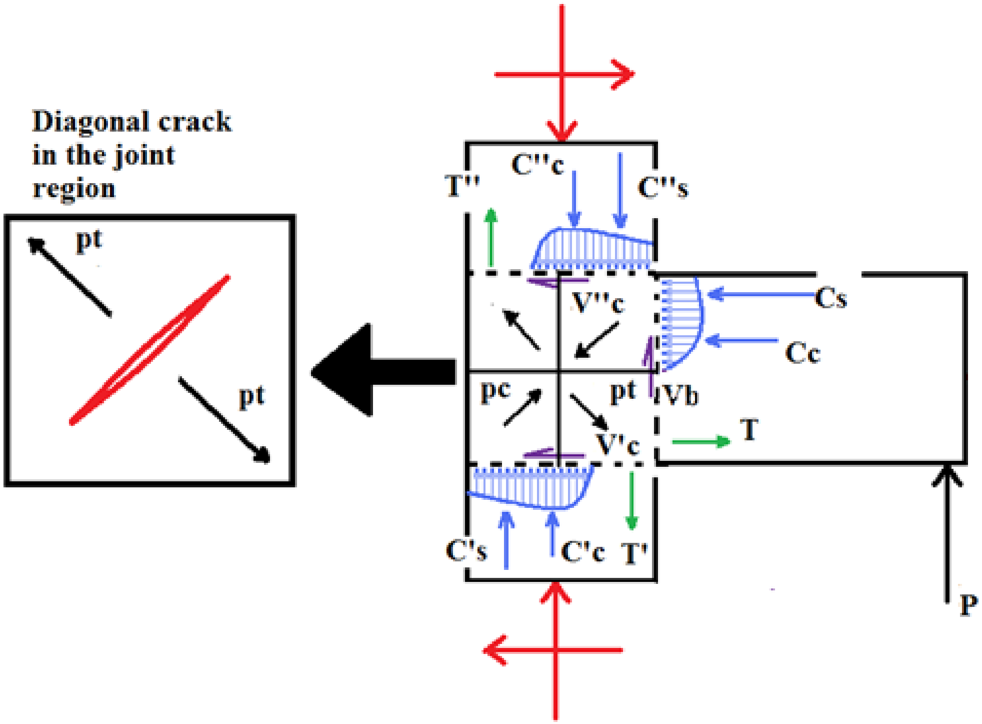

Figure 3.6: Formation of Diagonal Crack in BCJ in pull direction (Ahmed, 2012)

These forces promote diagonal cracks in the joint region, so if there is no reinforcement in the joint the joint strength degrade and joint will fail in shear. It have been also noticed that longitudinal reinforcement detailing also plays important role in joint efficiency. Some old detailing patterns in the BCJ joints are shown in Figure 3.7b and Figure 3.7c. The joint having bent-up longitudinal bars as shown in Figure 3.7b are less efficient as compared to the joint having longitudinal bars bent-in in as shown in Figure 3.7c because bent-in bars gives confinement to the joint. Still we need stirrups in the joint to confine the concrete.

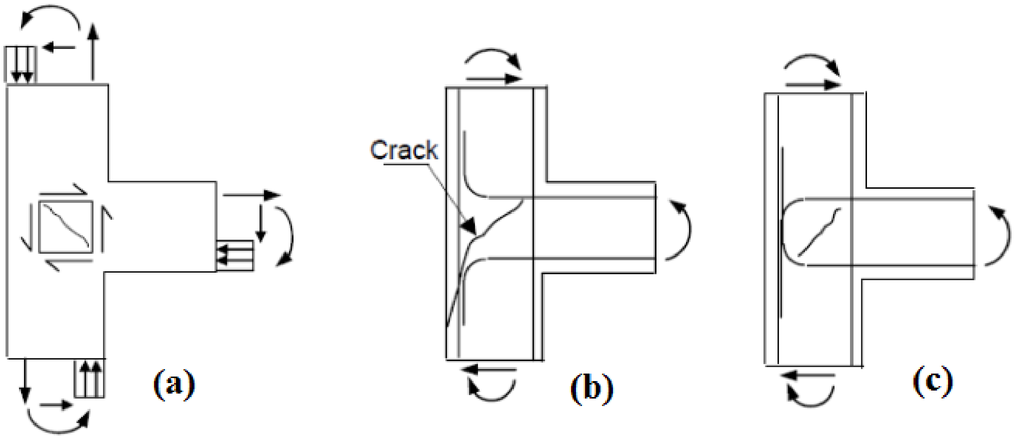

Figure 3.7: (a) BCJ Forces (b) Bent-up longitudinal rebar (c) Bent-in Longitudinal rebar

Priestly (1997) proposed some limitation of principal tensile stresses and post- cracking of BCJs which was modified by Pampanin et al. (2003) for different reinforcement detailing.

It has been noticed from there study that once diagonal cracks appeared joint strength start reducing and it depends on the reinforcement detailing and type of joint as shown in Figure 3.8.

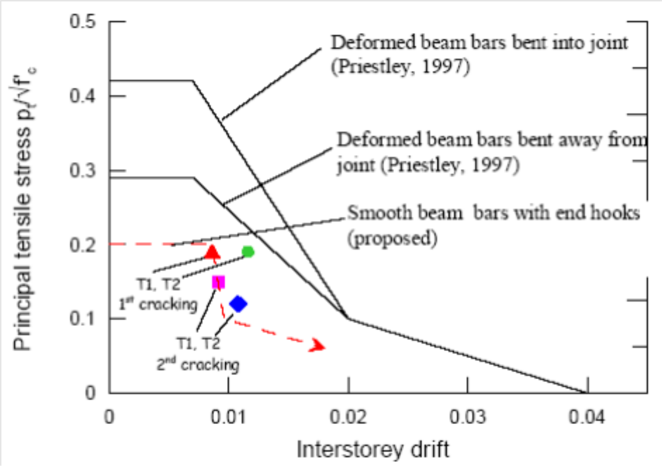

Figure 3.8: Limitation for principal tensile stresses, (Pampanin, 2003)

3.4 Mechanistic Model for Control and SMAs Retrofitted Specimens

As we know that the joint shear strength is combination of concrete shear strength, reinforcement and external material use for strengthening of joint. The joint shear strength for control specimens can be expressed as

$$V_j = V_c + V_{bs} \tag{3.8}$$

Where,

V_j : Total shear strength

V_c : Shear strength attributable to the concrete

V_{bs} : Shear strength attributable to the beam steel

Similarly for retrofitted specimens it can be determined using equation 3.9

$$V_j = V_c + V_{bs} + V_{SMA} \tag{3.9}$$

V_j : Total shear strength

V_c : Shear strength attributable to the concrete

V_{bs} : Shear strength attributable to the beam steel

V_{SMA} : Shear strength attributable to the SMAs sheets

Khatib at el. (2016) gave a unique approach to determine V_c which includes the effect of column axial load as shown in Figure 3.9. If axial load is known one can determine the joint shear strength due to the contribution of concrete.

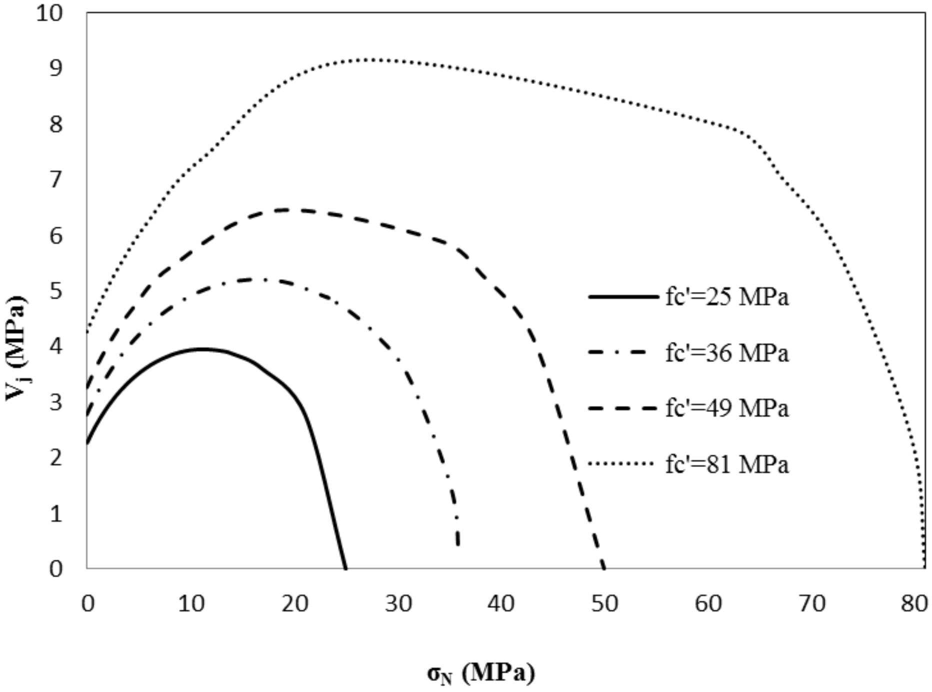

Figure 3.9: Joint Shear strength for different axial load (Khatib et al., 2016)

Bakir and Boduroglu (2002) investigated beam column joint and proposed a regression equation for the influence of beam reinforcement in joint shear strength. Equation 3.11 showed the normalized joint shear strength due to the beam reinforcement for regression curve as shown in Figure 3.10.

$$v_j \approx 0.7434\left(\frac{A_{sb}}{b_b d}\right)^{0.4289} \tag{3.11}$$

Where,

v_j is the normalized joint shear strength due to longitudinal reinforcement of beam and expressed in $(\text{MPa})^{0.5}$, A_{sb} is the total reinforcement area, b_b is the breadth of beam, d is the depth of the beam.

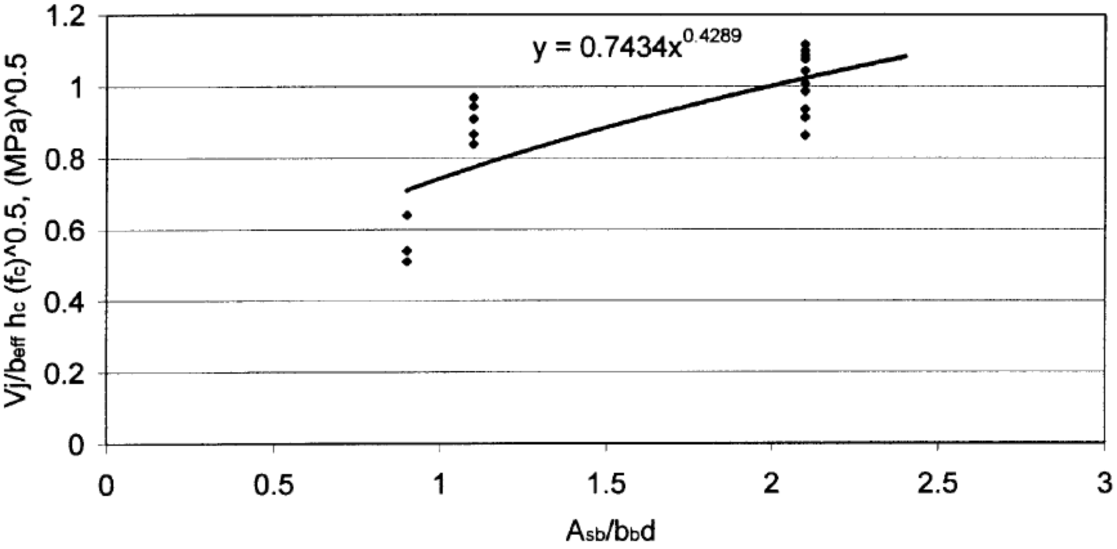

Figure 3.10: Beam Reinforcement influence in joint shear strength (Bakir and Boduroglu, 2002)

For SMA contribution one can use the concept of ties inside the joint and use the concept of truss analogy. V_{SMA} can be determined using equation 3.12.

$$V_{SMA} = \frac{A_v f_v d}{s}(\sin\alpha + \cos\alpha) \tag{3.12}$$

Where A_v: is the area of SMA sheet, f_v: stress in SMA sheet, d is the moment arm (approximately equal to effective depth), s is the spacing of SMA sheets α is the angle for diagonal compressive struts. If α = 90 equation 3.12 can be expressed as

$$V_{SMA} = \frac{A_v f_v d}{s} \tag{3.13}$$

CHAPTER 4

MATERIALS TESTING AND LOADING PROTOCOL

4.1 Introduction

To carry out the investigation of seismic prone beam-column joints experimental test were performed at KFUPM structural lab on 7 specimens with monotonic, cyclic and reverse cyclic loading protocols. These specimens include 3 control specimens and 4 retrofitted specimens. The reinforcement details for all specimens were same. Figure 4.1 shows the reinforcement detailing of specimens.

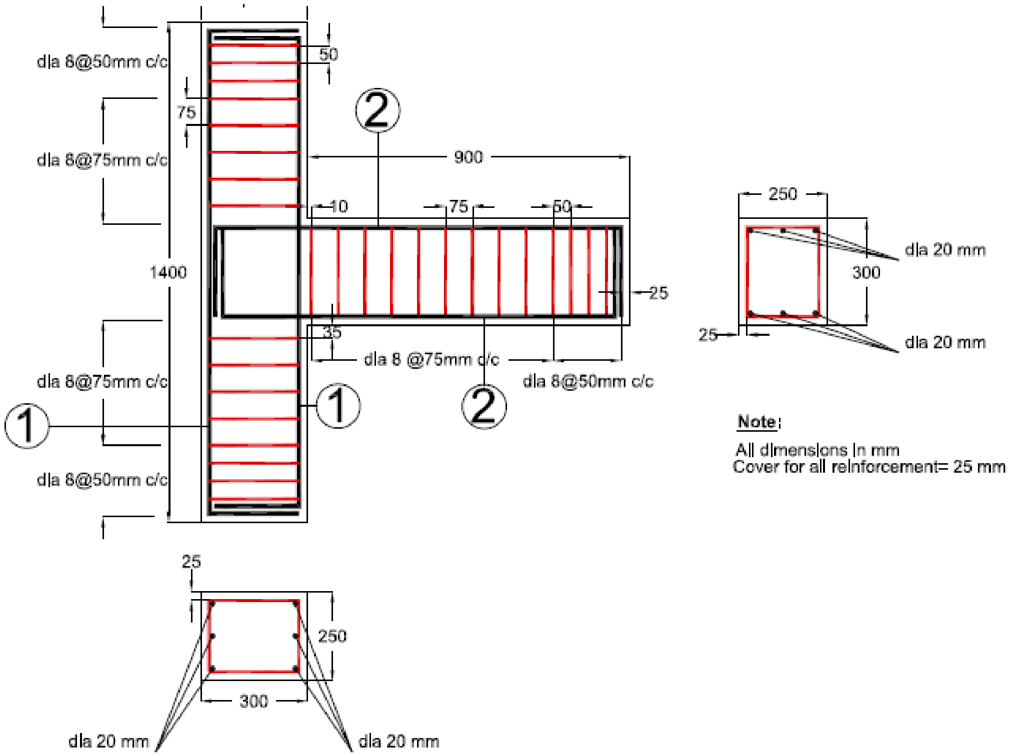

Figure 4.1: Reinforcement detailing for BCJ

The specimens were designed to fail in shear. Following tests were carried out to complete this study.

1. Uniaxial compression and tension test for the concrete
2. Rebar tension test
3. Shape Memory Alloys (SMAs) sheets tension test
4. XFR test for SMA sheet
5. Full scale BCJ test under monotonic, cyclic and reverse cyclic loading.

4.2 Concrete Properties

The concrete used in casting of these specimen were obtained from Saudi Ready Mix firm with a minimum designed strength of 25 MPa. The slump of concrete during casting was 102 and the maximum aggregate size used was 25 mm. During casting of full scale specimens concrete was took from the batch and 28 cylinders of 75 mm x 150 mm were cast. Uniaxial compression tests were done under monotonic as well cyclic loading whereas split cylinder test was utilized to get the tensile strength of concrete.

4.2.1 Compression Test

Three cylinders were tested after 8 days to get the average concrete strength. Three cylinders were prepared with the capping at the ends and strain gauges were installed on them to determine the strains in concrete. One strain gauge was installed in the horizontal direction and the second one was installed in the vertical direction. Figure 4.2 shows the prepared samples. The specimens were tested under control loading. Figure 4.3 shows the specimen under compression load and ultimate failure of all specimens. The average compressive strength obtained after 28 days is shown in Table 1.

Figure 4.2: Specimens with capping (left) and Specimen with Strain Gauges (right)

Figure 4.3: Cylinder specimens under compression load (left) and Ultimate failure in Cylinders (right)

Table 1: Average compressive strength of concrete

Specimen	Load (kN)	Area (mm^2)	Strength (MPa)	Average, f_c' (MPa)
Cylinder 1	136.4	4417.86	30.87	32.98
Cylinder 2	152.8	4417.86	34.58	
Cylinder 3	147.9	4417.86	33.48	

Cyclic response of concrete was also determined using loading and unloading protocol. The cyclic response of concrete is shown in Figure 4.4.

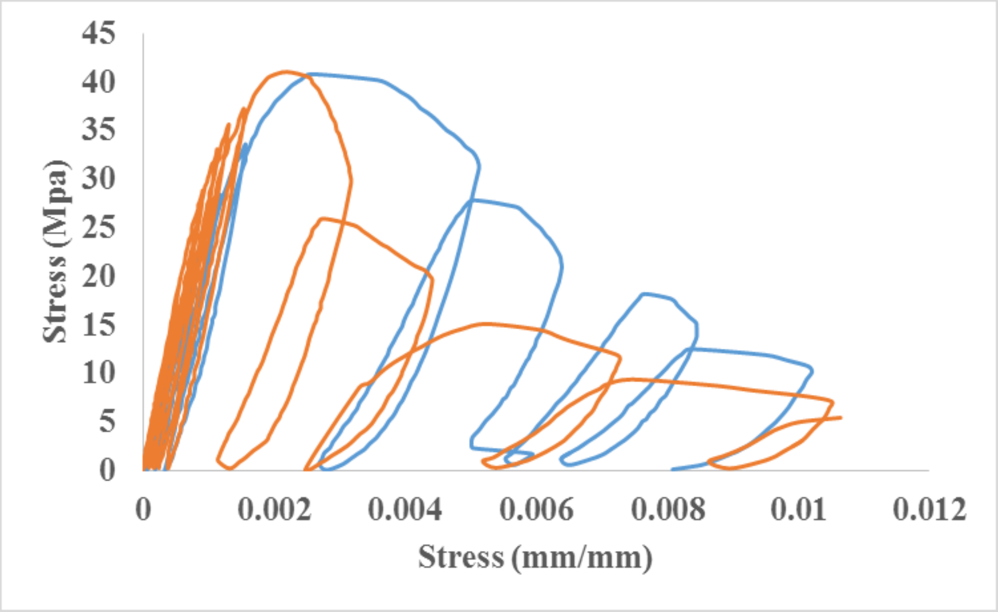

Figure 4.4: Cyclic response of concrete under compression

4.2.2 Tension Test

Split cylinder test was carried out on three specimens to find the indirect tensile strength of concrete. ASTM-D3967 test procedure was utilized. The test setup used and failure of specimens is shown in Figure 4.5. The average indirect tensile strength of concrete was obtained using equation 4.1. Table 2 shows the average tensile strength of concrete.

$$f_t = \frac{2P}{\pi l d} \qquad 4.1$$

Where *P, l* and *d* are the applied load, length and diameter of specimens respectively.

Figure 4.5: Split cylinder setup (left) and failure at ultimate load (right)

Table 2: Tensile strength of concrete

Specimen	Load (kN)	Area (mm2)	Tensile Strength (MPa)	Average, f_t (MPa)
Cylinder 1	50.7	5.66 e-05	2.86	2.58
Cylinder 2	45.9	5.66 e-05	2.59	
Cylinder 3	40.6	5.66 e-05	2.29	

4.3 Rebar Tensile Test

The tensile strength of reinforcement used in BCJs specimen were obtained using uniaxial tension test which was carried out in Universal tension machine available in structural material lab of KFUPM. The reinforcement used in all specimens were 20 mm and 8 mm diameters bars for longitudinal and transverse reinforcements. Figure 4.6 shows the test setup used for tension and failure of dia 20 mm rebar. The ultimate yield strength of dia 8 mm and 20 mm are given in Table 3. Figure 4.7 shows the stress- strain curve for dia 20 mm bar.

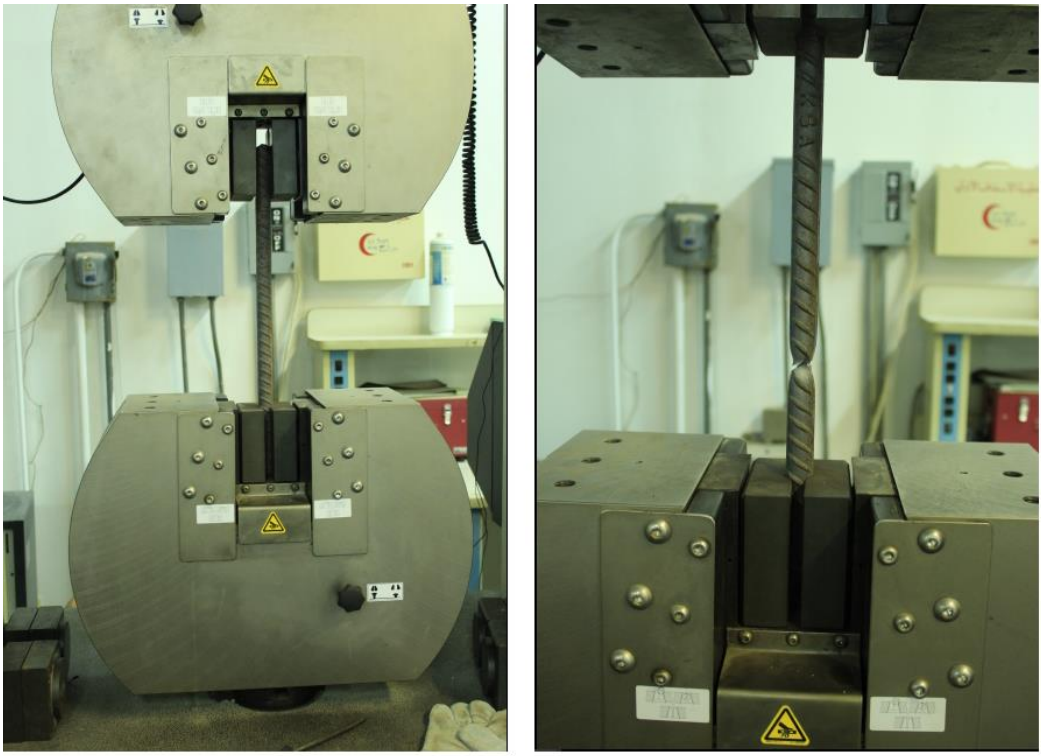

Figure 4.6: Tension test setup (left) and Failure of rebar (right)

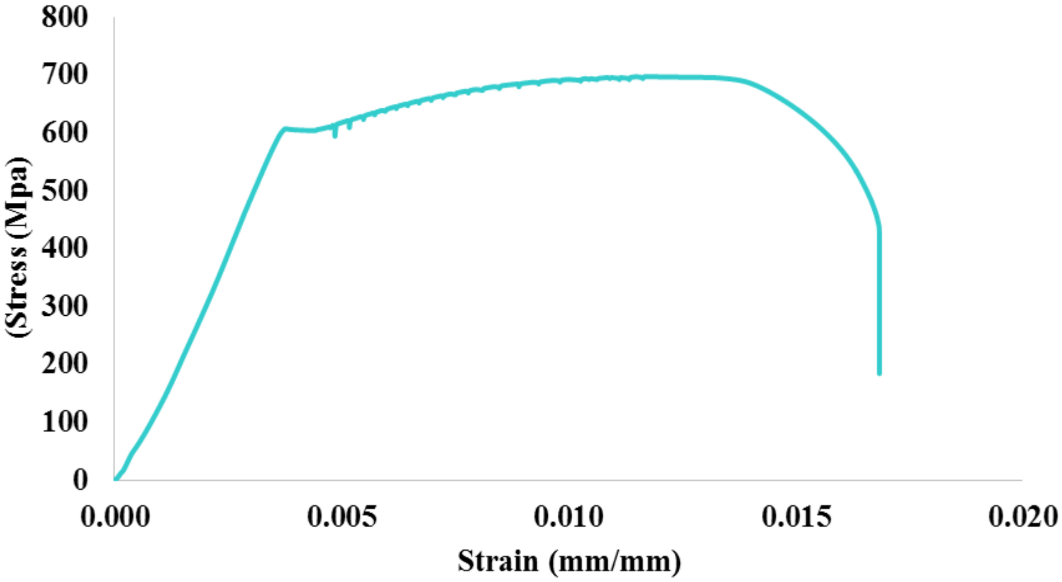

Figure 4.7: Stress-strain curve for dia 20 mm bar

Table 3: Tensile strength of rebars

Item	Diameter (mm)	f_y (MPa)
1	20	607.15
2	8	480.5

4.4 Shape memory Alloys Sheet Test

Shape memory alloys have unique property to undergo large deformation and return back to original position upon unloading, so to get the proper stress-strain response of SMAs sheets cyclic loading protocol were utilized. The material was obtained from China which can behave superelastic under normal temperature.

4.4.1 Preparation of SMAs sheet

The sheets obtained were not heat treated, so to get superelastic response activated sheets were heat treated. First of all sheets were heated in furnace for 30 minutes under a constant temperature of $350^{o}C$. After 30 minutes sheets were removed from furnace and immediately dipped into cold water. As the surface of SMAs sheets were smooth and there were chances of slippage of sheets from the grip of testing machine, so end grips were prepared. Sheets were hold in 2mm thick aluminum plates with high strength epoxy. Figure 4.8 shows the prepared specimen with aluminum grips for testing.

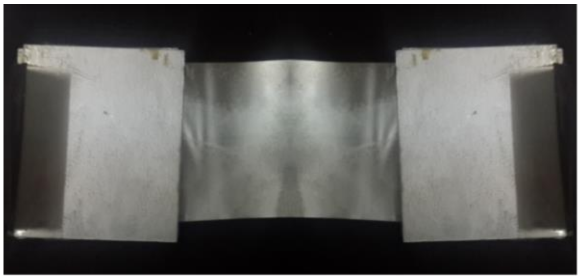

Figure 4.8: SMAs sheet with Aluminum grips

4.4.2 Testing of SMAs sheet

Two sheets were tested in universal testing machine under cyclic load with constant loading rate of 0.1 mm/ minutes. Each cycle were loaded up to 0.5 % strain. Figure 4.9 shows the test setup used for testing of SMAs sheets. The test was stopped once the specimens fails. The sheets were failed approximately at 29 % strain. It has been observed that maximum recovery of residual strain is achieved when sheets were loaded up to 8 % strain. Figure 4.10 shows the stress strain curve of SMAs sheets up to 8 % strain. Table 4 shows the stress-strain properties of SMAs sheets. Figure 4.11 shows the sheet at failure.

Figure 4.9: Test setup and testing SMAs Sheet

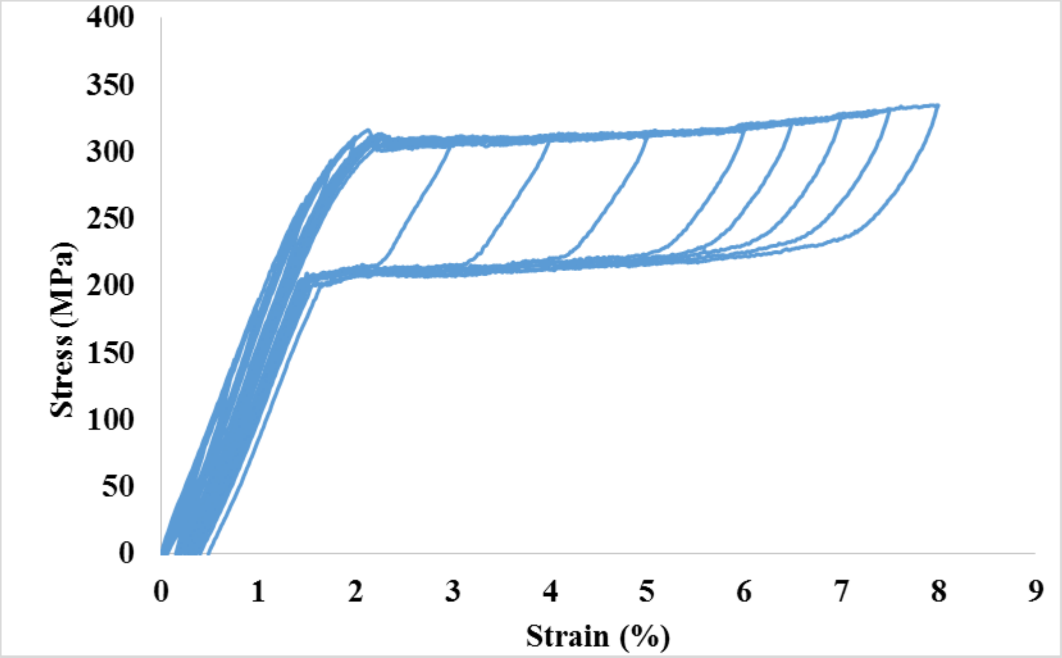

Figure 4.10: Stress-strain curve SMAs sheet

Table 4: Stress strain properties of SMAs sheets

Serial #	Description	Stress (MPa)	Strain (mm/mm)
1	Forward Transformation (Austenite To Martensite)	317.65	0.021
2	End of Forward Transformation	335.03	0.080
3	Phase Transformation (Martensite to Austenite)	237.03	0.071
4	End of Phase Transformation	207.30	0.015

Figure 4.11: Failure SMAs Sheet at ultimate load

4.4.3 X-Ray Fluorescence (XRF) Test for SMA sheet

XRF test was conducted to get the material composition for SMAs sheets in research institute of KFUPM. Square sheet of 1 cm were tested in XRF machine which shows 57.28 % nickel and 41.18 % titanium which is the major constituent of SMAs sheets. The XRF results are shown in

Serial #	**Symbol**	**Concentration (%)**
1	Ni	57.28
2	Ti	41.48
3	P	0.3493
4	Al	0.3427
5	Mg	0.176
6	Si	0.0813
7	Co	0.0755
8	Fe	0.0601
9	S	0.0282
10	Cr	0.0019
11	Others	0.125

4.5 Preparation of Specimens

4.5.1 Specimen preparation detailing

To investigate the cyclic response of beam-column joints strengthened with superelastic shape memory alloys (SMAs) 7 specimens were prepared. The specimens were deficient in joint shear strength with no transverse reinforcement. Three specimens were control and remaining four specimens were retrofitted by SMAs sheets with different configurations. The cross section of the beam and column were same with dimension of 250 mm x 300 mm. The beam length was taken 900 mm and the column height was 1400 mm. These dimension were selected based on the testing frame available in KFUPM lab and represents the average beam-column joint size. Six longitudinal reinforcements of dia 20 mm were provided in beams and column whereas dia 8 mm rebars were used for stirrups and ties. Figure 4.12 shows the schematic detailing of specimens.

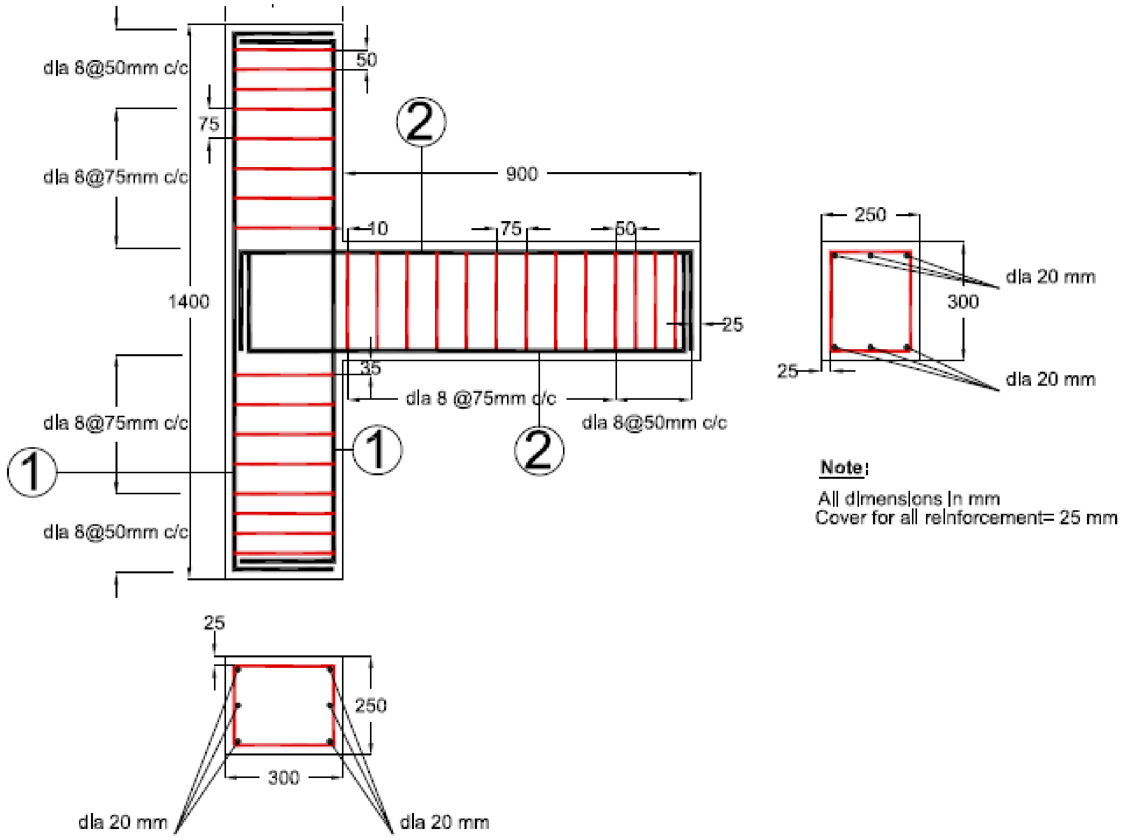

Figure 4.12: Schematic diagram for reinforcement detailing

4.5.2 Installation of Strain gauges

Six strain gauges were attached to the reinforcement surface of BCJ at a selective locations where maximum stresses can occurred during loading. Two strain gauges were installed on top flexural reinforcement of beam and two were installed at bottom reinforcement of beam near the interface of BCJ. One was installed on central longitudinal bar of column near the interface of BCJ. One was installed on first beam stirrup near the interface of BCJ. The location of the strain gauges are shown in Figure 4.13. Before applying the strain gauges rebar surfaces were prepared with sand paper to remove dust. Strain gauges were pasted using CN-Y adhesive (Cyanoacrylate) provided by the vender and wrapped by water proof duct tape to protect them during casting process as shown in Figure 4.14. At the end the resistance of strain gauges were checked using voltmeter which was 120 ohms to confirm their performance.

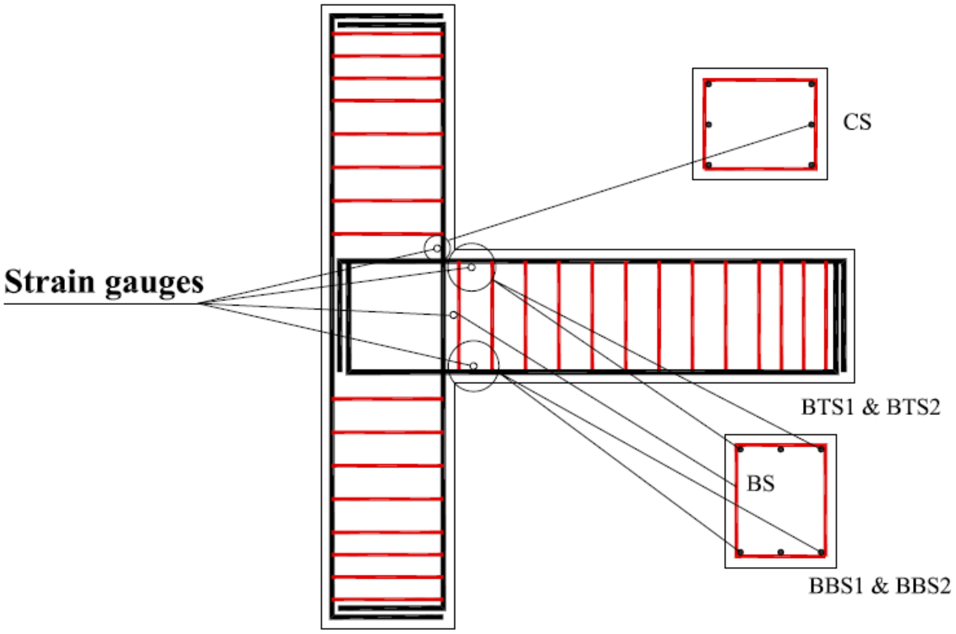

Figure 4.13: Schematic diagram for location of strain gauges installed on reinforcement

Note: CS: Column Bar strain gauge, BTS: Beam Top Bar strain gauge, BBS: Beam Bottom Bar strain gauge and BS: Beam Stirrups strain gauge

Figure 4.14: Strain gauge installed on reinforcement

4.5.3 Specimen casting

The specimens were cast at PRIANSA Precast Company. New smooth surface wooden formwork was utilized in casting of beam column joints. The corners of form work were sealed using silicon to prevent losing of water from the concrete. The concrete was provided by Saudi Ready Mix Company. The concrete was placed directly to the formwork from truck and vibrator was used to consolidate the concrete properly. The concrete surface was cured using wet jute and plastic sheets were utilized to cover the wet surface. Figure 4.15 shows cast BCJ specimen.

Figure 4.15: Specimen cast at PRAINSA Co.

4.5.4 Preparation of Retrofitted Specimens

As mentioned in section 4.5.1 four specimens were retrofitted by shape memory alloys sheets with different configuration to study the behavior of shear deficient retrofitted BCJs under cyclic and reverse cyclic loads. The SMAs sheets were bonded to the concrete surface using SIKA-DUR 330 epoxy as shown in Figure 4.16. The tensile strength of SIKA-DUR 330 epoxy is approximately 30 MPa with allowable elongation of 9 % after 7 days curing.

Figure 4.16: SIKA-DUR 330 Epoxy

The ends of SMAs sheets were tied with SIKA Wrap-230C which is mid-strength unidirectional carbon fibers. These CFRP sheets were wrapped around the cross -section to provide perfect anchorage system at the ends. Figure 4.17 shows the schematic diagram for retrofitted scheme used in this study. The SMAs sheets got from the vender were 75 mm wide and 1000 mm long. Due to the limitation of material the sheets were cut to 25 mm wide and required length for retrofitting. Figure 4.18 shows the prepared retrofitted samples.

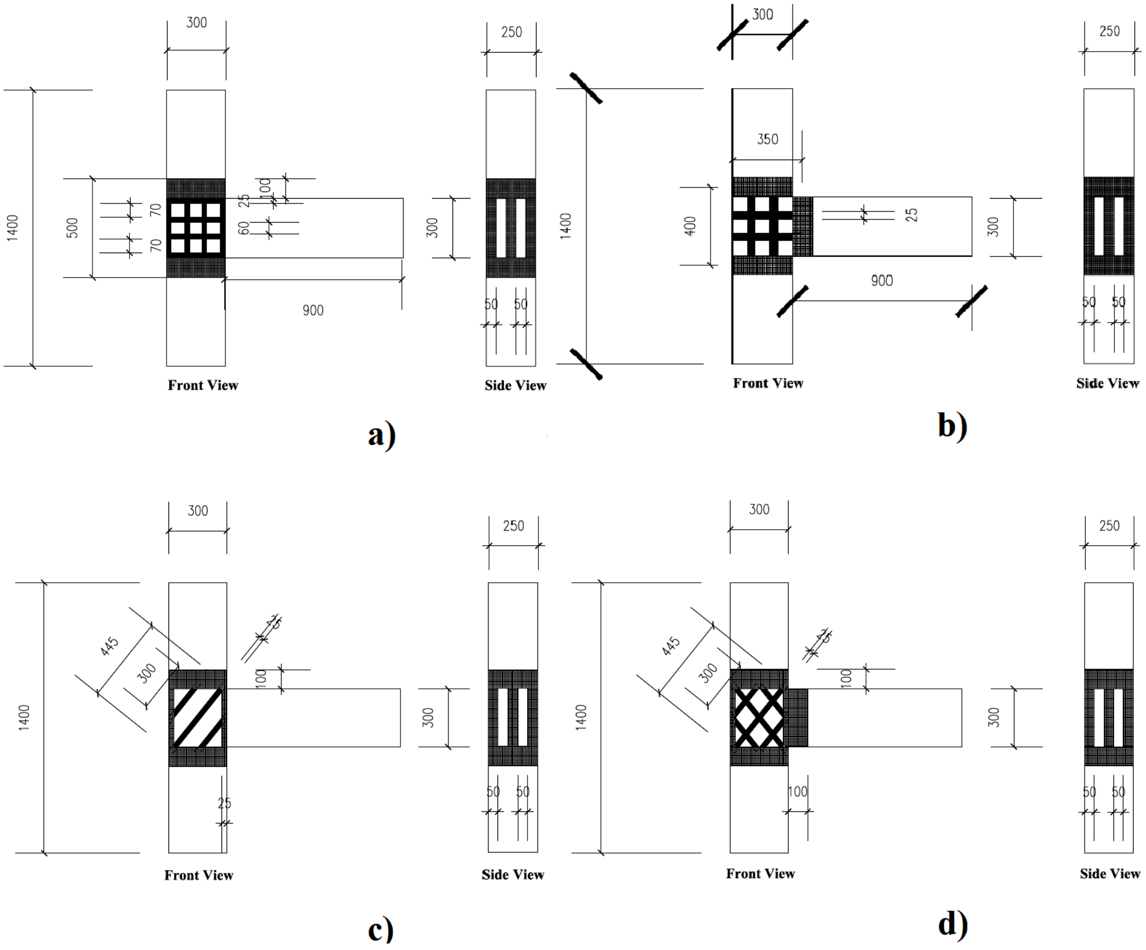

Figure 4.17: Schematic diagram of retrofitted samples a) BCJ-RC4S b) BCJ-RC2S c) BCJ-CIS d) BCJ-RCXS

Note: All dimensions are in mm

Figure 4.18: Retrofitted Specimens

4.6 Testing Setup

The specimens were installed in steel self-reacting loading frame of structural engineering lab of KFUPM. The specimen was placed in testing frame and hold from the top and bottom with steel clamping setup. Two hydraulic jacks were used to apply axial load in column and qua-static load on beam end. The capacity of jacks used for axial load is 30 tons whereas for beam load is 10 tons. Figure 4.19 shows the testing frame and setup used for testing of specimens. Figure 4.20 shows the location of hydraulic jacks.

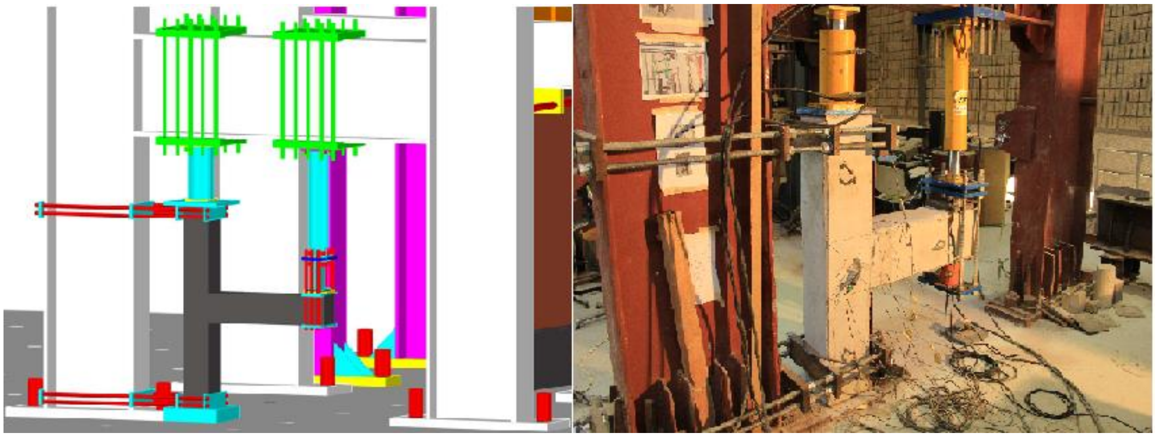

Figure 4.19: Schematic Diagram for testing setup (left) and testing setup used (right)

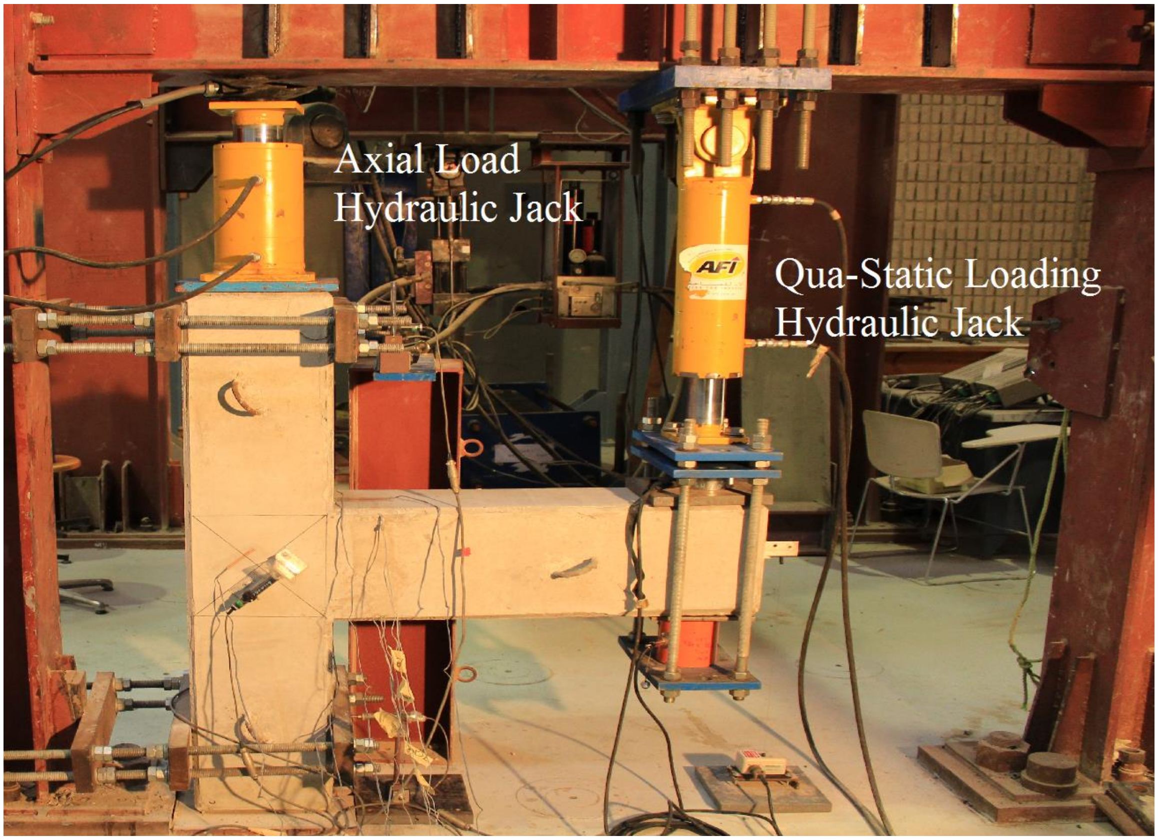

Figure 4.20: Loading Jacks used in testing program

4.7 Monitoring Instrumentation

Loads, strains in concrete and SMAs sheets and crack openings were monitored using load cells, strain gauges and LVDT's during testing of specimens. Two load cells were placed at the tip of beam to monitor load in push and pull. One load cell was placed at the top of column to monitor the axial load. Concrete strain gauges were installed on column (near the interface and back side face), beam (near the interface) and on joint front and back face on selective location to measure the concrete strains. High strain measuring strain gauges were installed on SMAs sheets to measure the strains in SMAs sheets. LVDT's were installed at top, bottom and joint region to measure the support rotation and crack opening in joint regions. Patriot (string type) LVDT was installed on beam tip to measure the tip deflection during testing. Figure 4.21 shows the location of load cells and LVDTs.

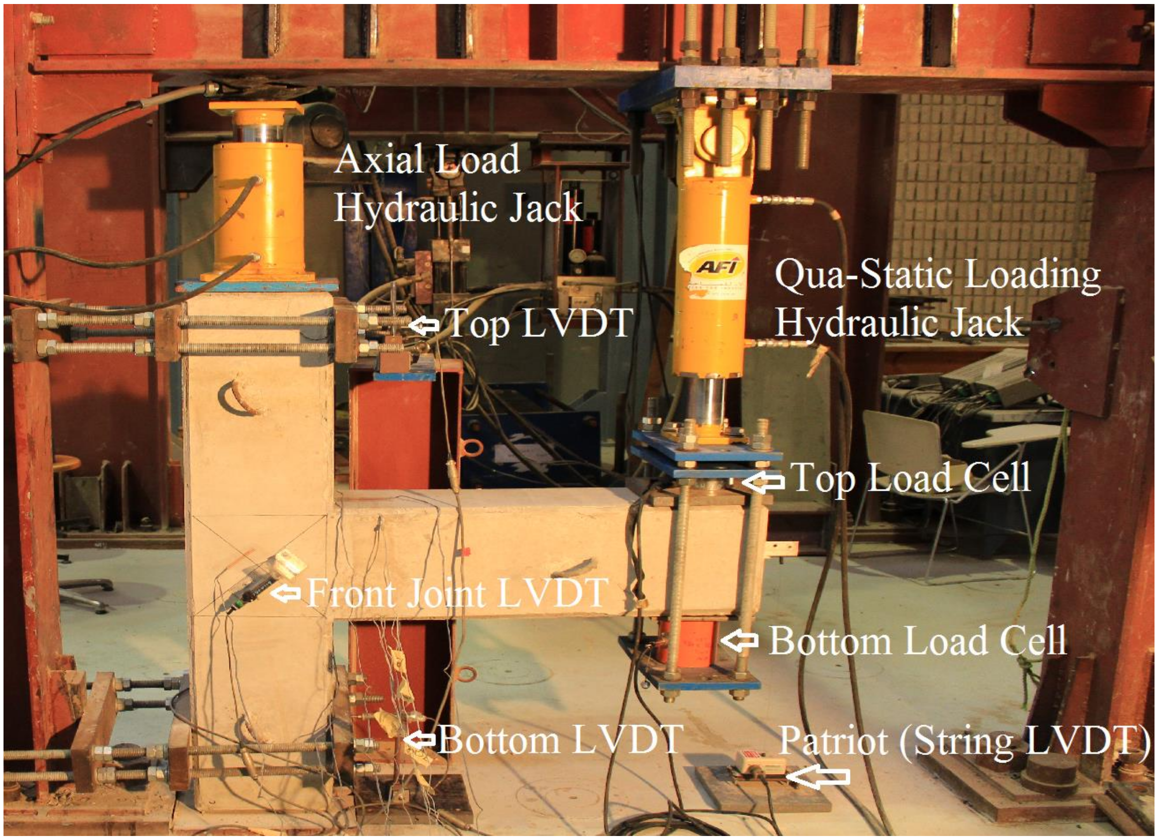

Figure 4.21: Location of load cells and LVDTs

4.8 Loading Protocol

Displacement control method was used to test the non-seismically and retrofitted specimens. The specimens were tested under monotonic, cyclic and reverse cyclic loading. The constant axial load (150 kN) was applied on the column top before apply the displacement on the beam tip. Using qua-static cyclic loading approach displacement was applied on beam tip. The beam tip was pushed and pulled till the failure of the specimens.

The loading protocols for control specimens are shown in Figure 4.22 for cyclic and reverse cyclic loading. Each cycle was repeated twice for control specimens whereas for retrofitted specimens cycles were not repeated because it was reported by the researcher that repeated cycles will cause debonding of strengthened material. Figure 4.23 shows the loading protocol used for retrofitted specimens for cyclic and reverse cyclic loading.

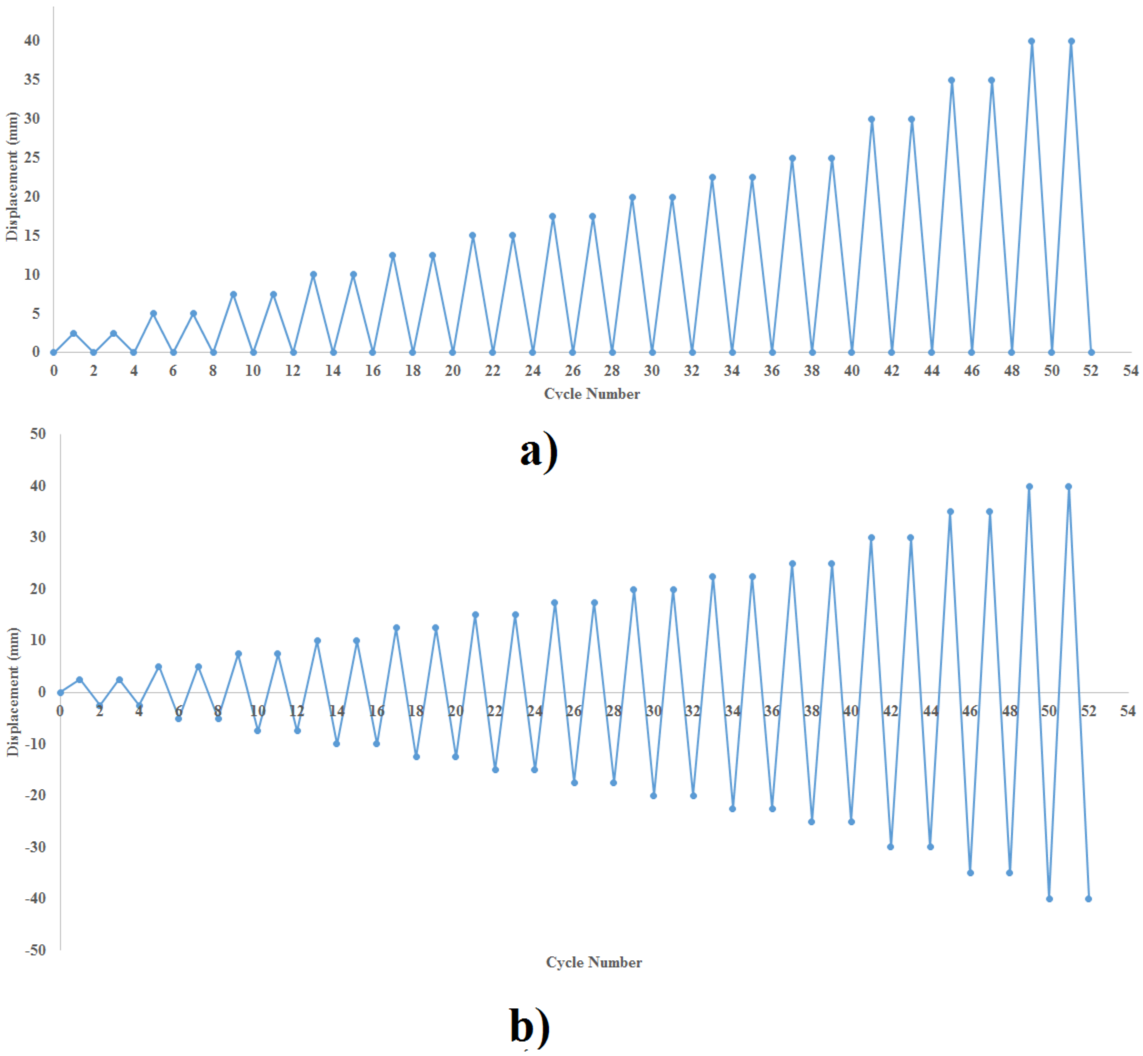

Figure 4.22: a) Cyclic loading and b) Reverse Cyclic Loading Protocol for control specimens

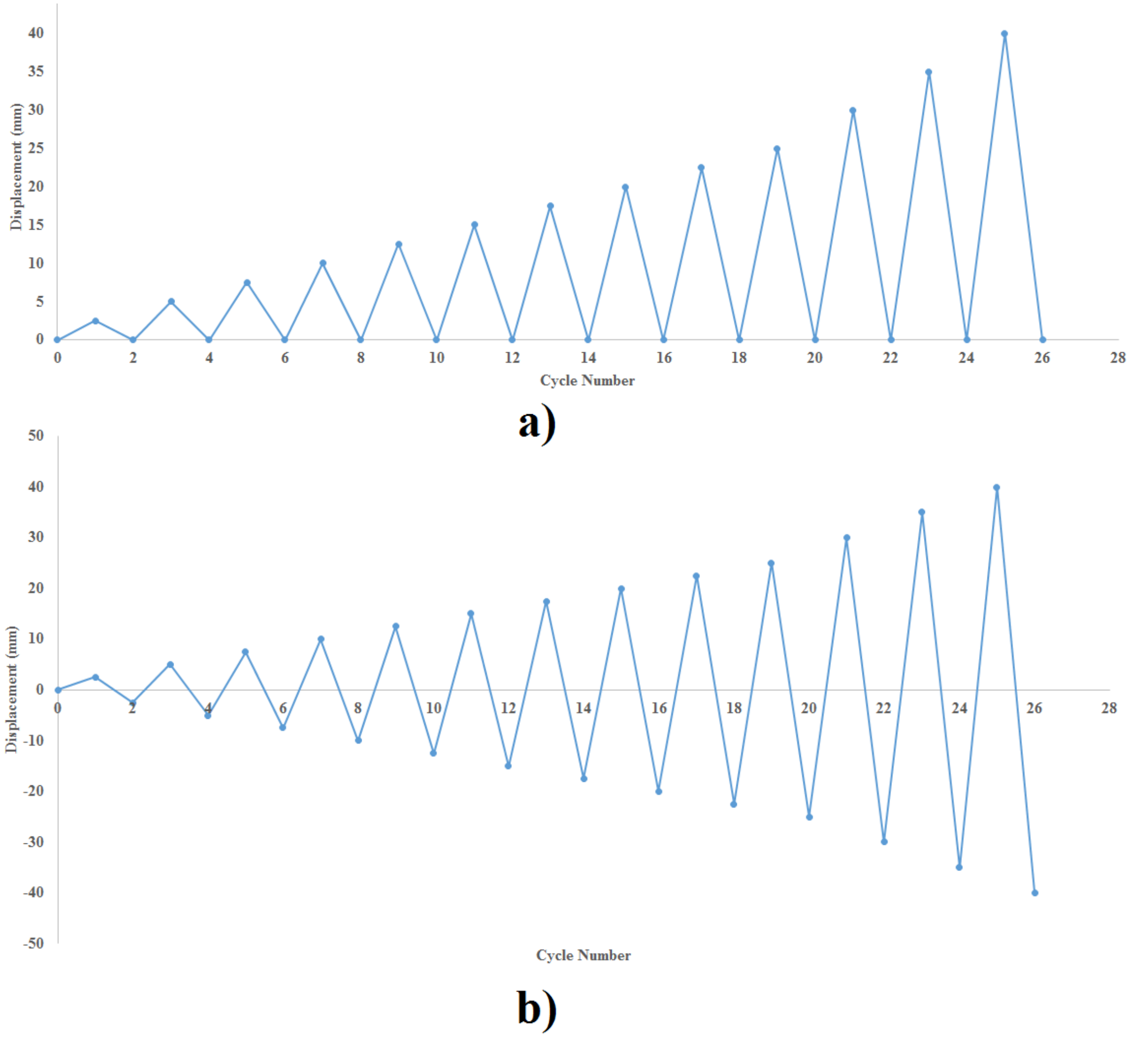

Figure 4.23: a) Cyclic loading and b) Reverses Cyclic loading Protocol for retrofitted Specimens

CHAPTER 5

EXPERIMENTAL RESULTS AND DISCUSSIONS

5.1 Introduction

Seven specimens were tested under monotonic, cyclic and reverse cyclic loading. These specimens include control and retrofitted specimens. Table 5 shows the description of specimens and loading protocol used to test the specimens.

Table 5: Description of specimens and loading Protocol

Serial#	Specimen	Description	Loading
1	BCJ-M	Control specimen	Monotonic
2	BCJ-CL	Control Specimen	Cyclic
3	BCJ-RC	Control Specimen	Reverse Cyclic
4	BCJ-RC4S	Retrofitted Specimen with 4 horizontal and 4 vertical sheets	Reverse cyclic
5	BCJ-RC2S	Retrofitted Specimen with 2 horizontal and 2 vertical sheets	Reverse cyclic
6	BCJ-RCXS	Retrofitted Specimen with cross sheets	Reverse Cyclic
7	BCJ-CLIS	Retrofitted Specimen with inclined sheets	Reverse Cyclic

Note: BCJ: Beam-Column Joint, CL: Cyclic Loading, RC: Reverse Cyclic, XS: Cross SMAs Sheets, IS: Inclined SMAs Sheets, M: Monotonic, 4S: 4 Vt. And Hz. Sheets, 2S: 2 Vt. And Hz. Sheets

5.2 Testing Results of BCJ-M

BCJ-M was tested under monotonic loading in push and pull directions, respectively. The sample was first pushed until the reduction of ultimate load than it was pulled to the complete failure of specimen. The ultimate load of 122.46 kN was achieved at the displacement of 20.46 mm in push direction. The load deflection response of BCJ-M is shown Figure 5.1. The first crack appeared was flexural and it was observed near the BCJ interface at load of 32 kN with a displacement of 2.1 mm. Similarly second, third, fourth and fifth flexural cracks were observed at load of 48 kN, 53 kN, 63 kN and 80 kN at displacement of 3.8 mm, 4.2 mm, 5.6 mm and 7.8 mm, respectively. The first shear crack in the joint region (back face) was observed at a load of 60 kN when beam was pushed up to 5.2 mm. Similarly second and third shear cracks at the back face were observed at load of 114 kN and 120 kN at displacement of 14.9 mm and 18.9 mm, respectively. The first shear crack in the joint region (front face) was observed at a load of 74 kN when beam was pushed up to 6.9 mm. Similarly second and third shear cracks at the front face were observed at load of 120 at displacement of 16.7 mm, respectively. Figure 5.2 shows the first flexural and shear cracks for the specimen BCJ-M. During loading widening of shear cracks were observed. The beam was later on pulled when the ultimate load reduced to 106.12 kN at displacement of 28.45 mm. 14.7 mm residual displacement was observed at zero load during pulling. The ultimate load observed in the pull direction was 104.2 kN at displacement of 20.28 mm. The beam was pulled till the complete failure of joint. The residual displacement upon unloading from pull direction was 57 mm. The specimen was failed completely in shear. Figure 5.3 shows the formation of cracks during testing of BCJ-M.

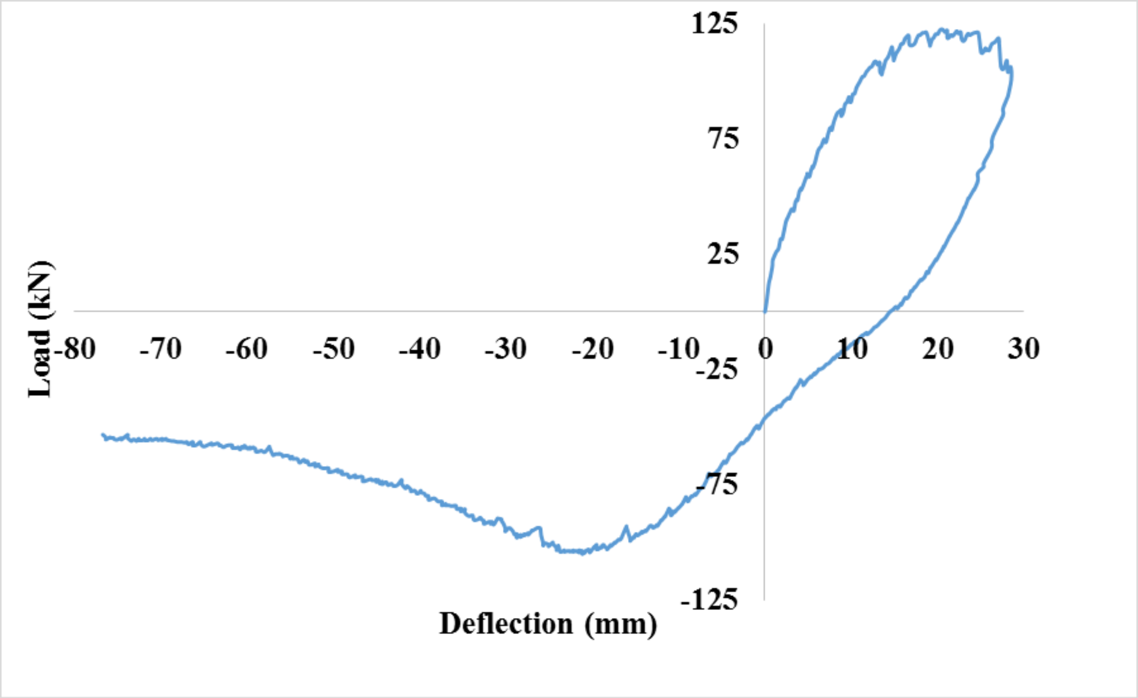

Figure 5.1: Load-Displacement Response of BCJ-M

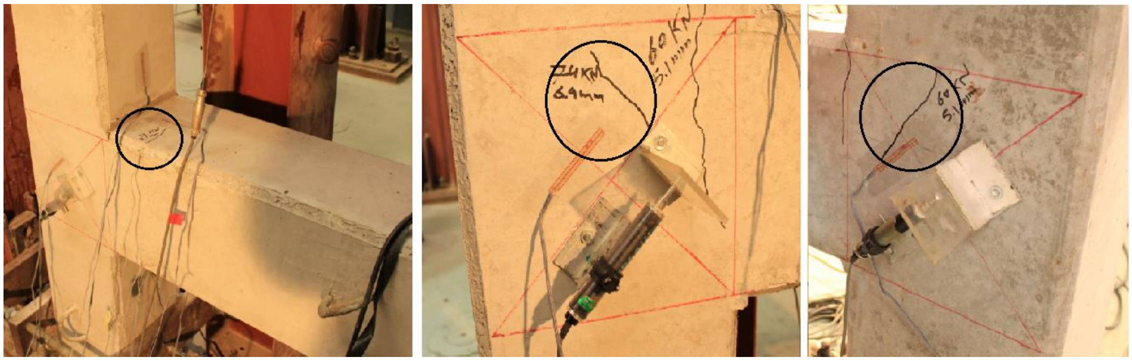

Figure 5.2: 1st Crack in Push Direction (left), 1st Shear crack on front face (central) and back face (right)

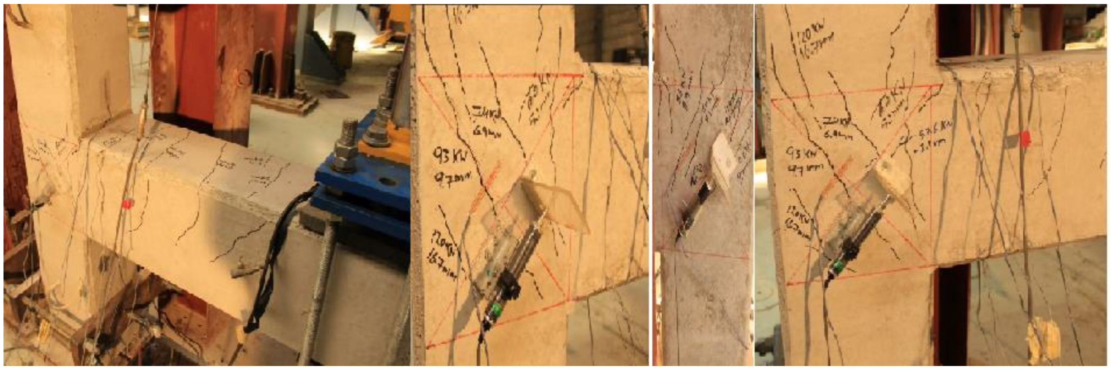

Figure 5.3: Formation of different flexural and shear cracks when beam was pushed

At failure the reinforcement was visible and spalling of concrete from the back face and front face of joint was occurred. Also rebar was visible at side face of the column. Figure 5.4 shows the ultimate failure of joint.

Figure 5.4: Failure of BCJ-M

LVDTs were used to measure the crack opening in the joint regions. It has been observed that crack width increased when the beam was pushed and pulled. Figure 5.5 shows the crack opening in the joint region.

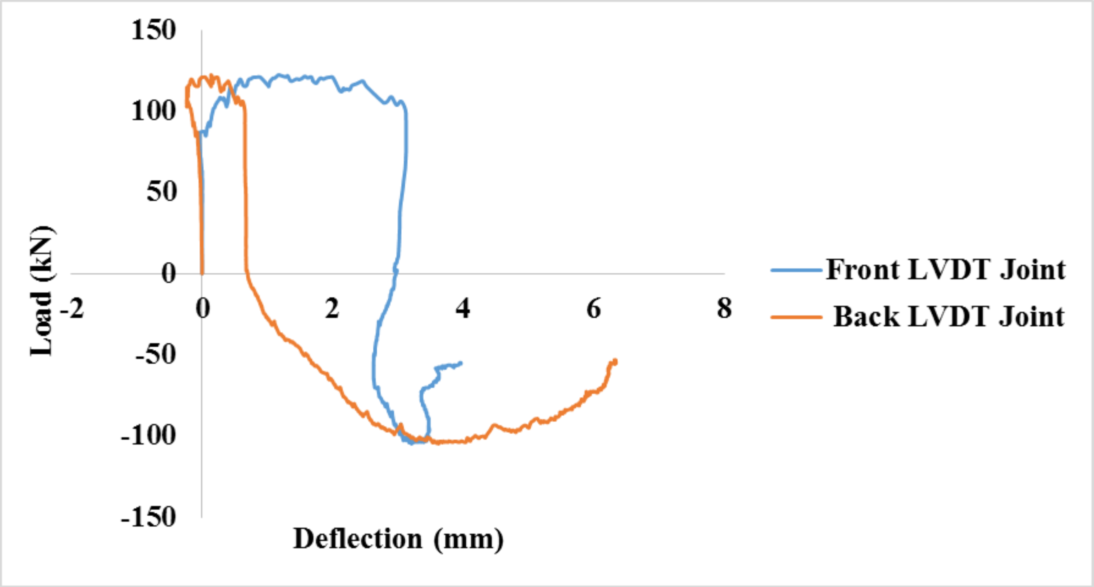

Figure 5.5: Crack opening in joint region

Reinforcement strain gauges were also monitored to observed strains in rebars. Figure 5.6 and Figure 5.7 shows the strains in beam reinforcements during push and pull directions. Figure 5.8 shows the strains in column rebar.

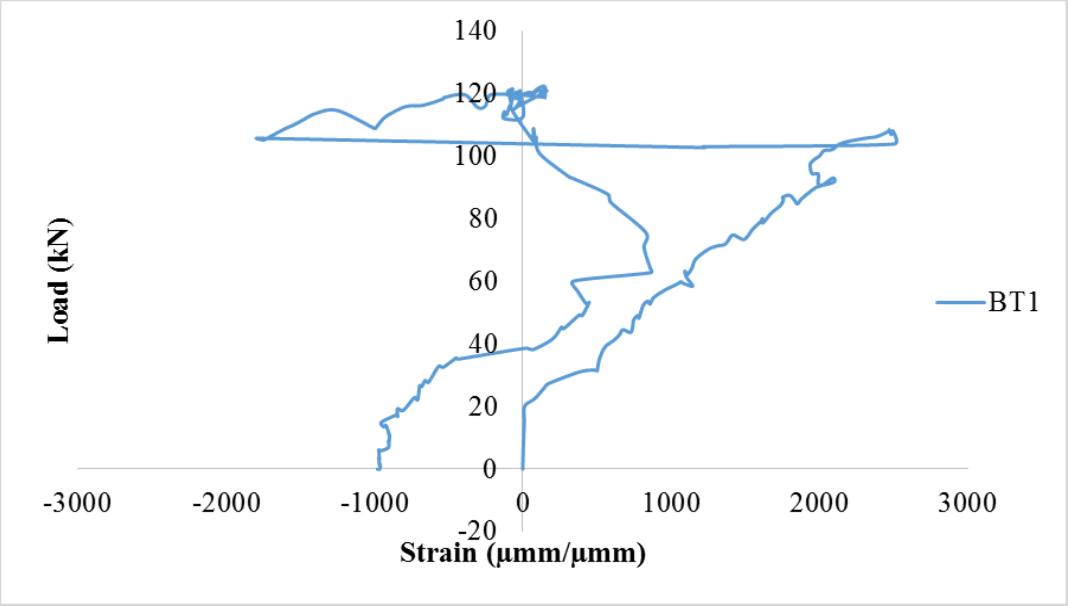

Figure 5.6: Load-Strain graph for rebar during pushed

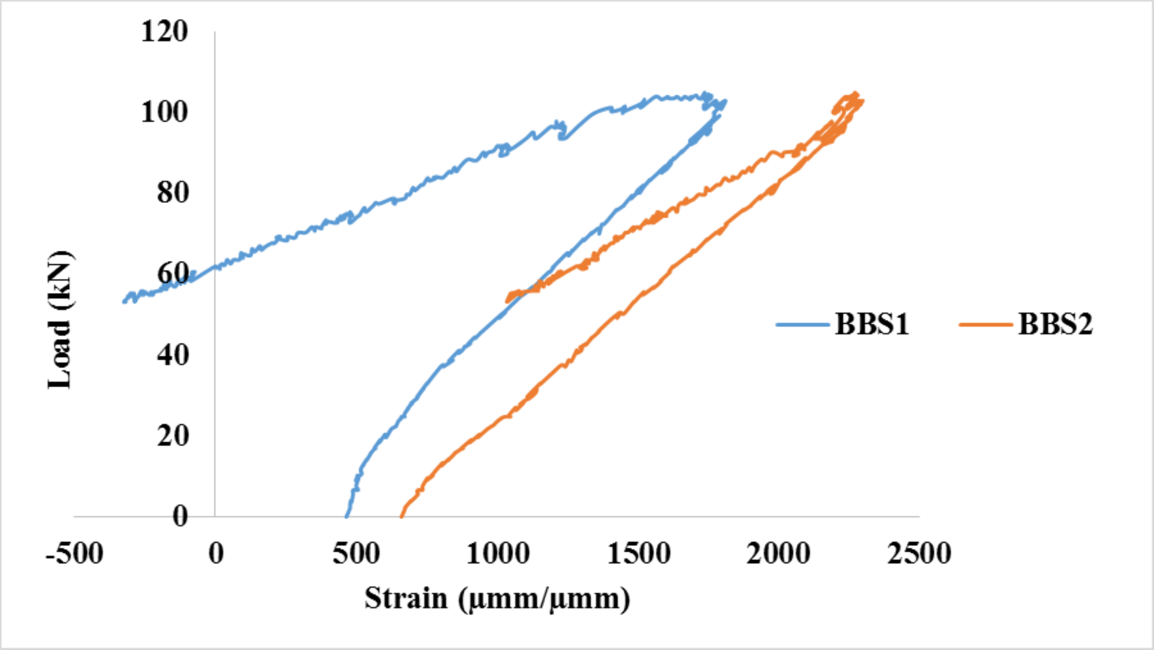

Figure 5.7: Load-Strain graph for rebar during pulled

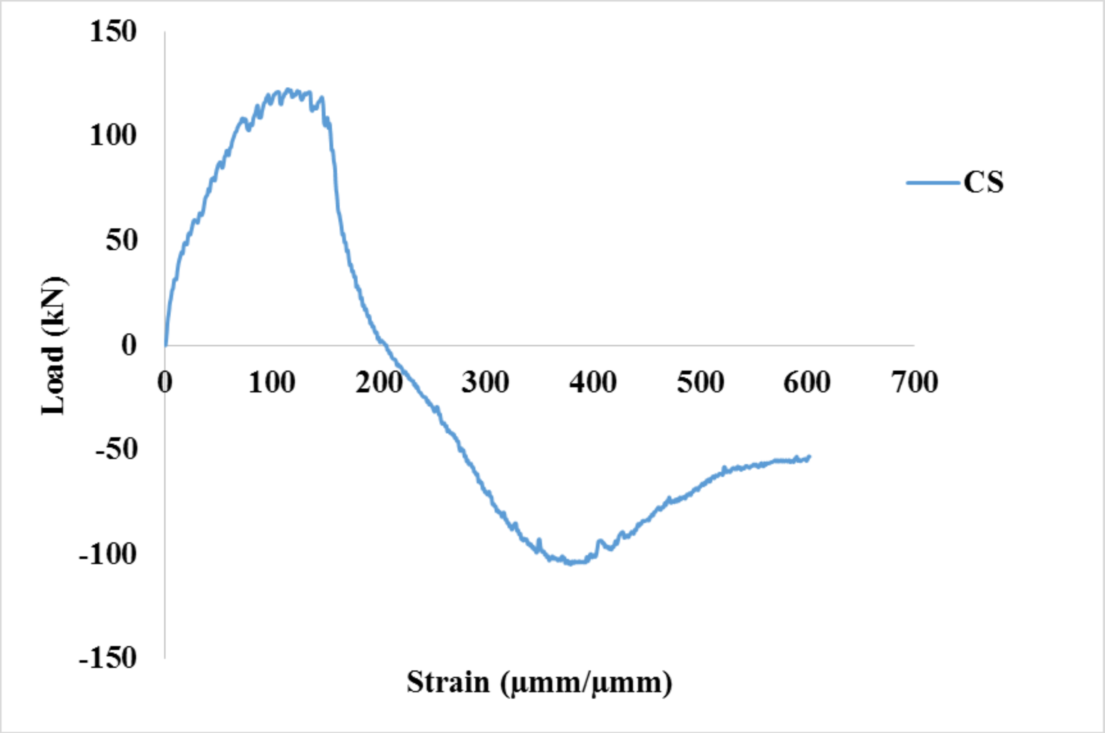

Figure 5.8 : Load-Strain graph for column rebar during push and pull

5.3 Testing Results of BCJ-CL

BCJ-CL was tested under cyclic loading. The ultimate load of 110.36 kN was achieved at the displacement of 22.362 mm. The load deflection response of BCJ-CL is shown Figure 5.9. The first crack appeared was flexural and it was observed near the BCJ interface at load of 42 kN with a displacement of 3.44 mm. Similarly second, third and fourth flexural cracks were observed at load of 49 kN, 49 kN and 50 kN at displacement of 4.5 mm, 4.5 mm and 5 mm, respectively. The first shear crack in the joint region (front face) was observed at a load of 59 kN when beam was pushed up to 6.4 mm. Similarly second and third shear cracks at the front face were observed at load of 67 kN and 71.3 kN at displacement of 8.3 mm and 9.6 mm, respectively. The first shear crack in the joint region (back face) was observed at a load of 59 kN when beam was pushed up to 6.4 mm.

Similarly second, third shear and fourth shear cracks at the back face were observed at load of 67 kN, 71.3 kN at displacement of 8.3mm and 9.6 mm, respectively. During loading widening of shear cracks were observed. During unloading residual displacement was observed throughout the test. The specimen was failed completely in shear. Figure 5.10 shows the formation of cracks during testing of BCJ-CL. Figure 5.11 shows shear cracks formation on the front and back face of joint region during loading and unloading cycles and the width of these cracks were recorded. These widths were compared later on with retrofitted specimens.

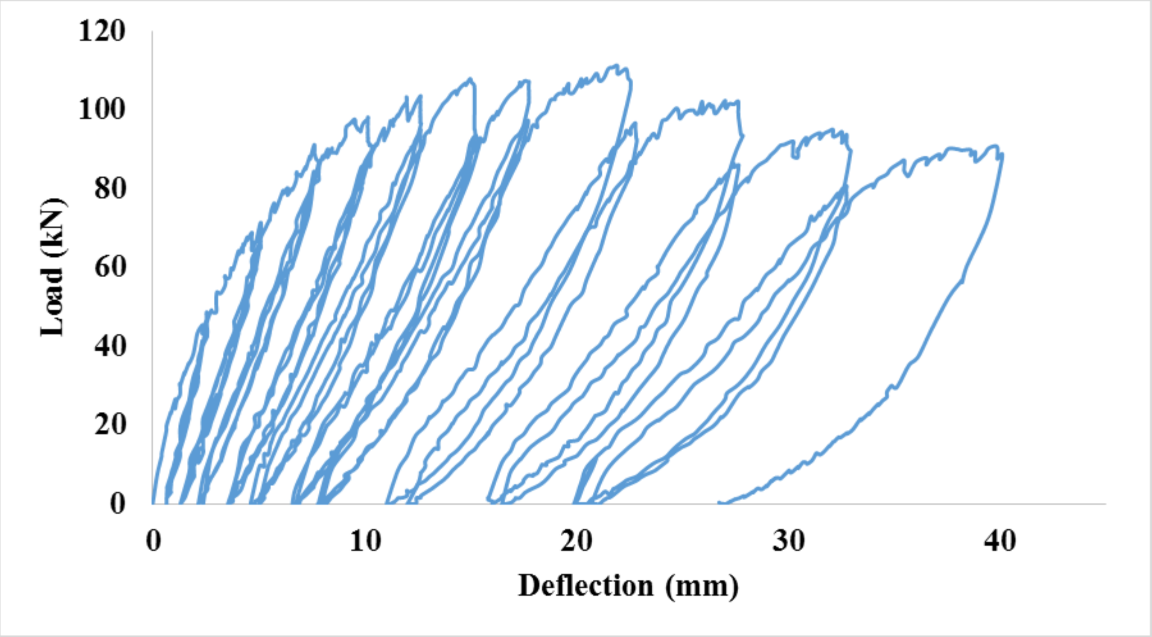

Figure 5.9: Load-Displacement response of BCJ-CL

Figure 5.10: Formation of cracks and widening of cracks during test

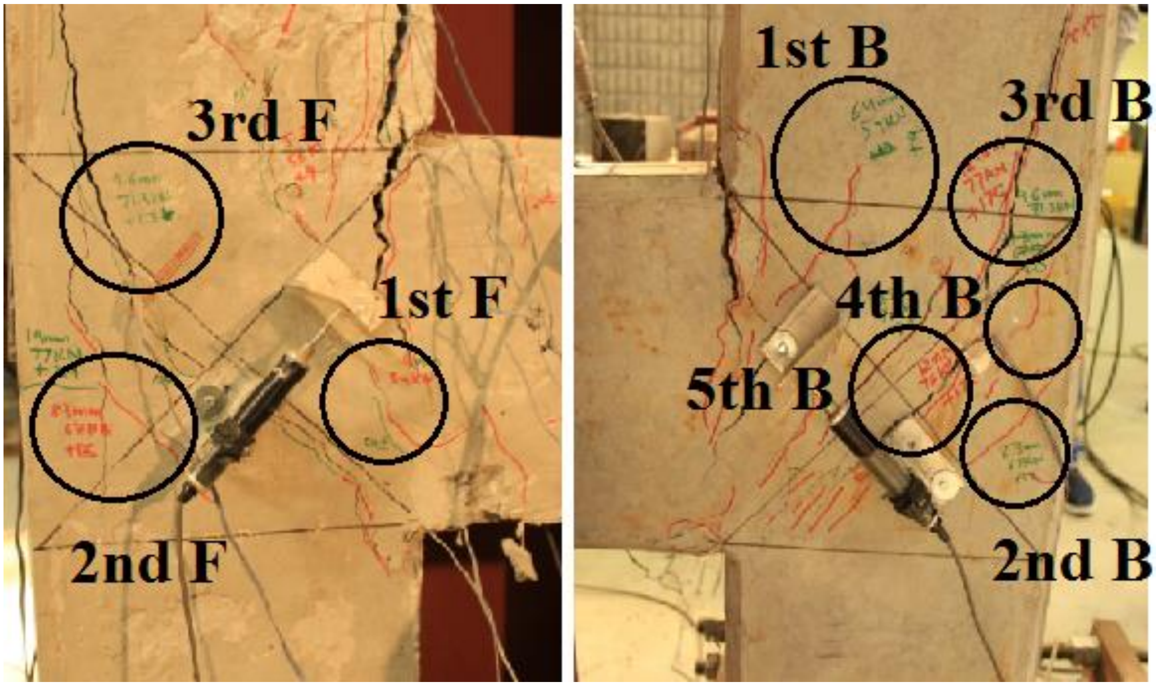

Figure 5.11: Shear cracks at Front (left) and Back (right) face of joint Interface during different loading cycles

At failure the reinforcement was visible and spalling of concrete from the back face and front face of joint was occurred. Also rebar was visible at side face of the column. Figure 5.12 shows the ultimate failure of joint.

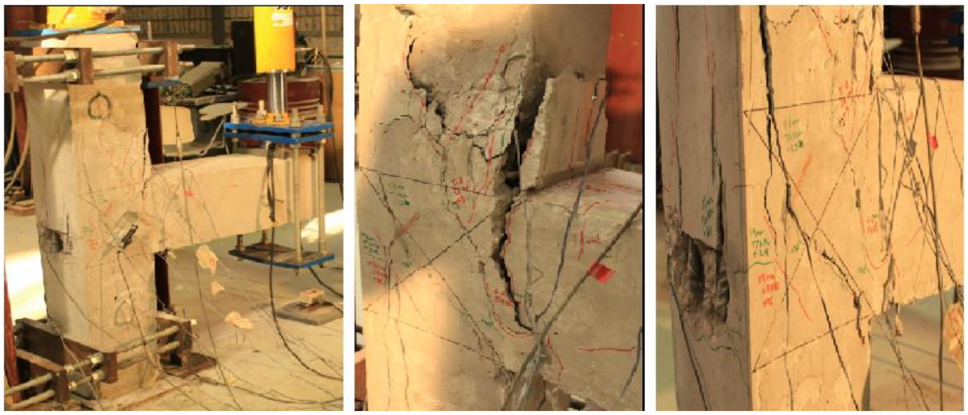

Figure 5.12: Failure of BCJ-CL

LVDTs were used to measure the crack opening in the joint regions. It has been observed that crack width increased during test. Figure 5.13 shows the crack opening in the joint region.

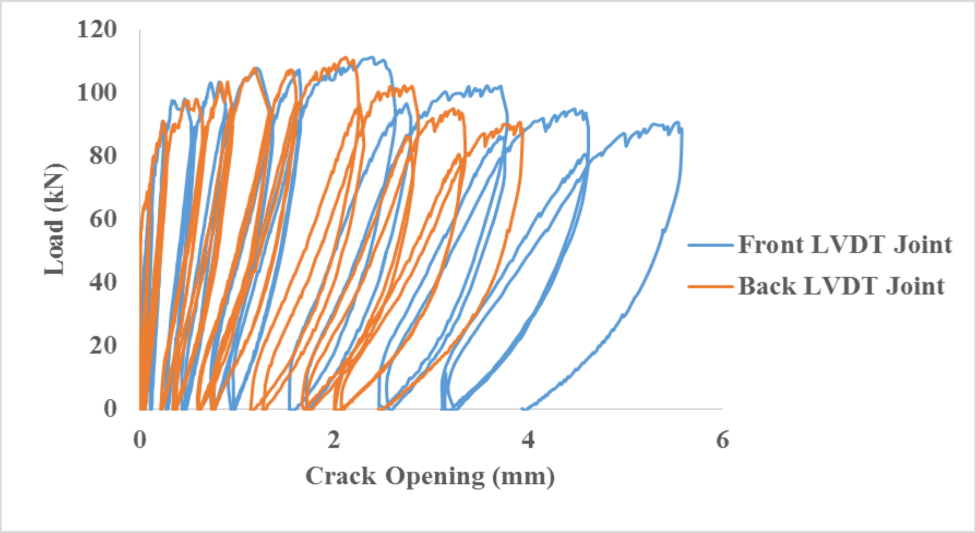

Figure 5.13: Crack opening in Joint region

Reinforcement strain gauges were also monitored to observed strains in rebars. Figure 5.14 shows the strains in beam reinforcements for loading and unloading. Figure 5.15 shows the strains in column rebar and beam stirrup.

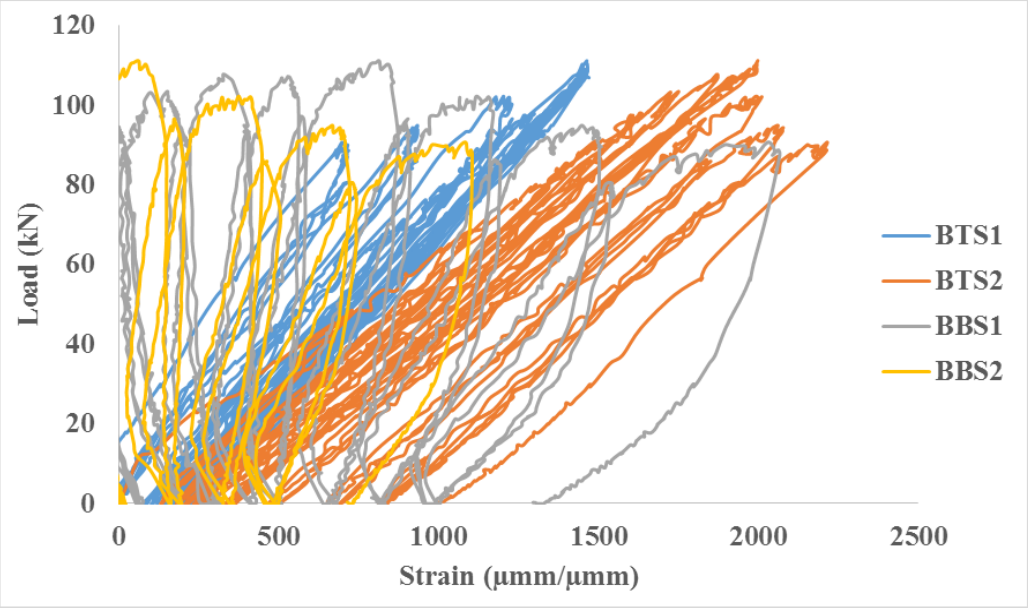

Figure 5.14: Beam reinforcement strains

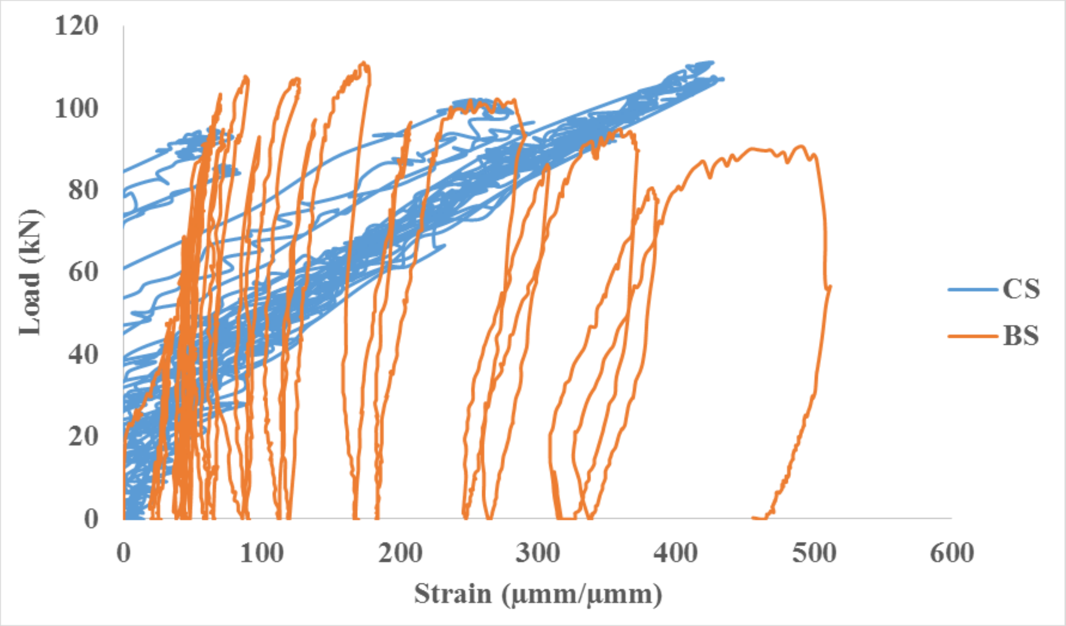

Figure 5.15: Column and beam stirrup reinforcement strains

Cracks in the joints were measured using crack measuring card as shown in Figure 5.16. Figure 5.17 show the cracks width subjected to loading and unloading at the front face of the joint BCJ-CL. Figure 5.18 show the cracks width subjected to loading and unloading at the back face of the joint BCJ-CL.

Figure 5.16: Crack width measurement using Crack measuring card

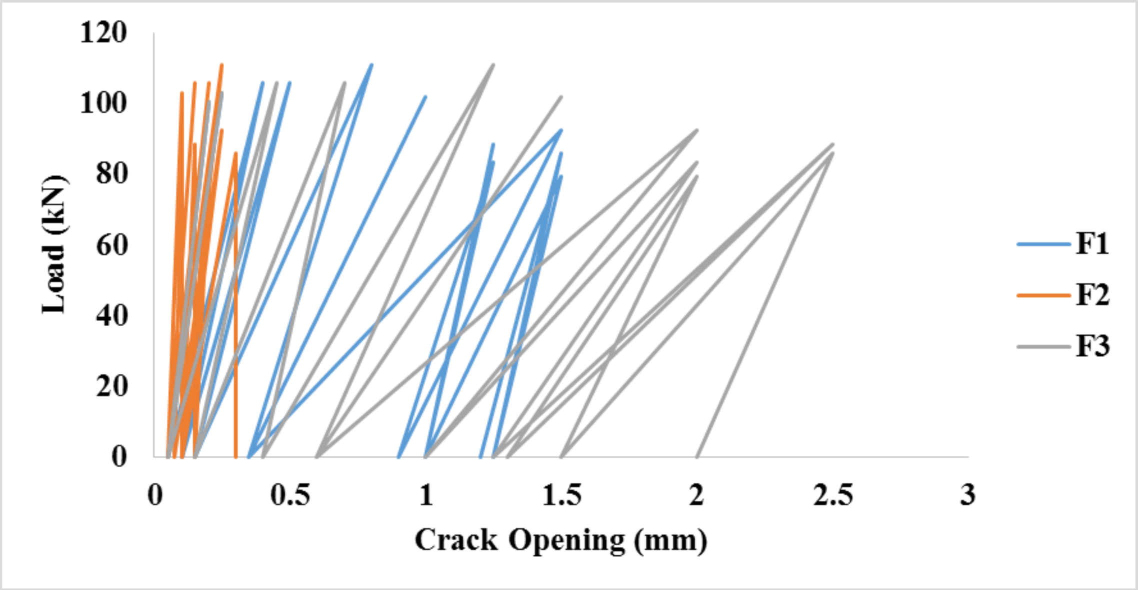

Figure 5.17: Cracks width at the front face of Joint region for BCJ-CL

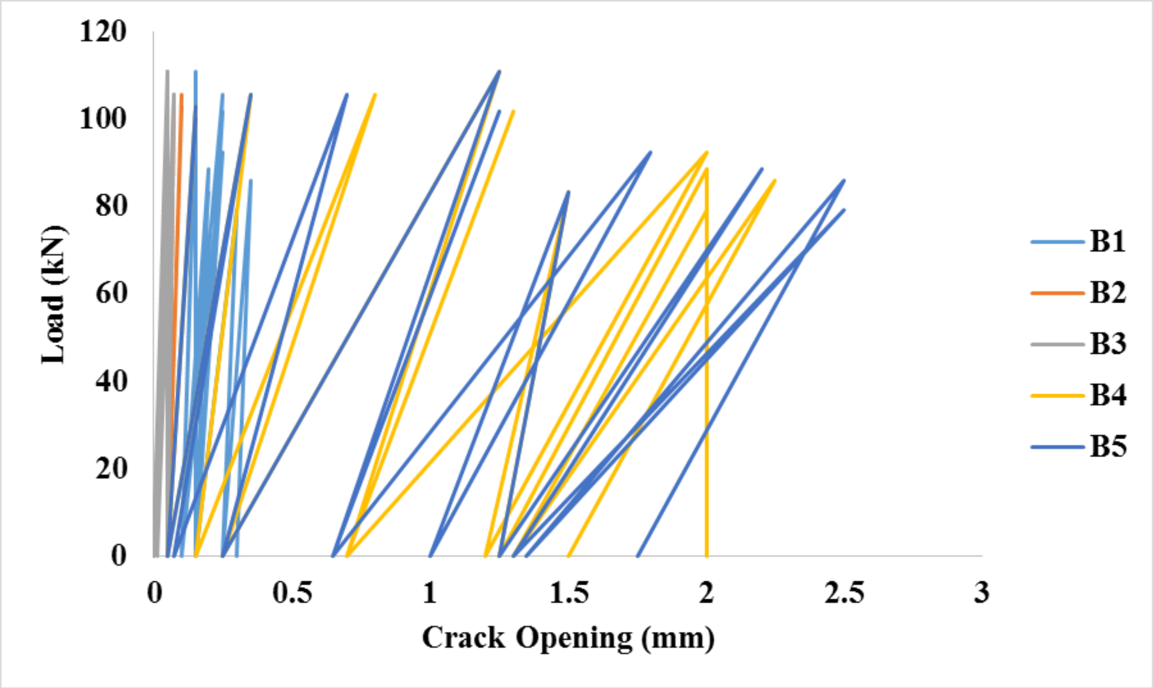

Figure 5.18: Cracks width at the back face of Joint region for BCJ-CL

5.4 Testing Results of BCJ-RC

BCJ-RC was tested under reverse cyclic loading. The ultimate load of 105.82 kN was achieved at the displacement of 14.98 mm in push direction and the ultimate load of 103.9 kN was achieved at the displacement of 16.52 mm in pull direction, respectively. The load deflection response of BCJ-RC is shown Figure 5.19. The hysteresis shows pinching effect due to the steel which doesn’t yield throughout the test. The first crack appeared was flexural at the top surface of beam when beam was pushed in first cycle and it was observed near the BCJ interface at load of 33 kN with a displacement of 2.2 mm. Similarly the first flexural crack was observed at the bottom face of beam in pull direction at a load of 34.5 kN with a displacement of 1.74 mm. The first shear crack in the front and back face of the joint region was observed at a load of 55 kN in 3rd push cycle with a displacement of 4.94 mm. The first shear crack in the front and back face of joint region was observed at a load of 44 kN and 62 kN in 3rd pull cycle with a displacement of 2.6 mm and 4.8mm, respectively. Figure 5.20 shows the 1st flexural and shear cracks in push and pull cycles. During last cycles joint cover concrete started falling and beam- column interface was also severely damaged. Reinforcement was visible from the side of columns, widening of shear cracks were also observed and these cracks extended into the column. During unloading residual displacement was also observed. The specimen was failed completely in shear. Figure 5.21 shows the formation of cracks during different cycles of BCJ-RC. Figure 5.22 and Figure 5.23 shows shear cracks formation on front and back face of joint region during push and pull cycle for which crack widths were measured during loading and unloading. These widths were compared later on with retrofitted specimens.

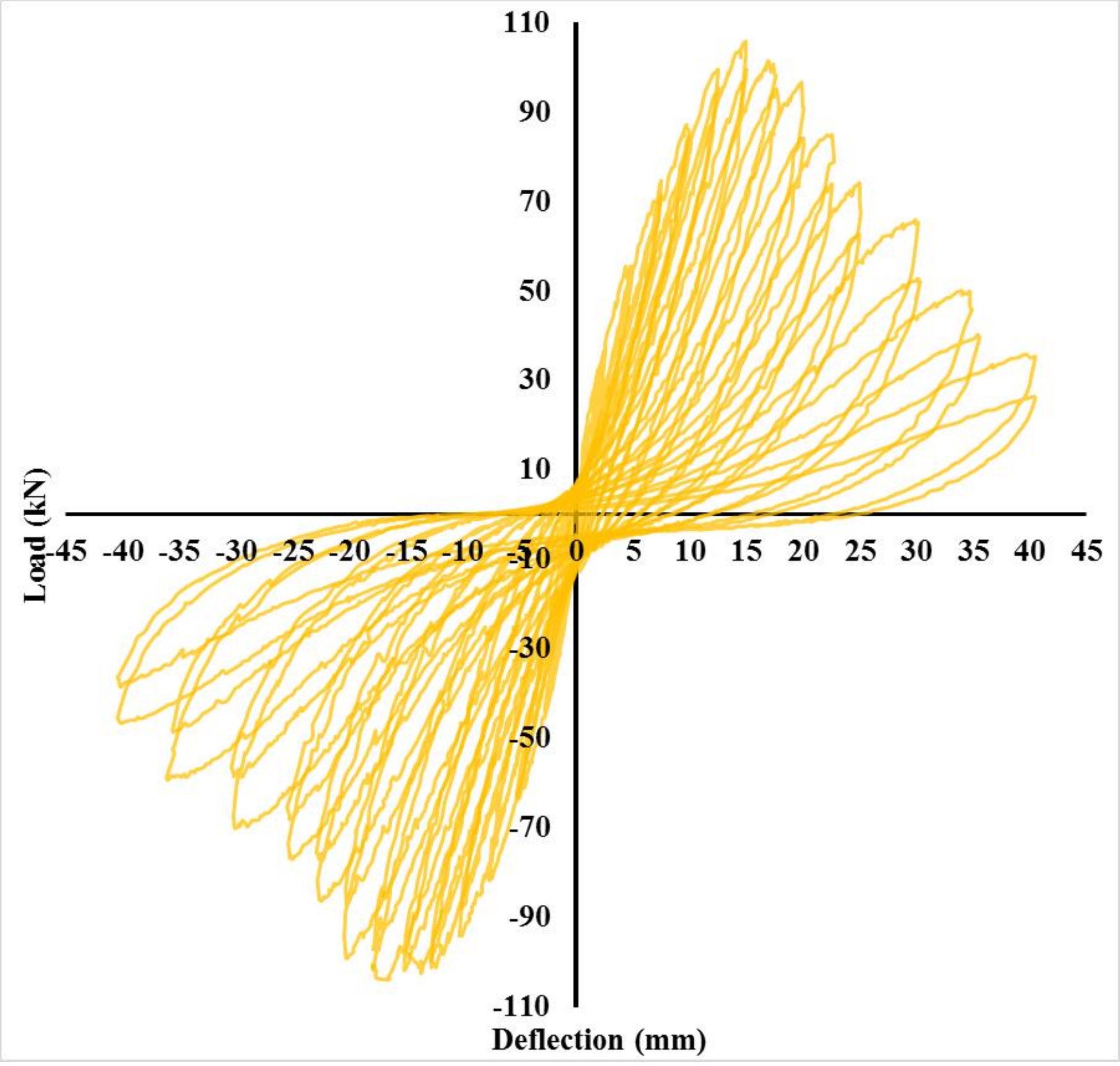

Figure 5.19: Hysteresis response of BCJ-RC

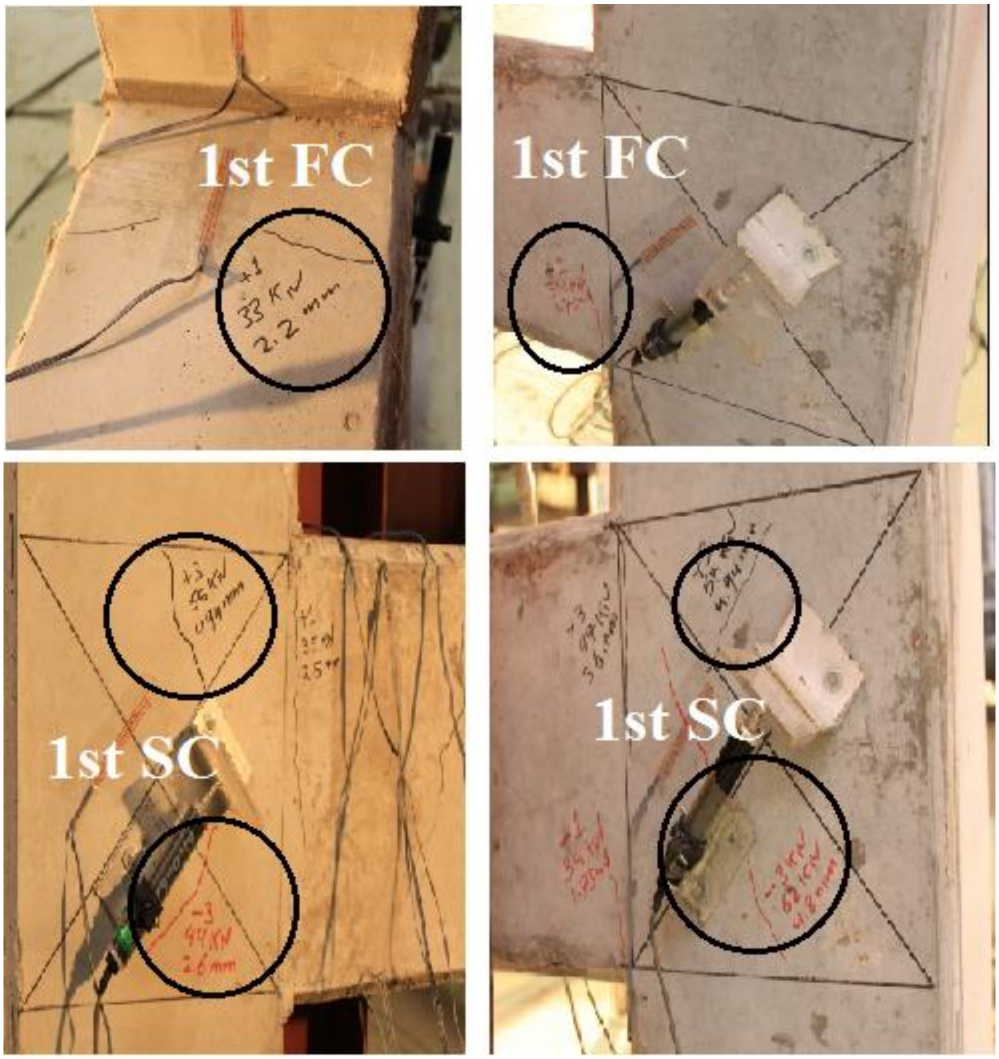

Figure 5.20: 1st Flexural and shear cracks in Front Face (left) and back face (right) for push and pull cycle

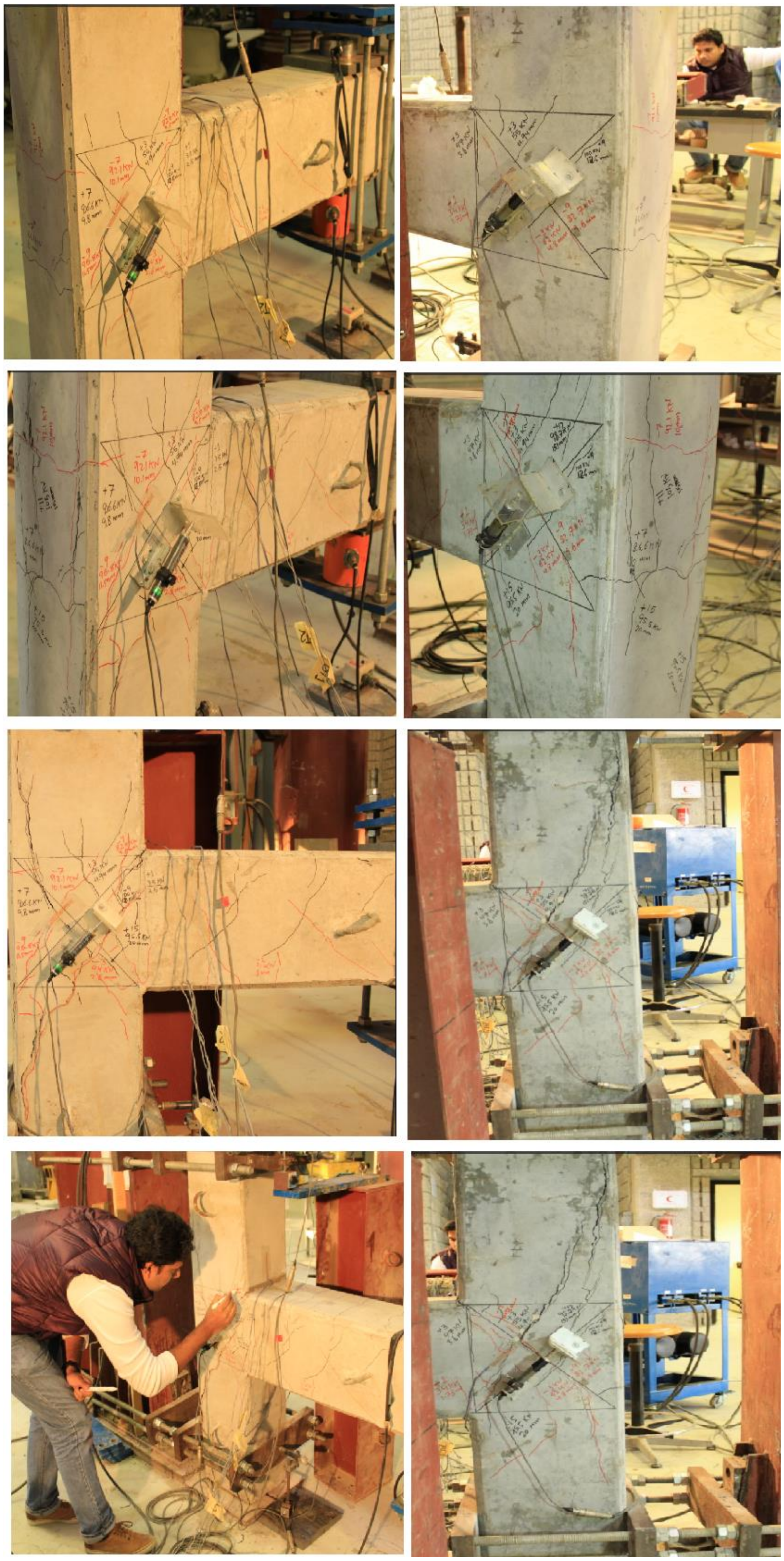

Figure 5.21: Formation of cracks on Front Face (left) and back face (right) of joint region during different cycles

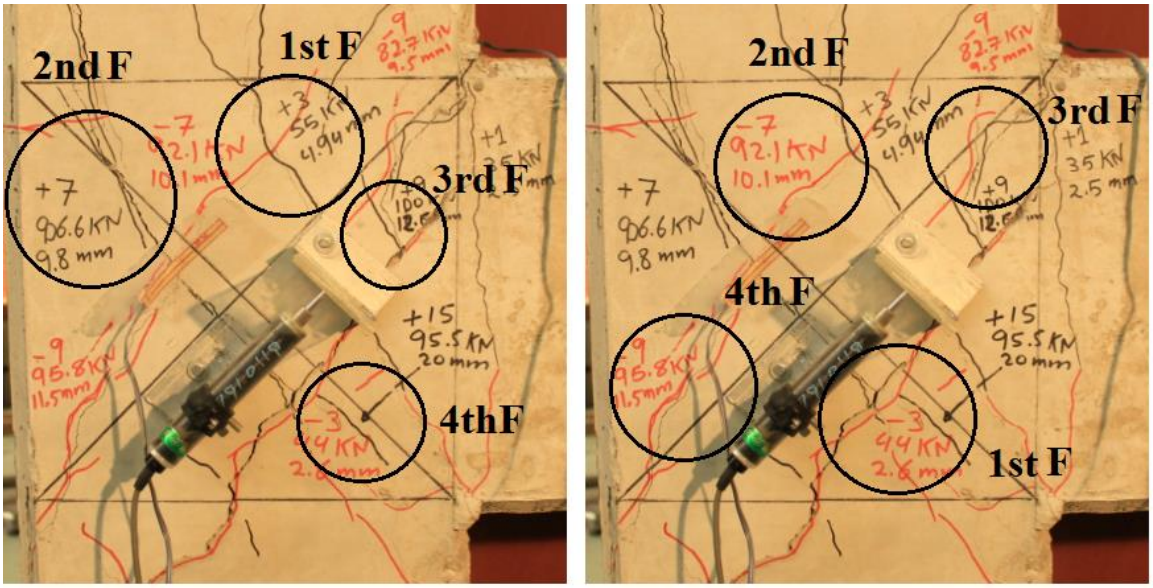

Figure 5.22: Shear cracks in push (left) and pull (right) cycles at the front face of joint region

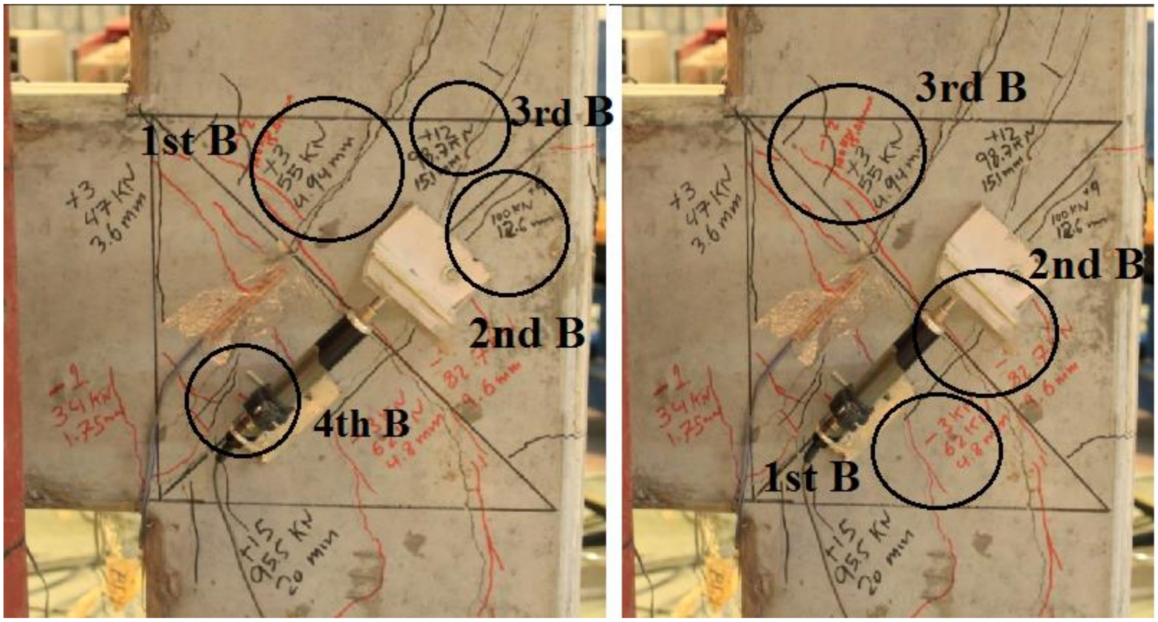

Figure 5.23: Shear cracks in push (left) and pull (right) cycles at the front face of joint region

Note: F stands for Front Face of Joint Region and B stands for Back Face

At failure the reinforcement was visible and spalling of concrete from the back face and front face of joint was occurred. Also rebar was visible at side face of the column. Figure 5.24 shows the ultimate failure of joint.

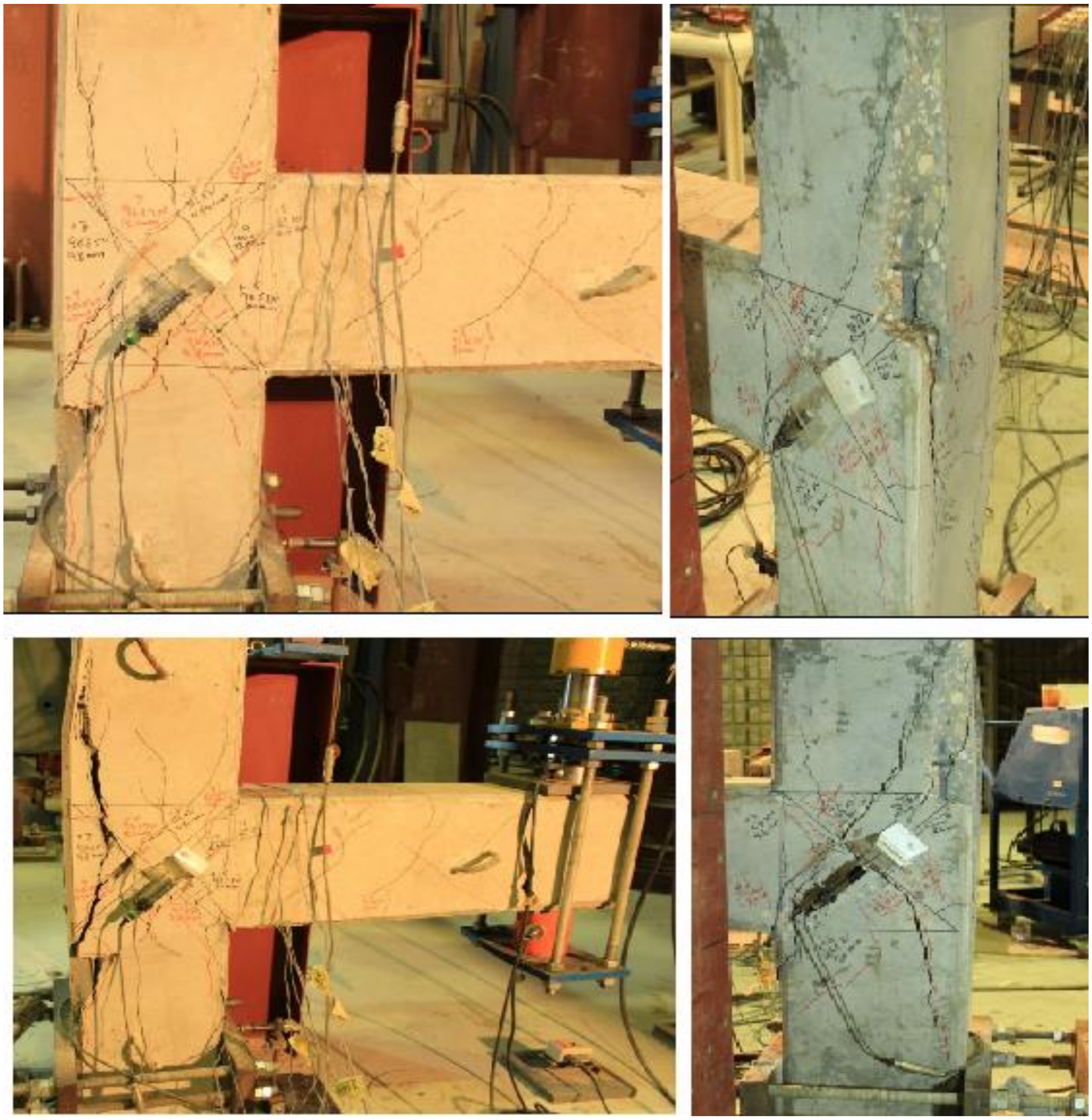

Figure 5.24: Failure of BCJ-RC

LVDTs were used to measure the crack opening in the joint regions. It has been observed that crack width increased during test. Figure 5.25 shows the crack opening in the joint region.

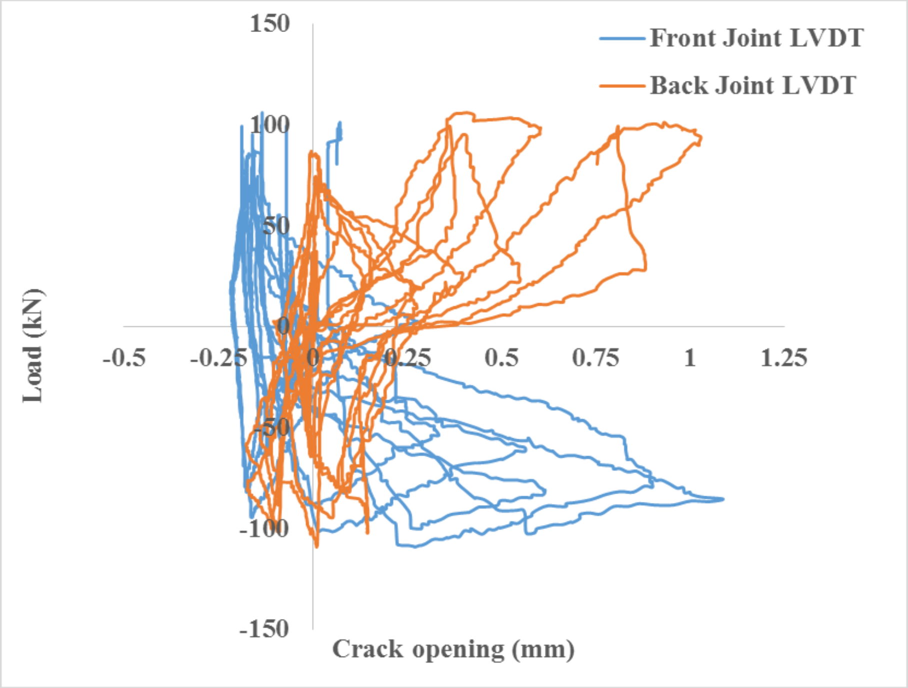

Figure 5.25: Crack opening in Joint region of BCJ-RC

Reinforcement strain gauges were also monitored to observed strains in rebars. Figure 5.26 shows the strains in beam reinforcements during push and pull directions. Figure 5.27 shows the strains in beam stirrup.

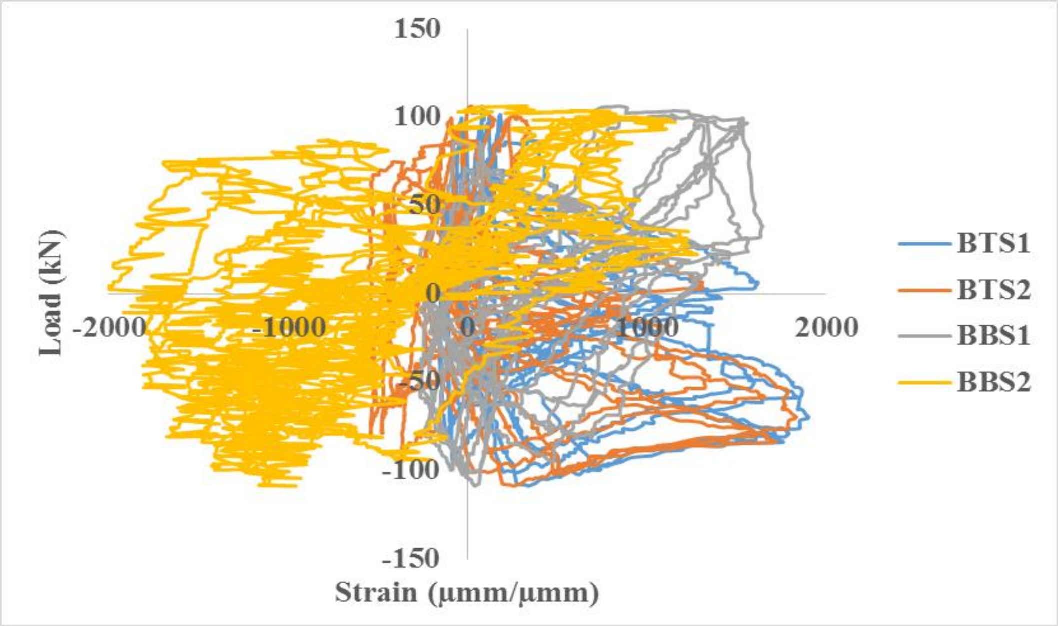

Figure 5.26: Strain in reinforcement for BCJ-RC

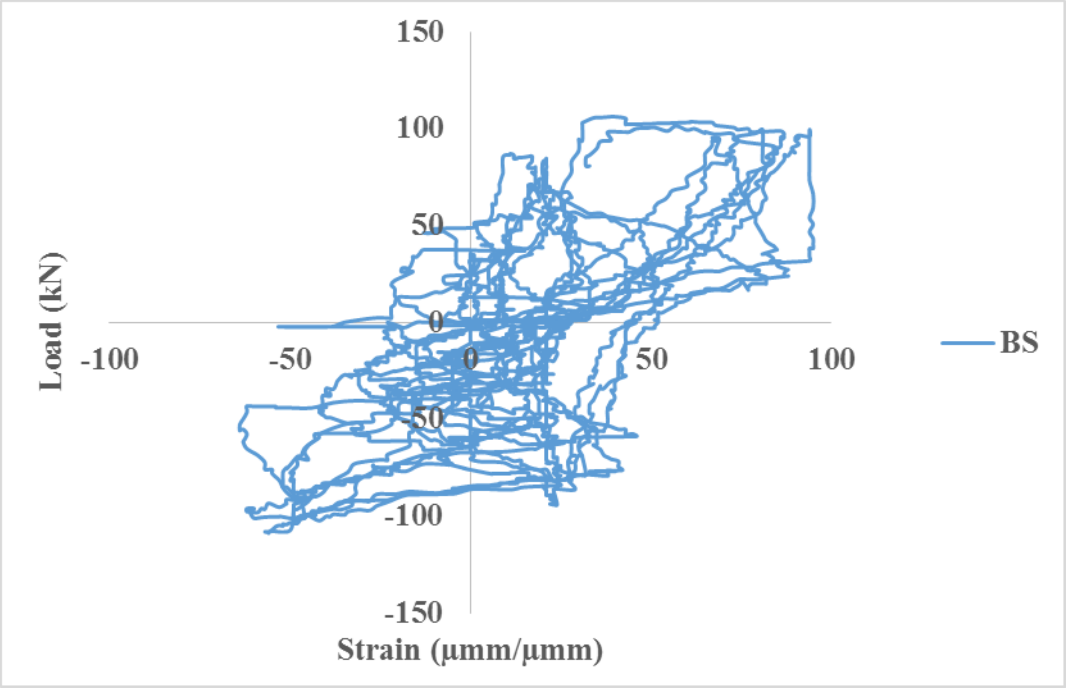

Figure 5.27: Strain in Beam Stirrup

Figure 5.28 show the cracks width at the front face of the joint BCJ-RC when push and unload to zero. Figure 5.29 show the cracks width at the back face of the joint BCJ-RC when push and unload to zero. Figure 5.30 show the cracks width at the front face of the joint BCJ-RC when pull and unload to zero. Figure 5.31 show the cracks width at the back face of the joint BCJ-RC when pull and unload to zero.

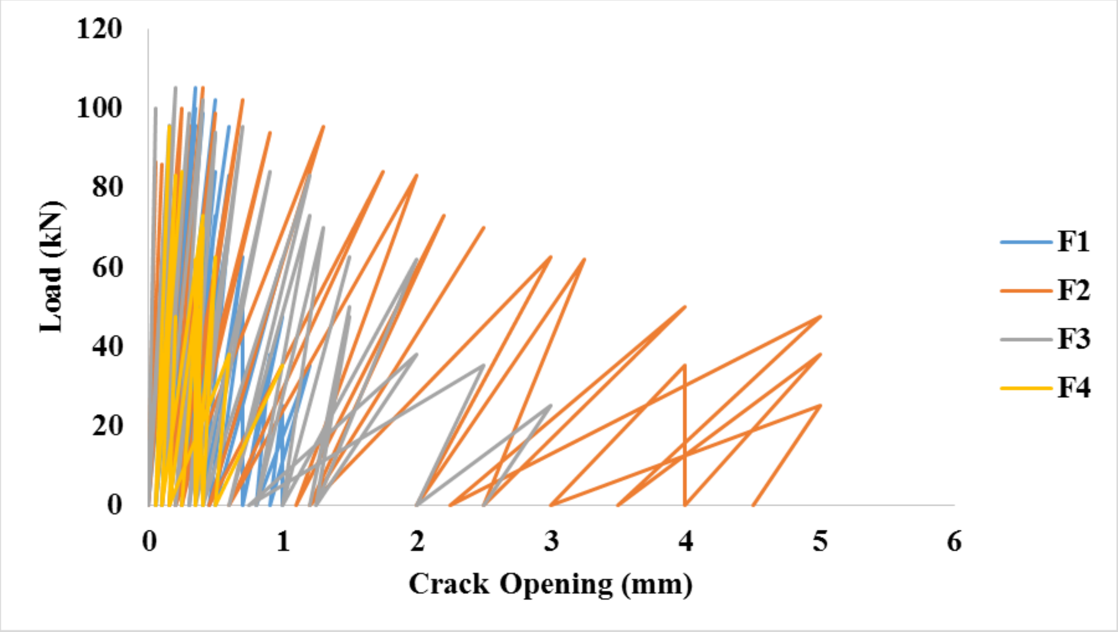

Figure 5.28: Cracks width at the front face of Joint region for BCJ-RC when push

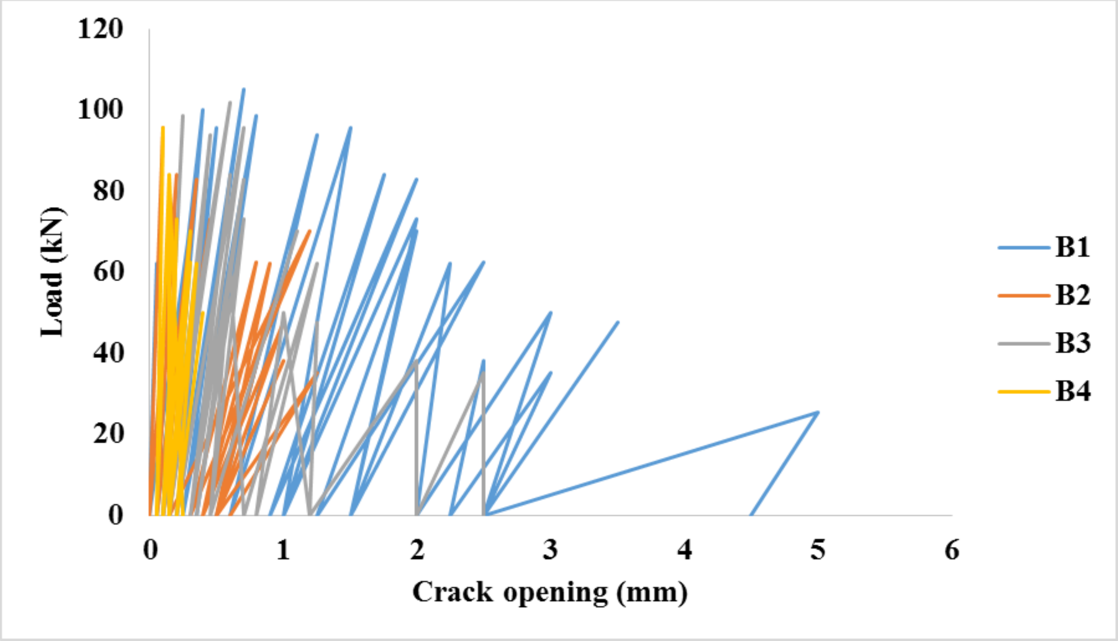

Figure 5.29: Cracks width at the front back of Joint region for BCJ-RC when push

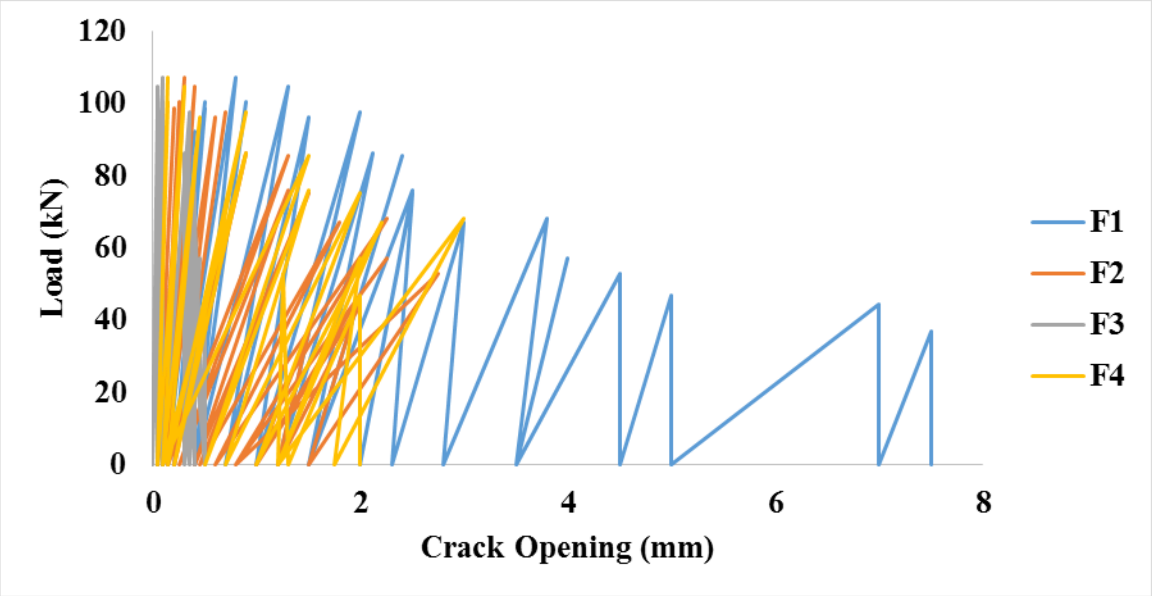

Figure 5.30: Cracks width at the front face of Joint region for BCJ-RC when pull

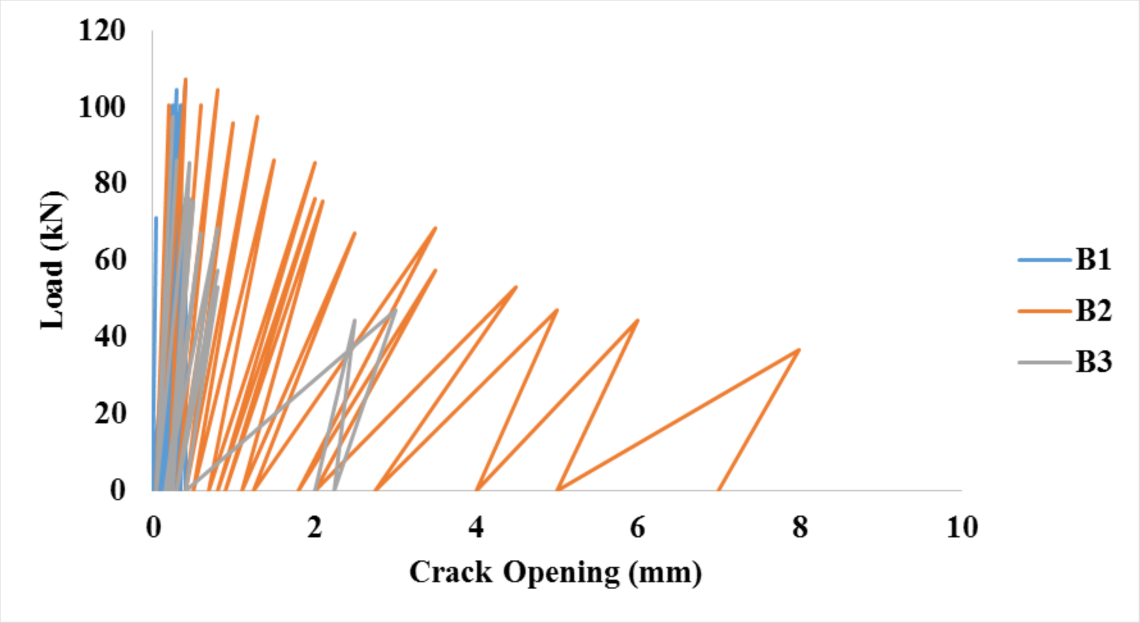

Figure 5.31: Cracks width at the front back of Joint region for BCJ-RC when pull

5.5 Testing Results of BCJ-CLIS

BCJ-CLIS was tested under cyclic loading. The ultimate load of 139.23 kN was achieved at the displacement of 24.88 mm. The load deflection response of BCJ-CLIS is shown

Figure 5.32. The initial cracks (3 cracks) were flexural and they were observed near the BCJ interface and different location of beam at load of 31 kN with a displacement of 2.2 mm. The first shear crack in the joint region (front face) was observed at a load of 53 kN when beam was pushed up to 4.4 mm. Similarly second and third shear cracks at the front face were observed at load of 117 kN at displacement of 15 mm, respectively. The first shear crack in the joint region (back face) was observed at a load of 78 kN when beam was pushed up to 7.5 mm. Similarly second and third shear cracks at the back face were observed at load of 96 kN, 117 kN at displacement of 10 mm and 15 mm, respectively. The specimen was failed completely in shear. Figure 5.33 shows the formation of cracks during different stages of testing of BCJ-CC. Figure 5.34 shows shear cracks formation on the front and back face of joint region during loading and unloading cycles and the width of these cracks were recorded. These widths were compared later on with BCJ-CL.

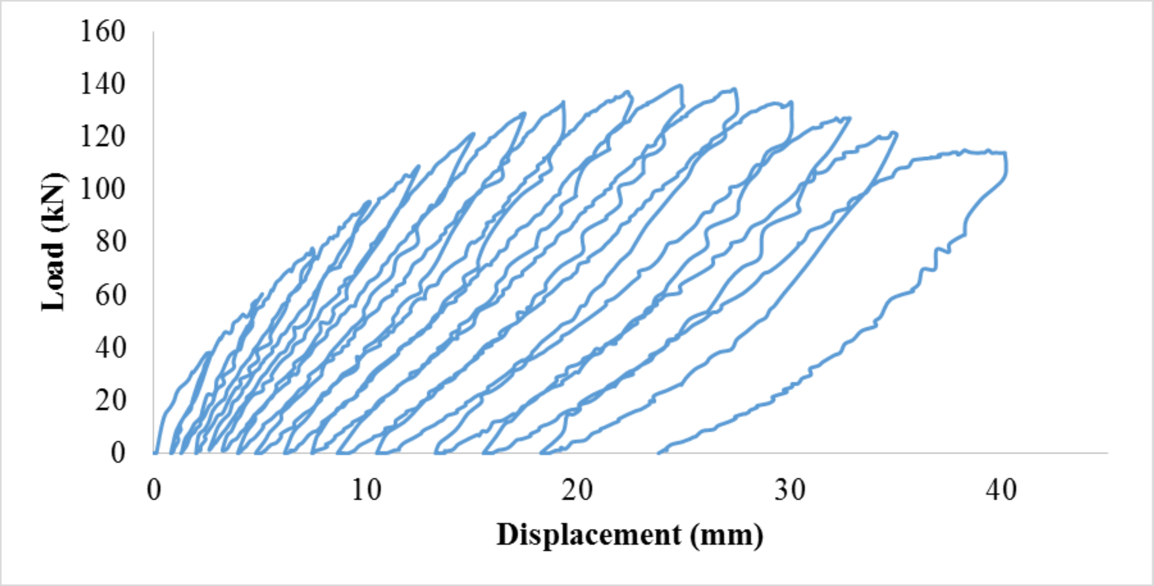

Figure 5.32: Load-Deflection curve for BCJ-CLIX

Figure 5.33: Formation of Cracks during test at different stages

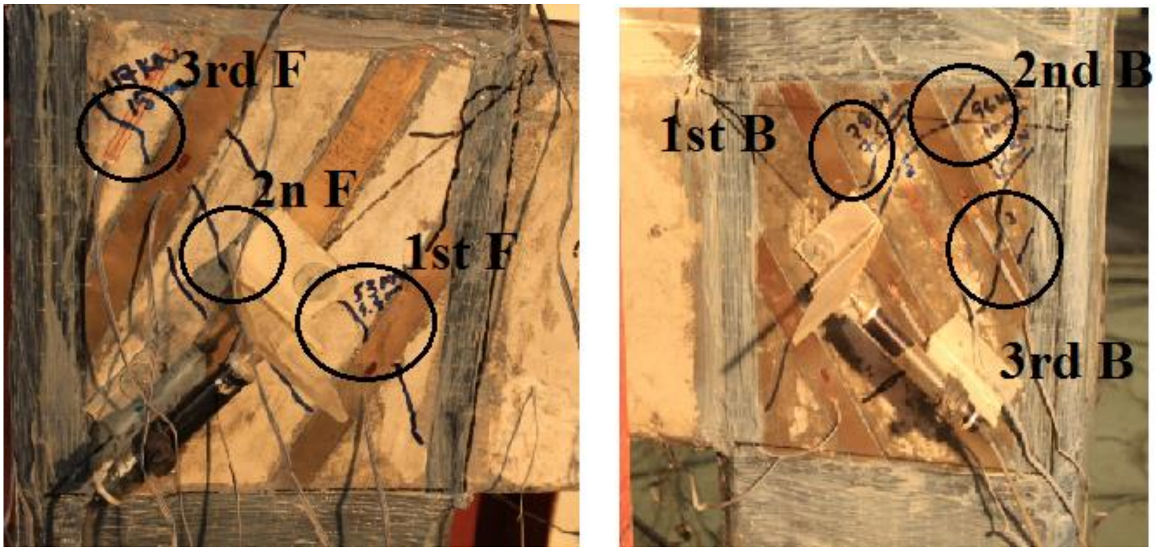

Figure 5.34: Shear crack at the front and back face of joint region of BCJ-CLIS

The test was stopped at the displacement of 40 mm, so that the results will be compared with control specimen. There was no spalling of concrete as it was observed in control BCJ-CL specimen. SMAs sheets increased the joint strength by 26% as well as give more residual strength as compared to the control specimen. The cracks width as compared to control specimen were also reduced in BCJ-CLIS. Figure 5.35 shows the cracks at the end of final cycle. LVDTs were used to measure the crack opening in the joint regions. Figure 5.36 shows the crack opening in the joint region during the test. Reinforcement strain gauges were also monitored to observed strains in rebars. Figure 5.37 shows the strains in beam reinforcements during cyclic loading.

Figure 5.35: Final cracks at the end of final cycle for BCJ-CLIS

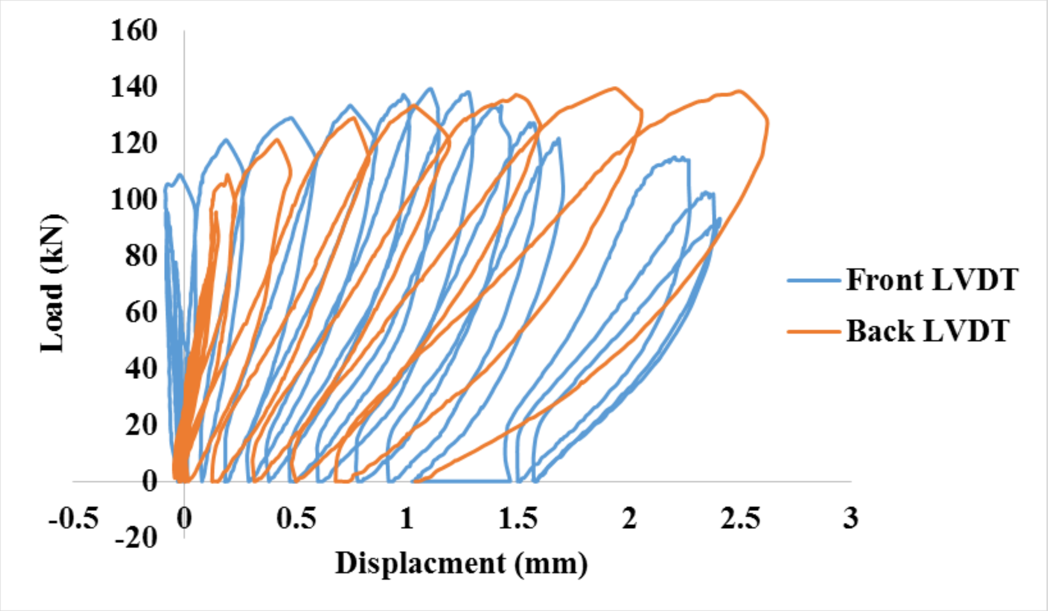

Figure 5.36: Crack opening at joint region

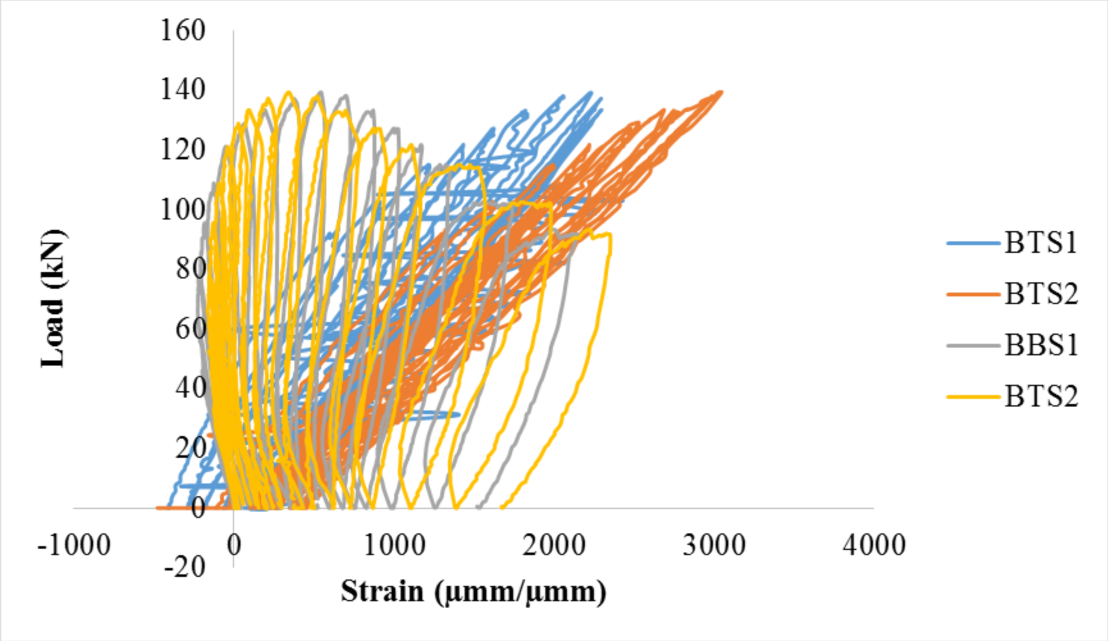

Figure 5.37: Reinforcement strain during cyclic loading

Strains in SMAs sheet were monitored using high strength strain gauges. Strain gauges were installed on all SMAs sheets. Also strain was measured using crack mouth opening device which was installed on SMAs sheet at a location of the major crack. Figure 5.38 and Figure 5.39 shows the SMAs sheet strains on front and back face of the joint.

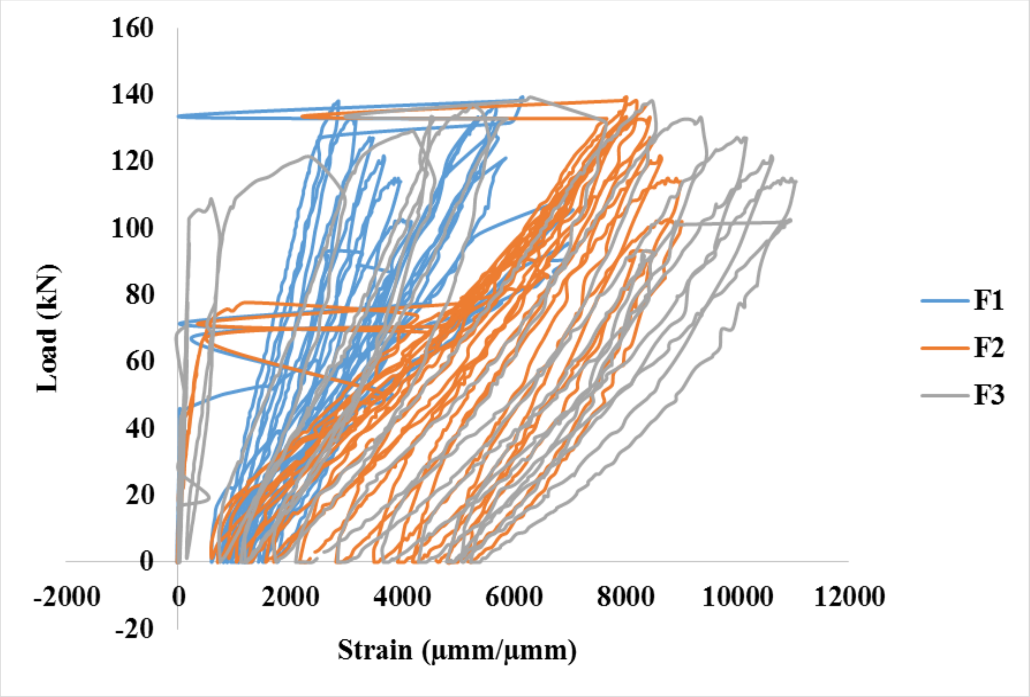

Figure 5.38: SMAs sheets strain attached to the front face of joint

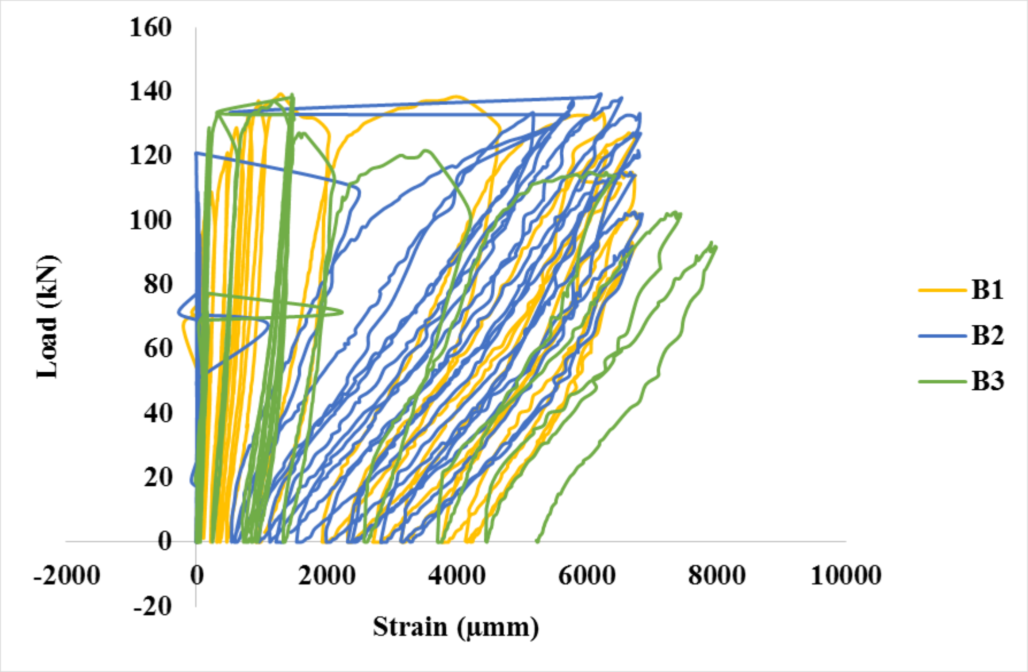

Figure 5.39: SMAs sheets strain attached to the back face of joint

Figure 5.40 shows the SMAs sheet strains obtained from CMOD at the location of crack. Figure 5.41 shows the strains in CFRP used to tie the ends of SMAs sheets and CFRP used at the back side of the column to protect 3d failure of column. The strain in CFRP were less than 1500 μmm which shows no contribution of CFRP in strengthening of joint and also confirmed by experimental test which will be shown section 5.9. Figure 5.42 show the cracks width at the front face of the joint BCJ-CL. Figure 5.43 show the cracks width at the back face of the joint BCJ-CL.

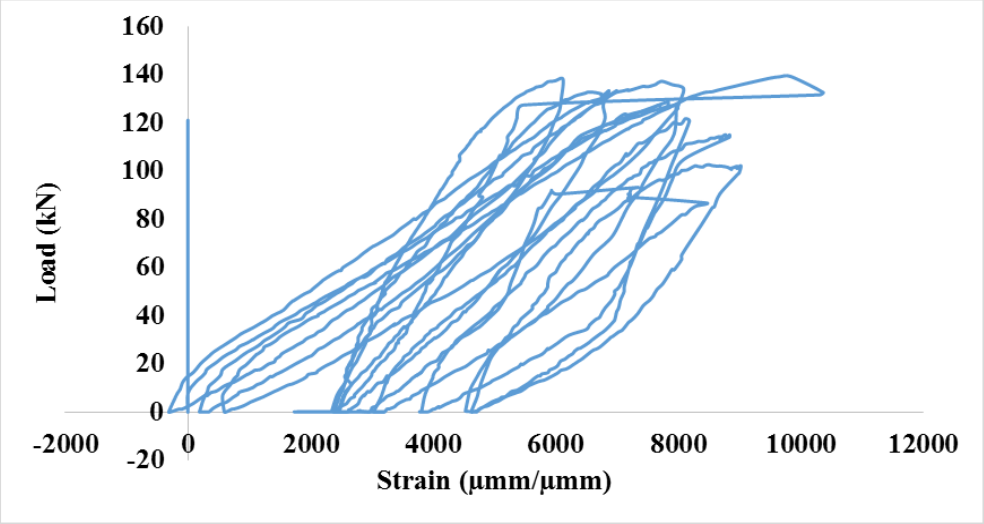

Figure 5.40: SMAs Sheet Strain at the location of crack obtained using CMOD

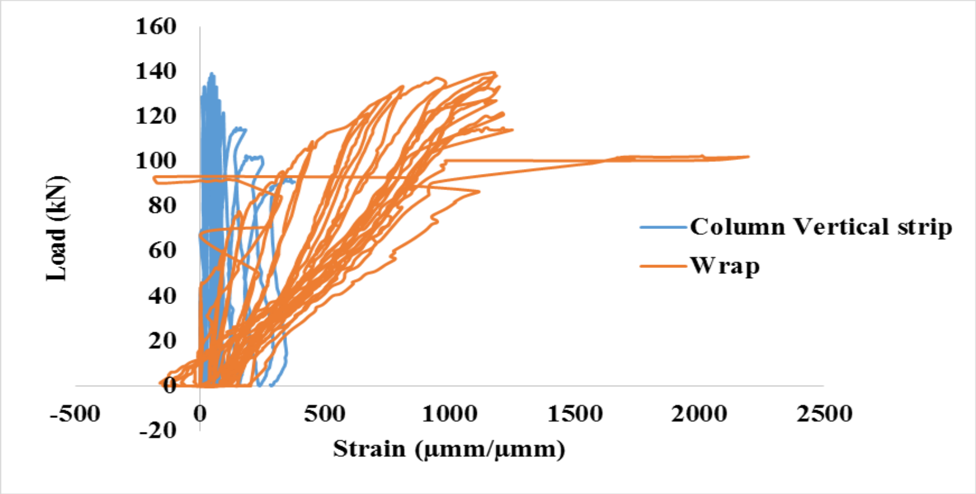

Figure 5.41: Load vs CFRP strains for BCJ-CLIS

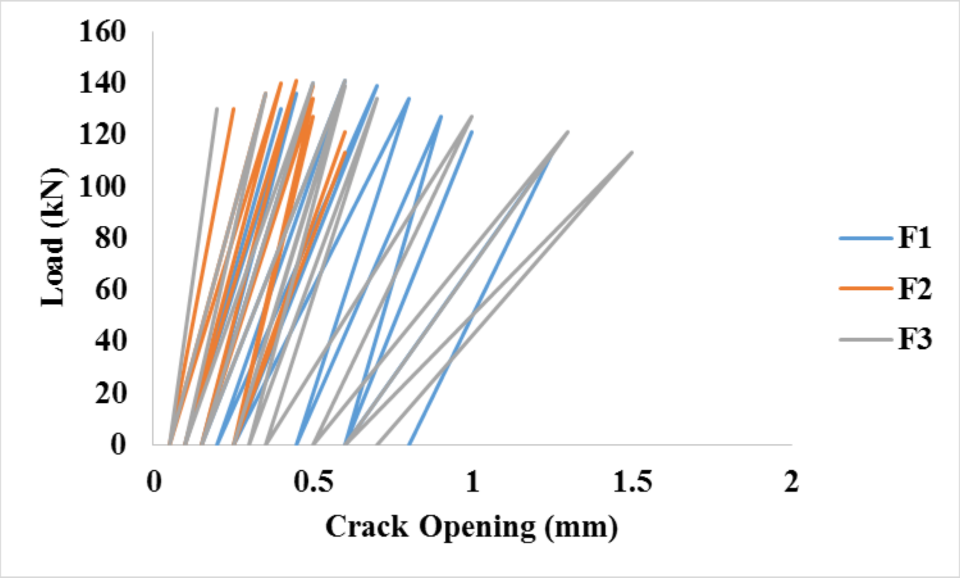

Figure 5.42: Cracks width at the front face of Joint region for BCJ-CLIS

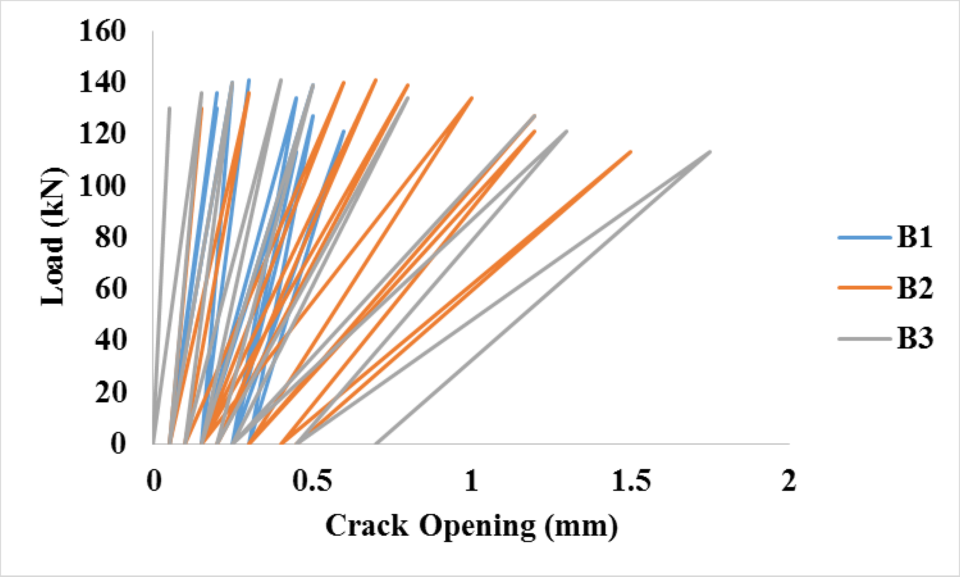

Figure 5.43: Cracks width at the back face of Joint region for BCJ-CLIS

5.6 Testing Results of BCJ-RC4S

BCJ-RC4S was tested under reverse cyclic loading. The ultimate load of 127.59 kN was achieved at the displacement of 19.86 mm in push direction and the ultimate load of 116.9 kN was achieved at the displacement of 18.54 mm in pull direction, respectively.

The load deflection response of BCJ-RC4S is shown Figure 5.44. The hysteresis shows pinching effect due to the steel which doesn't yield throughout the test. In the 1st cycle several flexural cracks were observed at the top surface of the beam in push direction at load of 36 kN with a displacement of 2.5 mm. Similarly few flexural cracks were observed in 1st cycle at the bottom face of beam in pull direction at a load of 29 kN with a displacement of 2.2 mm. The first shear crack in the front and back face of the joint region was observed at a load of 76 kN in 3rd push cycle with a displacement of 7.7 mm. The first shear crack in the front and back face of joint region was observed at a load of 64 kN and 74 kN in 3rd pull cycle with a displacement of 5.8 mm and 7.7 mm, respectively. Figure 5.45 shows the 1st flexural and shear cracks in push and pull cycles. The specimen was failed completely in shear. Figure 5.46 shows the formation of cracks during different cycles of BCJ-RC4S. Figure 5.47 and Figure 5.48 shows shear cracks formation on front and back face of joint region during push and pull cycle for which crack widths were measured during loading and unloading. These widths were compared with control specimens.

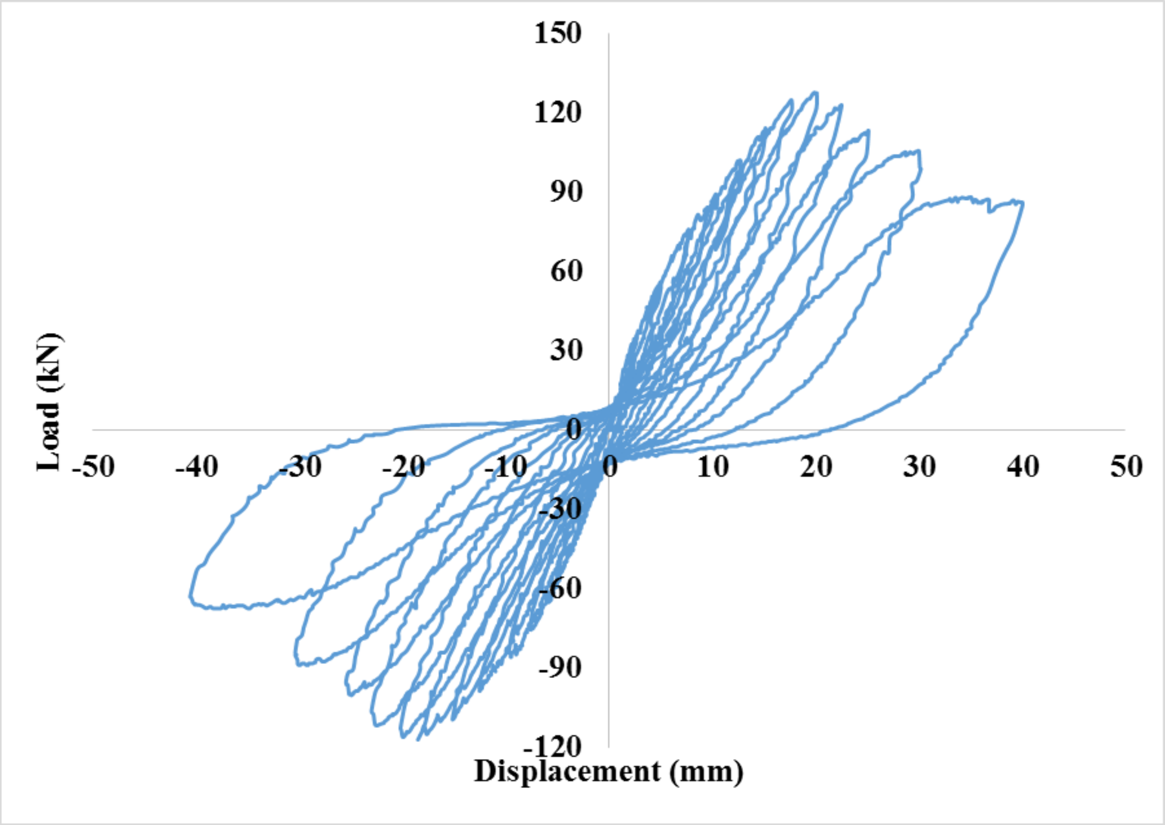

Figure 5.44: Load-deflection response of BCJ-RC4S under reverse cyclic load

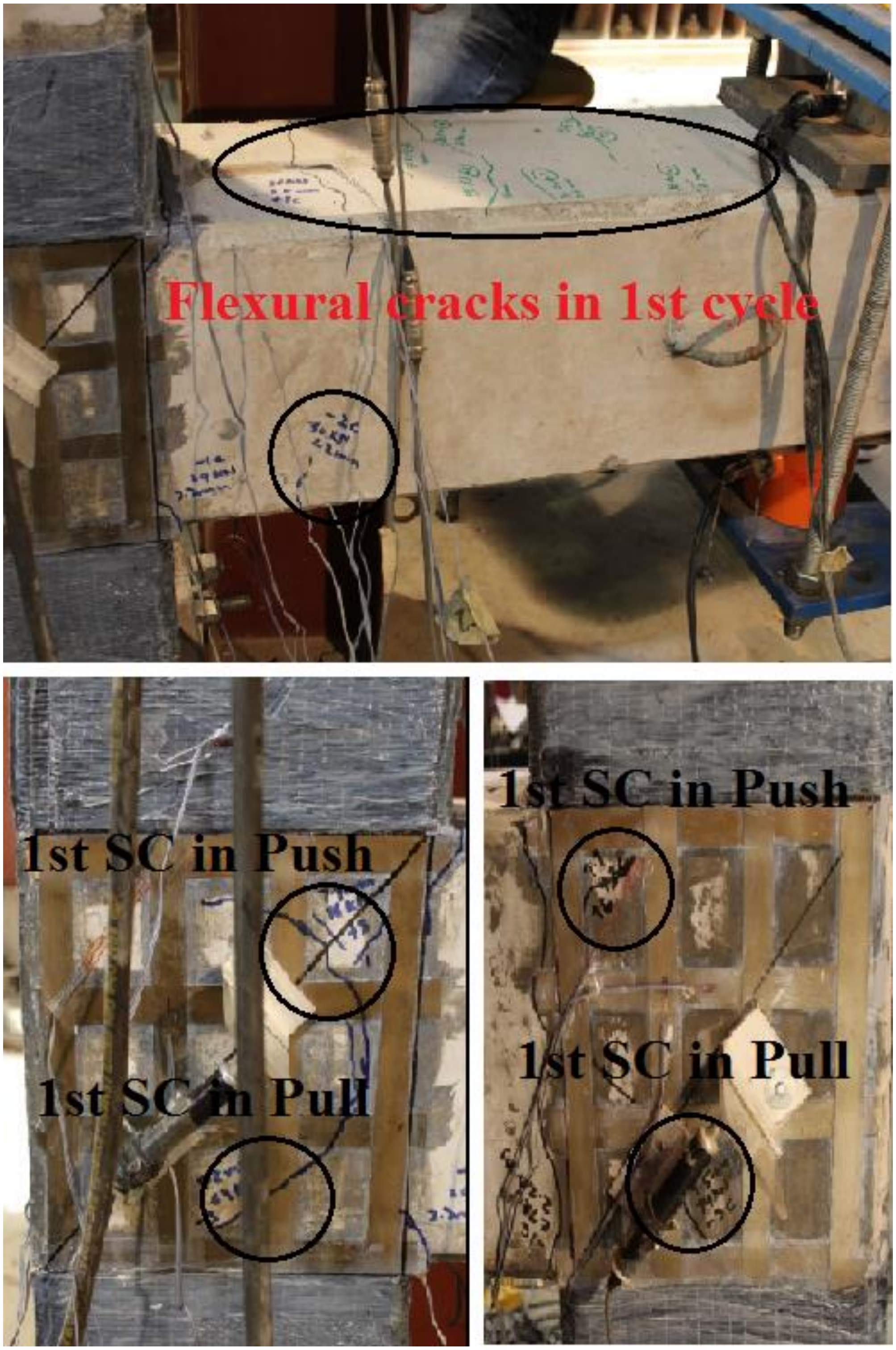

Figure 5.45: Formation of cracks in initial loading cycles

Figure 5.46: Formation of cracks on front (left) and back (right) faces of joint during different cycles

Figure 5.47: Shear cracks in push (left) and pull (right) cycles at the front face of joint region

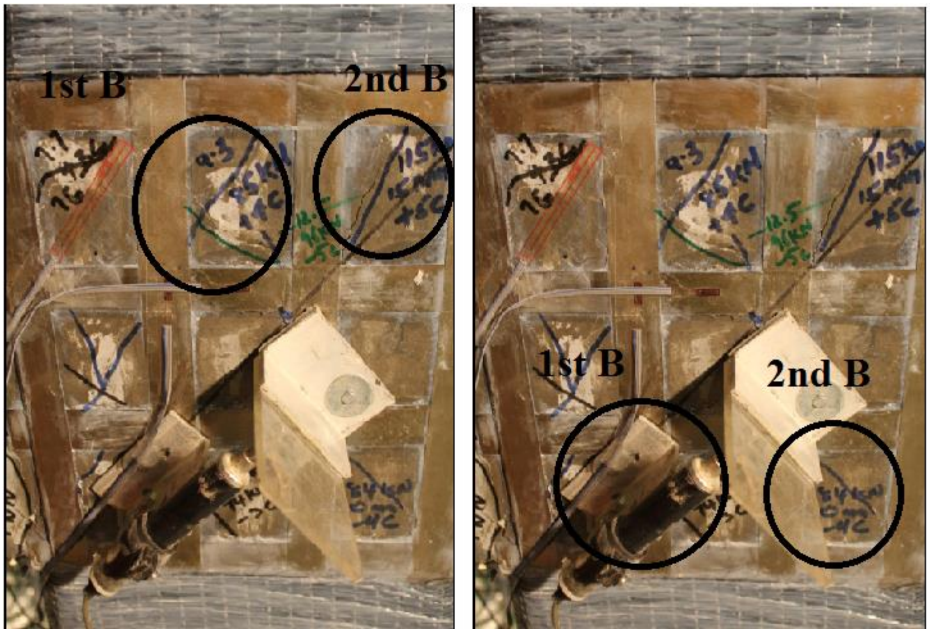

Figure 5.48: Shear cracks in push (left) and pull (right) cycles at the back face of joint region

The test was stopped at the displacement of 40 mm, so that the results will be compared with control specimen. There was no spalling of concrete as it was observed in control BCJ-RC specimen. SMAs sheets increased the joint strength by 20.58 % in push direction and 12.51 % in pull direction as well as give more residual strength as compared to the control specimen. The cracks width as compared to control specimen were also reduced in BCJ-RC4S. Figure 5.49 shows the cracks at the end of final cycle. LVDTs were used to measure the crack opening in the joint regions. Figure 5.50 shows the crack opening in the joint region. Reinforcement strain gauges were also monitored to observed strains in rebars. Figure 5.51 shows the strains in beam reinforcements during cyclic loading.

Figure 5.49: Final cracks at the end of final cycle for BCJ-RC4S

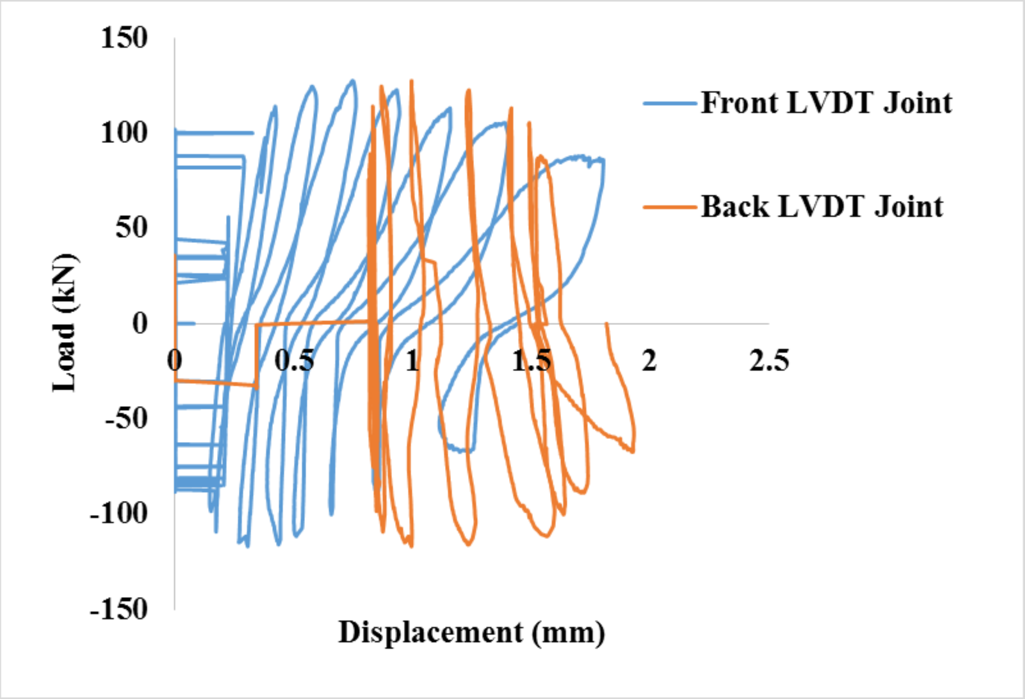

Figure 5.50: Crack opening the joint region for BCJ-RC4S

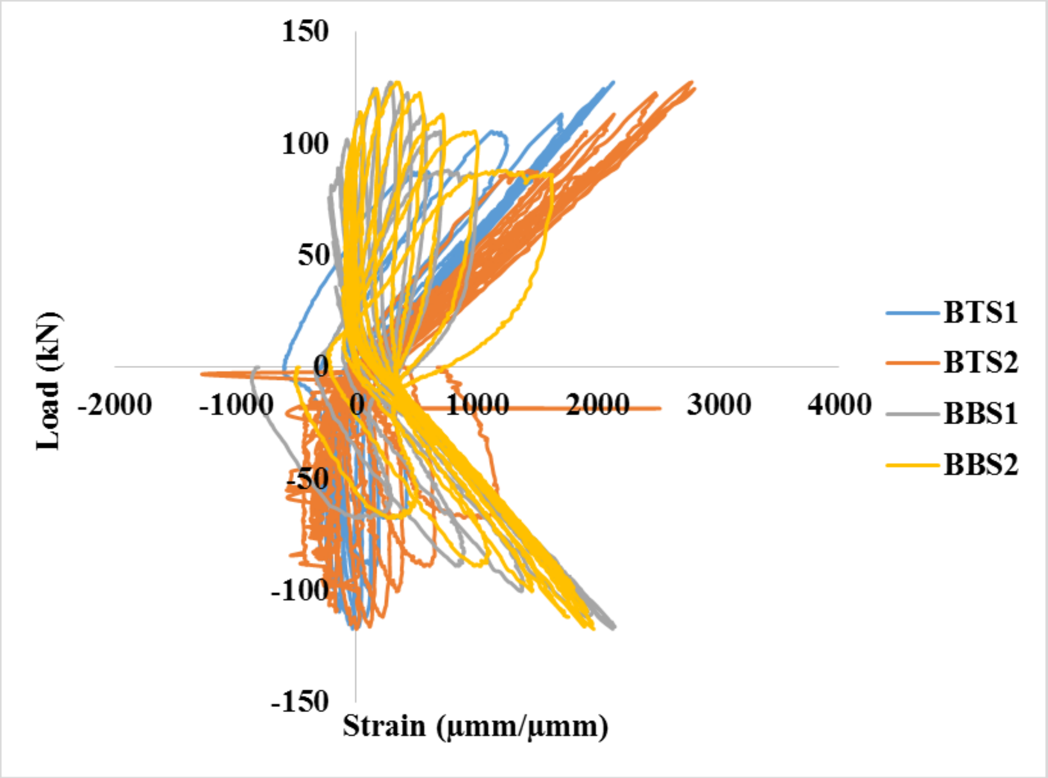

Figure 5.51: Reinforcement strain for BCJ-RC4S

Strains in SMAs sheet were monitored using high strength strain gauges. Strain gauges were installed on selective vertical and horizontal SMAs sheets. Figure 5.52 and Figure 5.53 shows the SMAs sheets strains on front and back face of the joint.

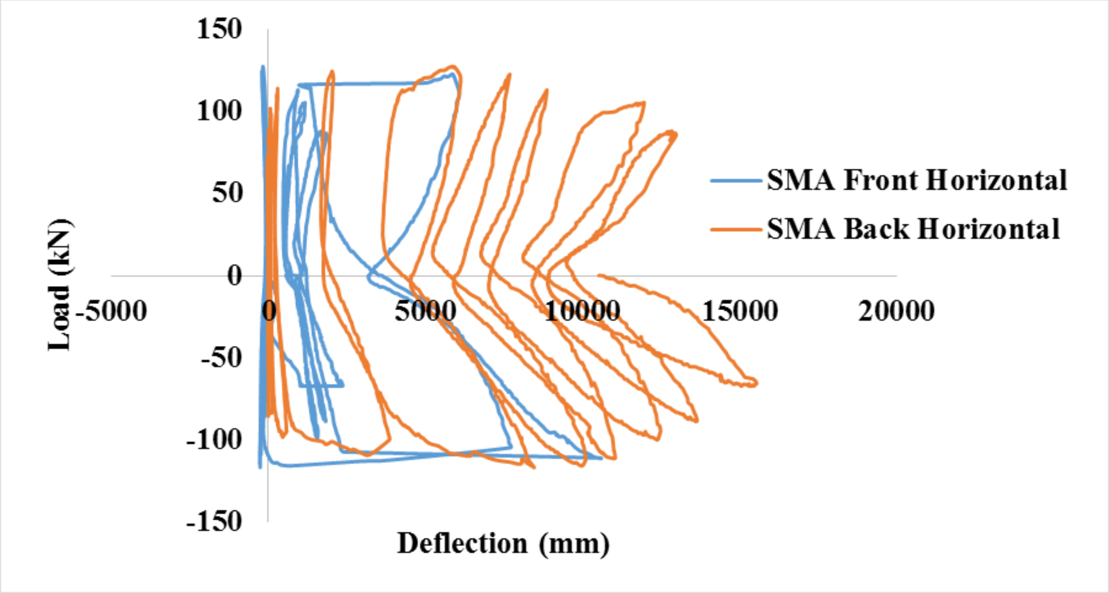

Figure 5.52: Strain in horizontal SMAs sheets for BCJ-RC4S

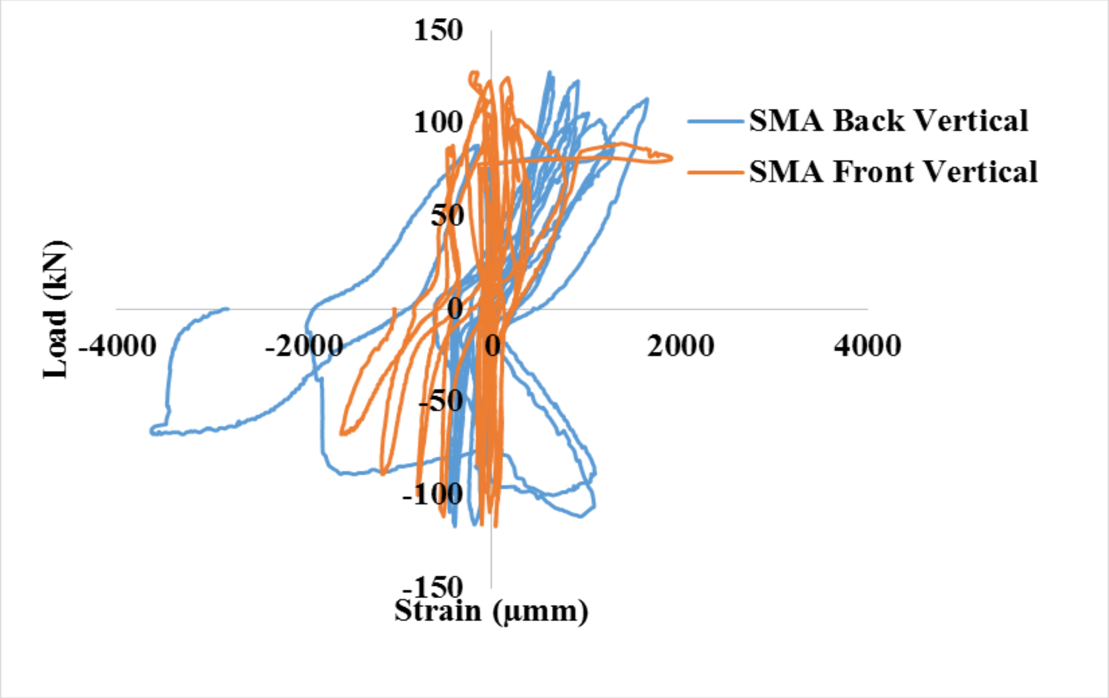

Figure 5.53: Strain in vertical SMAs sheets for BCJ-RC4S

Figure 5.54 shows the strains in CFRP used to tie the ends of SMAs sheets and CFRP used at the back side of the column to protect 3d failure of column. The strain in CFRP were less than 2000 µmm which shows no contribution of CFRP in strengthening of joint. Figure 5.55 show the cracks width at the front face of the joint BCJ-RC4S when push and unload to zero. Figure 5.56 show the cracks width at the back face of the joint BCJ-RC4S when push and unload to zero. Figure 5.57 show the cracks width at the front face of the joint BCJ-RC4S when pull and unload to zero. Figure 5.58 show the cracks width at the back face of the joint BCJ-RC4S when pull and unload to zero.

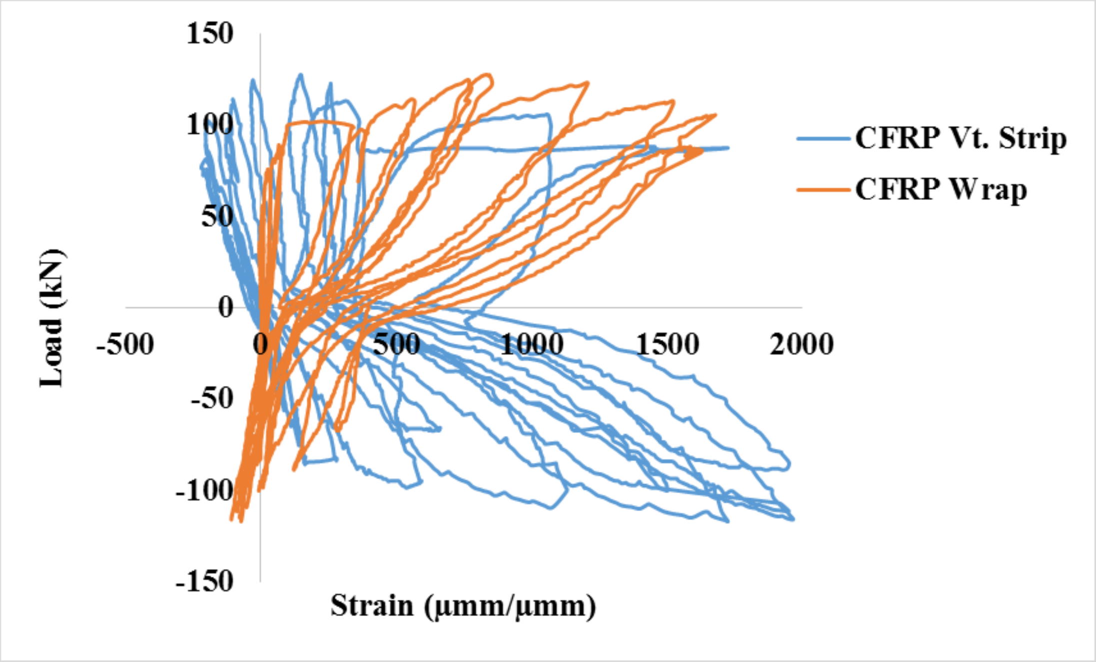

Figure 5.54: Load vs CFRP strains for BCJ-RC4S

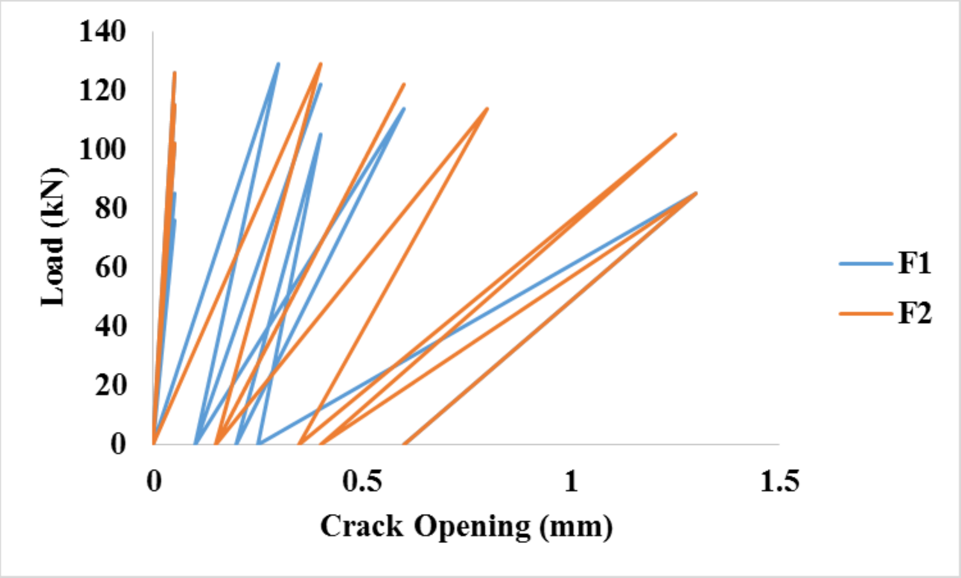

Figure 5.55: Cracks width at the front face of Joint region for BCJ-RC4S when push

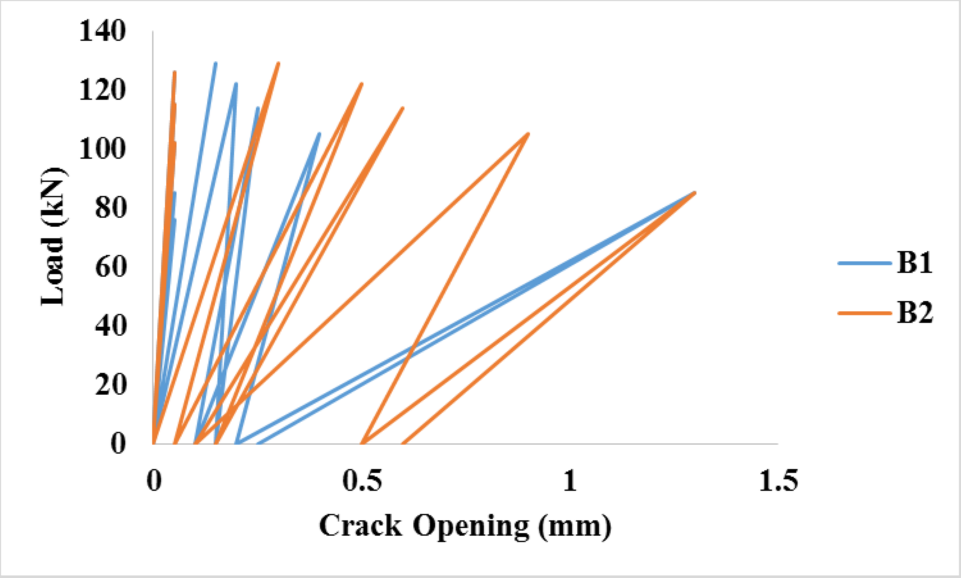

Figure 5.56: Cracks width at the back face of Joint region for BCJ-RC4S when push

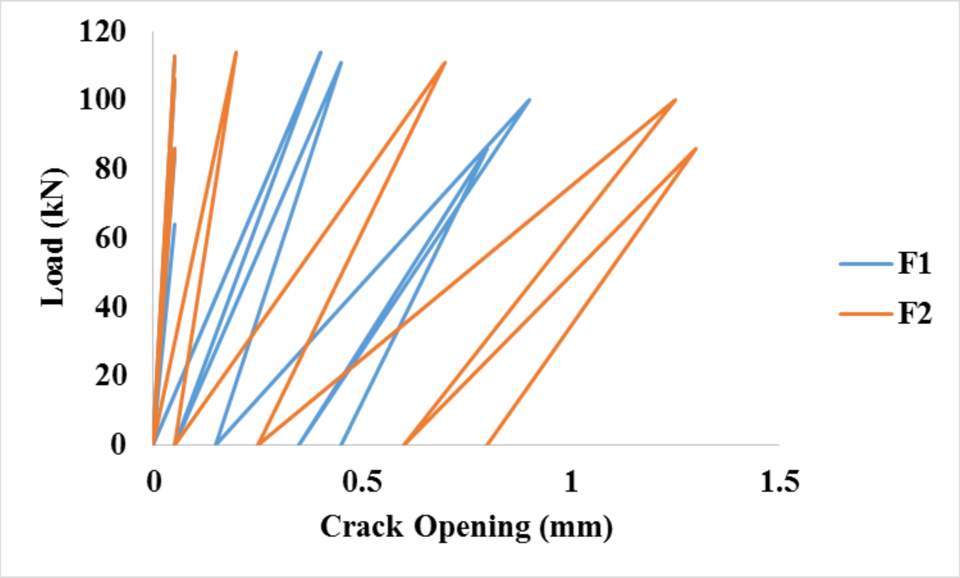

Figure 5.57: Cracks width at the front face of Joint region for BCJ-RC4S when pull

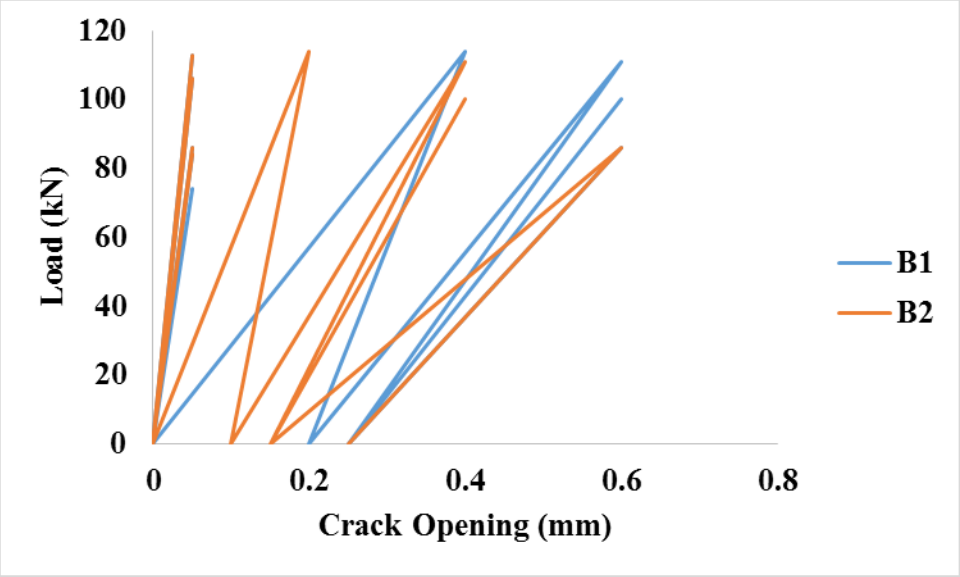

Figure 5.58: Cracks width at the back face of Joint region for BCJ-RC4S when pull

5.7 Testing Results of BCJ-RC2S

BCJ-RC2S was tested under reverse cyclic loading. The ultimate load of 120.76 kN was achieved at the displacement of 22.75 mm in push direction and the ultimate load of 125 kN was achieved at the displacement of 20.06 mm in pull direction, respectively. The load deflection response of BCJ-RC2S is shown Figure 5.59. The hysteresis shows pinching effect due to the steel which doesn't yield throughout the test. In the 1st cycle 1st flexural crack was observed at the top surface of the beam in push direction at load of 31 kN with a displacement of 1.8 mm. Similarly 1st flexural crack was observed in 1st pull cycle at the bottom face of beam at a load of 38 kN with a displacement of 2.2 mm. The first shear crack at the front and back face of the joint region was observed at a load of 70 kN in 3rd push cycle with a displacement of 7.5 mm. The first shear crack at the front and back face of the joint region was observed at a load of 69 kN in 3rd pull cycle with a displacement of 5.1 mm. Figure 5.60 shows the 1st flexural and shear cracks in push and pull cycles. The specimen was failed completely in shear. Figure 5.61 shows the formation of cracks during different cycles of BCJ-RC2S. Figure 5.62 and Figure 5.63 shows shear cracks formation on front and back face of joint region during push and pull cycle for which crack widths were measured during loading and unloading. These widths were compared with control specimens.

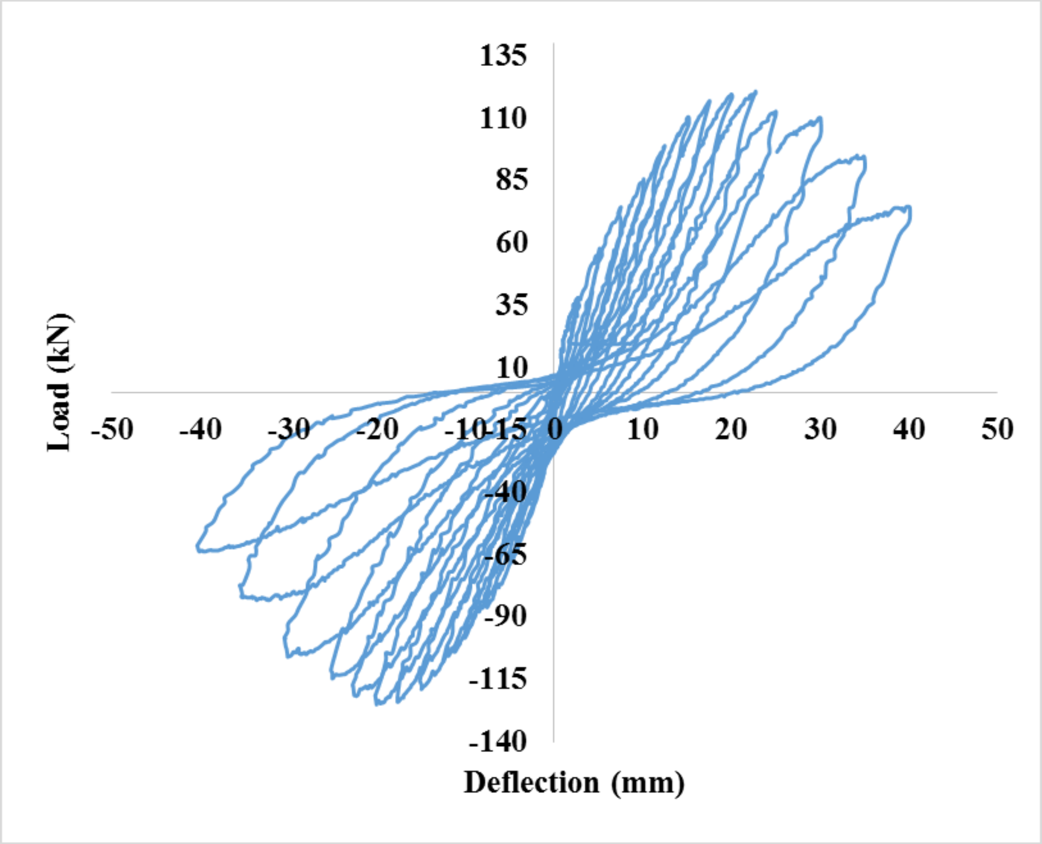

Figure 5.59: Load-deflection response of BCJ-RC2S under reverse cyclic load

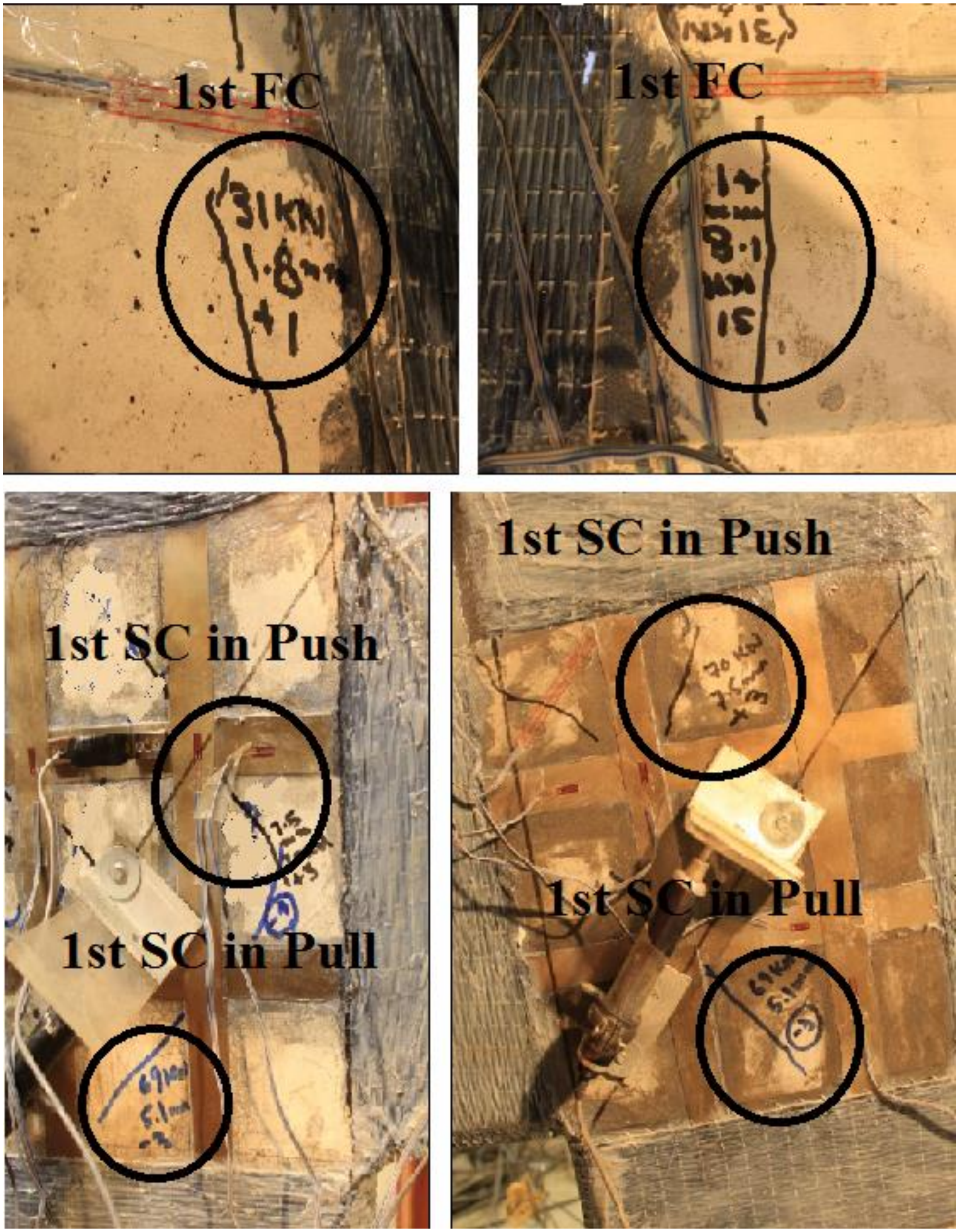

Figure 5.60: Formation of cracks in initial loading cycles

Figure 5.61: Formation of cracks on front (left) and back (right) faces of joint during different cycles

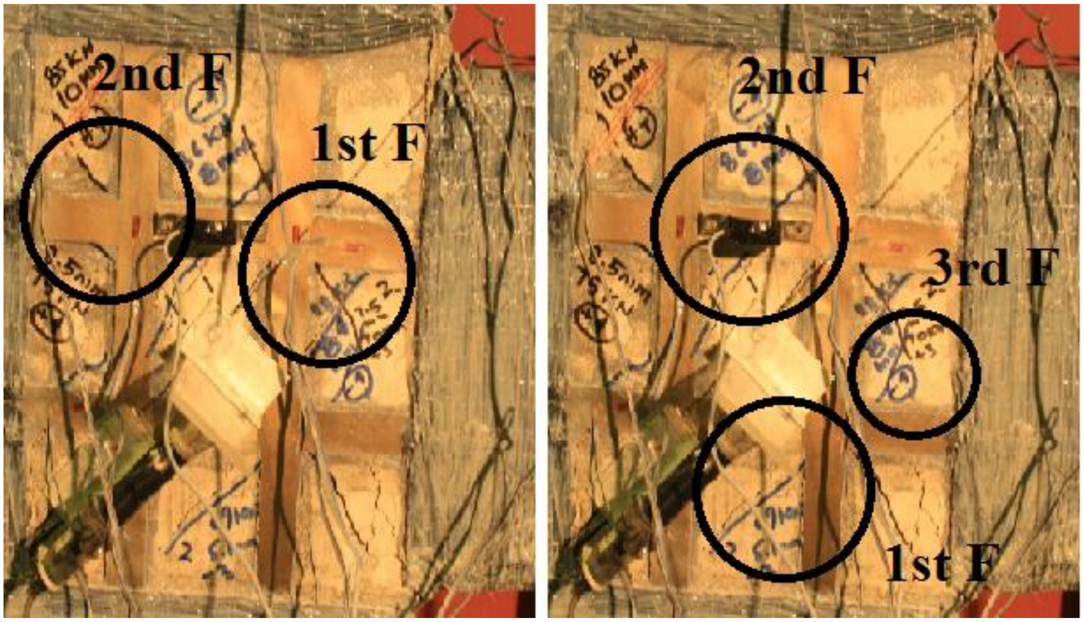

Figure 5.62: Shear cracks in push (left) and pull (right) cycles at the front face of joint region

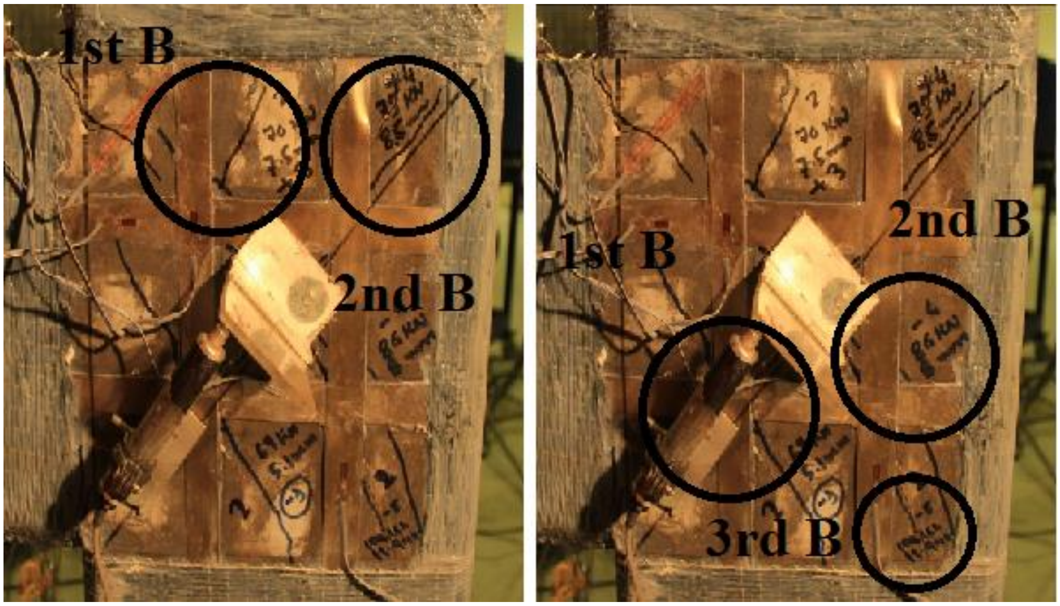

Figure 5.63: Shear cracks in push (left) and pull (right) cycles at the back face of joint region

The test was stopped at the displacement of 40 mm, so that the results will be compared with control specimen. There was no spalling of concrete as it was observed in control BCJ-RC specimen. SMAs sheets increased the joint strength by 14.12 % in push direction and 20.31 % in pull direction as well as give more residual strength as compared to the control specimen. The showed control cracking and the cracks width as compared to control specimen were also reduced in BCJ-RC2S. Figure 5.64 shows the cracks at the end of final cycle. LVDTs were used to measure the crack opening in the joint regions. Figure 5.65 shows the crack opening in the joint region. Reinforcement strain gauges were also monitored to observed strains in rebars. Figure 5.66 shows the strains in beam reinforcements during cyclic loading.

Figure 5.64: Final cracks at the end of final cycle for BCJ-RC2S

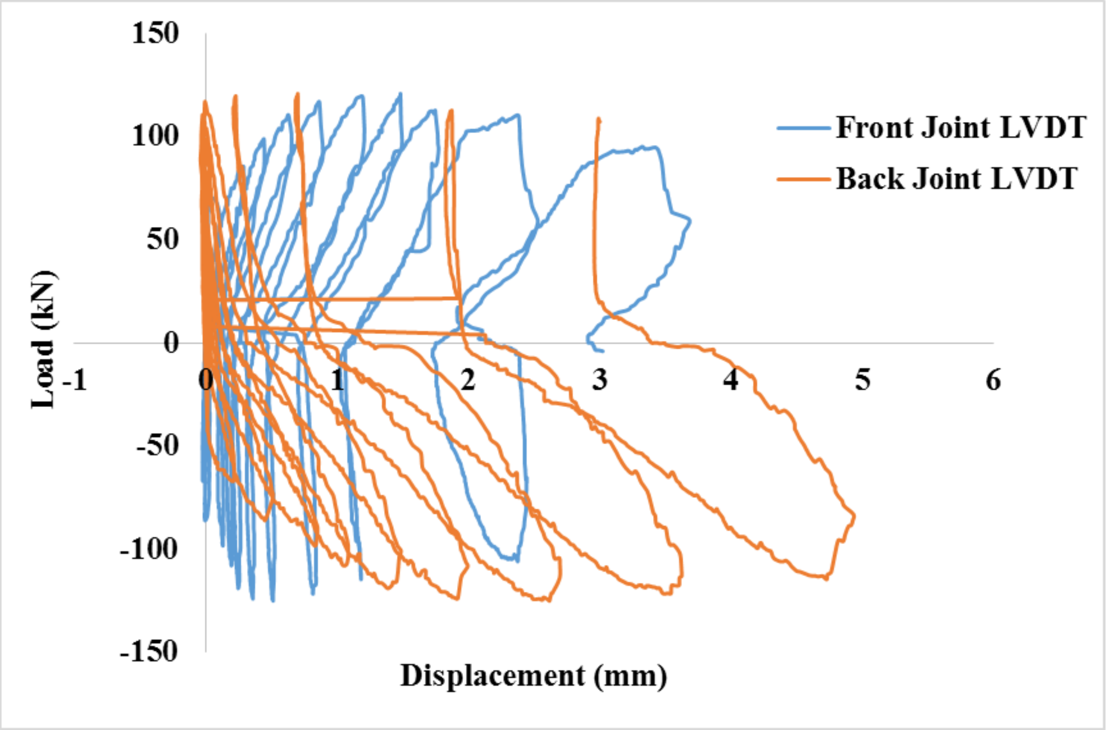

Figure 5.65: Crack opening the joint region for BCJ-RC2S

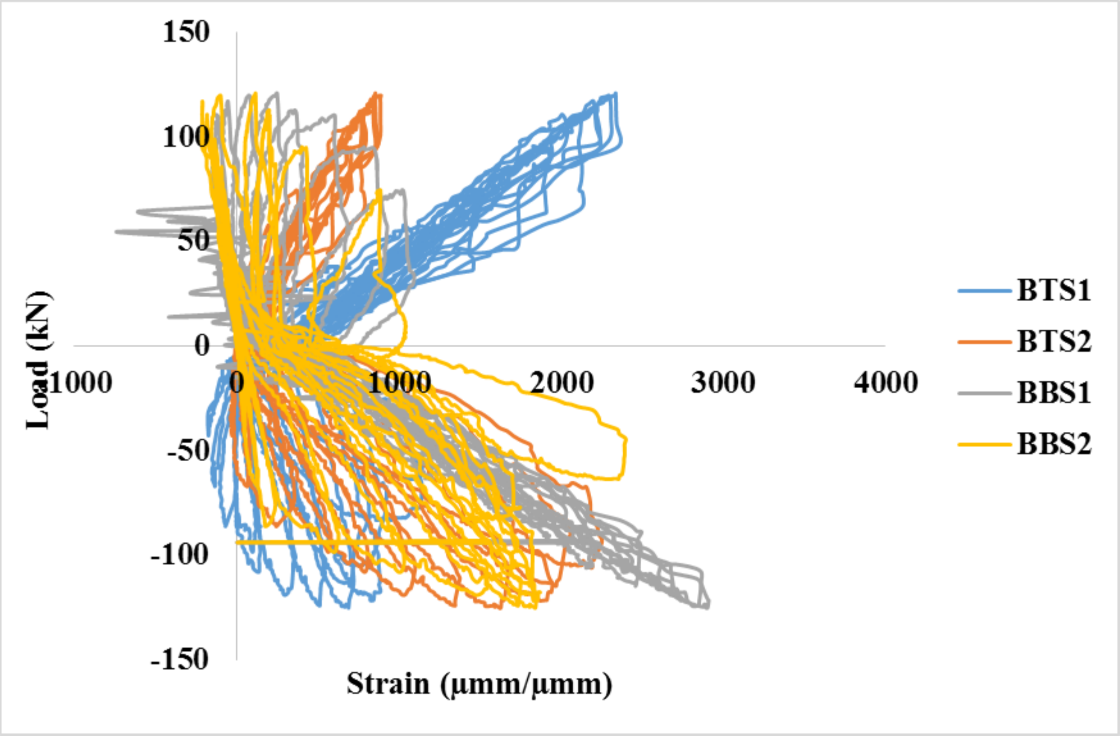

Figure 5.66: Reinforcement strain for BCJ-RC2S

Strains in SMAs sheet were monitored using high strength strain gauges. Strain gauges were installed on all vertical and horizontal SMAs sheets. Figure 5.67 and Figure 5.68 shows the SMAs sheets strains on the front and back face of the joint.

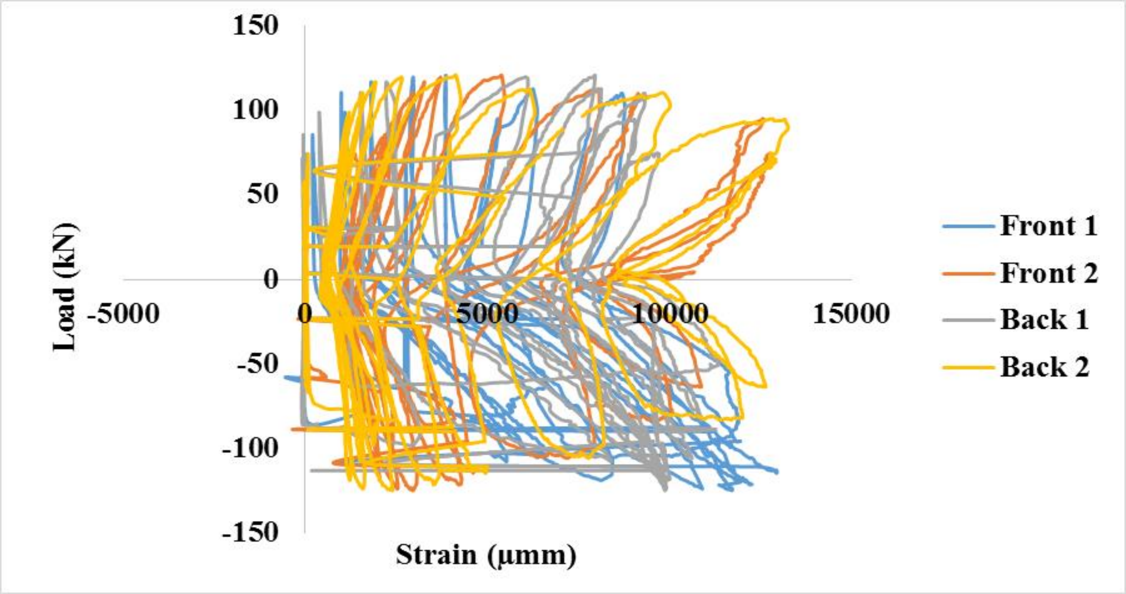

Figure 5.67: Strain in horizontal SMAs sheets for BCJ-RC2S

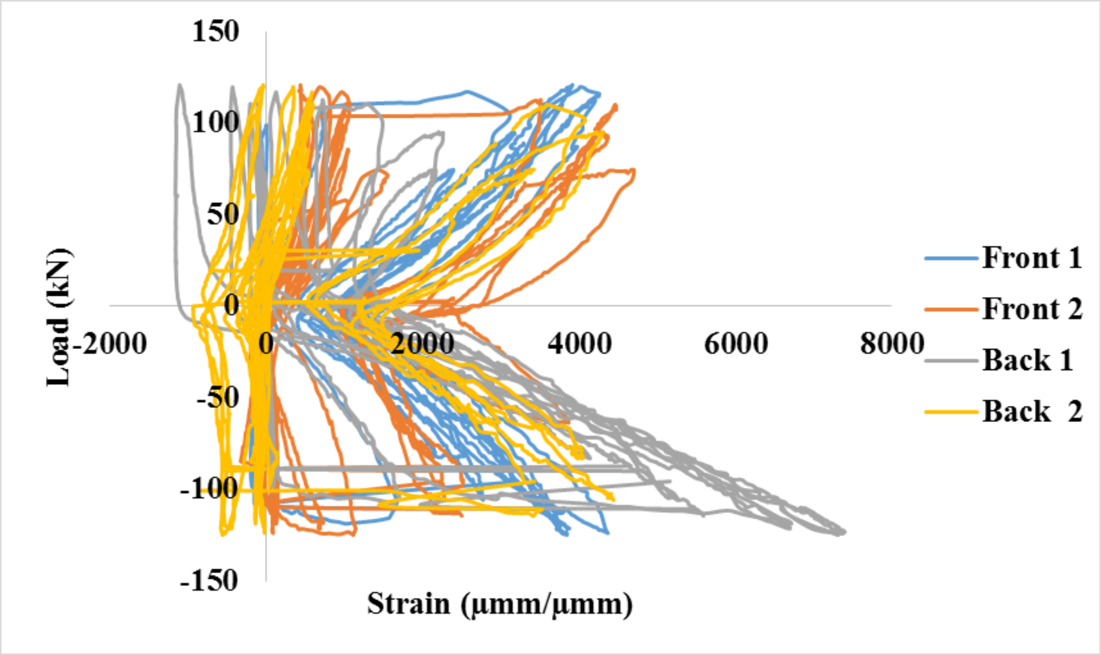

Figure 5.68: Strain in vertical SMAs sheets for BCJ-RC2S

Also strain was measured using crack mouth opening device which was installed on SMAs sheet. Figure 5.69 shows the strain measured using CMOD in horizontal SMAs sheet at location of crack. Strain obtained using CMOD shows the entrance of SMAs in transformation phase during the last cycle of loading and upon unloading maximum recovery of strain was observed. Figure 5.70 shows the strains in CFRP used to tie the ends of SMAs sheets and CFRP used at the back side of the column to protect 3d failure of column. The strain in CFRP were less than 2000 μmm which shows no contribution of CFRP in strengthening of joint. Figure 5.71 show the cracks width at the front face of the joint BCJ-RC2S when push and unload to zero. Figure 5.72 show the cracks width at the back face of the joint BCJ-RC2S when push and unload to zero. Figure 5.73 show the cracks width at the front face of the joint BCJ-RC2S when pull and unload to zero. Figure 5.74 show the cracks width at the back face of the joint BCJ-RC2S when pull and unload to zero.

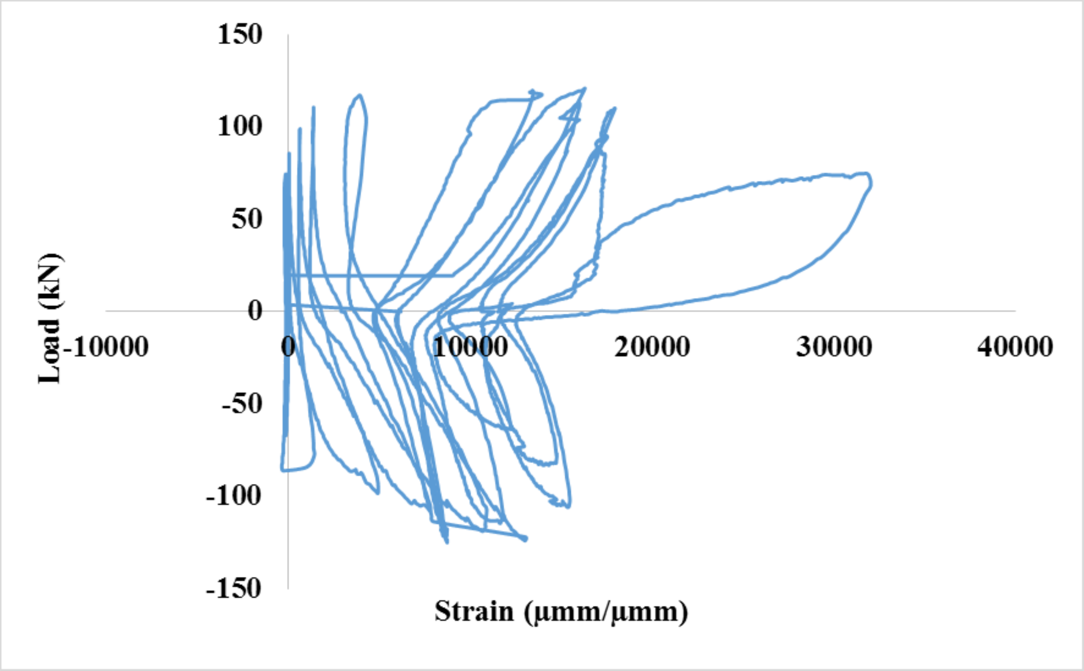

Figure 5.69: Strain measured on SMAs Sheet at location of crack using CMOD

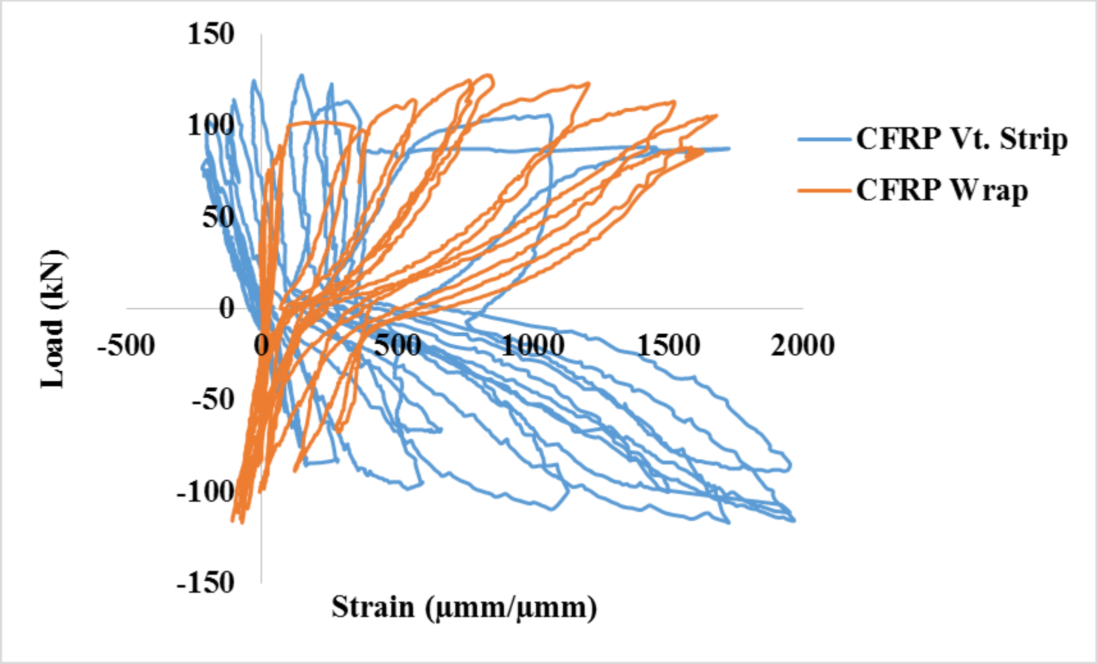

Figure 5.70: Load vs CFRP strains for BCJ-RC2S

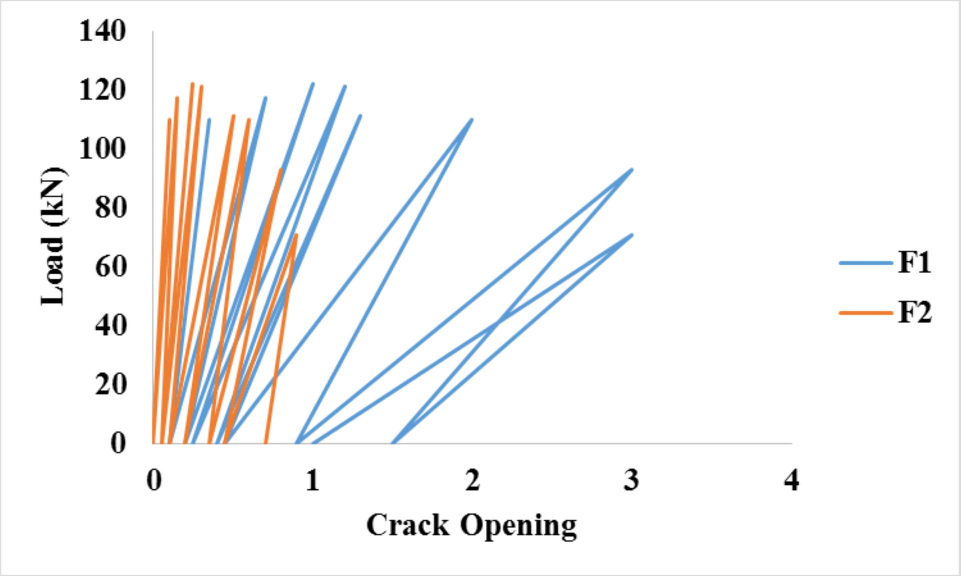

Figure 5.71: Cracks width at the front face of Joint region for BCJ-RC2S when push

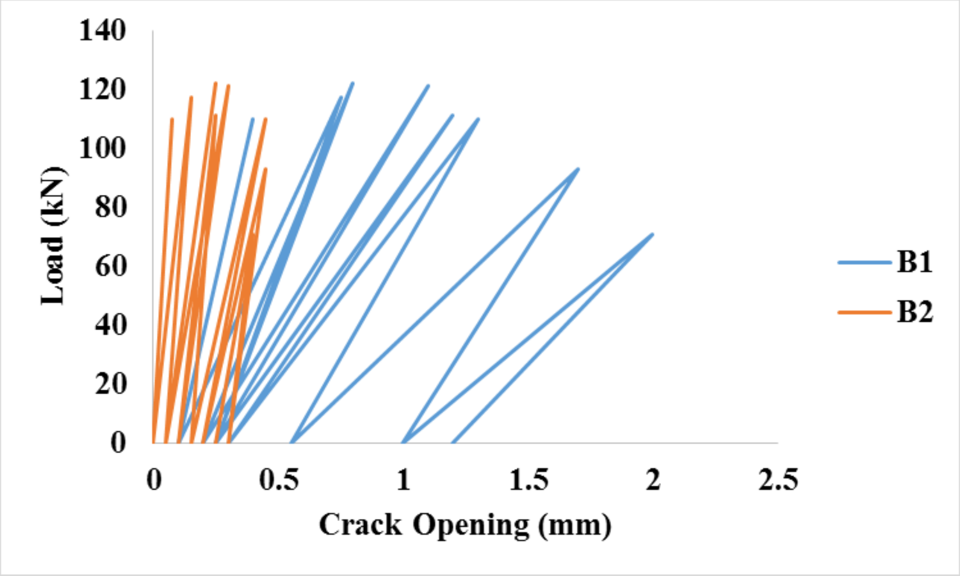

Figure 5.72: Cracks width at the back face of Joint region for BCJ-RC2S when push

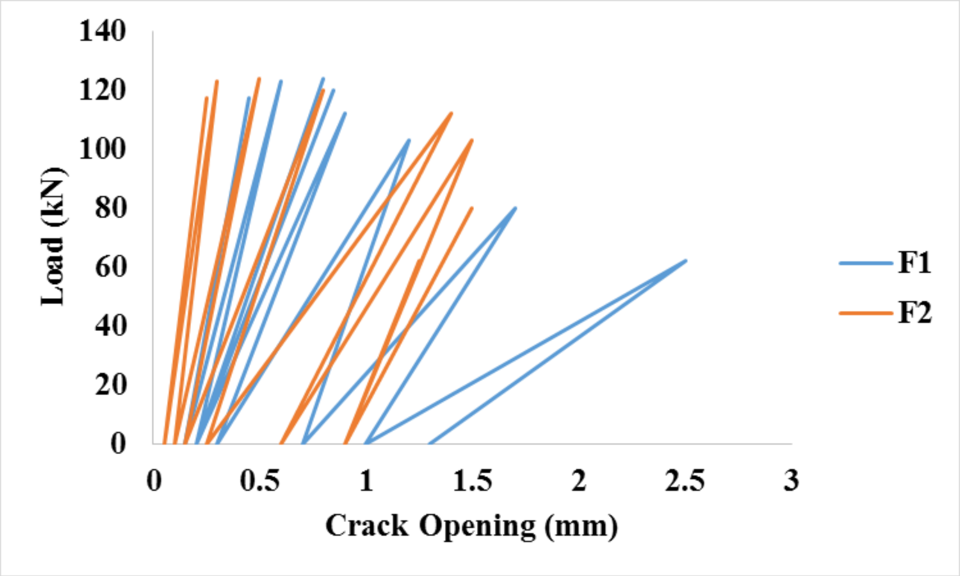

Figure 5.73: Cracks width at the front face of Joint region for BCJ-RC2S when pull

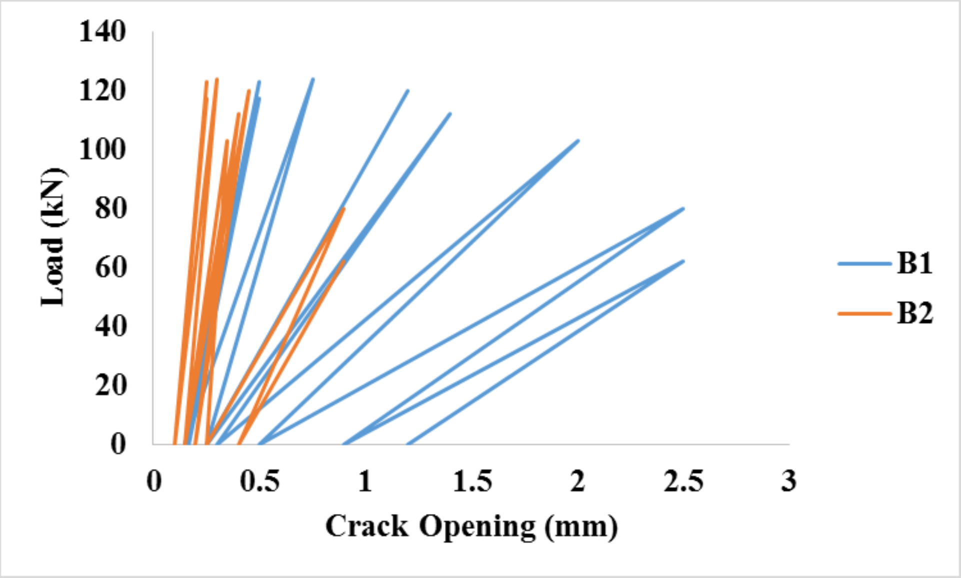

Figure 5.74: Cracks width at the back face of Joint region for BCJ-RC2S when pull

5.8 Testing Results of BCJ-RCXS

BCJ-RCXS was tested under reverse cyclic loading. The ultimate load of 114.32 kN was achieved at the displacement of 18.02 mm in push direction and the ultimate load of 111.6 kN was achieved at the displacement of 15.32 mm in pull direction, respectively. The load deflection response of BCJ-RCXS is shown Figure 5.75. The hysteresis shows pinching effect due to the steel which doesn't yield throughout the test. In the 2nd cycle several flexural cracks were observed at the top surface of the beam in push direction at load of 48 kN with a displacement of 4 mm. Likewise, few flexural cracks were observed in 1st cycle at the bottom face of beam in pull direction at a load of 38 kN with a displacement of 2.3 mm. The first shear crack at the front face of the joint region was observed at a load of 64 kN in 2nd pull cycle with a displacement of 5 mm whereas two shear cracks were observed at the back face of the joint region at a load of 69 kN in 3rd push cycle with a displacement of 7 mm. Figure 5.76 shows the 1st flexural and shear cracks in push and pull cycles. The specimen was failed completely in shear. Figure 5.77 shows the formation of cracks during different cycles of BCJ-RCXS. Figure 5.78 and Figure 5.79 shows shear cracks formation on front and back face of joint region during push and pull cycle for which crack widths were measured during loading and unloading. These widths were compared with control specimens.

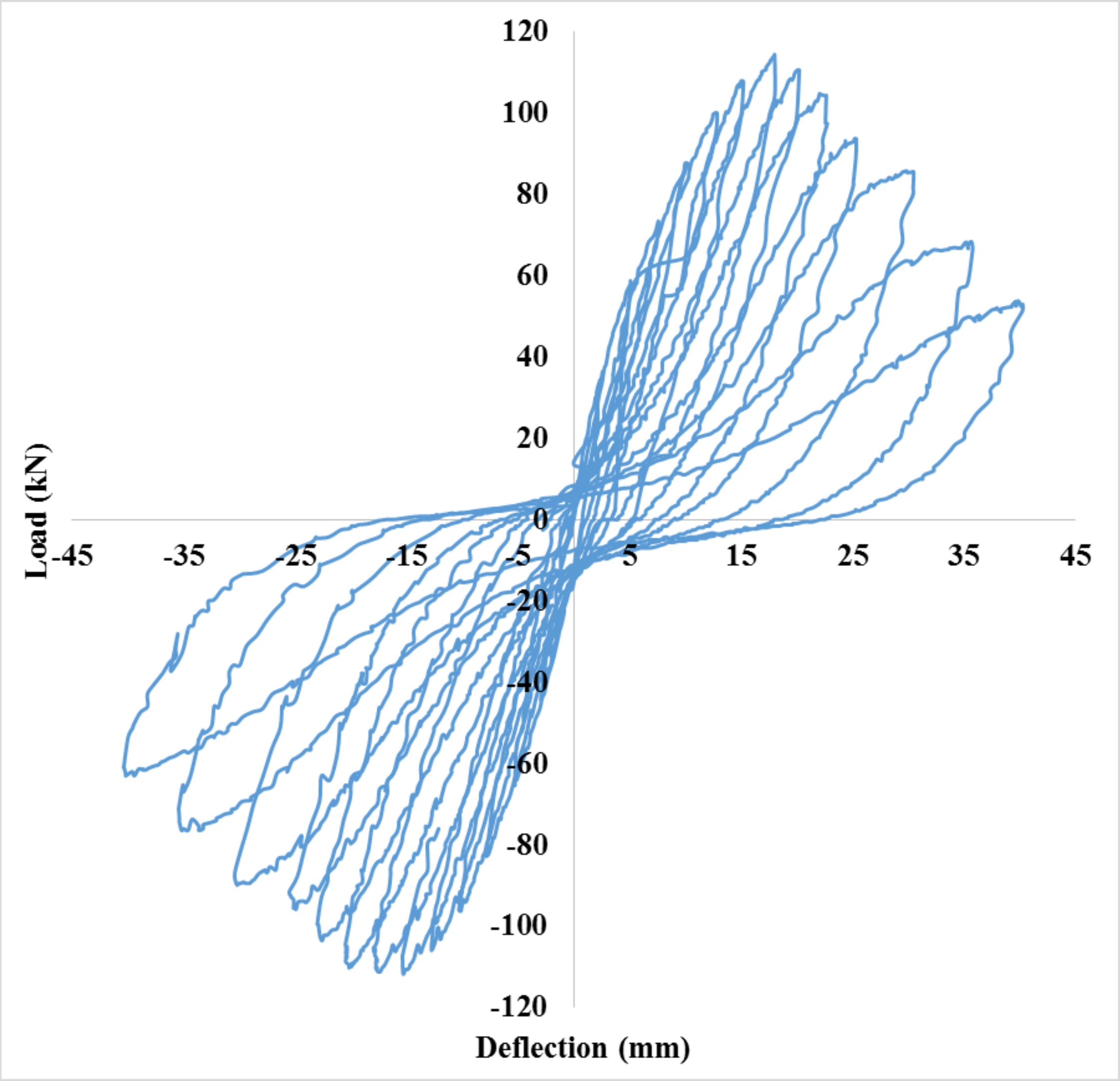

Figure 5.75: Load-deflection response of BCJ-RCXS under reverse cyclic load

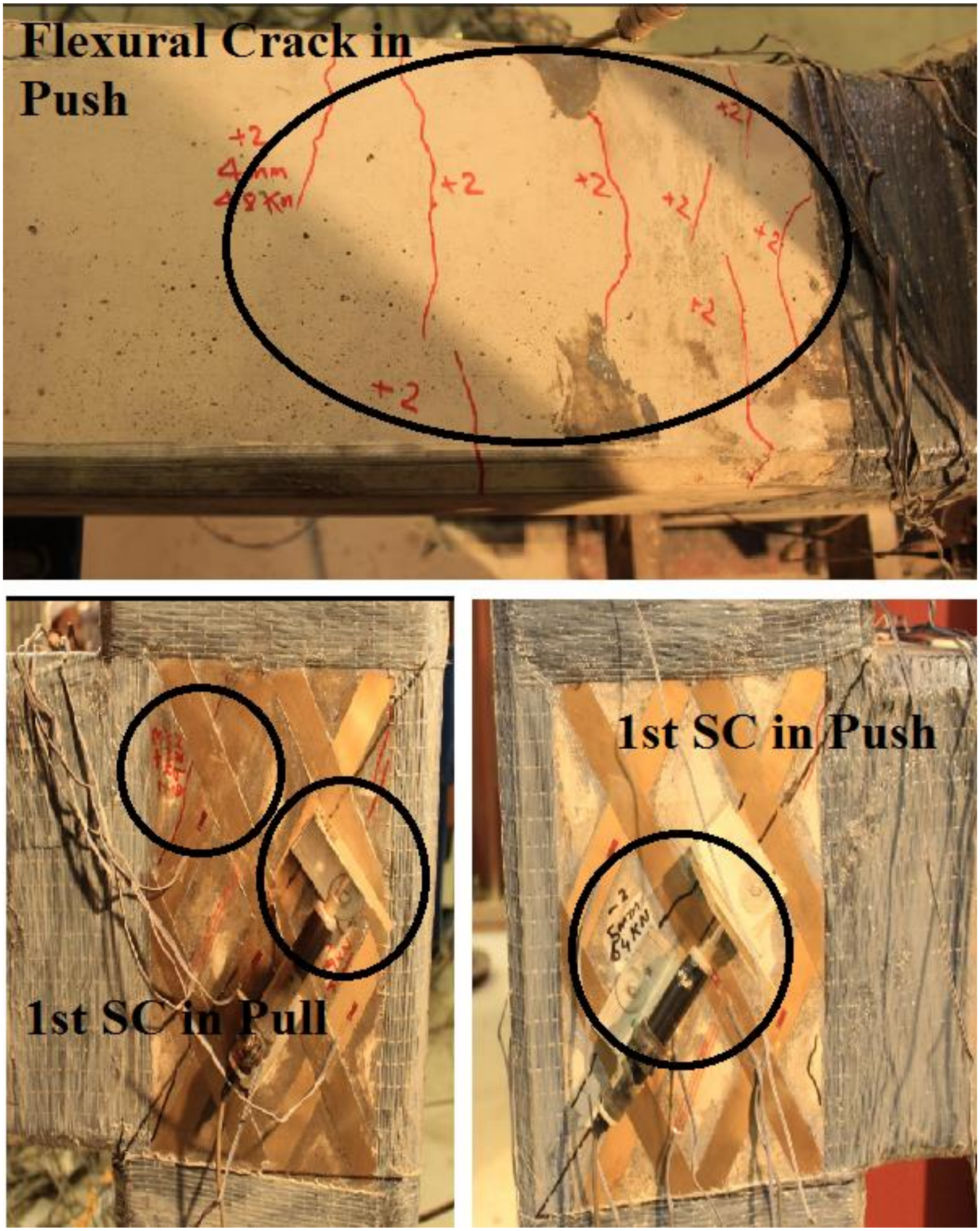

Figure 5.76: Formation of cracks in initial loading cycles

Figure 5.77: Formation of cracks on front (left) and back (right) faces of joint during different cycles

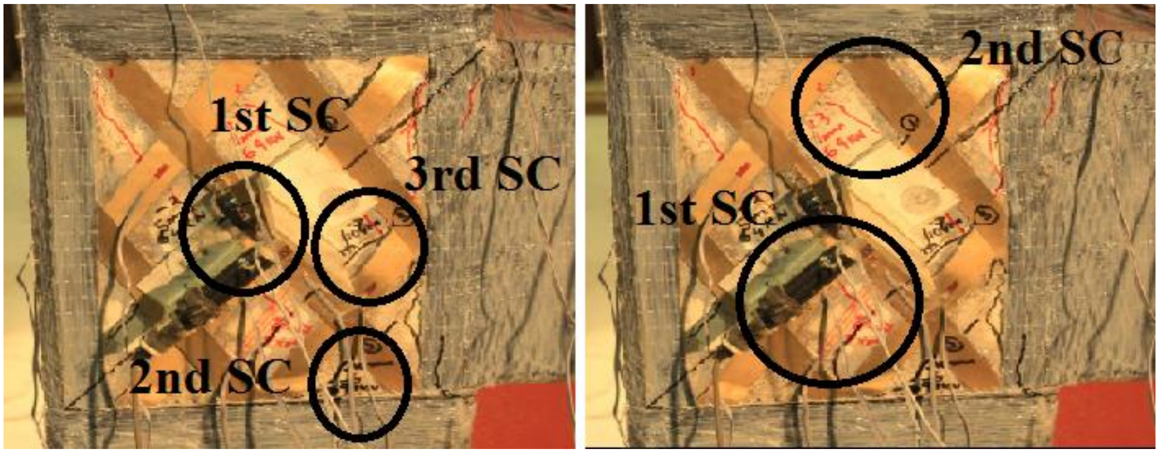

Figure 5.78: Shear cracks in push (left) and pull (right) cycles at the front face of joint region

Figure 5.79: Shear cracks in push (left) and pull (right) cycles at the back face of joint region

The test was stopped at the displacement of 40 mm, so that the results will be compared with control specimen. There was no spalling of concrete as it was observed in control BCJ-RC specimen. SMAs sheets increased the joint strength by 8.03 % in push direction and 7.41 % in pull direction as well as give more residual strength as compared to the control specimen. The specimen showed control cracking and the cracks width as compared to control specimen were also reduced in BCJ-RCXS. Figure 5.80 shows the cracks at the end of final cycle. LVDTs were used to measure the crack opening in the joint regions. Figure 5.81 shows the crack opening in the joint region. Reinforcement strain gauges were also monitored to observed strains in rebars. Figure 5.82 shows the strains in beam reinforcements during cyclic loading.

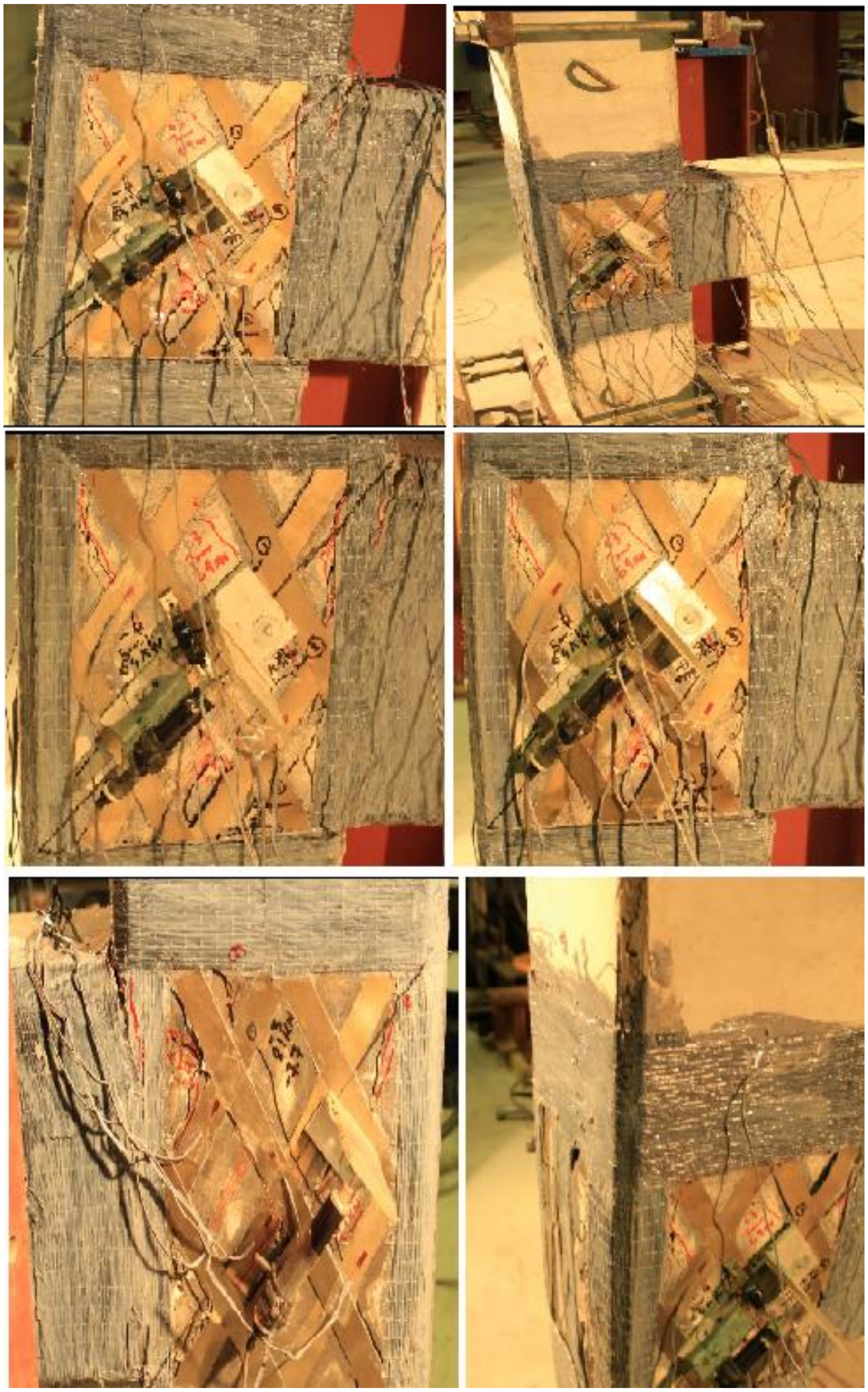

Figure 5.80: Final cracks at the end of final cycle for BCJ-RCXS

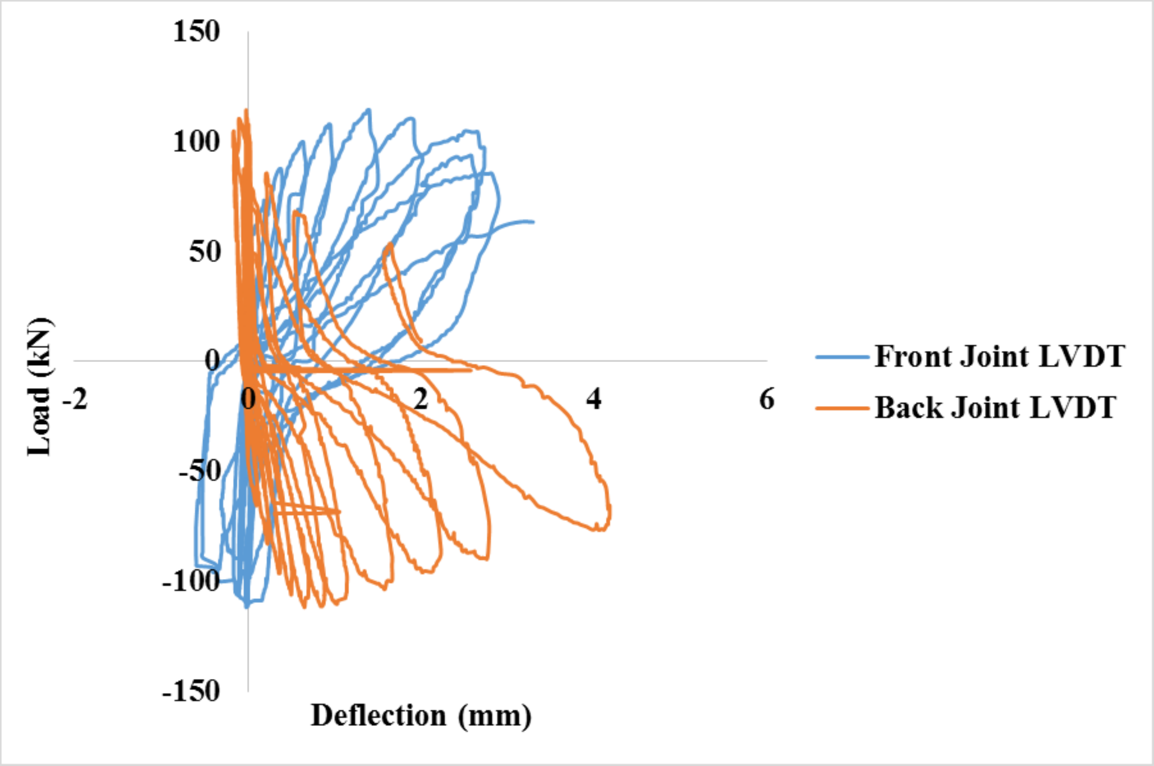

Figure 5.81: Crack opening the joint region for BCJ-RCXS

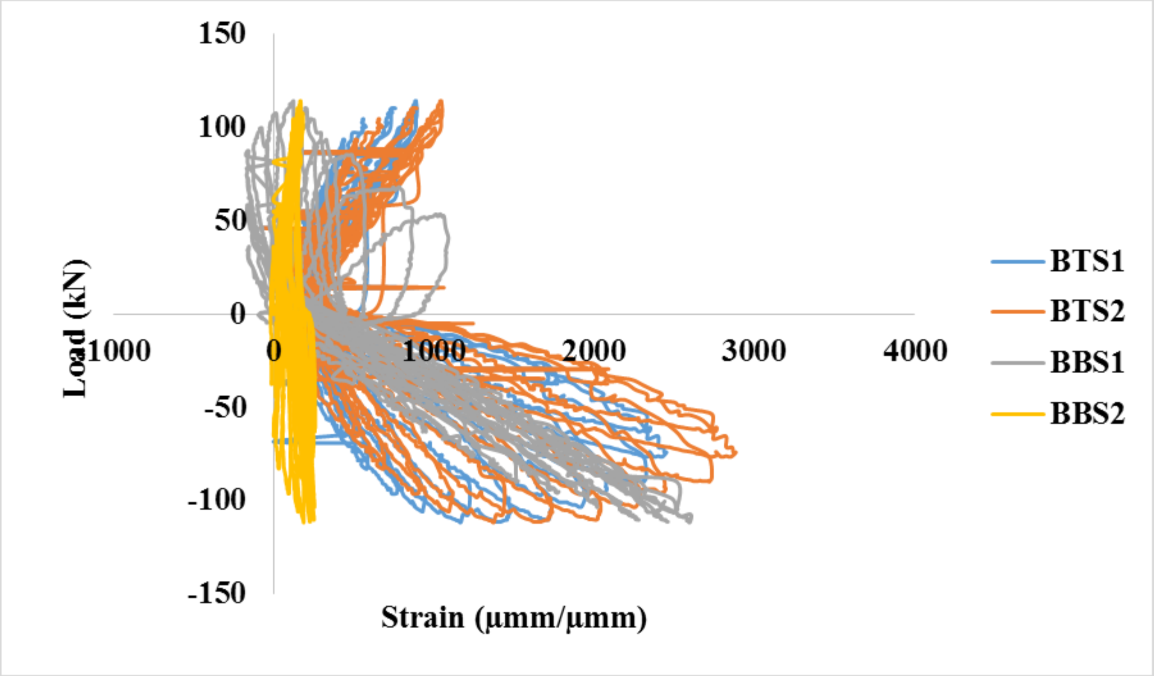

Figure 5.82: Reinforcement strain for BCJ-RCXS

Strains in SMAs sheet were monitored using high strength strain gauges. Strain gauges were installed on selective inclined SMAs sheets. Figure 5.83 and Figure 5.84 shows the SMAs sheets strains on front and back face of the joint.

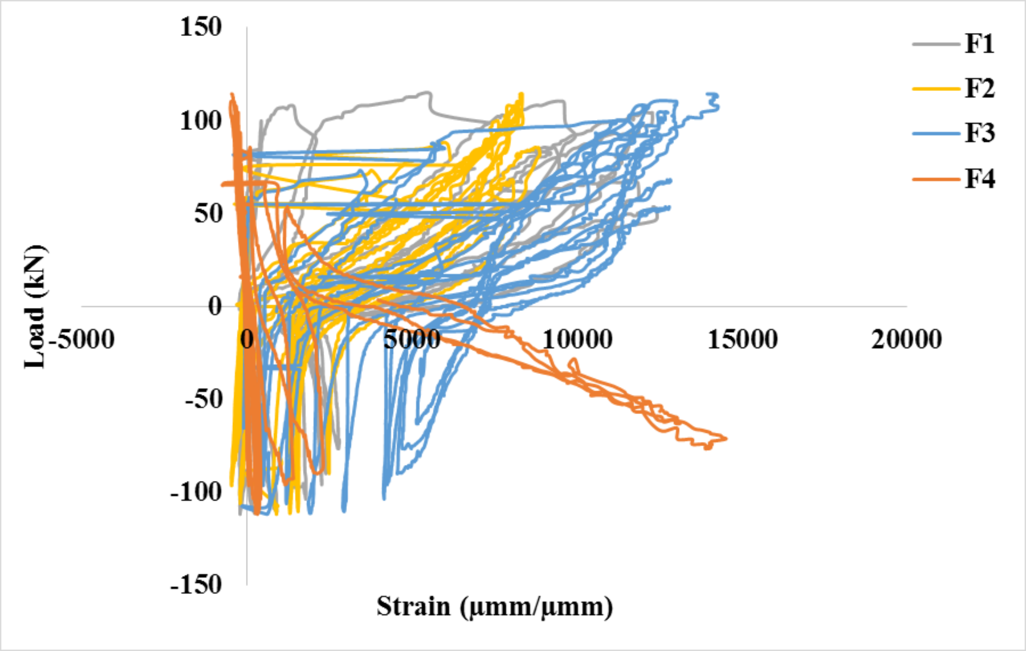

Figure 5.83: Strain in front SMAs sheets for BCJ-RCXS

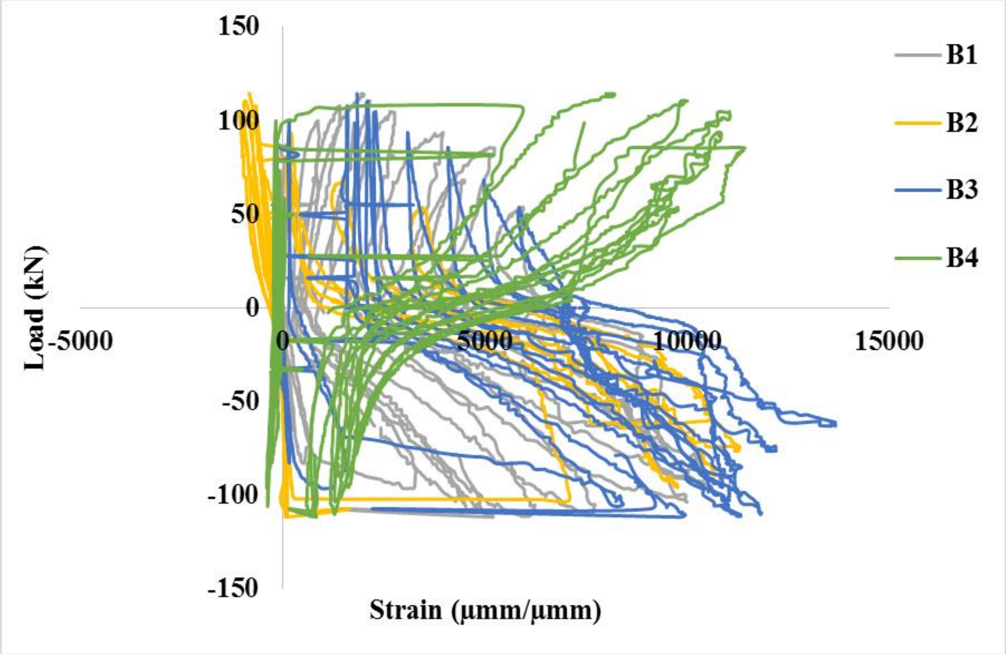

Figure 5.84: Strain in back SMAs sheets for BCJ-RCXS

Also strain was measured using crack mouth opening device which was installed on SMAs sheet once the crack appeared in joint region. Figure 5.85 shows the strain measured using CMOD SMAs sheet at location of crack. Strain obtained using CMOD shows the entrance of SMAs sheets in transformation phase during the last cycles of loading and upon unloading maximum recovery of strains were observed. Figure 5.86 shows the strains in CFRP used to tie the ends of SMAs sheets and CFRP used at the back side of the column to protect 3D failure of column. The strain in CFRP were less than 2000 µmm which shows no contribution of CFRP in strengthening of joint. Figure 5.87 show the cracks width at the front face of the joint BCJ-RCXS when push and unload to zero. Figure 5.88 show the cracks width at the back face of the joint BCJ-RCXS when push and unload to zero. Figure 5.89 show the cracks width at the front face of the joint BCJ-RCXS when pull and unload to zero. Figure 5.90 show the cracks width at the back face of the joint BCJ-RCXS when pull and unload to zero.

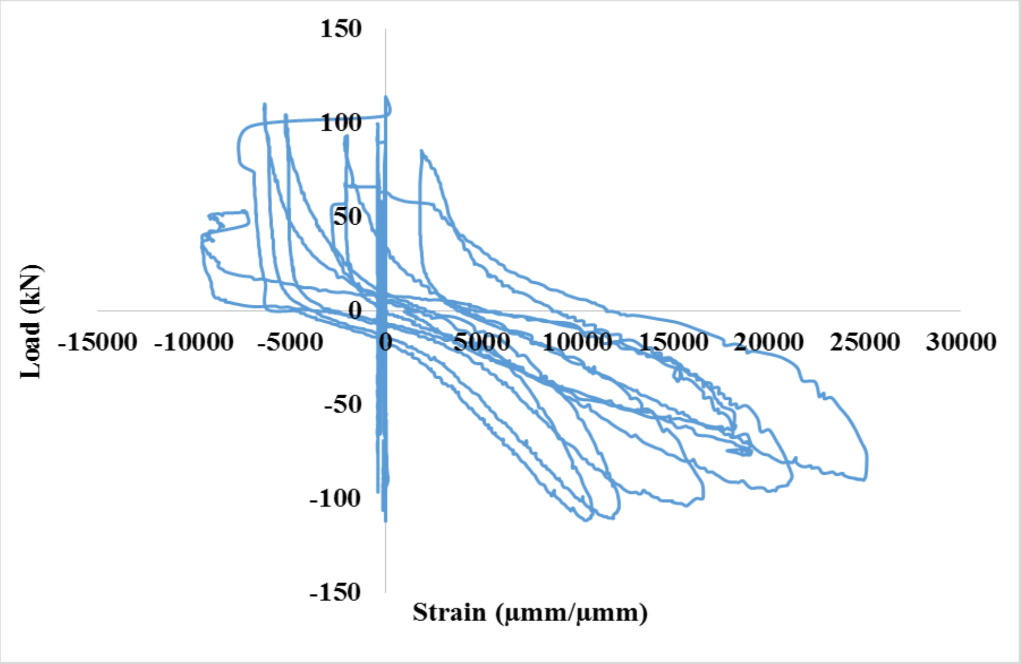

Figure 5.85: Strain measured on SMAs Sheet at location of crack using CMOD

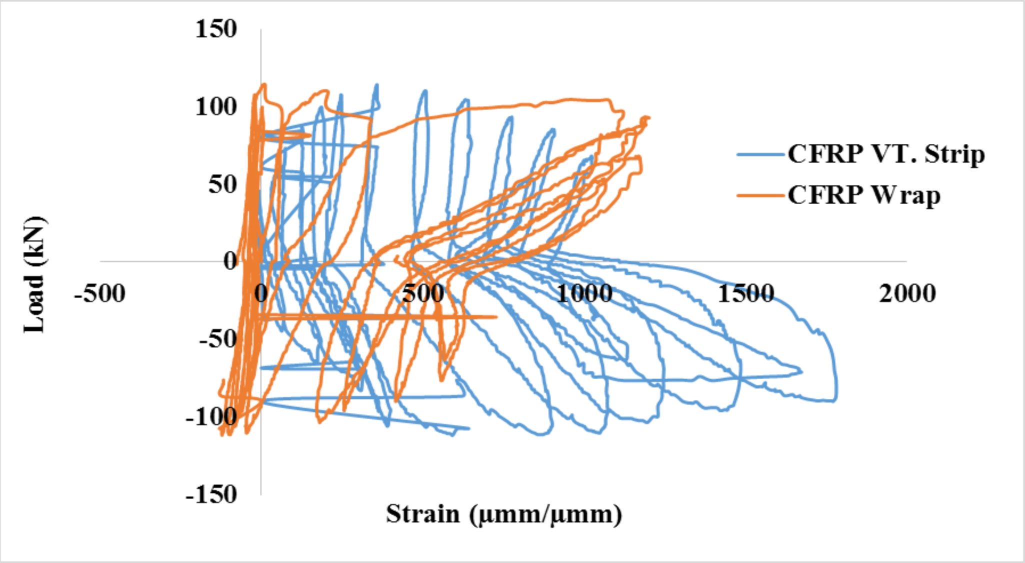

Figure 5.86: Load vs CFRP strains for BCJ-RCXS

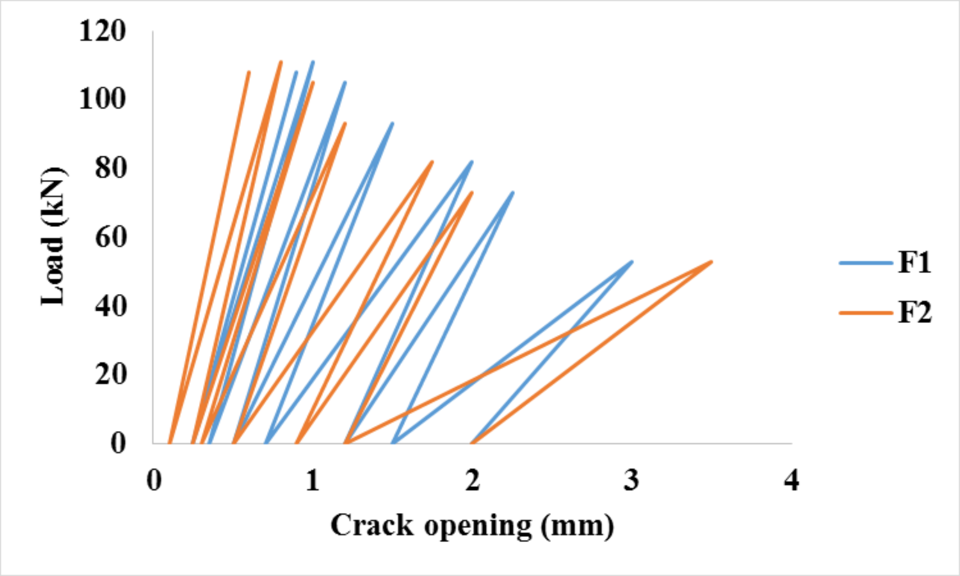

Figure 5.87: Cracks width at the front face of Joint region for BCJ-RCXS when push

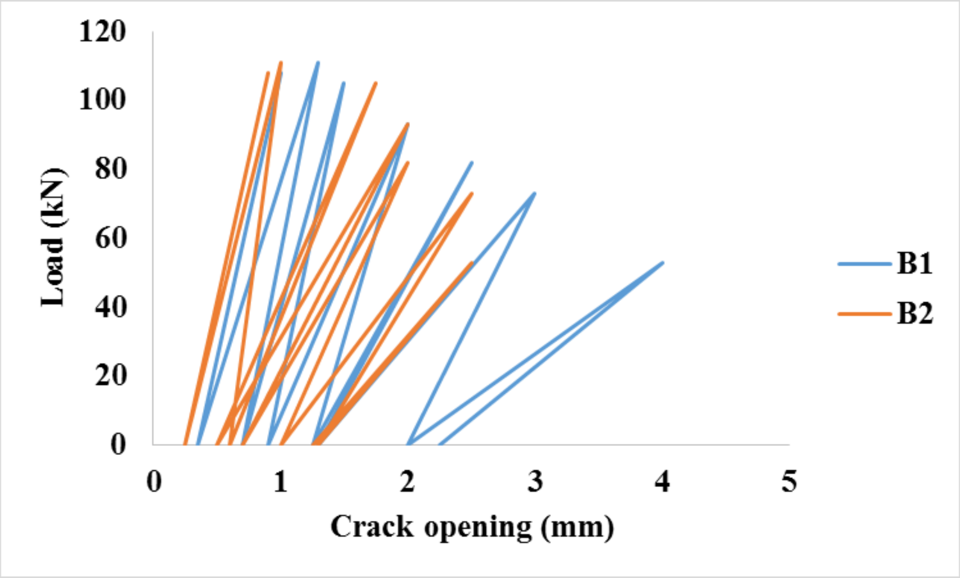

Figure 5.88: Cracks width at the back face of Joint region for BCJ-RCXS when push

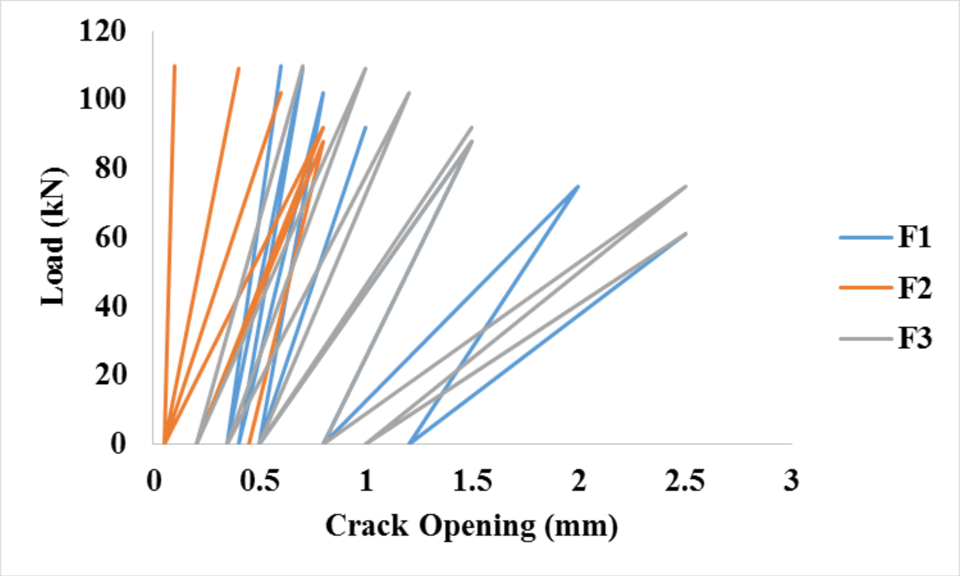

Figure 5.89: Cracks width at the front face of Joint region for BCJ-RCXS when pull

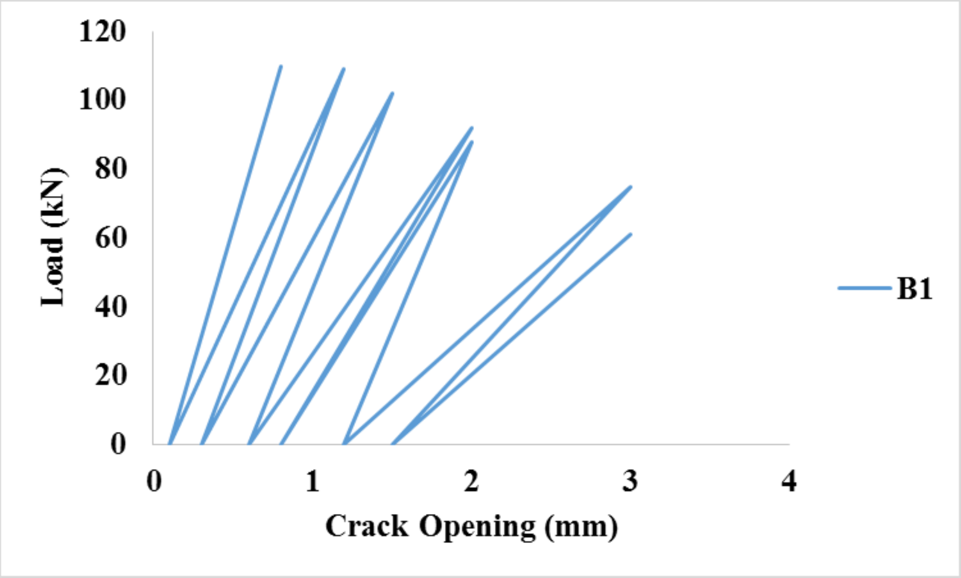

Figure 5.90: Cracks width at the back face of Joint region for BCJ-RCXS when pull

5.9 Testing Results of BCJ-CFRP Specimen

To verify the effect of CFRP wrap and vertical strips attached to the side of column a control specimen was prepared with CFRP wrap at the ends and vertical strips at the side of the column without any SMAs sheets in the joint region. The specimen was an extra sample available from previous study done by Ahmed (2012) in KFUPM lab. The sample was cast by 18 mm dia longitudinal bars and 8 mm transverse reinforcement. The results of this specimen were compared with the control specimen of Ahmed (2012) study which failed also in shear. The schematic diagram of CFRP specimen and prepared specimen in testing frame is shown in Figure 5.91 and Figure 5.92.

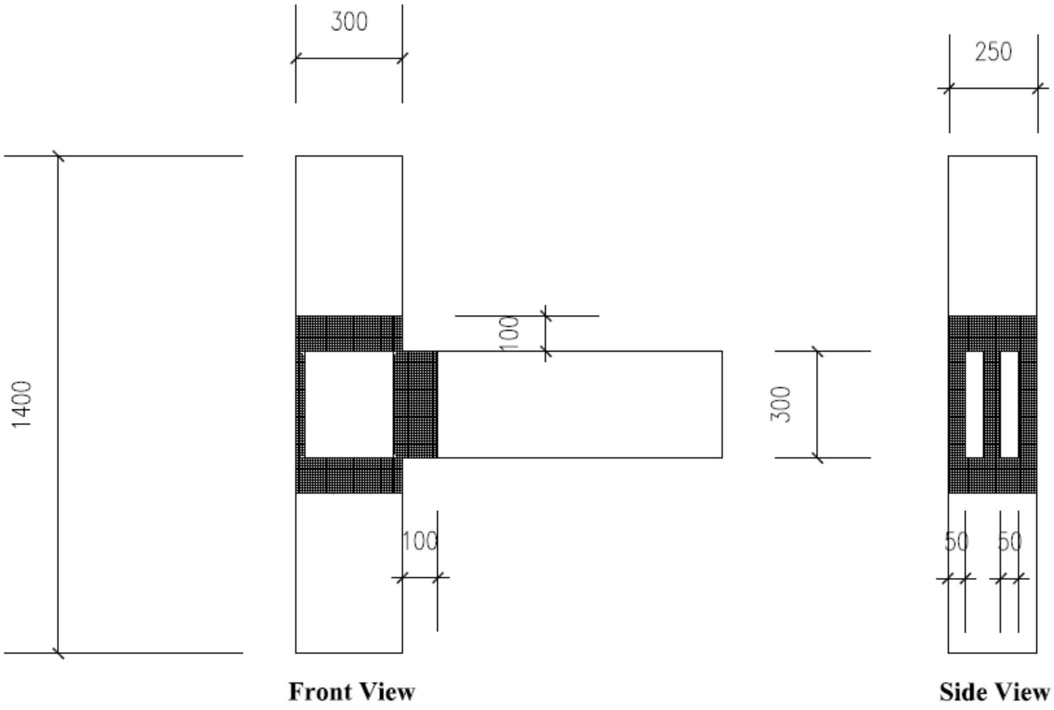

Figure 5.91: Schematic diagram for BCJ-CFRP specimen

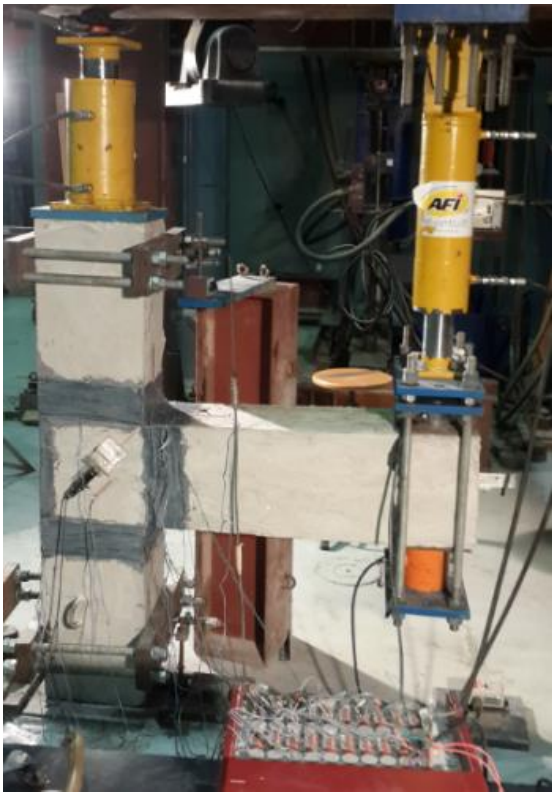

Figure 5.92: BCJ-FRP specimen in testing frame

The load deflection response of the CFRP specimen showed that there was no contribution of CFRP wrap and vertical strips used at the side of column in shear strength enhancement. This indicates that CFRP just helped in anchoring the ends of the SMAs sheets. Figure 5.93 shows the load deflection response of CFRP specimen and control specimen tested by Ahmed (2012).

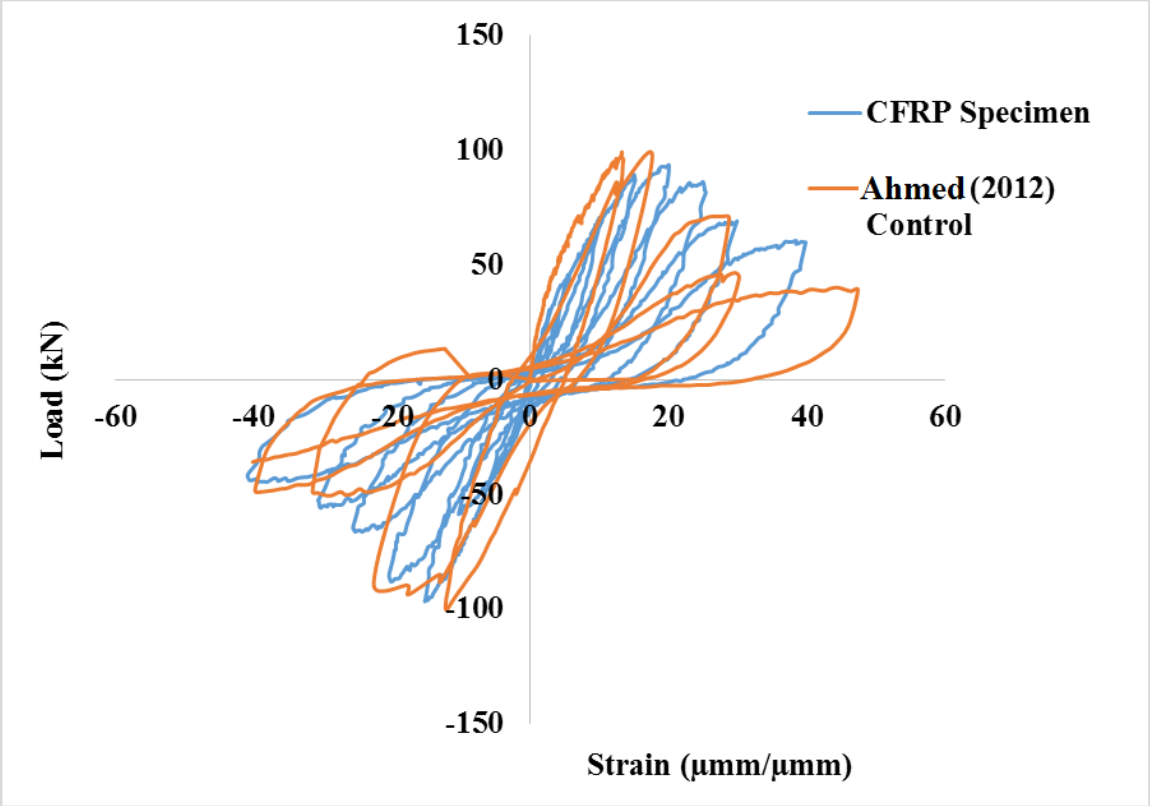

Figure 5.93: CFRP Control Specimen vs Ahmed Control Specimen without CFRP

The test was stopped at 40 mm deflection and specimens failed in shear. During the last cycles spalling of concrete cover was observed as well as reinforcement was also visible. Figure 5.94 shows the formation of cracks during different cycles. Figure 5.95 shows the cracks in the joint region at the ultimate failure.

Figure 5.94: Formation of cracks during different cycles in CFRP specimen

Figure 5.95: Cracks in the joint at ultimate failure

5.10 Comparison of Specimen under cyclic loading

The comparison of specimen BCJ-CL and BCJ-CLIS are shown in Figure 5.96. It has been observed that with the usage of SMA joint shear strength enhanced as well as residual strength also increased. BCJ-CLIS showed control cracking as compared to BCJ-CL also reduced number of crack in the joint region. SMA also helped in reducing the crack width upon unloading. The ultimate load for BCJ-CLIS was 139.23 kN which is 26 % more than the ultimate load (110.36 kN) of BCJ-CL. Figure 5.97 shows the envelope of control and retrofitted specimens under cyclic loading.

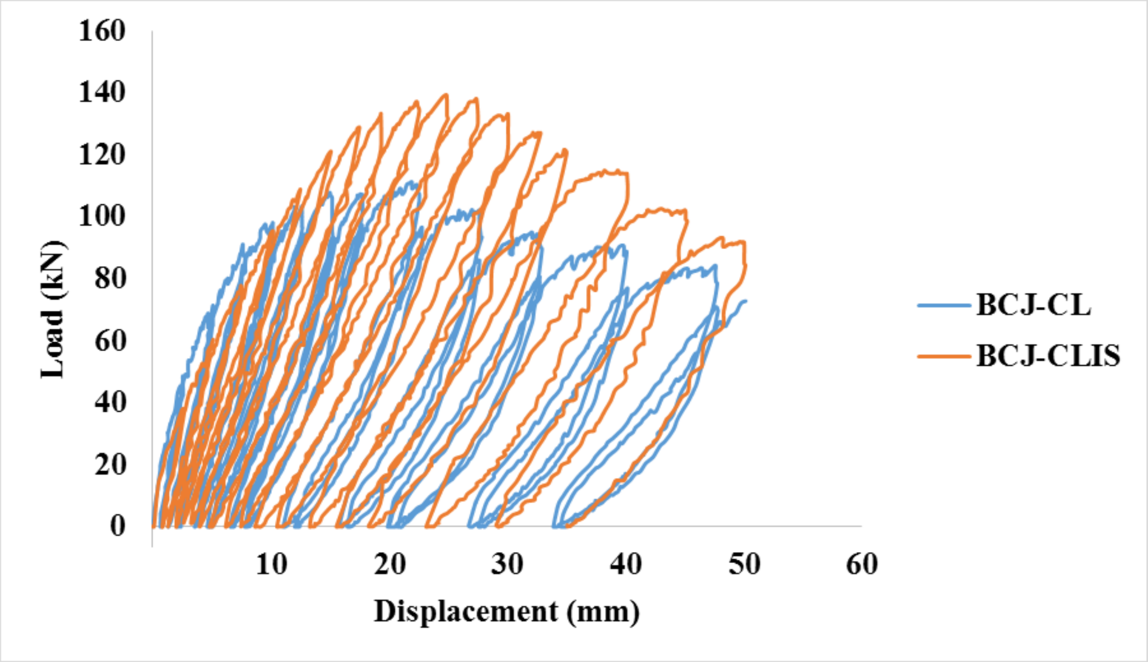

Figure 5.96: Comparison of BCJ-CL and BCJ-CLIS

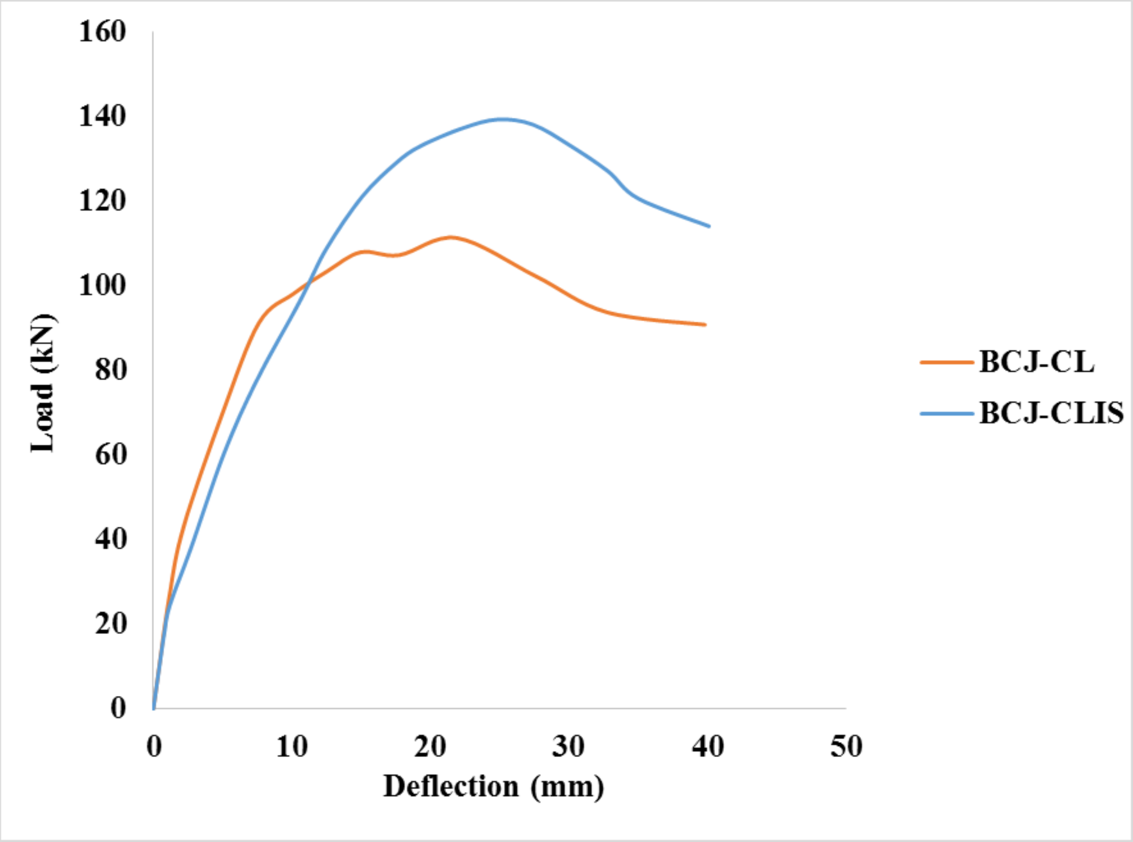

Figure 5.97: Envelope of control and retrofitted specimens under cyclic loading

5.11 Comparison of Specimen under reverse cyclic loading

The comparison of specimen BCJ-RC and BCJ-RC4S are shown in Figure 5.98. It has been observed that with the usage of 4 SMAs sheet in horizontal and vertical directions, joint shear strength enhanced as well as residual strength also increased. BCJ-RC4S showed control cracking as compared to BCJ-RC also reduced number of crack in the joint region. SMA also helped in reducing the crack width upon unloading. The ultimate load for BCJ-RC4S was 127.59 kN in push direction and 116.9 kN in pull direction which is 20.58 % and 12.51 % more as compared to the BCJ-RC specimen ultimate load in push and pull directions.

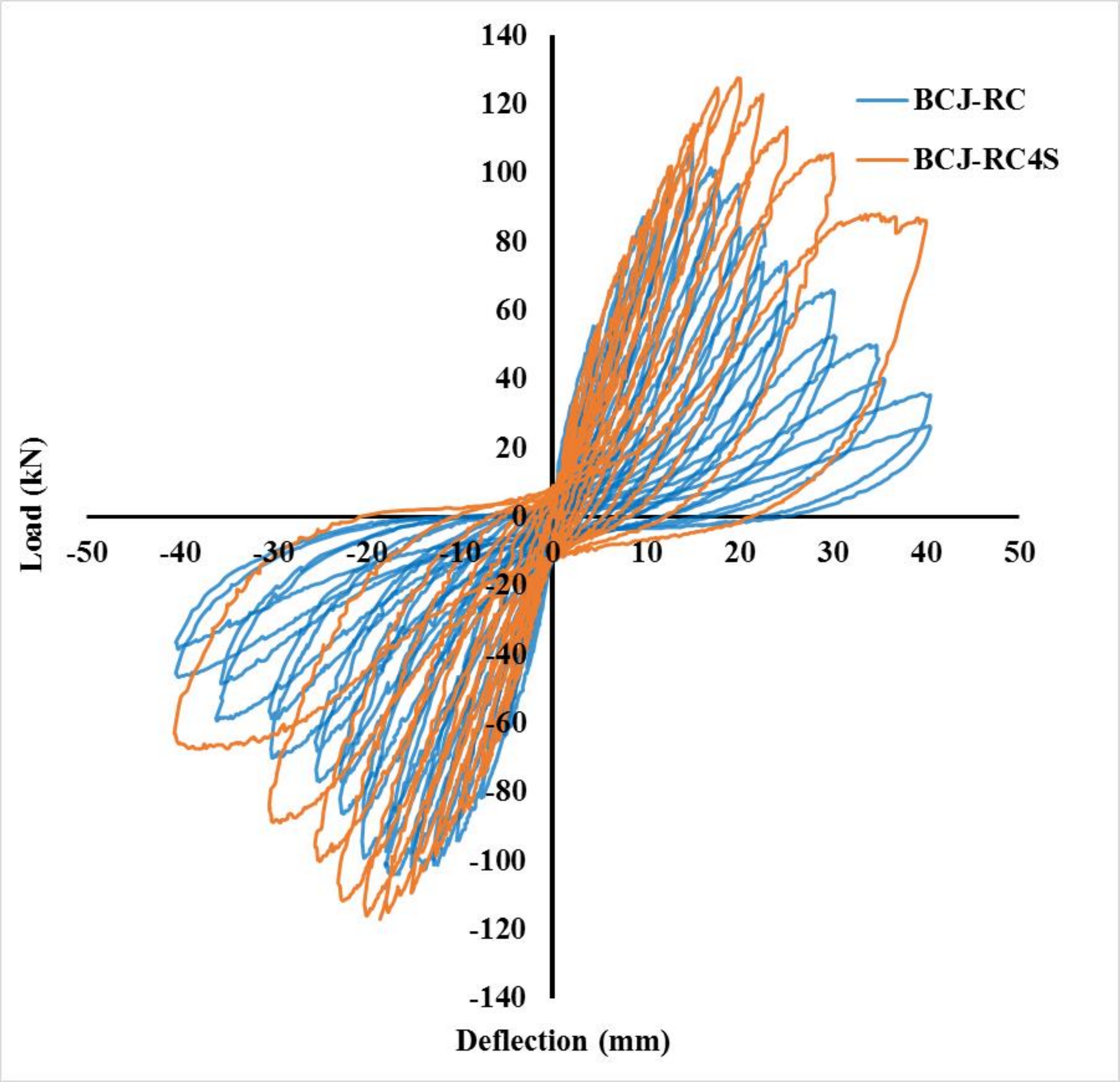

Figure 5.98: Comparison of BCJ-CL and BCJ-RC4S

The comparison of specimen BCJ-RC and BCJ-RC2S are shown in Figure 5.99. It has been observed that with the usage of 2 SMAs sheet in horizontal and vertical directions, joint shear strength enhanced as well as residual strength also increased. BCJ-RC2S showed control cracking as compared to BCJ-RC also reduced number of crack in the joint region. SMA also helped in reducing the crack width upon unloading. The ultimate load for BCJ-RC2S was 120.76 kN in push direction and 125 kN in pull direction which is 14.12 % and 20.31 % more as compared to the BCJ-RC specimen ultimate load in push and pull directions.

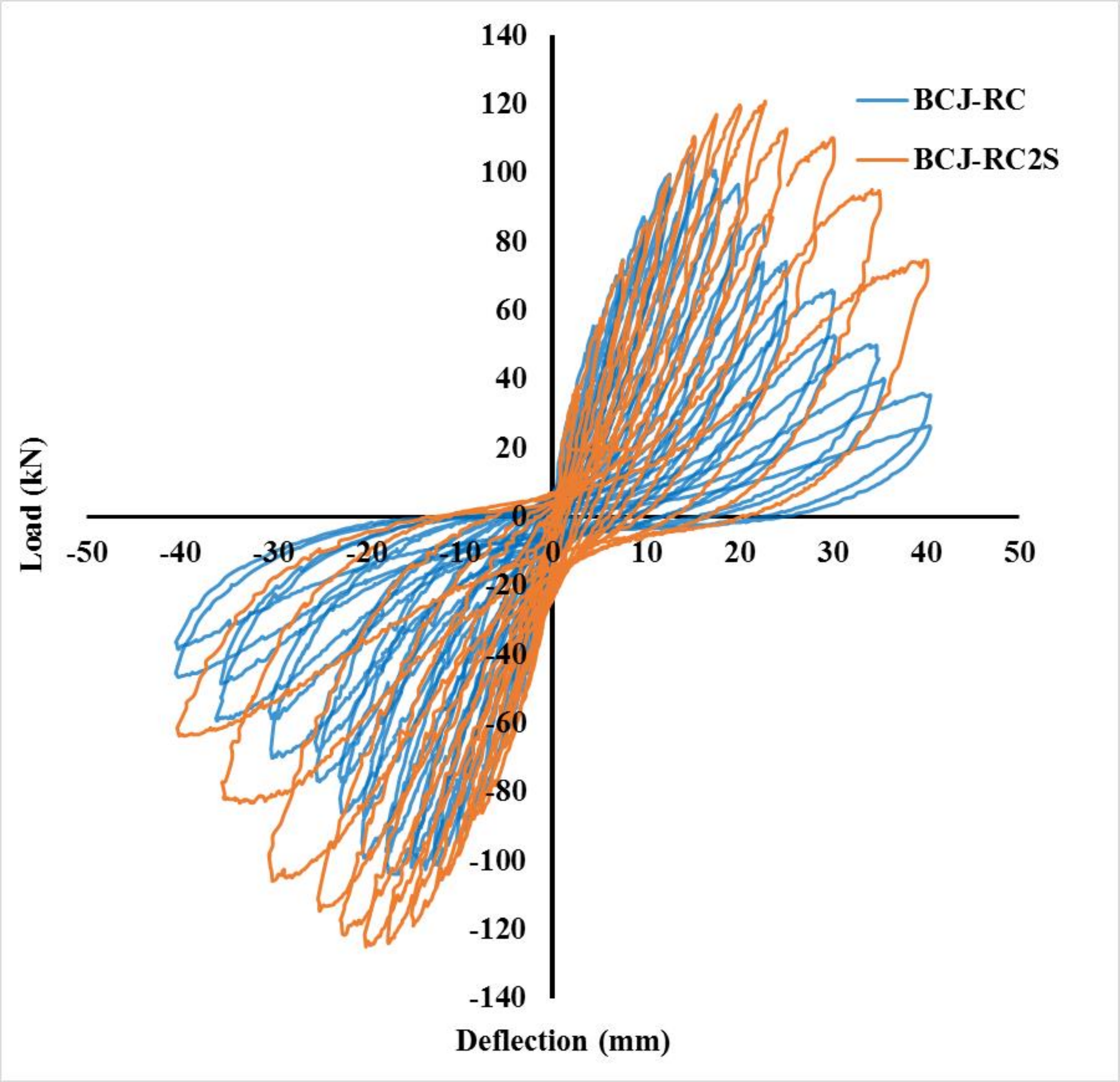

Figure 5.99: Comparison of BCJ-CL and BCJ-RC2S

The comparison of specimen BCJ-RC and BCJ-RCXS are shown in Figure 5.100. It has been observed that with the usage of cross SMAs sheets in the joint region, joint shear strength enhanced as well as residual strength also increased. BCJ-RCXS showed control cracking as compared to BCJ-RC also reduced number of crack in the joint region. SMA also helped in reducing the crack width upon unloading. The ultimate load for BCJ-RCXS was 114.32 kN in push direction and 111.6 kN in pull direction which is 8.03 % and 7.41 % more as compared to the BCJ-RC specimen ultimate load in push and pull directions.

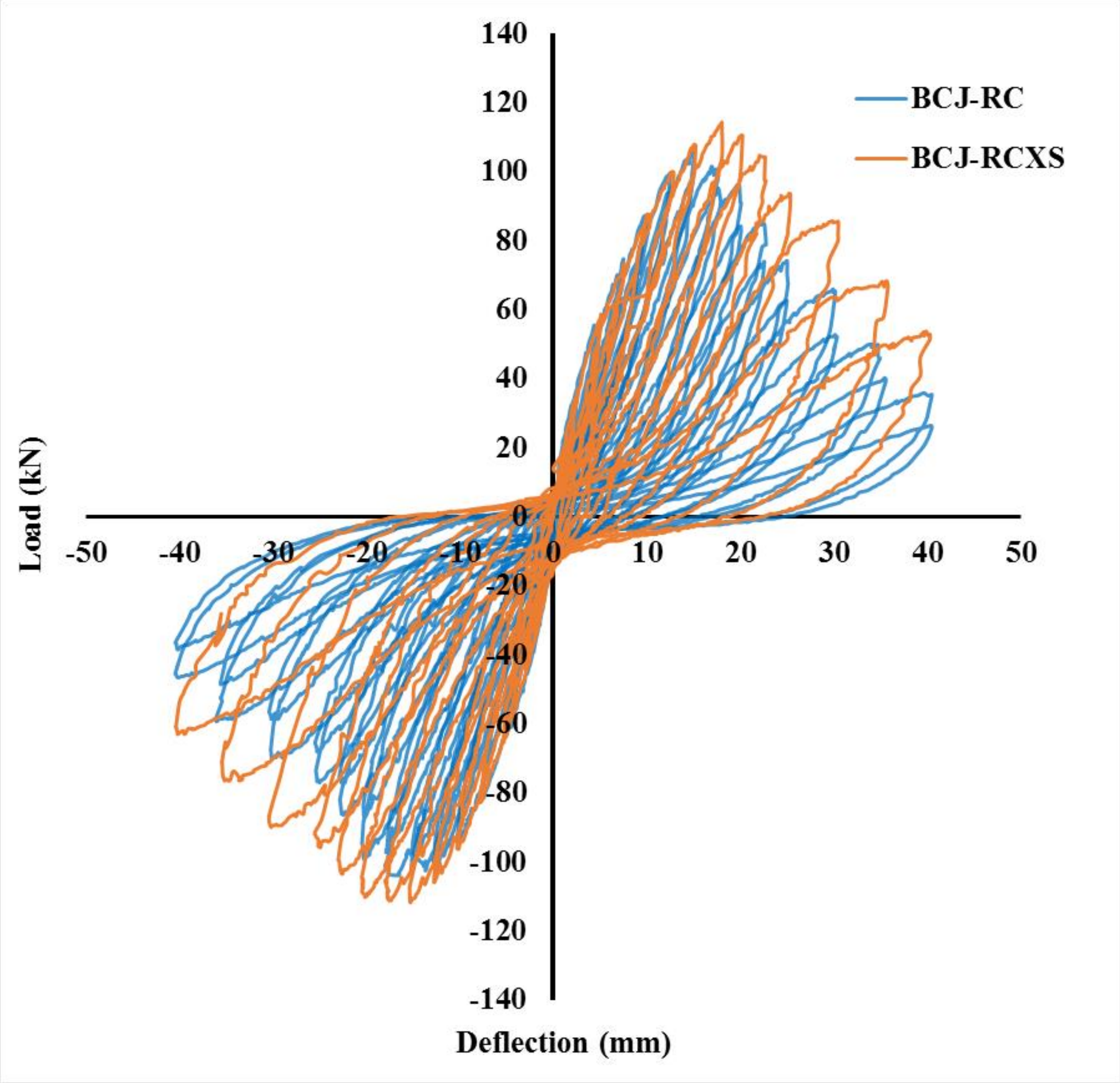

Figure 5.100: Comparison of BCJ-CL and BCJ-RCXS

Figure 5.101 shows the comparison of all specimens under reverse cyclic load. Figure 5.102 shows the cyclic envelope of control and retrofited specimen under reverse cyclic load. Table 6 shows the load, displacemnt and enhancement of load after retrofitting.

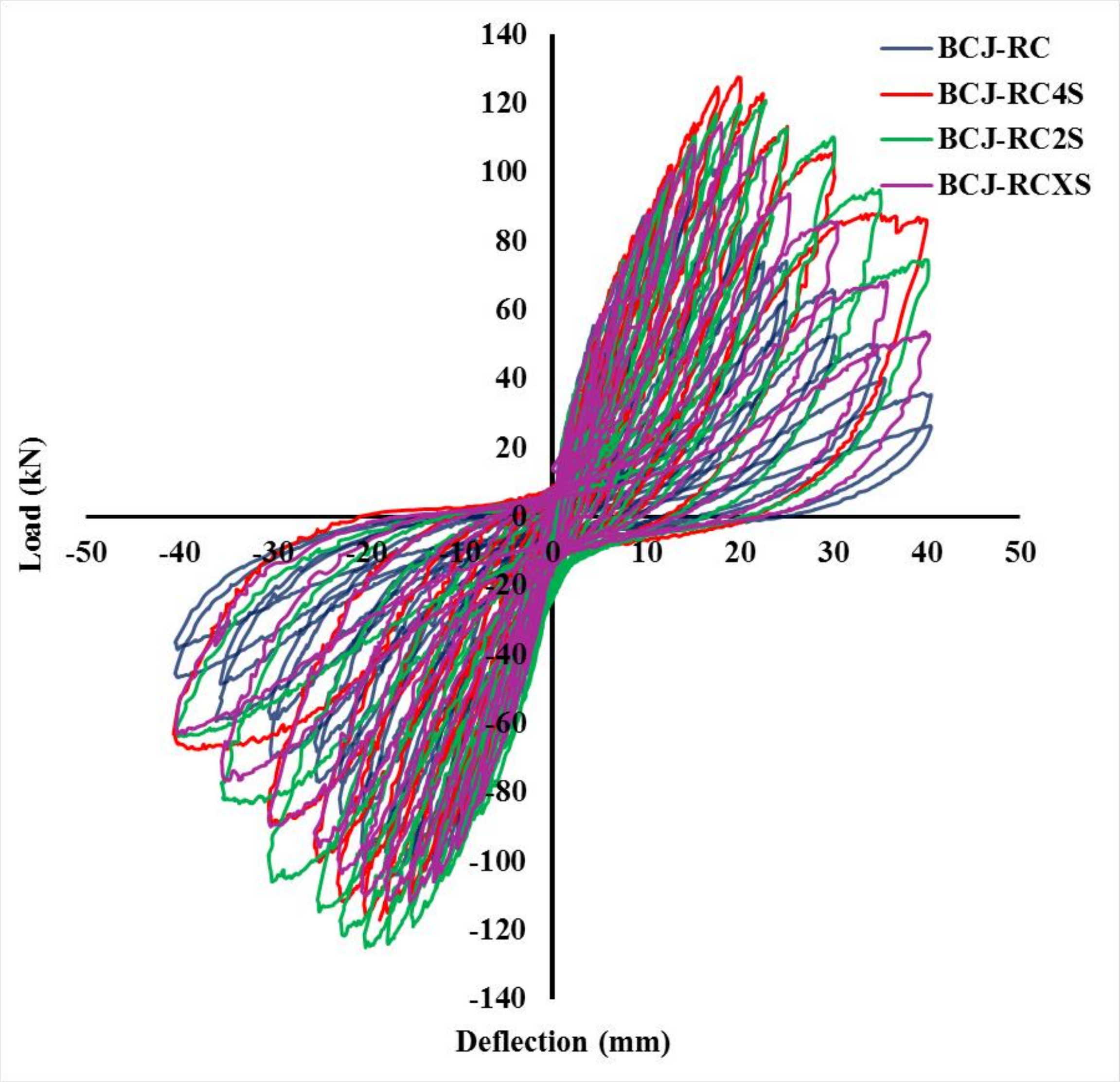

Figure 5.101: Comparison of control and retrofitted specimens under reverse cyclic load

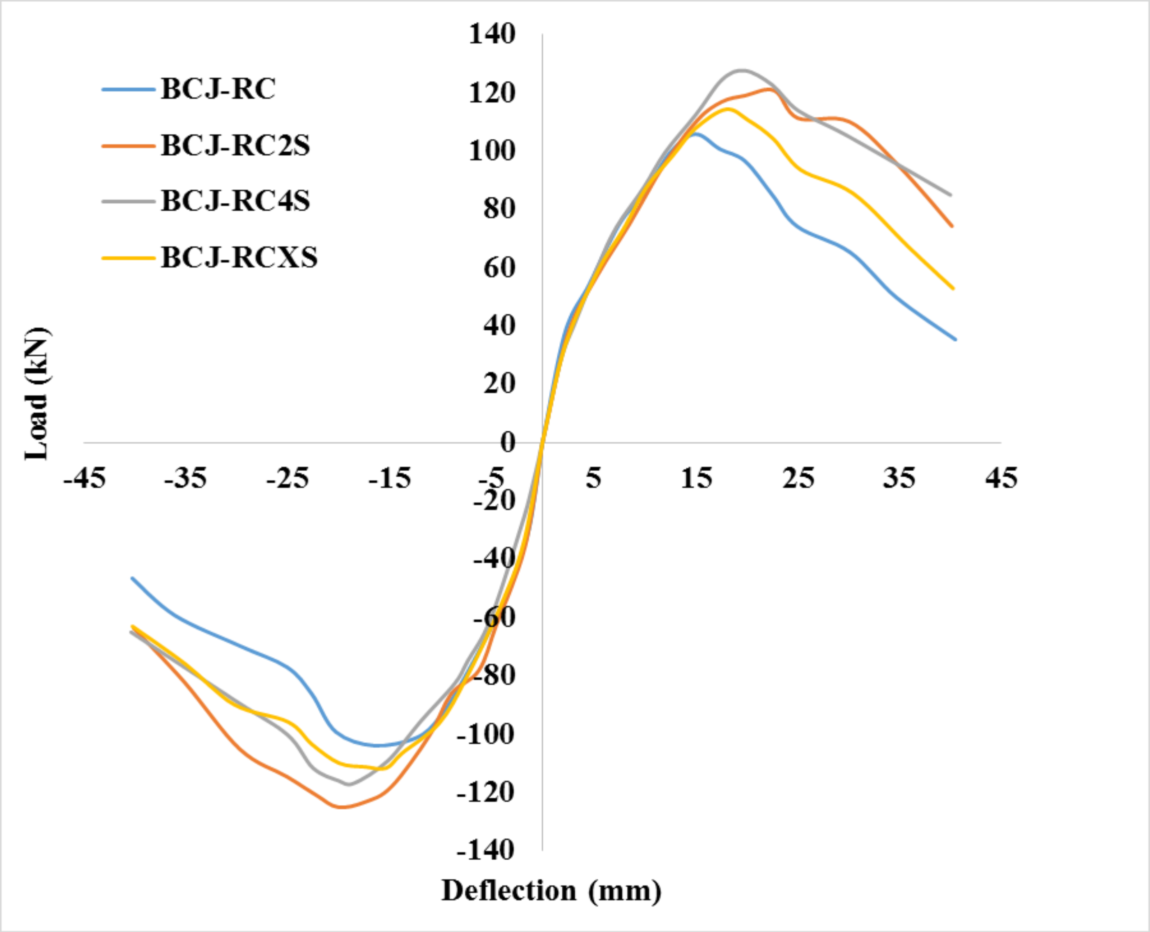

Figure 5.102: Hysteresis envelope of control and retrofitted specimen

Table 6: Comparison of all specimens in terms of load enhancement

Specimen	Ultimate load kN		Displacement mm		Enhancement %	
	Push	Pull	Push	Pull	Push	Pull
BCJ-M	122.46	104.2	20.46	20.28	-	-
BCJ-CL	110.36	-	22.362	-	-	-
BCJ-RC	105.82	103.9	14.98	16.25	-	-
BCJ-CLIS	139.23	-	24.88	-	26	-
BCJ-RC4S	127.59	116.9	19.86	18.54	20.58	12.51
BCJ-RC2S	120.76	125	22.75	20.05	14.12	20.31
BCJ-RCXS	114.32	111.6	18.02	15.32	8.03	7.41

5.12 Joint Shear Capacity from Proposed Mechanistic Model

5.12.1 Experimental joint shear strength at ultimate load for BCJ-RC

The experimental joint shear strength can be determined from the strain gauge readings recorded experimentally and the applied loads as explained earlier in section 3.1.

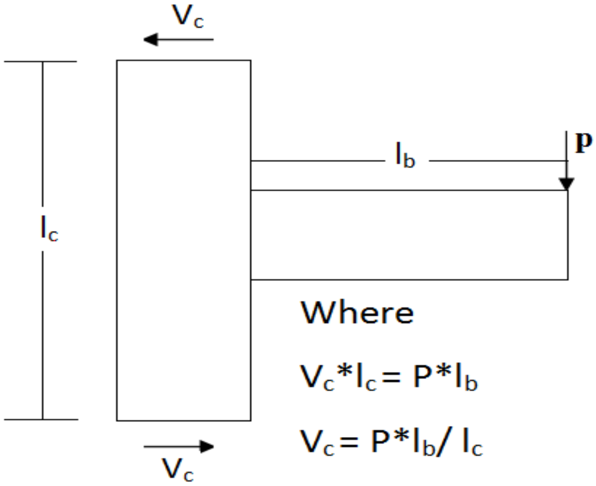

Figure 5.103: Joint Shear strength

As we know,

$$V_j = T - V_c$$

$$V_j = \varepsilon_s \times E_s \times A_s - \frac{Pl_b}{l_c}$$

$$V_j = 0.0022 \times 195 \times 942.45 - \frac{105.82 \times 900}{1400}$$

$$V_j = 317.91kN$$

5.12.2 Joint shear strength for BCJ-RC using Mechanistic Model

As we know that

$$V_j = V_c + V_s$$

From curve shown in Figure 3.9 proposed by Khatib et al. (2016)

$v_j = 3.48$ MPa for concrete strength of 33 MPa

$$V_c = v_j \times A_j$$

$$V_c = \frac{3.48 \times 300 \times 300}{1000} = 313.2\,\text{kN}$$

From equation proposed by Bakir and Boduroglu (2002)

$$V_s = 0.7434\left(\frac{942.45}{250 \times 275}\right)^{0.4289} \times \frac{\sqrt{33} \times 300 \times 300}{1000} = 61.04\ \text{kN}$$

$$V_j = 313.2 + 61.04 = 374.24\,\text{kN}$$

5.12.3 Experimental joint shear strength at ultimate load for BCJ-RC4S

The experimental joint shear strength can be determined from the strain gauge readings recorded experimentally and the applied loads as explained earlier in section 3.1.

As we know,

$$V_j = T - V_c$$

$$V_j = \varepsilon_s \times E_s \times A_s - \frac{Pl_b}{l_c}$$

$$V_j = 0.0025 \times 195 \times 942.45 - \frac{127.59 \times 900}{1400}$$

$$V_j = 377.42kN$$

5.12.4 Joint shear strength for BCJ-RC4S using Mechanistic Model

As we know that

$$V_j = V_c + V_s + V_{SMA}$$

From curve shown in Figure 3.9 proposed by Khatib et al. (2016)

$v_j = 3.48$ MPa for concrete strength of 33 MPa

$$V_c = v_j \times A_j$$

$$V_c = \frac{3.48 \times 300 \times 300}{1000} = 313.2\,\text{kN}$$

From equation proposed by Bakir and Boduroglu (2002)

$$V_s = 0.7434\left(\frac{942.45}{250 \times 275}\right)^{0.4289} \times \frac{\sqrt{33} \times 300 \times 300}{1000} = 61.04\ \text{kN}$$

$$V_{SMA} = \frac{A_{SMA} f_{SMA} d}{s}$$

$$V_{SMA} = \frac{0.15 \times 25 \times 2 \times 0.016 \times 15000 \times 275}{90 \times 1000} = 5.5\,\text{KN}$$

$$V_j = 313.2 + 61.04 + 5.5 = 379.74\,\text{kN}$$

Using above approach the shear capacity of control specimens and retrofitted specimens were calculated. Table 7 shows the comparison between experimental and mechanistic model joint shear capacity for all specimens.

Table 7: Comparison of Joint shear capacity for specimens

Specimen	V_{test} kN	$V_{Predicted}$ kN	V_{test} (MPa)	$V_{prdicted}$ (MPa)	$\frac{V_{predicted}}{V_{test}}$ (MPa)
BCJ-M	379.25	374.24	4.21	4.16	0.99
BCJ-RC	317.91	374.24	3.53	4.16	1.18
BCJ-CL	296.61	374.24	3.29	4.16	1.26
BCJ-RC4S	377.42	379.74	4.19	4.21	1.00
BCJ-RC2S	351.86	378.95	3.91	4.21	1.08
BCJ-RCXS	386	377.45	4.29	4.19	0.98
BCJ-CLIS	461.64	380.47	5.12	4.23	0.83

CHAPTER 6

FINITE ELEMET SIMULATION OF SMAS SHEET RETROFITTED BEAM-COLUMN JOINTS

6.1 Introduction

Finite element simulations becomes an important tool these day to study the behavior of complex problems. Many studies have been conducted on beam-column joints using finite element softwares to idealize the behavior of experimental studies. In the recent years researchers have used wide range of finite element soft wares which includes ANSYS, ABAQUS, DIANA and Vector 2 etc. to study the response of beam-column joints. In this study ABAQUS 6.13 software was utilized to study the response of control and retrofitted specimens.

ABAQUS 6.13 has vast range of constitutive models for metals, rubber and concrete etc. The Damage Plasticity Model (DPM) for concrete was utilized in this study to model the behavior of concrete, which is well-known for modeling concrete structures. The non-linear mechanisms that are considered in modeling are cracking and crushing of concrete and yielding of reinforcement. For modeling of SMAs sheets user defined material model was utilized using UMAT subroutine. The SMA VUMAT subroutine considered the Auricchio et al. (1996) material model for SMA (Nitinol).

6.2 Plastic Damage Model Review

The Plastic damage model for concrete in ABAQUS 6.13 was proposed by Lubliner et al. (1989) and Lee and Fenves (1998) to understand the elasto-plastic behavior. The elastic-plastic response of the concrete damaged plasticity model is described in terms of the effective stress $\bar{\sigma}$ and the hardening variable $\tilde{\varepsilon}^{pl}$ with scalar isotropic damage.

$$\bar{\sigma} = D_o^{el} : (\varepsilon - \varepsilon^{pl}) \in \left\{ \bar{\sigma} \middle| F(\bar{\sigma}, \tilde{\varepsilon}^{pl}) \leq 0 \right\} \tag{6.1}$$

$$\dot{\tilde{\varepsilon}}^{pl} = h(\bar{\sigma}, \bar{\varepsilon}^{pl}).\dot{\hat{\varepsilon}}^{pl} \tag{6.2}$$

$$\dot{\varepsilon}^{pl} = \dot{\lambda} \frac{\partial G(\bar{\sigma})}{\partial \bar{\sigma}} \tag{6.3}$$

Where:

$\dot{\lambda}$ and F obey the Kuhn-Tucker conditions: $\dot{\lambda} F = 0; \dot{\lambda} \geq 0; F \leq 0$. The Cauchy stress is calculated in terms of the stiffness degradation variable, $d = d(\bar{\sigma}, \tilde{\varepsilon}^{pl})$ and the effective stress as:

$$\sigma = (1 - d)\bar{\sigma} \tag{6.4}$$

The constitute relations for the elastic-plastic response, equations 6.1-6.3 are decoupled from the stiffness degradation response, equation 6.4, which makes the model attractive for an effective numerical implementing.

In general, the CDP mode consists of following fundamental concepts: (i) strain rate decomposition, (ii) stress-strain relation, (iii) stiffness degradation and hardening rule, (iv) yield function, and (v) flow rule.

6.2.1 Strain Rate Decomposition

Additive strain rate decomposition is assumed for the rate-independent model:

$$\dot{\varepsilon} = \dot{\varepsilon}^{el} + \dot{\varepsilon}^{pl} \tag{6.5}$$

Where:

$\dot{\varepsilon}$ is the total strain rate.

$\dot{\varepsilon}^{el}$ is the elastic part of the strain rate.

$\dot{\varepsilon}^{pl}$ is the plastic part of the strain rate.

6.2.2 Stress-Strain Relation

The stress-strain relations are governed by scalar damaged elasticity:

$$\sigma = (1-d)D_o^{el} : (\varepsilon - \varepsilon^{pl}) = D^{el} : (\varepsilon - \varepsilon^{pl}) \tag{6.6}$$

$$D^{el} = D_o^{el}(1-d) \tag{6.7}$$

Where:

σ is Cauchy stress tensor.

d is the scalar stiffness degradation variable, which can take values in the range from zero (undamaged material) to one (fully damaged material).

ε is the strain tensor.

ε^{pl} is the plastic strain tensor.

D_o^{el} the initial (undamaged) elastic stiffness of the material.

D^{el} is the degraded elastic stiffness tensor.

The effective stress tensor is defined as:

$$\bar{\sigma} = D_o^{el} : (\varepsilon - \varepsilon^{pl}) \tag{6.8}$$

In the formulation, it is necessary to propose the evolution of the scalar degradation variable to be a function of effective stress and effective plastic strain.

$$d = d(\bar{\sigma} : \tilde{\varepsilon}^{pl}) \tag{6.9}$$

In CDP model, the stiffness degradation is initially isotropic and defined by degradation variable d_c in a compression zone and variable d_t in tension zone.

Thus, finally the Cauchy stress tensor σ is related to the effective stress tensor $\bar{\sigma}$ through the scalar degradation parameter $(1-d)$:

$$\sigma = (1-d)\bar{\sigma} \tag{6.10}$$

6.2.3 Stiffness Degradation and Hardening Rule

Damage in concrete is characterized by two variables, $\tilde{\varepsilon}_c^{pl}$ and $\tilde{\varepsilon}_t^{pl}$ which are plastic strains in tension and compression, respectively.

The evolution equations of the hardening variables $\tilde{\varepsilon}_c^{pl}$ and $\tilde{\varepsilon}_t^{pl}$ are conveniently formulated by considering uniaxial loading conditions first and then extended to multiracial conditions.

6.2.4 Uniaxial Conditions

It is assumed that the uniaxial stress-strain curves can be converted into stress versus plastic strain curves of the form:

$$\sigma_t = \sigma_t(\tilde{\varepsilon}_t^{pl}, \dot{\tilde{\varepsilon}}_t^{pl}, ...) \tag{6.11}$$

$$\sigma_c = \sigma_c(\tilde{\varepsilon}_c^{pl}, \dot{\tilde{\varepsilon}}_c^{pl}, ...) \tag{6.12}$$

Where the subscripts t and c refer to tension and compression, respectively; $\dot{\tilde{\varepsilon}}_t^{pl}$ and $\dot{\tilde{\varepsilon}}_c^{pl}$ are the equivalent plastic strain rates, $\tilde{\varepsilon}_t^{pl} = \int_0^t \dot{\tilde{\varepsilon}}_t^{pl} dt$ and $\tilde{\varepsilon}_c^{pl} = \int_0^c \dot{\tilde{\varepsilon}}_c^{pl} dc$ are the equivalent plastic strains. The effective plastic strain rates under compression are given as:

$$\dot{\tilde{\varepsilon}}_t^{pl} = \dot{\tilde{\varepsilon}}_{11}^{pl} \tag{6.13}$$

$$\dot{\tilde{\varepsilon}}_c^{pl} = \dot{\tilde{\varepsilon}}_{11}^{pl} \tag{6.14}$$

When the concrete specimen is unloaded from any point on the strain softening branch of the stress-strain curves, the unloading response is observed to be weakened, the elastic stiffness of the material appears to be damaged or degraded. The degradation of the elastic stiffness is significantly different between tension and compression tests; in either case, the effect is more pronounced as the plastic strain increases. The degraded response of concrete is characterized by two independent uniaxial damage variables, d_t and d_c, which are assumed to be functions of the plastic strains.

$$d_t = d_t(\tilde{\varepsilon}_t^{pl}, ...) \tag{6.15}$$

$$d_c = d_c(\tilde{\varepsilon}_c^{pl}, ...) \tag{6.16}$$

The evaluations of the damage parameter have been studied extensively and it can take several forms. The most used model for describing the variation of the damaged parameter d is based on the plastic energy dissipated during loading in which d will be the ratio between plastic energy dissipated up to certain plastic strain and the total plastic energy. This can be descripted as shown in equation 6.17.

$$d_t = \frac{\int_0^{\tilde{\varepsilon}_t^{pl}} d_t(\tilde{\varepsilon}_t^{pl})}{\int_0^{\tilde{\varepsilon}_{tf}^{pl}} d_t(\tilde{\varepsilon}_t^{pl})} \tag{6.17}$$

Equation 6.17 can be interpreted as shown in Figure 6.1.

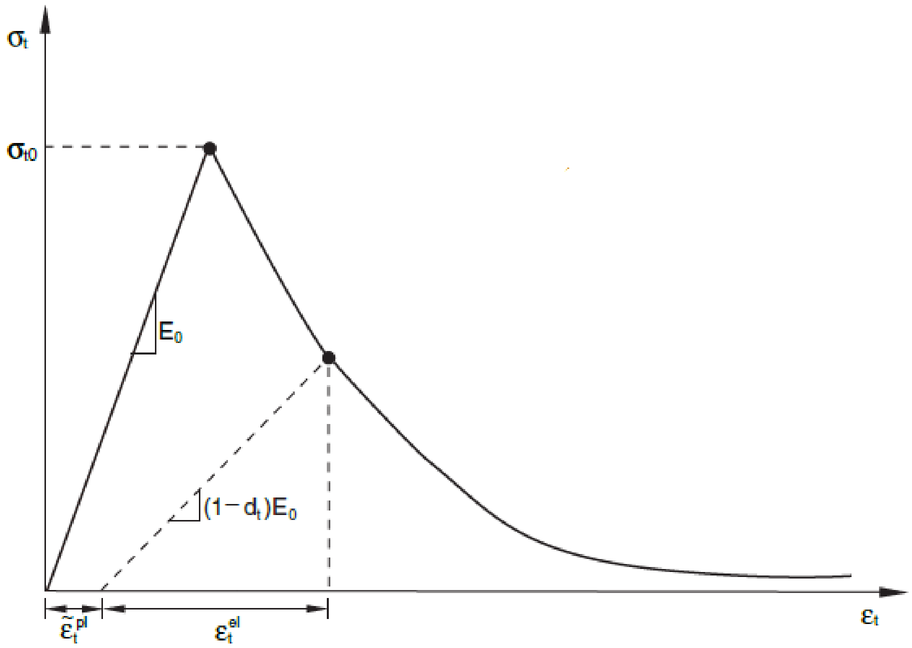

Figure 6.1: Variation of tension damage parameter d_t (ABAQUS Manual)

Similarly, the compression damage can be calculated as shown in Equation 6.18.

$$d_c = \frac{\int_0^{\tilde{\varepsilon}_c^{pl}} d_c(\tilde{\varepsilon}_c^{pl})}{\int_0^{\tilde{\varepsilon}_{cf}^{pl}} d_c(\tilde{\varepsilon}_c^{pl})} \tag{6.18}$$

The graphical interpretation of equation 6.18 is shown in Figure 6.2.

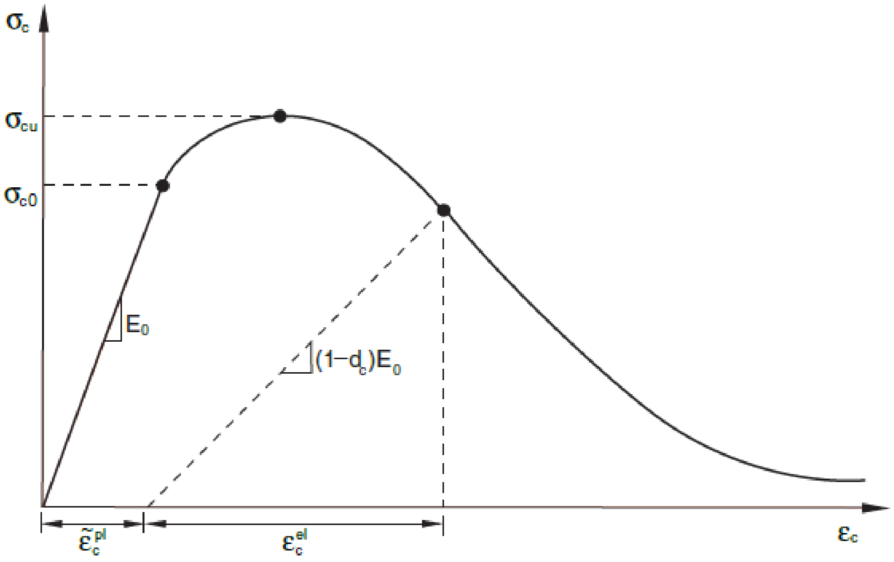

Figure 6.2: Variation of compression damage parameter d_c (ABAQUS Manual)

The uniaxial degradation variables are increasing functions of the equivalent plastic strains. They can take values for the undamaged material ranging from zero to one for the fully damaged material as shown in Figure 6.3.

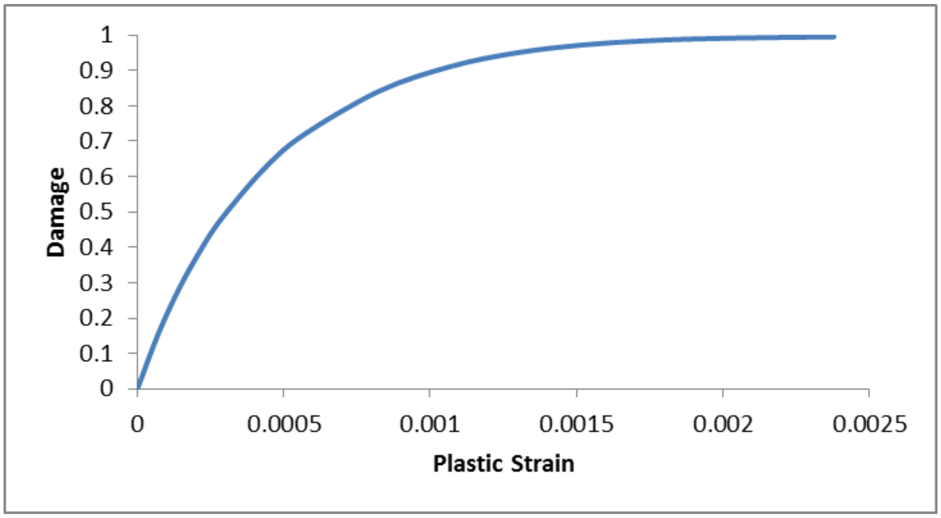

Figure 6.3: Variation damage parameter 'd_c' with respect to effective plastic strain $\tilde{\varepsilon}^{pl}$

If E_o is the initial (undamaged) elastic stiffness of the material, the stress-strain relations under uniaxial tension and compression loading are, respectively:

$$\sigma_t = (1-d_t)E_o(\varepsilon_t - \tilde{\varepsilon}_t^{pl}) \tag{6.19}$$

$$\sigma_c = (1-d_c)E_o(\varepsilon_c - \tilde{\varepsilon}_c^{pl}) \tag{6.20}$$

The effective uniaxial cohesion stresses, $\bar{\sigma}_t$ and $\bar{\sigma}_c$ are given as:

$$\bar{\sigma}_t = \frac{\sigma_t}{(1-d_t)} = E_o(\varepsilon_t - \tilde{\varepsilon}_t^{pl}) \tag{6.21}$$

$$\bar{\sigma}_c = \frac{\sigma_c}{(1-d_c)} = E_o(\varepsilon_c - \tilde{\varepsilon}_c^{pl}) \tag{6.22}$$

The effective uniaxial cohesion stresses determine the size of the yield or failure surface.

6.2.5 Yield Function

The yield function $F(\bar{\sigma}, \tilde{\varepsilon}^{pl})$ represents a surface in effective stress space which determines the state of failure or damage. For the in viscid plastic-damage model the yield function can be expressed as:

$$F(\bar{\sigma}, \tilde{\varepsilon}^{pl}) \leq 0 \tag{6.23}$$

The plastic-damage concrete model uses a yield condition based on the yield function originally proposed by Lubliner et al. (1989) and incorporates the modifications proposed subsequently Lee and Fenves (1998) to account for different evolution of strength under tension and compression. In terms of effective stresses, the yield function takes the form (the classical two-parameter Drucker-Prager model) is a special case of equation 6.24.

$$F\left(\bar{\sigma}, \tilde{\varepsilon}^{pl}\right) = \frac{1}{1-\alpha}\left(\bar{q} - 3\alpha\bar{p} + \beta\left(\tilde{\varepsilon}^{pl}\right)\left\langle\hat{\bar{\sigma}}_{\max}\right\rangle - \gamma\left\langle-\hat{\bar{\sigma}}_{\max}\right\rangle\right) - \bar{\sigma}_c\left(\tilde{\varepsilon}_c^{pl}\right) \leq 0 \tag{6.24}$$

Where:

α, γ are dimensionless material constants.

$\bar{p}$ is the effective hydrostatic pressure.

$$\bar{p} = -\frac{1}{3}\bar{\sigma}_{ii} = -\frac{1}{3}\bar{I}_1 \tag{6.25}$$

$\bar{q}$ is the Mises equivalent effective stress.

$$\bar{q} = \sqrt{\frac{3}{2}\bar{s}_{ij}s_{ij}} = \sqrt{3\bar{J}_2} \tag{6.26}$$

$\bar{s}_{ij}$ is the deviatoric component of effective stress $\bar{\sigma}$.

$\hat{\bar{\sigma}}_{\max}$ is the algebraically maximum eigenvalue of $\bar{\sigma}$.

The function $\beta\left(\tilde{\varepsilon}^{pl}\right)$ is given as:

$$\beta\left(\tilde{\varepsilon}^{pl}\right) = \frac{\bar{\sigma}_c\left(\tilde{\varepsilon}_c^{pl}\right)}{\bar{\sigma}_t\left(\tilde{\varepsilon}_t^{pl}\right)}\left(1-\alpha\right) - \left(1+\alpha\right) \tag{6.27}$$

$\bar{\sigma}_c, \bar{\sigma}_t$ are the effective stresses in compression and tension, respectively, and obtained from simple material testing i.e. uniaxial tension and compression and expressed as:

$$\bar{\sigma}_c\left(\tilde{\varepsilon}_c^{pl}\right) = \frac{\sigma_c}{(1-d_c)} = E_o(\varepsilon_c - \tilde{\varepsilon}_c^{pl}) \tag{6.28}$$

$$\bar{\sigma}_t\left(\tilde{\varepsilon}_t^{pl}\right) = \frac{\sigma_t}{(1-d_t)} = E_o(\varepsilon_t - \tilde{\varepsilon}_t^{pl}) \tag{6.29}$$

The $\beta\left(\tilde{\varepsilon}^{pl}\right)$ parameter controls the size of the yield surface in regions where $\hat{\bar{\sigma}}_{\max} \geq 0$ whereas γ controls the shape of the trace of yield surface in the deviatoric plane for stress states of biaxial and tri-axial compression $\hat{\bar{\sigma}}_{\max} \leq 0$.

In biaxial compression, with $\hat{\bar{\sigma}}_{\max} = 0$, equation 6.24 reduces to the well-known Drucker-Prager yield condition. By applying yield criteria given in equation 6.24 for uniaxial compression and equal biaxial compression (where, $\hat{\bar{\sigma}}_{\max} = 0$) and we can get α:

$$\alpha = \frac{\left(\sigma_{b0}/\sigma_{c0}\right)-1}{2\left(\sigma_{b0}/\sigma_{c0}\right)-1} \tag{6.30}$$

where:

σ_{c0} is compressive strength of concrete under uniaxial compression.

σ_{b0} is compressive strength of concrete under biaxial compression.

Where α ranges from 0.08 to 0.12 and σ_{b0}/σ_{c0} are in between 1.10 to 1.16 for concrete Lubliner et al. (1989).

The coefficient γ contributes only if there is tri-axial compression when $\hat{\bar{\sigma}}_{\max} \leq 0$ and can be found by comparing the yield conditions along the tensile and compressive meridians. By definition, the Tensile Meridian (TM) is the locus of stress states satisfying the condition $\hat{\bar{\sigma}}_{\max} = \hat{\bar{\sigma}}_1 = \hat{\bar{\sigma}}_2 \geq \hat{\bar{\sigma}}_3$, and the Compressive Meridian (CM) is the locus of stress states such that $\hat{\bar{\sigma}}_{\max} = \hat{\bar{\sigma}}_1 = \hat{\bar{\sigma}}_2 \geq \hat{\bar{\sigma}}_3$, where $\hat{\bar{\sigma}}_1, \hat{\bar{\sigma}}_2$ and $\hat{\bar{\sigma}}_3$ are the eigenvalues of the effective stress tensor.

One may show in general:

$$\bar{s}_1 = \frac{2}{\sqrt{3}}\sqrt{\bar{J}_2}\cos\theta \tag{6.31}$$

$$\bar{s}_2 = \frac{2}{\sqrt{3}}\sqrt{\bar{J}_2}\cos\theta\left(\frac{2\pi}{3}-\theta\right) \tag{6.32}$$

$$\bar{s}_3 = \frac{2}{\sqrt{3}}\sqrt{\bar{J}_2}\cos\theta\left(\frac{2\pi}{3}+\theta\right) \tag{6.33}$$

Where $\bar{s}_i$ the principal values of the effective are deviatoric stress tensor $\bar{s}_{ij}$ and θ is the projection angle of $\bar{\sigma}_1$ in the deviatoric plane. For the tension meridian, $\theta = 0$ whereas for the compression meridian $\theta = 60^o$.

Putting the values of θ in expressions for $\bar{s}_i$ and expressing $\bar{\sigma}_1$ in terms of $\bar{s}_1$.

$$\left(\hat{\bar{\sigma}}_{\max}\right)_{TM} = \bar{\sigma}_1 = \bar{s}_1 - \bar{p} = \frac{2}{\sqrt{3}}\sqrt{\bar{J}_2} - \bar{p} = \frac{2\bar{q}}{3} - \bar{p} \qquad (6.34)$$

$$\left(\hat{\bar{\sigma}}_{\max}\right)_{CM} = \bar{\sigma}_1 = \bar{s}_1 - \bar{p} = \frac{1}{\sqrt{3}}\sqrt{\bar{J}_2} - \bar{p} = \frac{\bar{q}}{3} - \bar{p} \qquad (6.35)$$

With $\hat{\bar{\sigma}}_{\max} < 0$, the corresponding yield conditions are:

$$\left(\frac{2}{3}\gamma + 1\right)\bar{q} - \left(\gamma + 3\alpha\right)\bar{p} = \left(1 - \alpha\right)\bar{\sigma}_c \qquad \text{(TM)} \qquad (6.36)$$

$$\left(\frac{1}{3}\gamma + 1\right)\bar{q} - \left(\gamma + 3\alpha\right)\bar{p} = \left(1 - \alpha\right)\bar{\sigma}_c \qquad \text{(CM)} \qquad (6.37)$$

Let $K_c = \bar{q}_{(TM)} / \bar{q}_{(CM)}$ for any given value of the hydrostatic pressure $\bar{p}$ with $\hat{\bar{\sigma}}_{\max} < 0$; then:

$$K_c = \frac{\gamma + 3}{2\gamma + 3} \qquad (6.38)$$

The coefficient γ is, therefore, evaluated as:

$$\gamma = \frac{3\left(1 - K_c\right)}{2K_c - 1} \qquad (6.39)$$

K_c value varies from 0.66 to 0.8 (Lubliner et al., 1989)

If $\hat{\bar{\sigma}}_{\max} > 0$, the yield conditions along the tensile and compressive meridians reduce to:

$$\left(\frac{2}{3}\beta+1\right)\bar{q}-\left(\beta+3\alpha\right)\bar{p}=\left(1-\alpha\right)\bar{\sigma}_c \qquad \text{(TM)} \qquad (6.40)$$

$$\left(\frac{1}{3}\beta+1\right)\bar{q}-\left(\beta+3\alpha\right)\bar{p}=\left(1-\alpha\right)\bar{\sigma}_c \qquad \text{(CM)} \qquad (6.41)$$

Let $K_c=\bar{q}_{(TM)}/\bar{q}_{(\mathrm{C}M)}$ for any given value of the hydrostatic pressure $\bar{p}$ with $\hat{\bar{\sigma}}_{\max}>0$ then:

$$K_t=\frac{\beta+3}{2\beta+3} \qquad (6.42)$$

Typical yield surfaces are shown in Figure 6.4 in the deviatoric plane for $\hat{\bar{\sigma}}_{\max}\leq 0$ and Figure 6.5 shows plane-stress conditions.

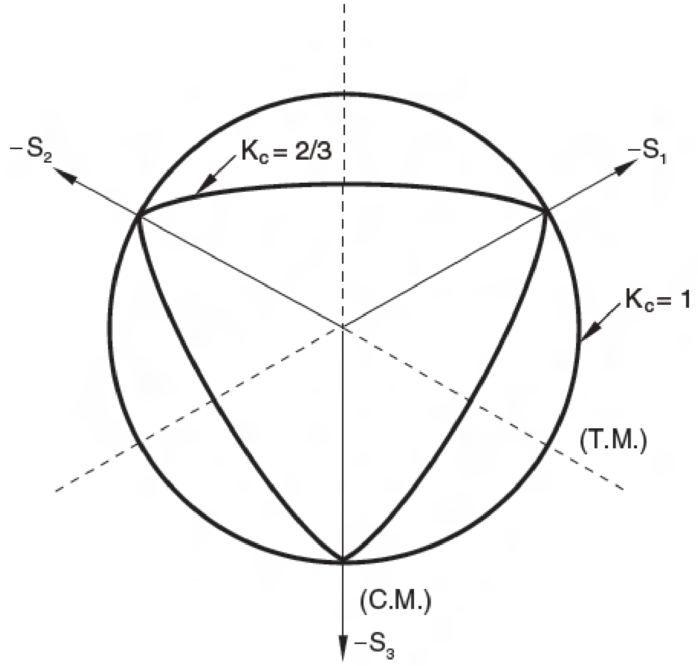

Figure 6.4: Deviatoric plane yield surface for *Kc* (ABAQUS Manual)

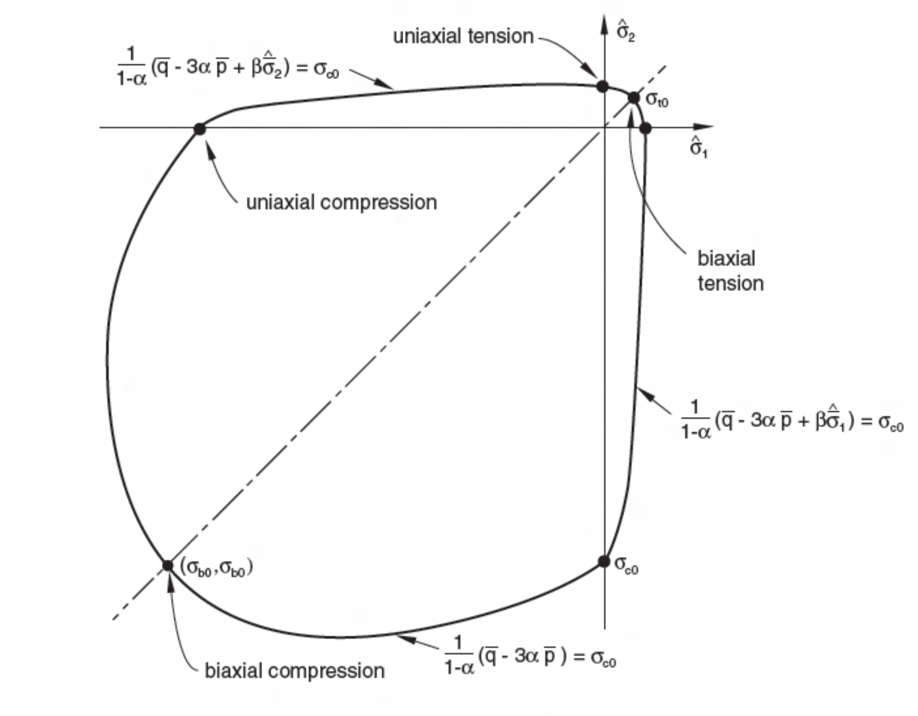

Figure 6.5: Concrete stress yield surface (ABAQUS Manual)

6.2.6 Flow Rule

Plastic flow is governed by a flow potential function $G(\bar{\sigma})$ according to non-associative flow rule:

$$\dot{\varepsilon}^{pl} = \dot{\lambda}\frac{\partial G(\bar{\sigma})}{\partial \bar{\sigma}} \tag{6.43}$$

Where $\dot{\lambda}$ is the non-negative plastic multiplier. The plastic potential is defined in the effective stress space. The model uses non-associated plasticity; therefore, requiring the solution of nonsymmetrical equations. The fundamental group of the constitutive parameters consists of four values, which identify the shape of the potential flow surface and the yield surface. In this model for the flow potential *G*, the Drucker-Prager hyperbolic function is accepted in the form:

$$G = \sqrt{\left(\in \sigma_{t0} \tan \psi\right)^2 + \bar{q}^2} - \bar{p} \tan \psi \tag{6.44}$$

Where, ψ is the dilation angle measured in the *p–q* plane at high confining pressure; σ_{t0} is the uniaxial tensile stress at failure; and $\in$ is a parameter, referred to as the eccentricity, that defines the rate at which the function approaches the asymptote (the flow potential tends to a straight line as the eccentricity tends to zero). This flow potential, which is continuous and smooth, ensures that the flow direction is defined uniquely.

6.3 SMA (Nitinol) VUMAT Subroutine

The behavior of SMA is very difficult to model numerically. Recently different models have been proposed by Pelton (1994), Aurricchio (1996, 1997) and Qidwai (2000) to model the behavior of SMAs. Most of these models are used for modeling of uniaxial behavior of SMA which is relatively straightforward as compared to the 3D stress-strain behavior. To model the behavior of SMAs sheet a user defined subroutine VUMAT was used to model the behavior. VUMAT was written based on the work proposed by Aurricchio et al. (1997). The model follows the concept of Lubliner (1996) generalized plasticity. The total strain is decomposed in to elastic strain and transformation strain as shown in equation 6.45.

$$\Delta\varepsilon = \Delta\varepsilon^{el} + \Delta\varepsilon^{tr} \tag{6.45}$$

The transformation strain from austenite to martensite is given in equation 6.46.

$$\Delta\varepsilon^{tr} = a\Delta\zeta \frac{\partial F}{\partial \sigma} \tag{6.46}$$

Where, ζ is the fraction of martensite and F is a transformation potential. This is also true for backward transformation from martensite to austenite but only the stress levels are different.

The transformation intensity follows the stress potential law as given in equation 6.47.

$$\Delta\zeta = f(\sigma,\zeta)\Delta F \tag{6.47}$$

As we know that change in temperature causes shift of stress levels in which transformation can occurs. To model this shift linear Drucker-Prager approach can be used to transformation potential which is given equation 6.48.

$$F = \bar{\sigma} - p\tan\beta + CT \tag{6.48}$$

Where p, T, β and C is the pressure, temperature and material parameters and $\bar{\sigma}$ is the von-Mises yield stress. The material parameters can be determined from direct uniaxial tension test. The superelastic-plastic behavior of SMAs based on uniaxial test and loading and unloading behavior for VUMAT used is shown in Figure 6.6 and Figure 6.7

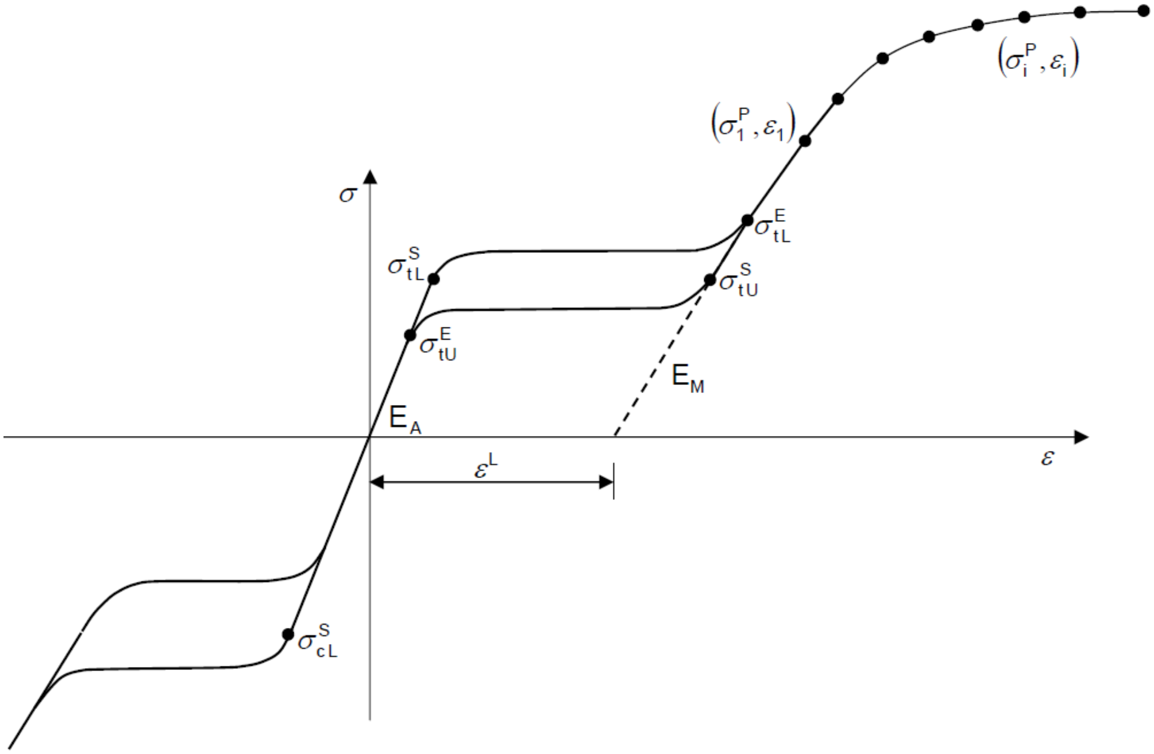

Figure 6.6: Superelastic-plastic behavior of SMAs based on uniaxial test

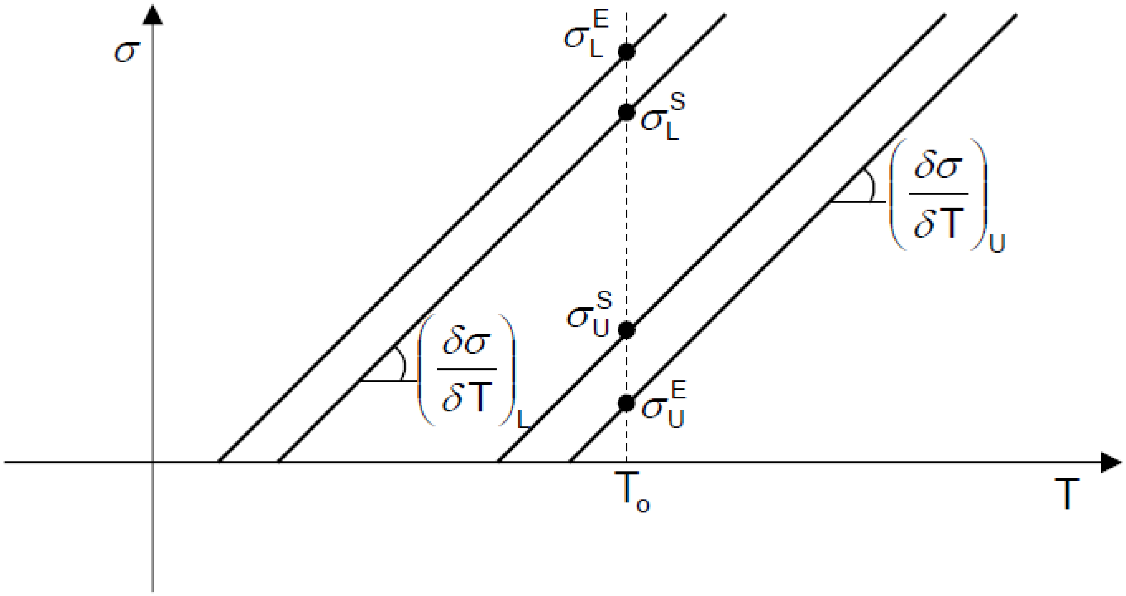

Figure 6.7: Loading and Unloading behavior of SMAs

For superelastic behavior 14 material constants are required. Following are the material constant required for VUMAT

E_A : Austenite Elasticity

ν_A : Austenite Poison ratio

E_M : Martensite Elasticity

ν_M : Martensite Poison ratio

ε^L : Transformation strain

$\left(\frac{\delta\sigma}{\delta T}\right)_L$: Rate of change of stress corresponding to temperature during loading

σ_L^S : Start of transformation loading

σ_L^E : End of transformation loading

T_O : Reference temperature

$\left(\frac{\delta\sigma}{\delta T}\right)_U$: Rate of change of stress corresponding to temperature during unloading

σ_U^S : Start of transformation unloading

σ_U^E : End of transformation unloading

σ_{CL}^S : Start of transformation stress during loading in compression, as a positive value

ε_V^L : Volumetric transformation strain

6.4 Beam-Column Joint Modeling in ABAQUS

3D non-linear finite element models were created for control and retrofitted specimens using ABQUS 6.13. The dimensions and boundary conditions were taken similar to the experiment program. Figure 6.8 shows the model of BCJ-M, BCJ-CL and BCJ-RC in ABAQUS. Figure 6.9 shows the model of BCJ-CLIS in ABAQUS. Figure 6.10 shows the model of BCJ- RC4S, BCJ-RC2S and BCJ-RCXS in ABAQUS.

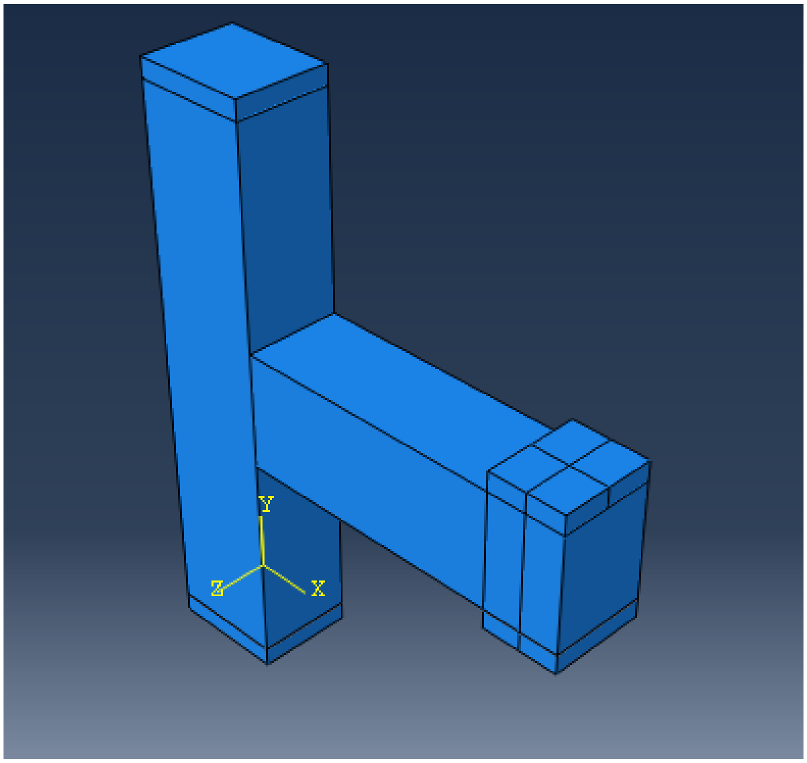

Figure 6.8: Control specimens model in ABAQUS

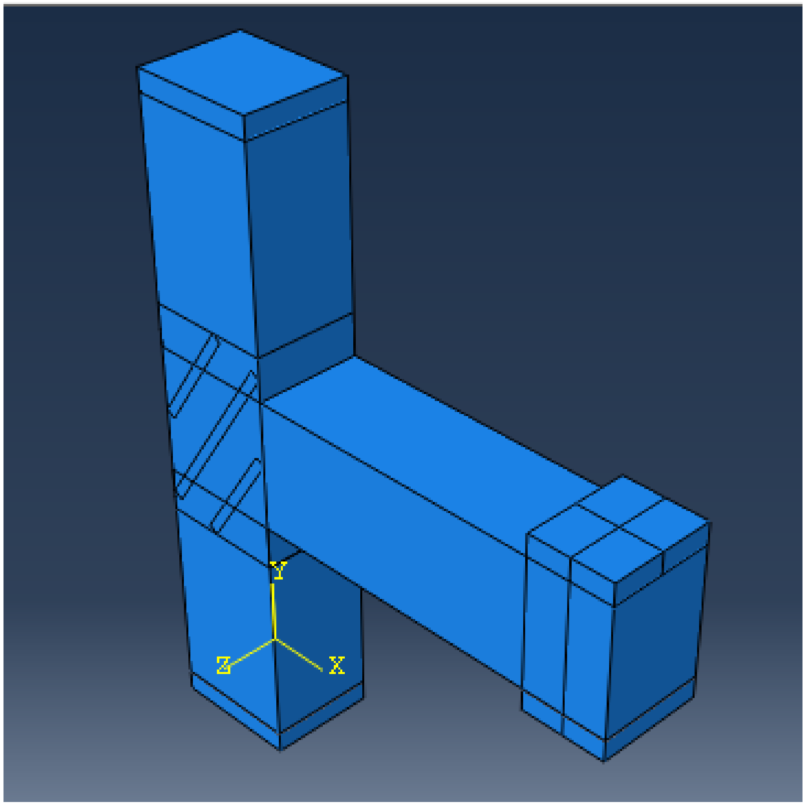

Figure 6.9: BCJ-CLIS model in ABAQUS

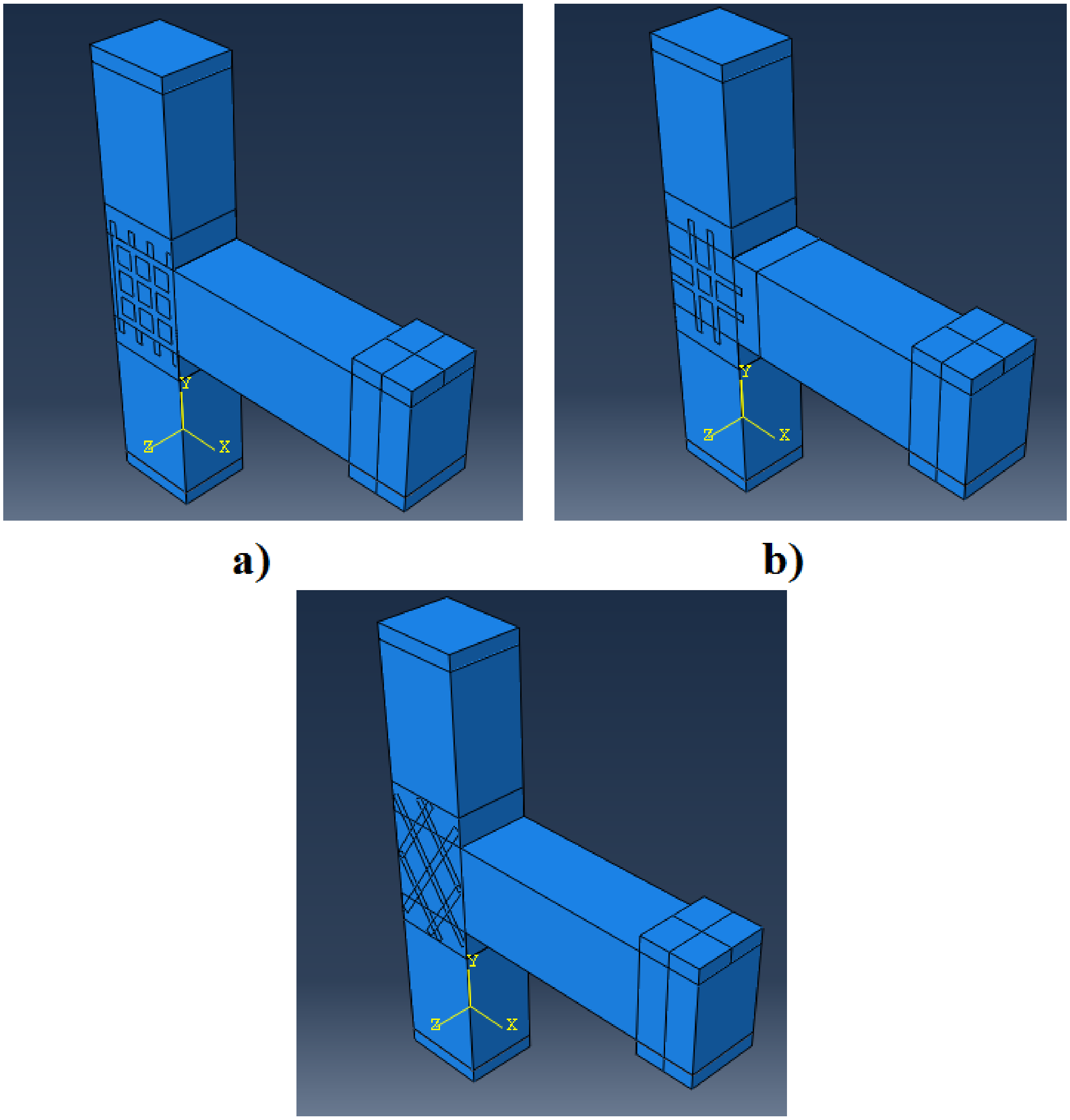

a)

b)

c)

Figure 6.10: a) BCJ-RC4S b) BCJ-RC2S and c) BCJ-RCXS models in ABAQUS

6.5 Material Models

6.5.1 Concrete Damage Plasticity Model

It has been observed in CDP model review that several parameters are required to perform simulation of concrete material in ABAQUS. These parameters were found experimentally and some were took as recommended by Lubliner et al. (1989) and Lee and Fenves (1998). Table 8 gives the CPD model parameters associated with concrete. Also to model the plastic response of the concrete uniaxial stress-plastic strain data for both concrete in compression and tension have been used in the plastic damage model. The actual concrete compressive stress-strain curve under cyclic load was idealized based on Tsai stress-strain curve to get smooth stress-plastic strain response and it is shown in Figure 6.11. Concrete under tension can be modeled using tension softening approach or by tension stiffening approach. In this study concrete under tension was modeled using tension stiffening approach and the stress-plastic strain curve for concrete was obtained using CEB modeling approach is shown in Figure 6.12.

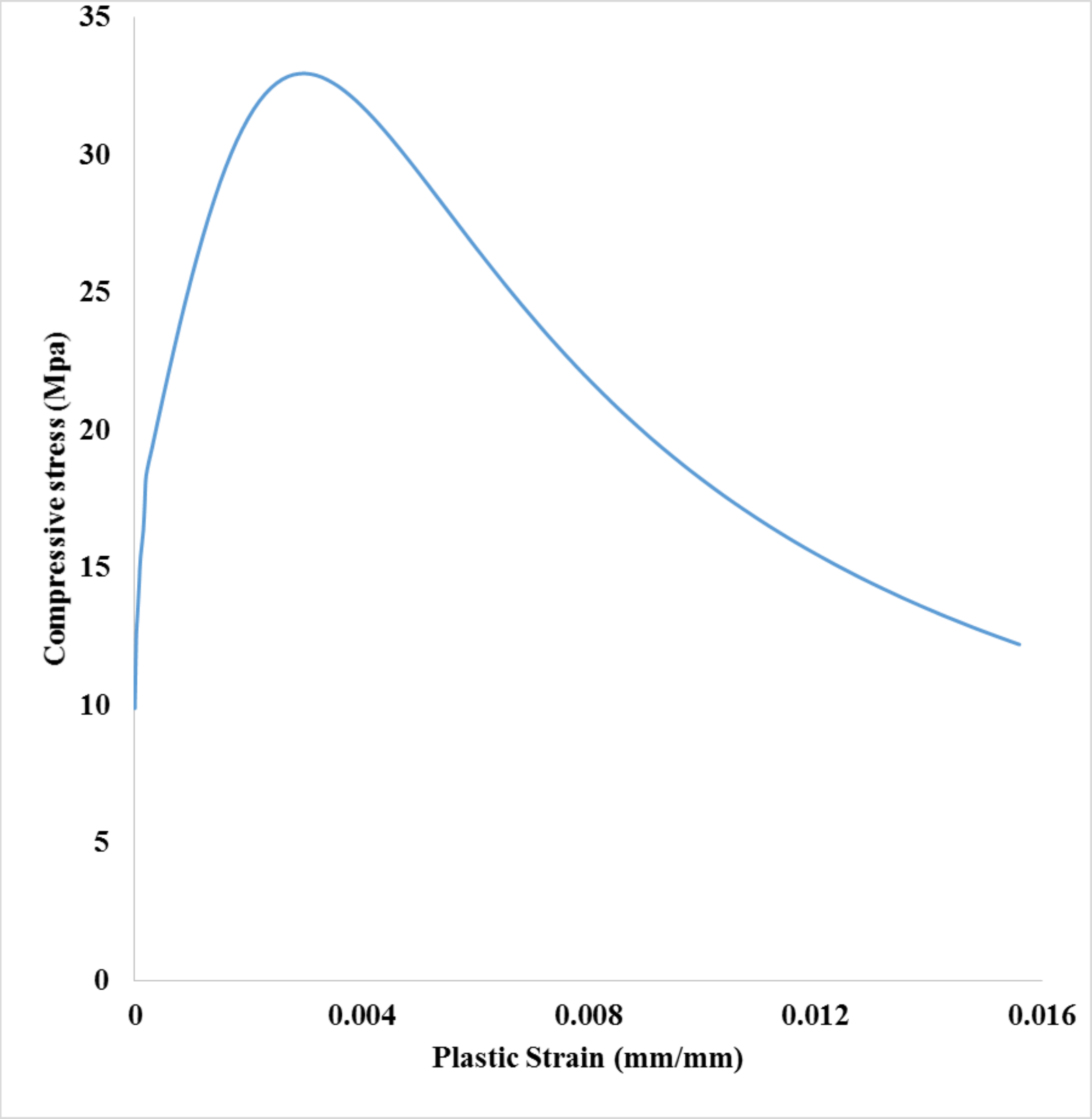

Figure 6.11: Plastic strain vs stress in compression for concrete

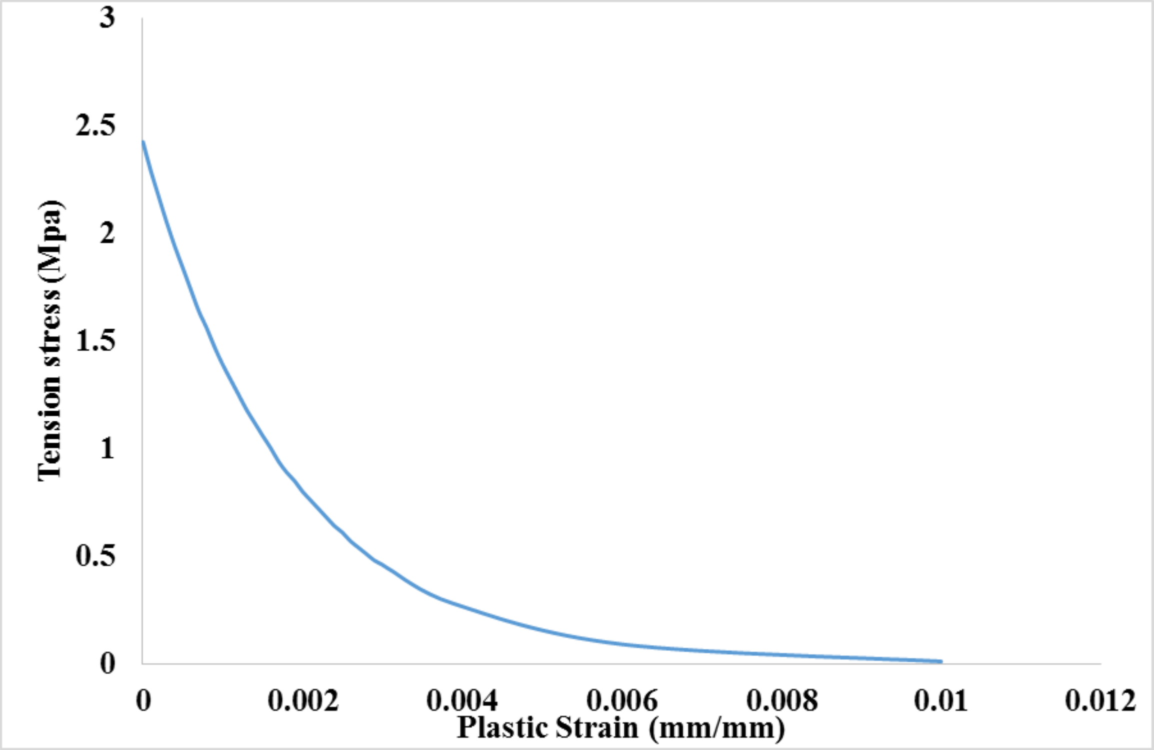

Figure 6.12: Plastic strain vs stress in tension for concrete

The hardening and softening rule is shown in Table 8. The evolution of the compressive and tension damage components d_c and d_t are obtained using equations 6.49 and 6.50 suggested by Birtel and Mark (2006).

$$d_c = 1 - \frac{\sigma_c E_c^{-1}}{\varepsilon_c^{pl}\left(\frac{1}{b_c} - 1\right) + \sigma_c E_c^{-1}} \tag{6.49}$$

$$d_t = 1 - \frac{\sigma_t E_c^{-1}}{\varepsilon_t^{pl}\left(\frac{1}{b_t} - 1\right) + \sigma_t E_c^{-1}} \tag{6.50}$$

Where b_c and b_t are constant factors use for curve fitting upon unloading and range from $0 < b_c, b_t \leq 1$.

Table 8: Concrete Parameters used in Plastic Damage Model

Mass Density (Tone/mm^3)	**Young's Modulus (MPa)**	**Poisson's Ratio**	**Dilation Angle Ψ (Degree)**	**Eccentricity ε**	f_{bo}/f_{co}	**K**
2.4E-009	26987.2	0.19	36	0.1	1.16	0.67

Where:

Ψ: Dilation angle.

ε: Eccentricity which define the flow potential tends to a straight line as the eccentricity tend to zero.

f_{bo}/f_{co} : Ratio of initial biaxial compressive yield stress to initial uniaxial compressive yield stress (the default value is 1.16).

K: is the ratio of the second stress invariant on the tensile meridian (TM) to that on the compressive meridian (CM), the default value is 0.67.

The damage evolution for concrete under tension and compression is shown in Figure 6.13 and Figure 6.14.

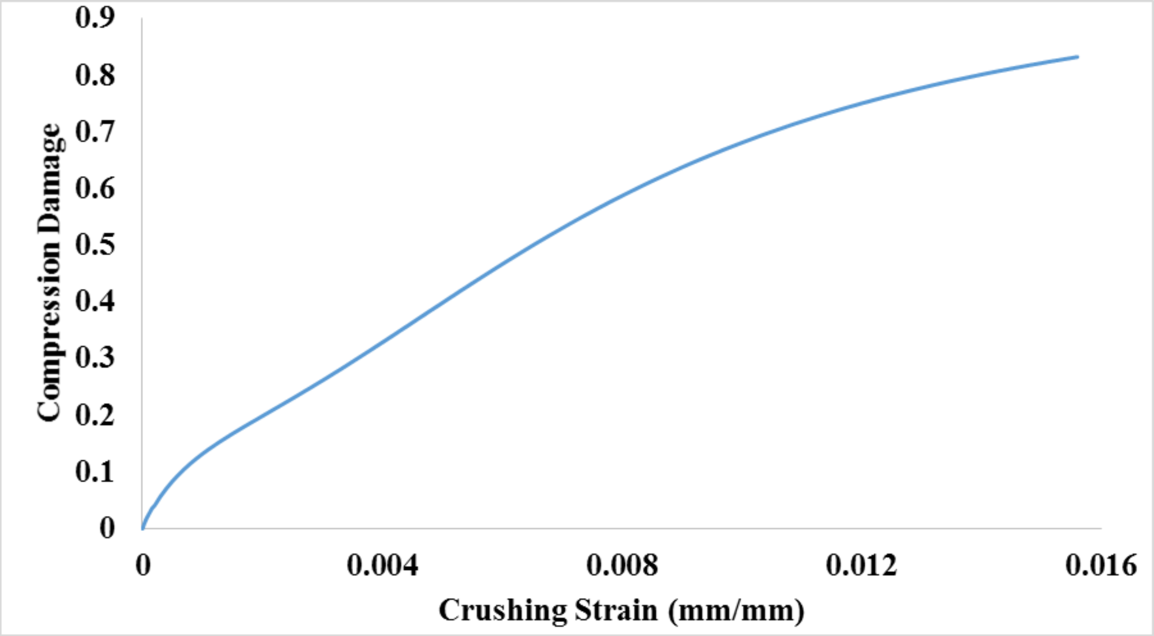

Figure 6.13: Damage evolution for concrete under compression

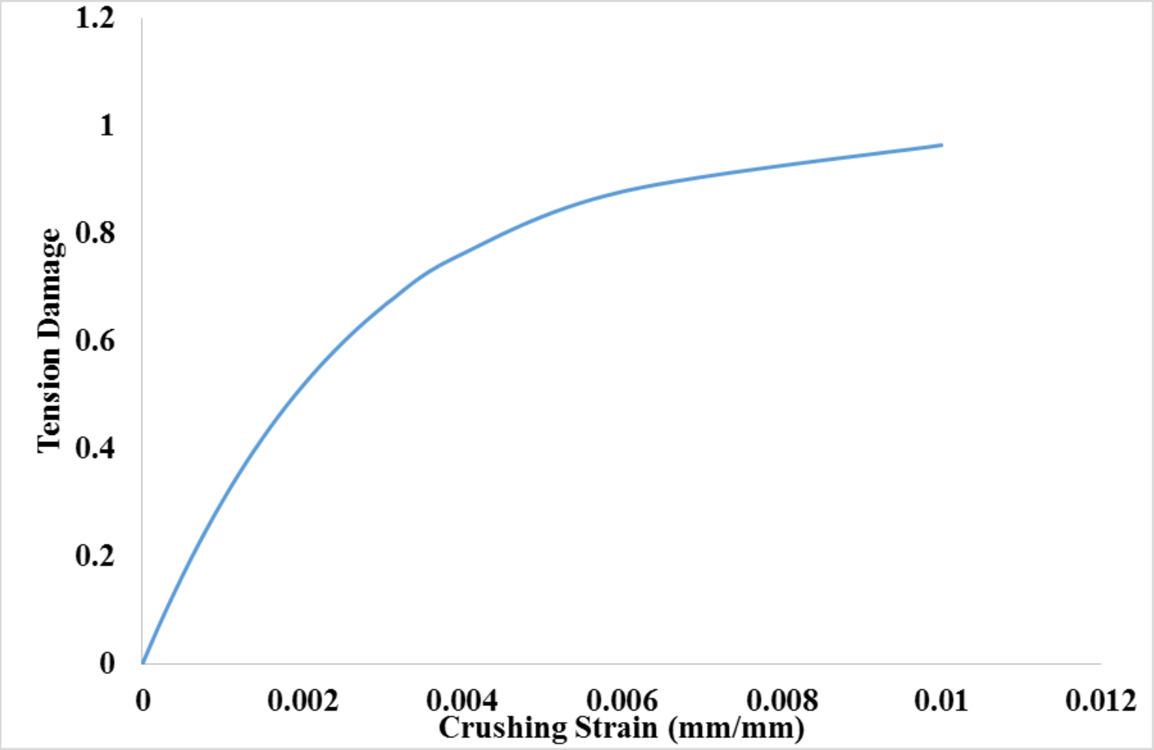

Figure 6.14: Damage evolution for concrete under tension

6.5.2 Steel Reinforcement

In ABAQUS, reinforcement in concrete structures is typically provided by means of rebars, which are one-dimensional rods that can be defined singly or embedded in oriented surfaces. Rebars are typically used with metal plasticity models to describe the behavior of the rebar material and are superposed on a mesh of standard element types used to model the concrete. For steel reinforcement elastic-plasticity with strain hardening was utilized. The stress-plastic strain was obtained from the uniaxial tension test. The stress-strain curve entered in ABAQUS for the 20 dia steel reinforcement is shown in Figure 6.15.

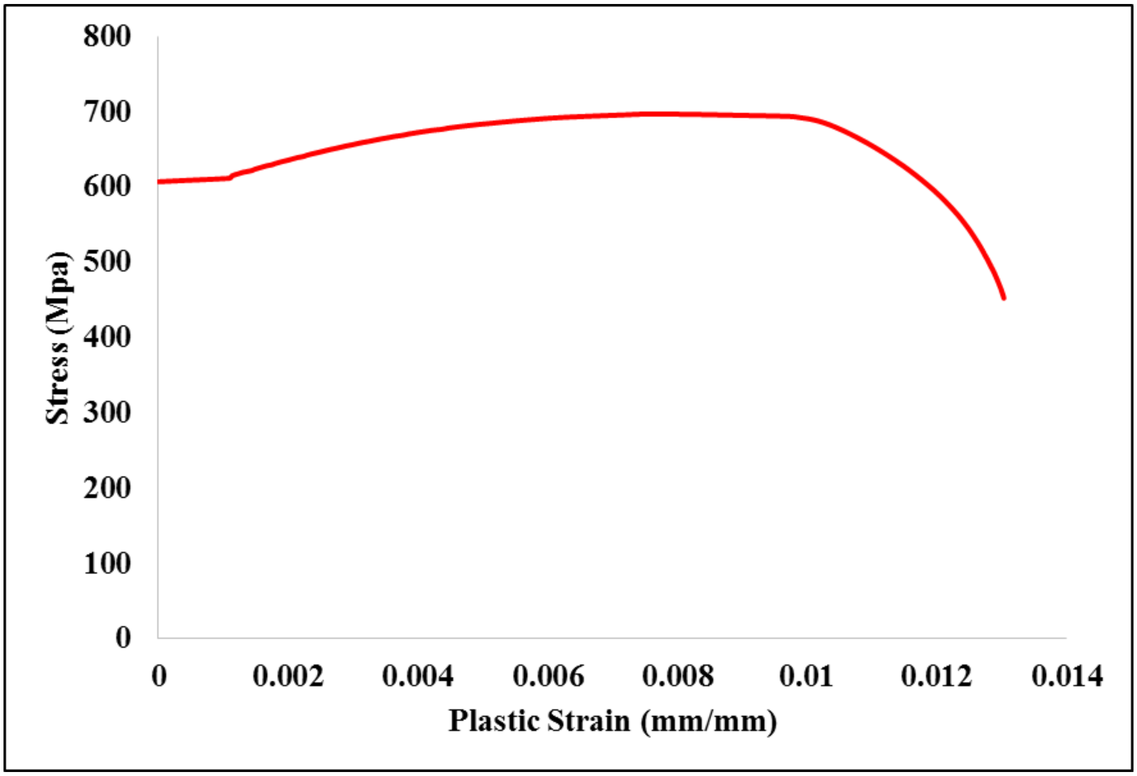

Figure 6.15: Stress-plastic strain for dia 20 mm bar used in ABAQUS

6.5.3 CFRP Material Model

A linear elastic lamina model for CFRP was used to model the CFRP wraps and CFRP vertical strips to hold the SMAs sheets. It has been observed in the experimental study of BCJs there were no failure of bond between concrete and CFRP, so perfect bond was utilized to model the interface of CFRP and concrete. The material properties for CFRP is shown in Table 9.

Table 9: Material properties for CFRP

E_1 (MPa)	**E_2 (MPa)**	v_{12}	G_{12} **(MPa)**	G_{13} **(MPa)**	G_{23} **(MPa)**	σ_u **(MPa)**
70000	7000	0.1	5000	10	10	800

6.5.4 SMAs sheet Material Model

The SMA VUMAT was used to model the behavior of SMAs sheets. The uniaxial stress strain curve for SMAs sheets were obtained from uniaxial cyclic tension test. The experimental uniaxial stress strain curve was idealized and utilized in ABAQUS. Figure 6.16 shows the idealized curve used in ABAQUS for SMAs sheets in ABAQUS. During experimental study some debonding of SMAs sheets were observed from some locations. To get actual response of SMAs sheets cohesive interface was utilized to model the bond of concrete and SMAs sheets using linear elastic traction-separation law. In the linear elastic traction separation model, the behavior can be molded either though coupled or uncoupled low.

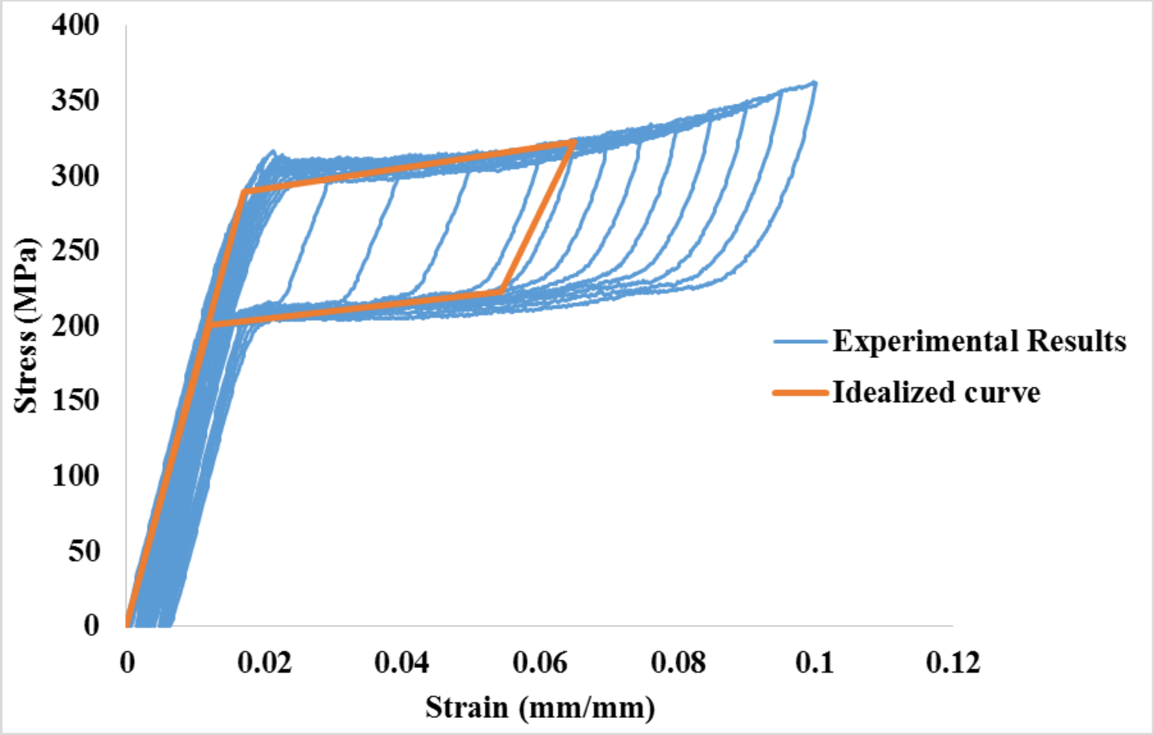

Figure 6.16: Idealized curve up to 6.5 % for SMAs sheets used in ABAQUS

In the coupled low behavior, the traction stress vector is related to the separation vector though a full-populated stiffens matrix as shown in equation 6.51.

$$\begin{Bmatrix} t_n \\ t_s \\ t_t \end{Bmatrix} = \begin{bmatrix} K_{nn} & K_{ns} & K_{nt} \\ K_{ns} & K_{ss} & K_{st} \\ K_{nt} & K_{st} & K_{tt} \end{bmatrix} \begin{Bmatrix} \delta_n \\ \delta s \\ \delta t \end{Bmatrix} = K\delta \qquad (6.51)$$

For the uncoupled behavior, the off diagonal terms are set to be zero as shown in equation 6.52

$$\begin{Bmatrix} t_n \\ t_s \\ t_t \end{Bmatrix} = \begin{bmatrix} K_{nn} & 0 & 0 \\ 0 & K_{ss} & 0 \\ 0 & 0 & K_{tt} \end{bmatrix} \begin{Bmatrix} \delta_n \\ \delta s \\ \delta t \end{Bmatrix} = K\delta \qquad (6.52)$$

For the traction stress vector for separation law was taken uncouple and the values of K_{nn}, K_{ss} and K_{tt} taken for modeling cohesive interaction are shown in Table 10.

Table 10: Stiffness coefficients for cohesive interface

K_{nn} MPa/mm	K_{ss} MPa/mm	K_{tt} MPa/mm
18	32	32

6.6 Element Type, Loads, Meshing and Boundary Condition

Dynamic explicit analysis in ABAQUS was used in this simulation. The element used for each part of the model and description of the element is shown in Table 11. The interaction between the beam-column joint interface and the CFRP was assumed to be perfect bond whereas for SMAs sheets cohesive interface was assumed. Rebars interface were modeled as an embedded (perfect bond) with concrete. Figure 6.17 shows the meshing of control beam column joint.

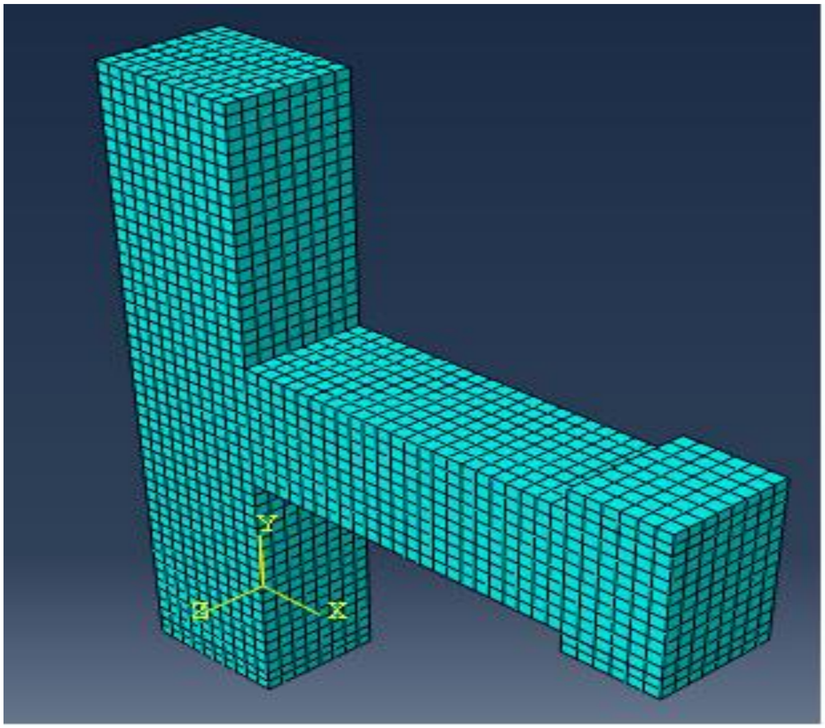

Figure 6.17: Meshing of control specimen model in ABAQUS

The top end of the column surface was constrained in x and z-direction and the bottom end of the column was constrained in x, y, and z -direction. The tip of beam was constrained in y-direction for application of displacement which was taken as 40 mm at which test was stopped for all specimens. A constant axial load of 150 kN was applied on the column as pressure load equal to 2 MPa. Figure 6.18 shows the load and boundary condition for the model. The steel reinforcement model as linear element as shown in Figure 6.19.

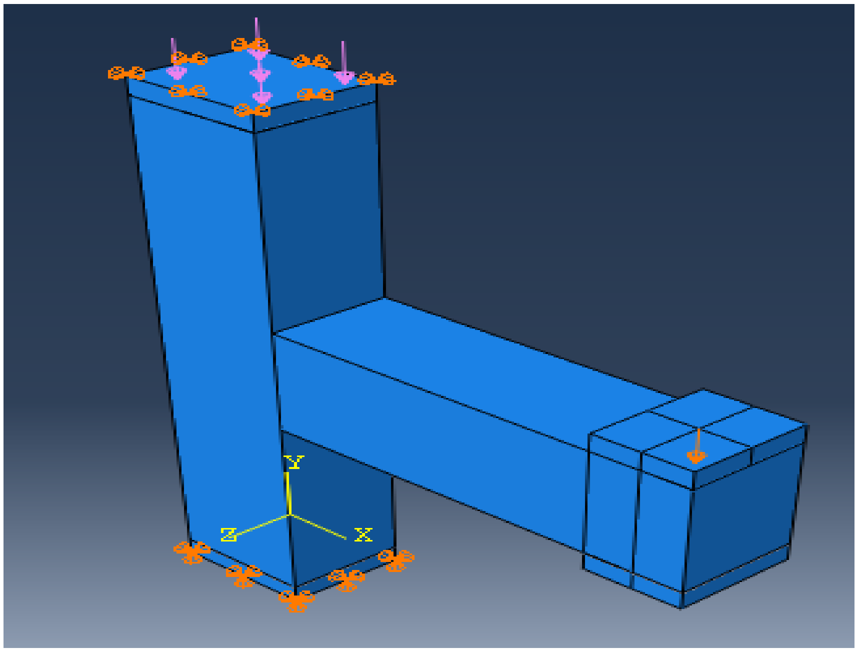

Figure 6.18: Loads and Boundary conditions used in ABAQUS model

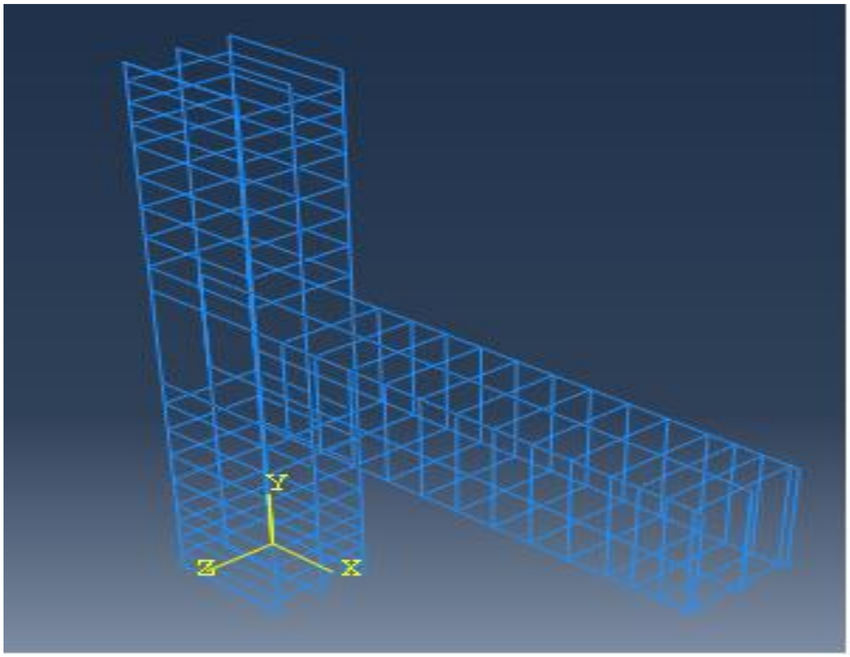

Figure 6.19: Reinforcement modeled in ABAQUS

Table 11: Element used for modeling

Part	Element	Element Description
Concrete	C3D8R	8-node linear brick reduced integration element
Steel Plates	C3D8R	8-node linear brick reduced integration element
Rebars	T3D2	2-node truss element
CFRP	S4R	4-node doubly curved thin or thick shell reduced integration element
SMA sheets	S4R	4-node doubly curved thin or thick shell reduced integration element

6.7 Numerical Simulations of Control Specimens

The aim of FEM simulation was to simulate the load deflection response of all specimens. To achieve this objective number of trials were done to calibrate the material parameters to match the experimental and numerical simulations results. The results of numerical simulations showed good agreement with the experimental result.

6.7.1 Numerical Simulations of BCJ-M

The numerical simulation were done up to the failure of specimen. The beam tip was pushed up to the displacement of 40 mm. Figure 6.20 shows the load-deflection response of FEM simulations and experimental results for BCJ-M.

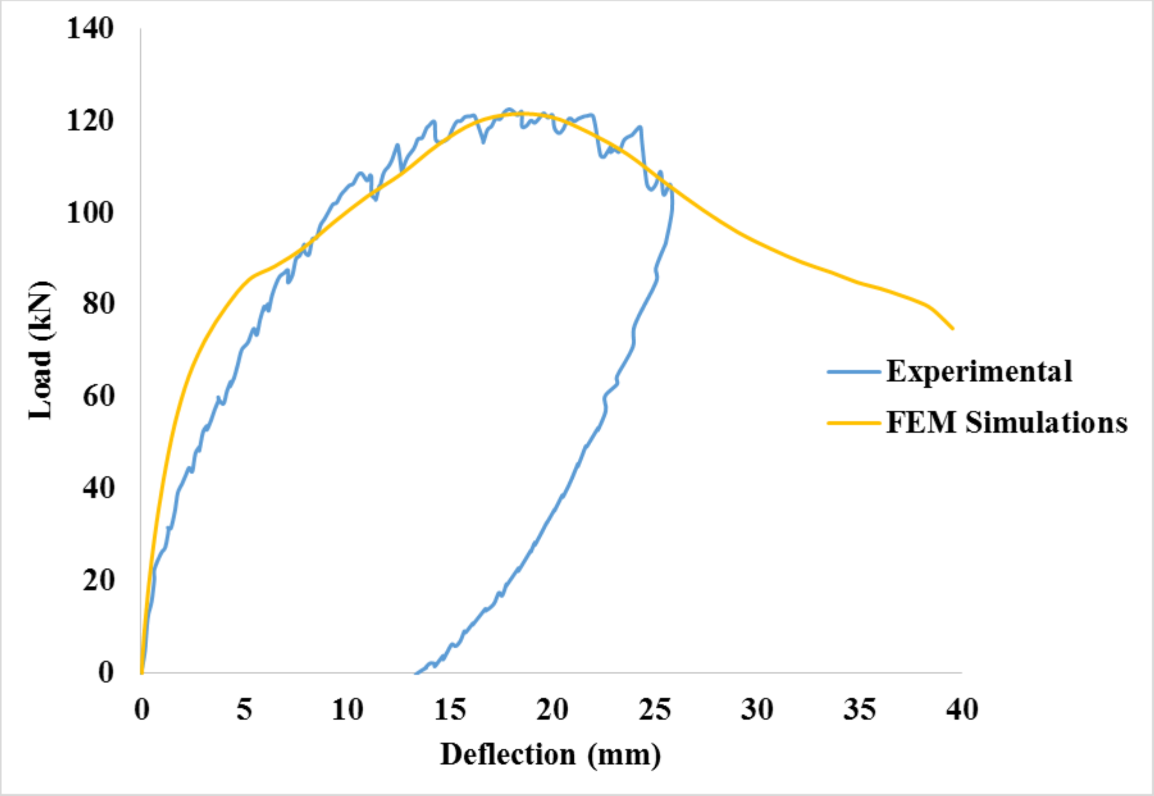

Figure 6.20: Comparison of load-displacement response for BCJ-M

It has been observed that FEM simulations showed good agreement with the experimental results. FEM results were stiffer initially but later on curve matches closely with experimental results. The ultimate load of 121.41 kN was achieved at displacement of 18.11 mm whereas in case of experimental it was 122.46 mm at displacement of 20.46 mm. The maximum stress in steel at ultimate load corresponding to 18.11 mm displacement is shown in Figure 6.21 which clearly indicates that there is no yielding of steel and the maximum stresses in steel was 430 MPa which is lesser than the yield stress of steel. The stress S11, S22 and S12 in concrete are shown in Figure 6.22, Figure 6.23 and Figure 6.24 at ultimate load.

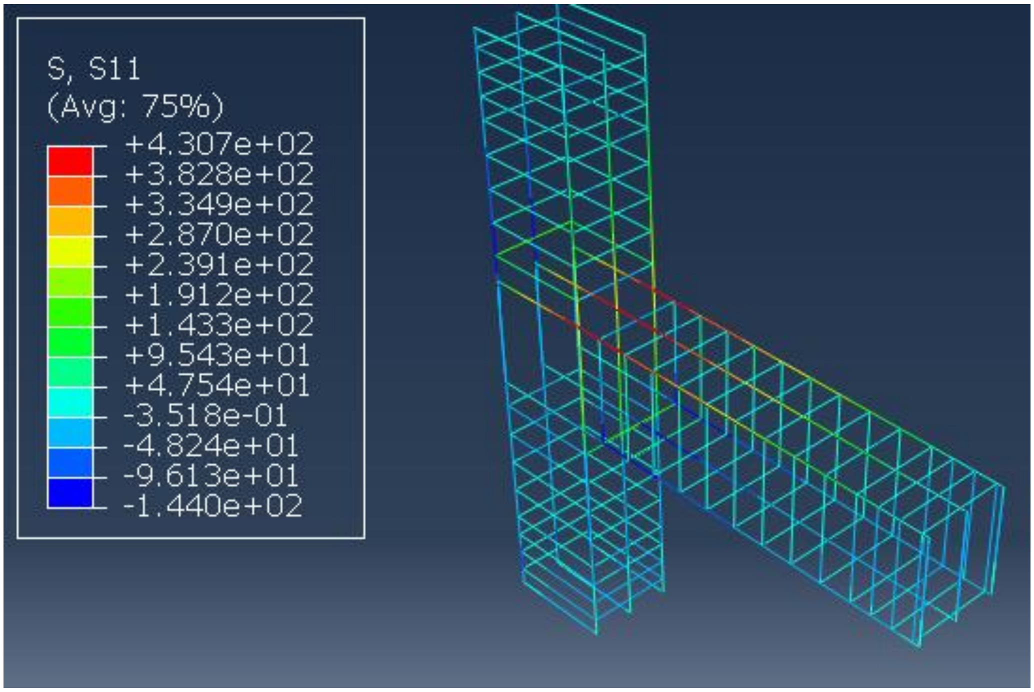

Figure 6.21: Steel stresses at the ultimate load corresponding to 18.18 mm displacement for BCJ-M

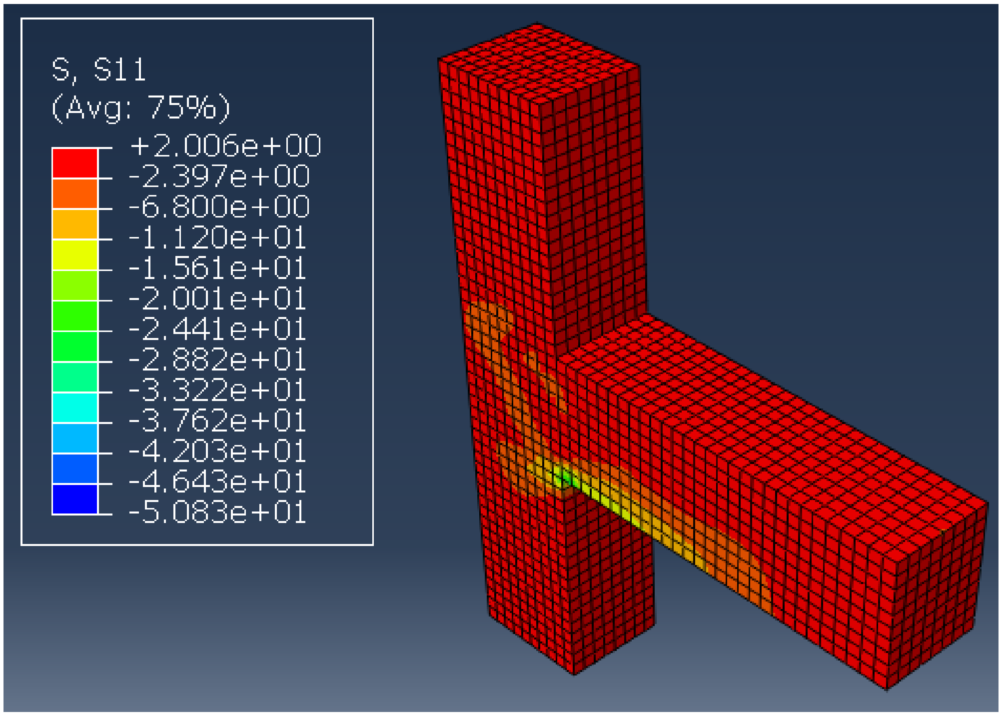

Figure 6.22 : Stress S11 in concrete at the ultimate load corresponding to 18.18 mm displacement for BCJ-M

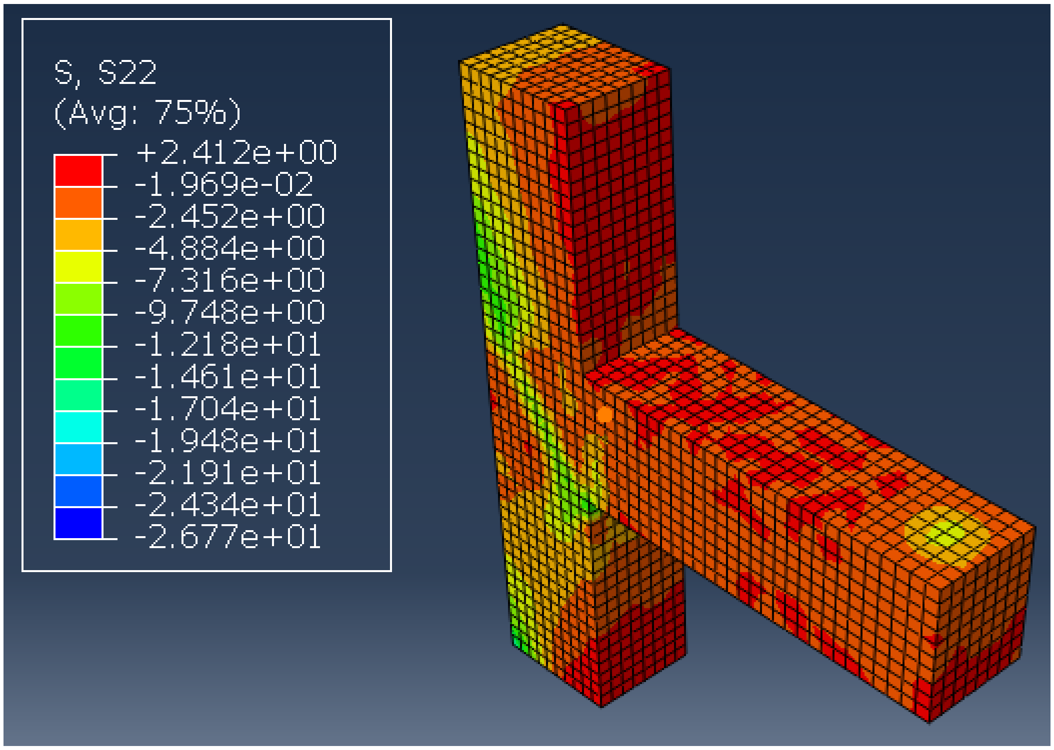

Figure 6.23: Stress S22 in concrete at the ultimate load corresponding to 18.18 mm displacement for BCJ-M

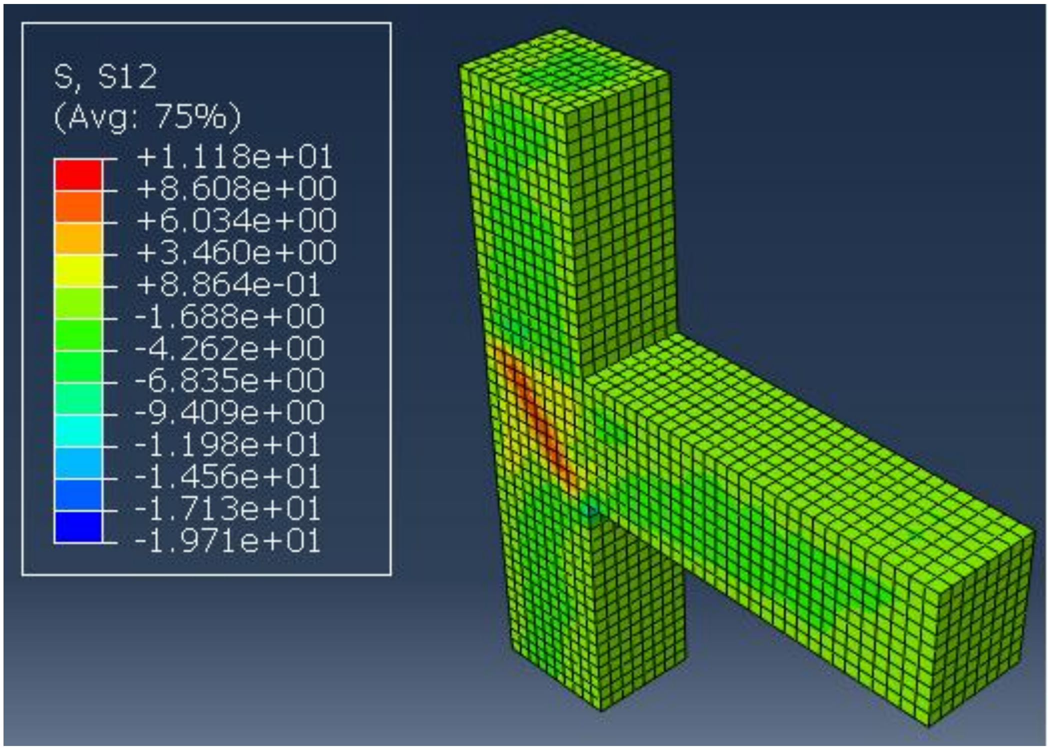

Figure 6.24: Stress S12 in concrete at the ultimate load corresponding to 18.18 mm displacement for BCJ-M

Figure 6.25 shows the damage evolution in concrete at ultimate load. Figure 6.26 shows the comparison of experimental cracks pattern and concrete damage in FEM model for BCJ-M at displacement of 40 mm which shows good agreement.

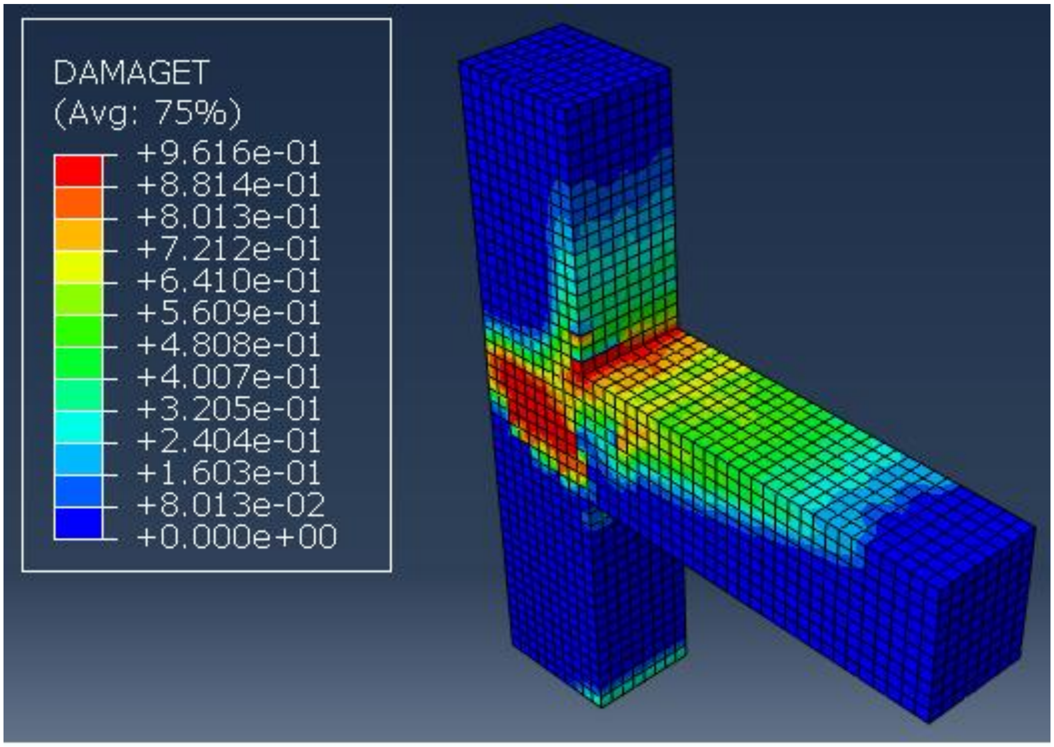

Figure 6.25: Concrete damage at the ultimate load corresponding to 18.18 mm displacement for BCJ-M

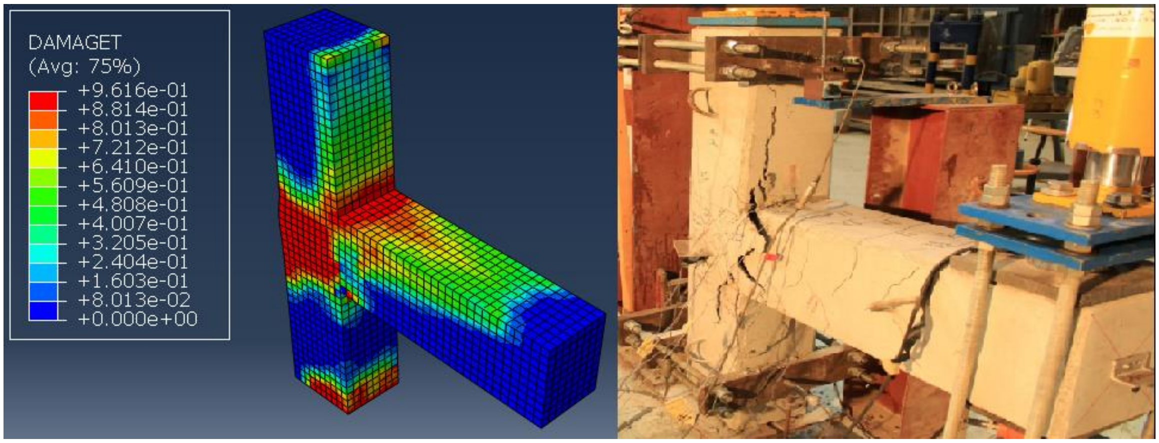

Figure 6.26: Comparison of crack pattern and concrete damage for BCJ-M at displacement of 40 mm

6.7.2 Numerical Simulations of BCJ-CL

It has been reported by many researcher that ABAQUS cannot model pinching hysteresis. To get pinching hysteresis one can use user develop concrete material model and element to get pinching effect. As this study doesn't focus on the developing of user subroutine for concrete, so hysteresis envelopes were model for all specimens under cyclic or reverse cyclic loading. The numerical simulation were done up to the failure of specimen. The beam tip was pushed up to the displacement of 40 mm. Figure 6.27 shows the load-deflection response of FEM simulations and experimental results for BCJ-CL.

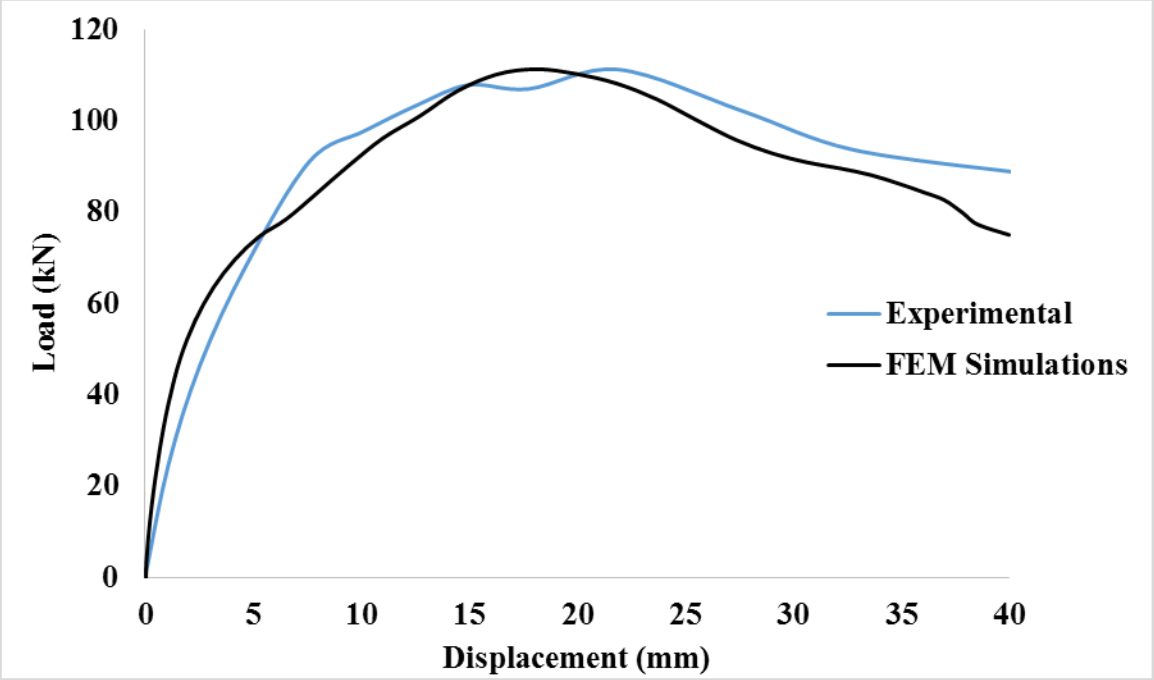

Figure 6.27: Comparison of load-displacement response for BCJ-CL

It has been observed that FEM simulations showed good agreement with the experimental results. FEM results were stiffer initially but later on curve matches closely with experimental results. The ultimate load of 111.33 kN was achieved at displacement of 18.10 mm whereas in case of experimental it was 111.25 mm at displacement of 21.93 mm. The maximum stress in steel at ultimate load corresponding to 18.10 mm displacement is shown in Figure 6.28 which clearly indicates that there is no yielding of steel and the maximum stresses in steel was 402 MPa which is lesser than the yield stress of steel. The stress S11, S22 and S12 in concrete are shown in Figure 6.29, Figure 6.30 Figure 6.31 at ultimate load.

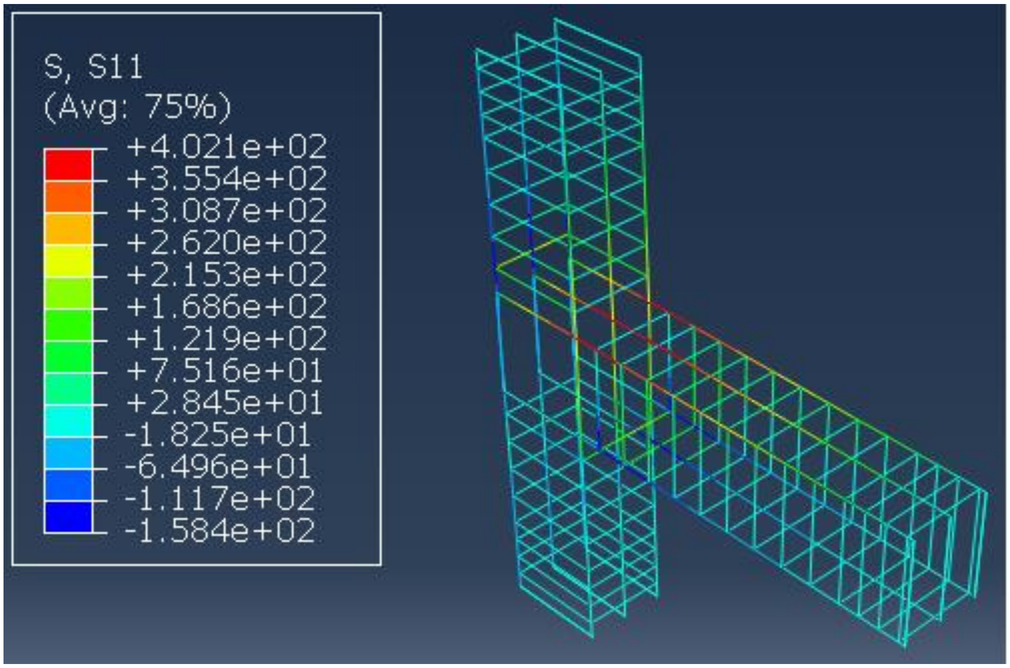

Figure 6.28: Steel stresses at the ultimate load corresponding to 18.10 mm displacement for BCJ-CL

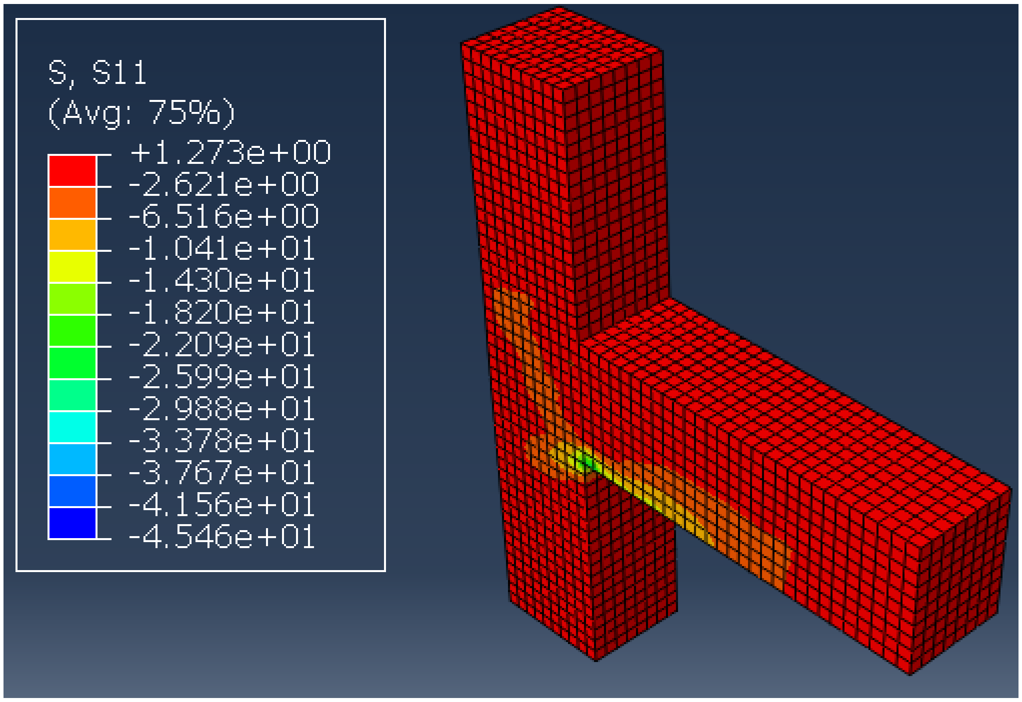

Figure 6.29: Stress S11 in concrete at the ultimate load corresponding to 18.10 mm displacement for BCJ-CL

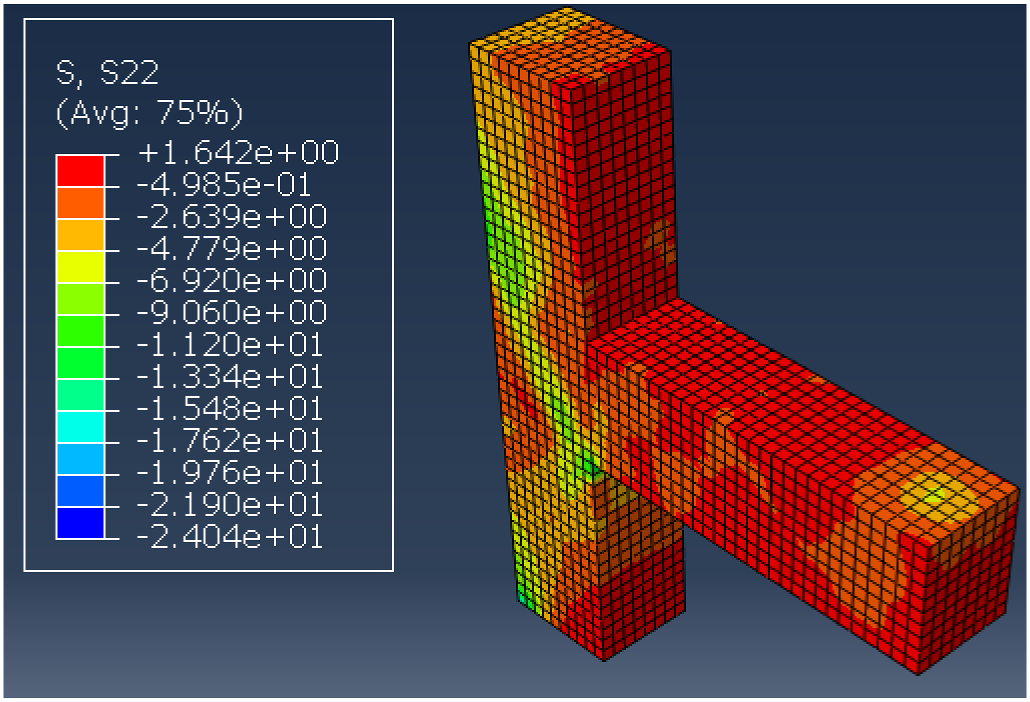

Figure 6.30: Stress S22 in concrete at the ultimate load corresponding to 18.10 mm displacement for BCJ-CL

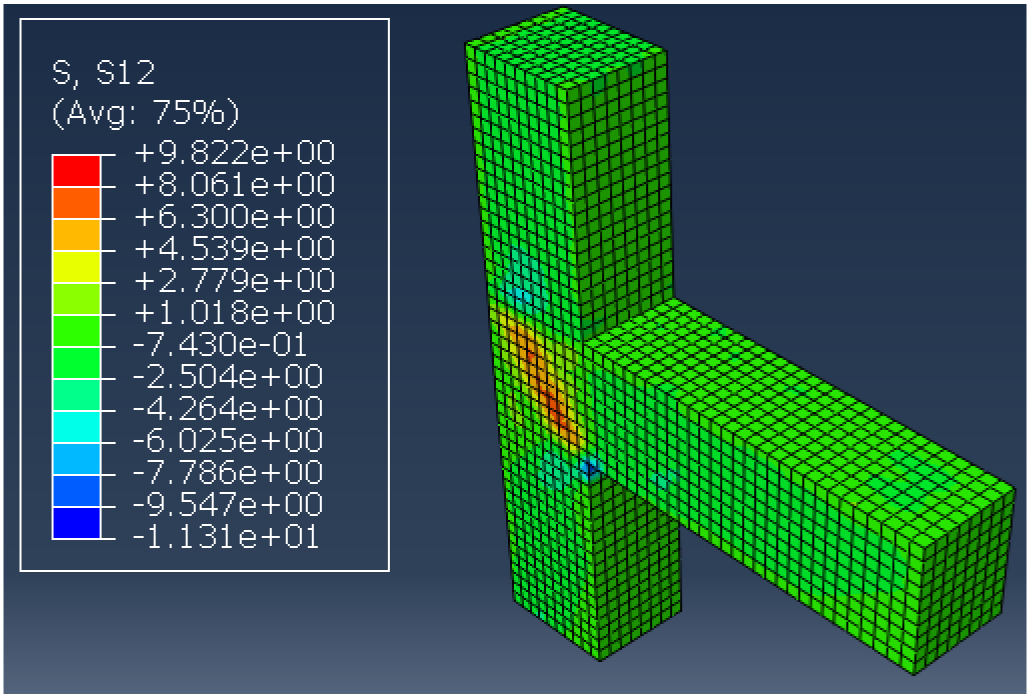

Figure 6.31: Stress S12 in concrete at the ultimate load corresponding to 18.18 mm displacement for BCJ-M

Figure 6.32 shows the damage evolution in concrete at ultimate load. Figure 6.33 shows the comparison of experimental cracks pattern and concrete damage in FEM model for BCJ-CL at displacement of 40 mm which shows good agreement.

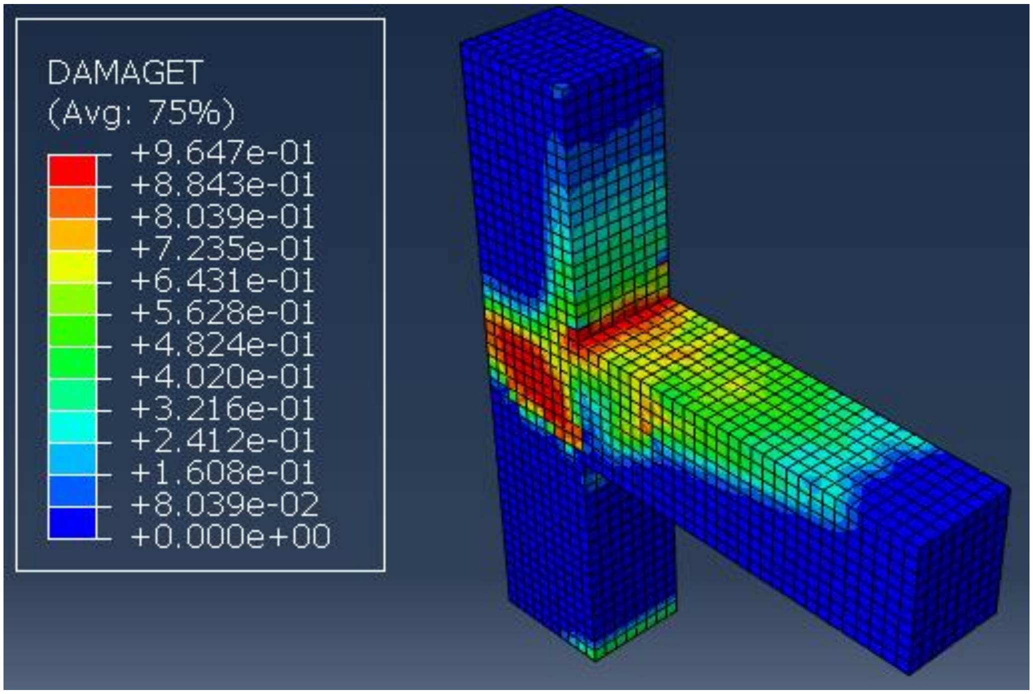

Figure 6.32: Concrete damage at the ultimate load corresponding to 18.10 mm displacement for BCJ-M

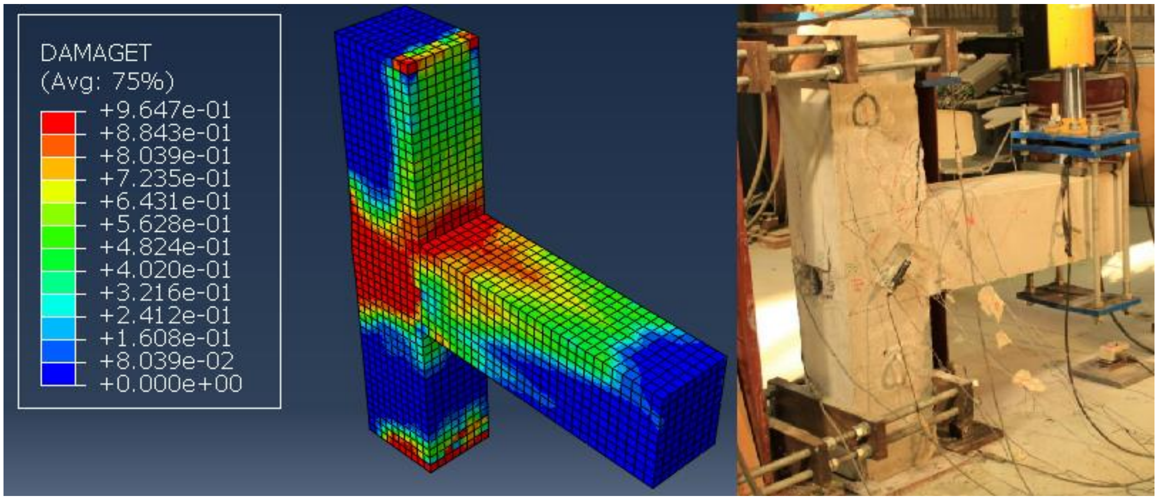

Figure 6.33: Comparison of crack pattern and concrete damage for BCJ-M at displacement of 40 mm

6.7.3 Numerical Simulations of BCJ-RC

It has been reported by many researcher that ABAQUS cannot model pinching hysteresis. To get pinching hysteresis one can use user develop concrete material model and element to get pinching effect. As this study doesn't focus on the developing of user subroutine for concrete, so hysteresis envelopes were model for all specimens under reverse cyclic loading. The numerical simulation were done up to the failure of specimen. The beam tip was pushed up to the displacement of 40 mm. Figure 6.34 shows the load-deflection response of FEM simulations and experimental results for BCJ-RC.

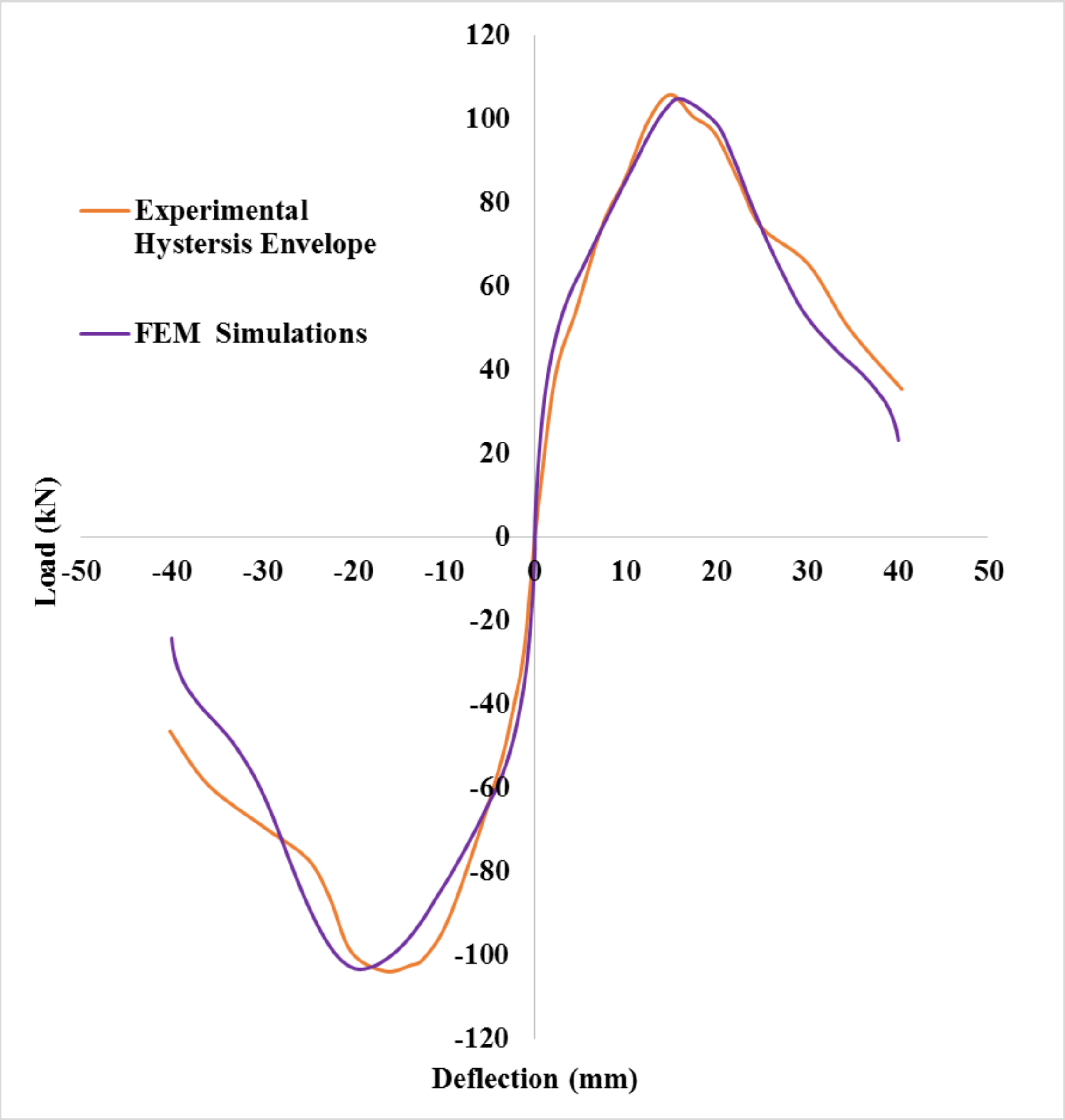

Figure 6.34: Comparison of load-displacement response for BCJ-RC

It has been observed that FEM simulations showed good agreement with the experimental results. FEM results were stiffer initially but later on curve matches closely with experimental results. The ultimate load of 104.72 kN and 103.26 kN was achieved at displacement of 16.24 mm and 19.24 mm whereas in case of experimental it was 105.82 kN and 103.9 kN at displacement of 14.98 mm and 16.52 mm in push and pull directions, respectively. The maximum stress in steel at ultimate load corresponding to 14.98 mm displacement in push direction is shown in Figure 6.35 which clearly indicates that there is no yielding of steel and the maximum stresses in steel was 396 MPa which is lesser than the yield stress of steel. Similarly Figure 6.36 shows the steel stress in pull direction. The stress S11, S22 and S12 in concrete for push direction are shown in Figure 6.37, Figure 6.38 and Figure 6.39 at ultimate load. The stress S11, S22 and S12 in concrete for pull direction are shown in Figure 6.40, Figure 6.41 and Figure 6.42 at ultimate load.

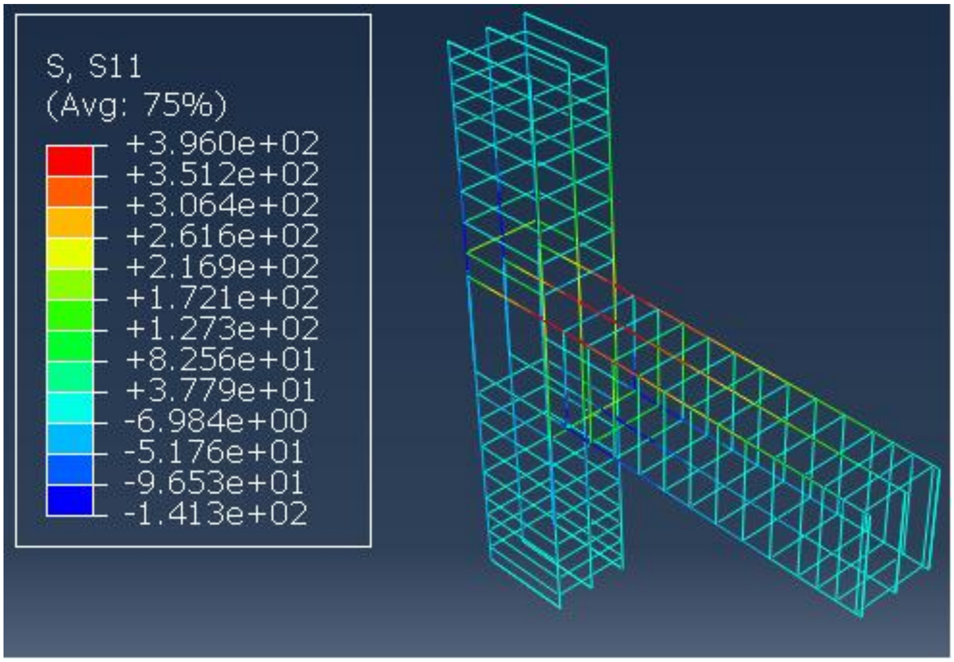

Figure 6.35: Steel stresses at the ultimate load corresponding to 14.98 mm displacement for BCJ-RC in push direction

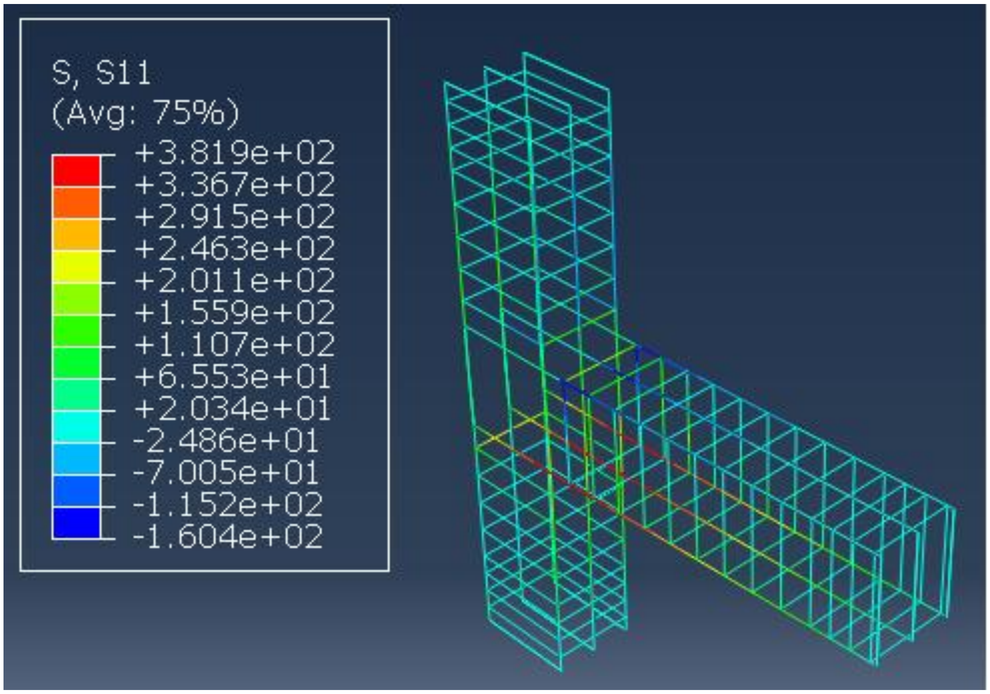

Figure 6.36: Steel stresses at the ultimate load corresponding to 16.52 mm displacement for BCJ-RC in pull direction

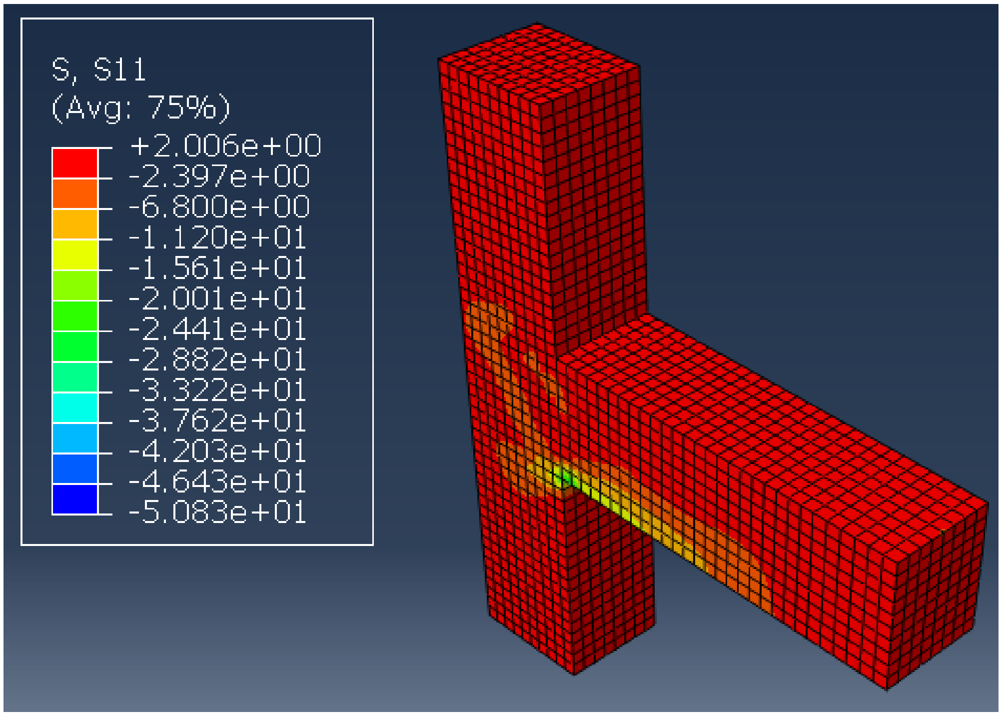

Figure 6.37: Stress S11 in concrete at the ultimate load corresponding to 14.98 mm displacement for BCJ-RC in push direction

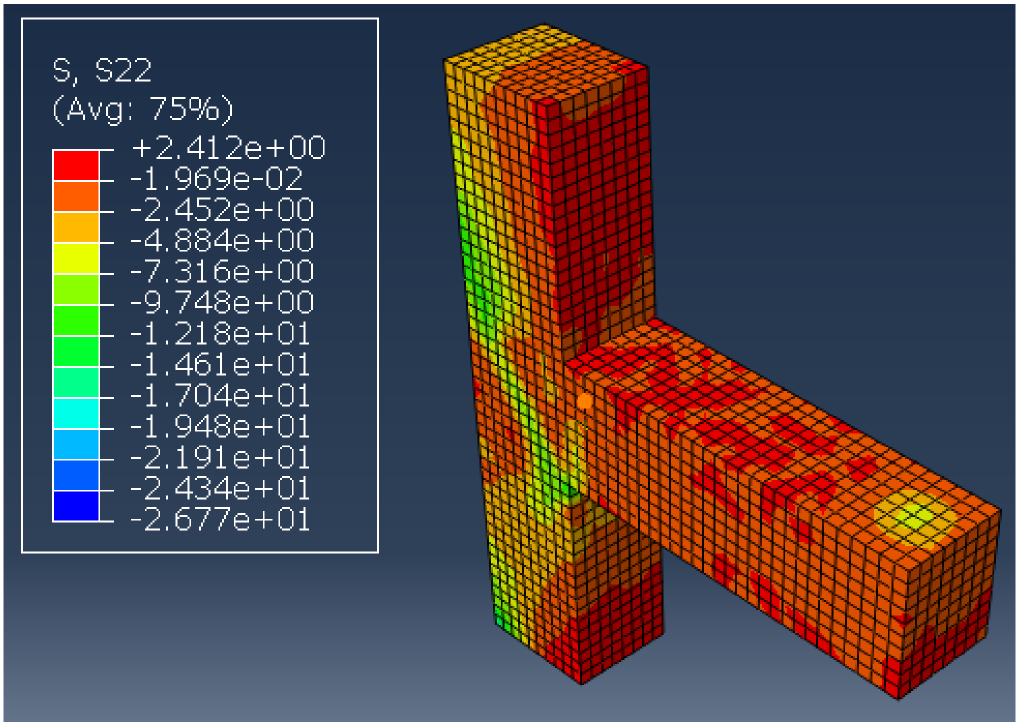

Figure 6.38: Stress S22 in concrete at the ultimate load corresponding to 14.98 mm displacement for BCJ-RC in push direction

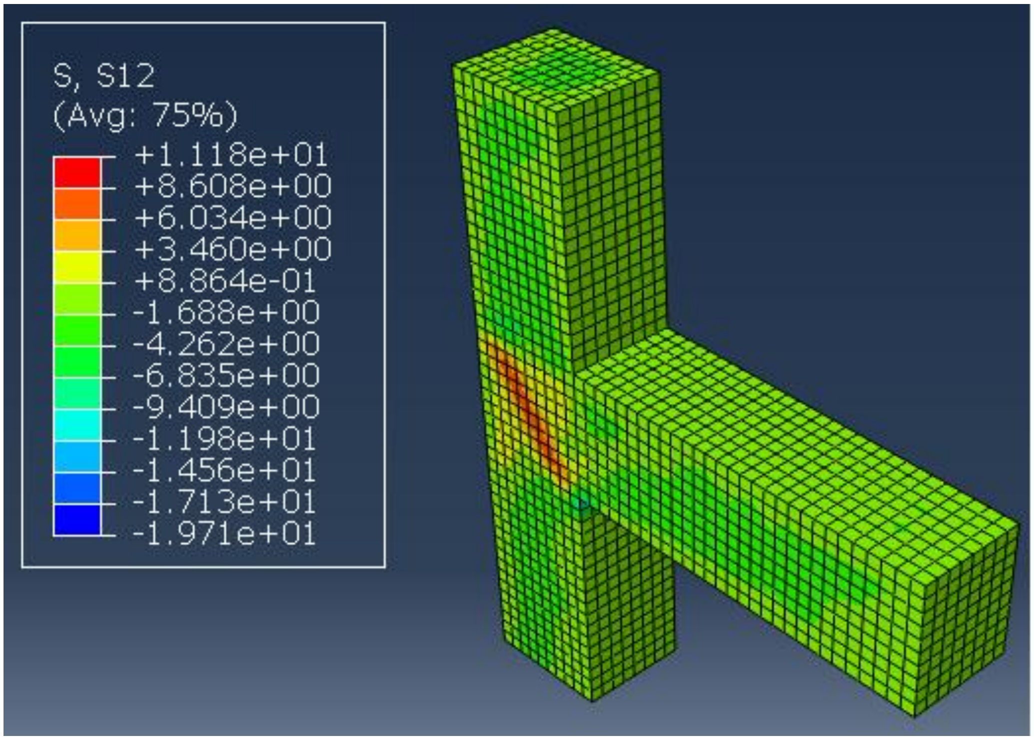

Figure 6.39: Stress S12 in concrete at the ultimate load corresponding to 14.98 mm displacement for BCJ-RC in push direction

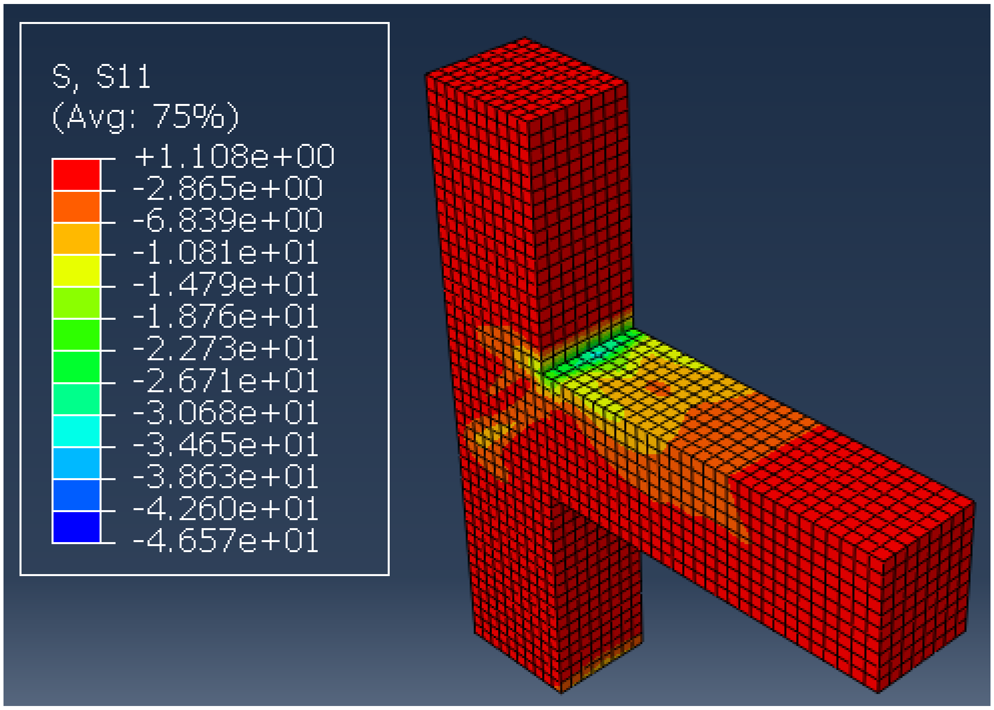

Figure 6.40: Stress S11 in concrete at the ultimate load corresponding to 16.52 mm displacement for BCJ-RC in pull direction

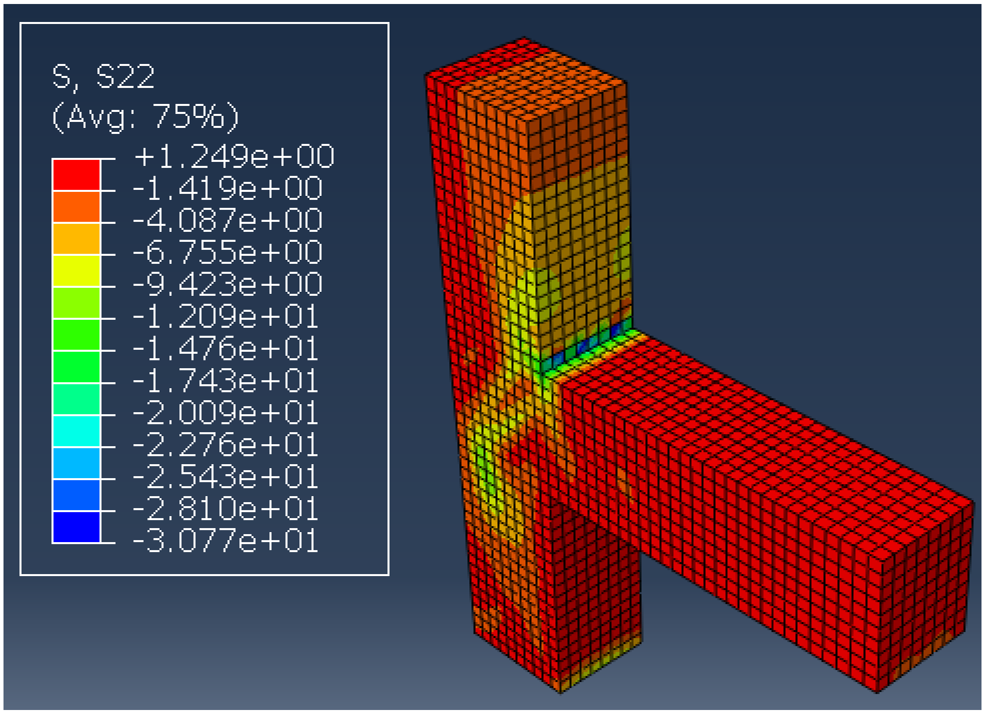

Figure 6.41: Stress S22 in concrete at the ultimate load corresponding to 16.52 mm displacement for BCJ-RC in pull direction

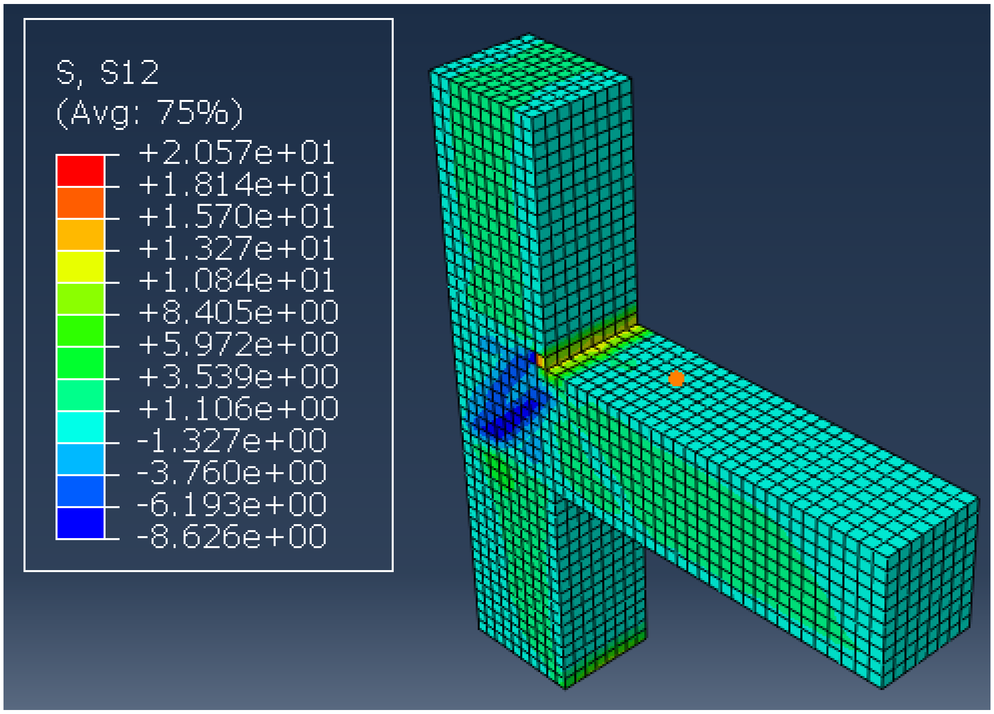

Figure 6.42: Stress S12 in concrete at the ultimate load corresponding to 16.52 mm displacement for BCJ-RC in pull direction

Figure 6.43 shows the damage evolution in concrete at ultimate load in push direction. Figure 6.44 shows the damage evolution in concrete at ultimate load in pull direction. Figure 6.45 shows the comparison of experimental cracks pattern and concrete damage in FEM model for BCJ-RC at displacement of 40 mm in push and pull direction which shows good agreement.

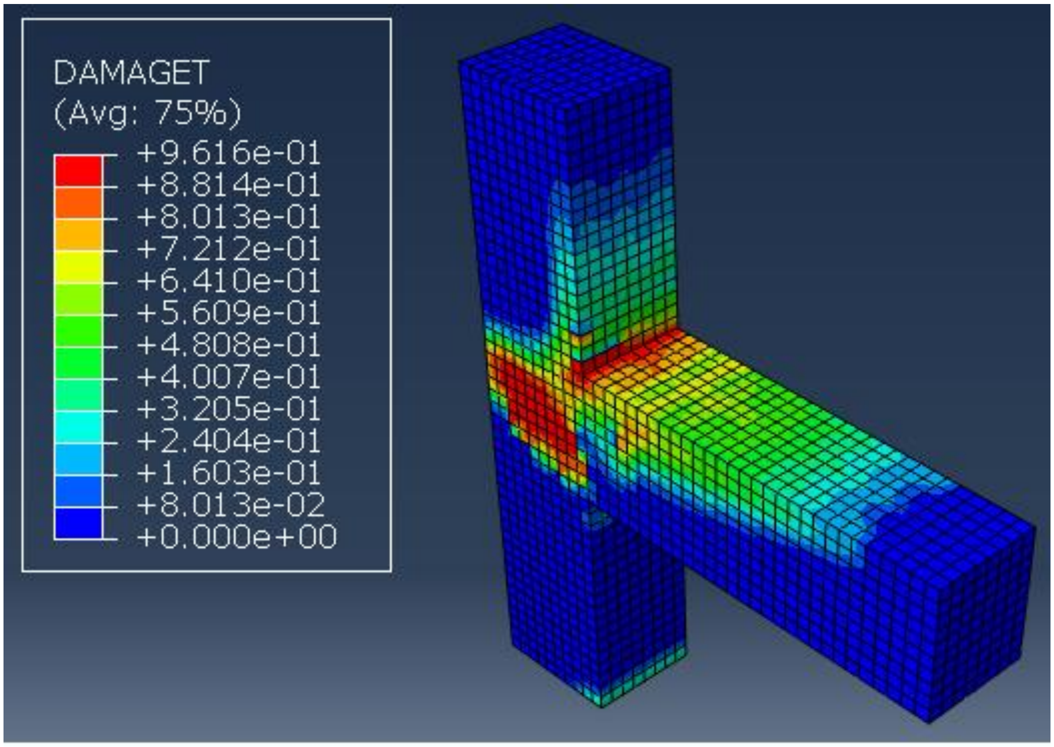

Figure 6.43: Concrete damage at the ultimate load corresponding to 14.98 mm displacement for BCJ-RC in push direction

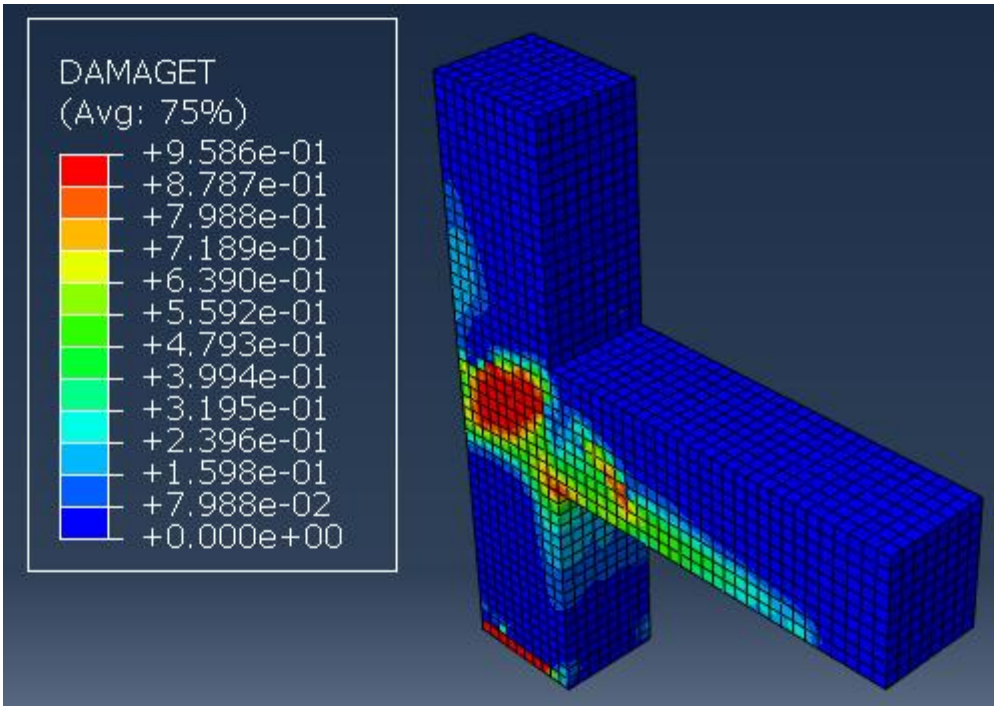

Figure 6.44: Concrete damage at the ultimate load corresponding to 16.52 mm displacement for BCJ-RC in pull direction

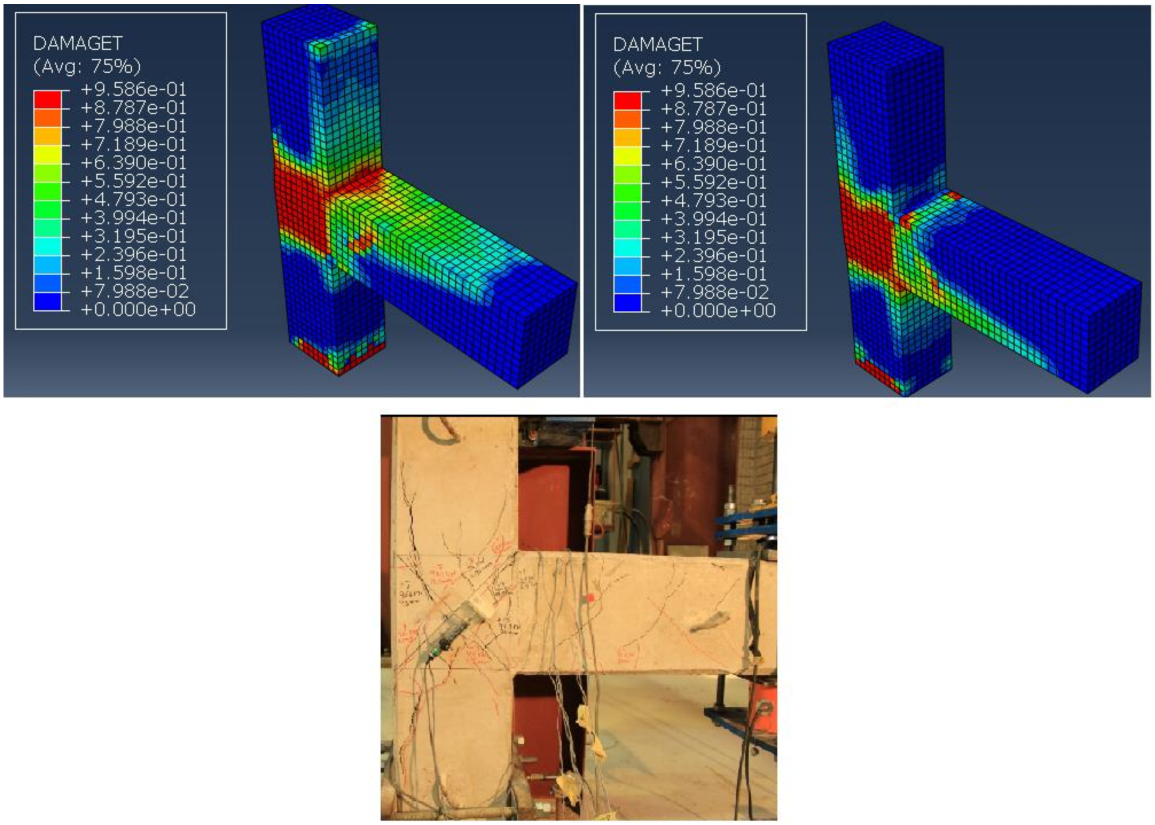

Figure 6.45: Comparison of crack pattern and concrete damage for BCJ-RC at displacement of 40 mm in push and pull directions

6.8 Numerical Simulations of Retrofitted Specimens

6.8.1 Numerical Simulations of BCJ-RC4S

It has been reported by many researcher that ABAQUS cannot model pinching hysteresis. To get pinching hysteresis one can use user develop concrete material model and element to get pinching effect. As this study doesn’t focus on the developing of user subroutine for concrete, so hysteresis envelopes were model for all specimens under reverse cyclic loading. The numerical simulation were done up to the failure of specimen. The beam tip was pushed up to the displacement of 40 mm. Figure 6.46 shows the load-deflection response of FEM simulations and experimental results for BCJ-RC4S.

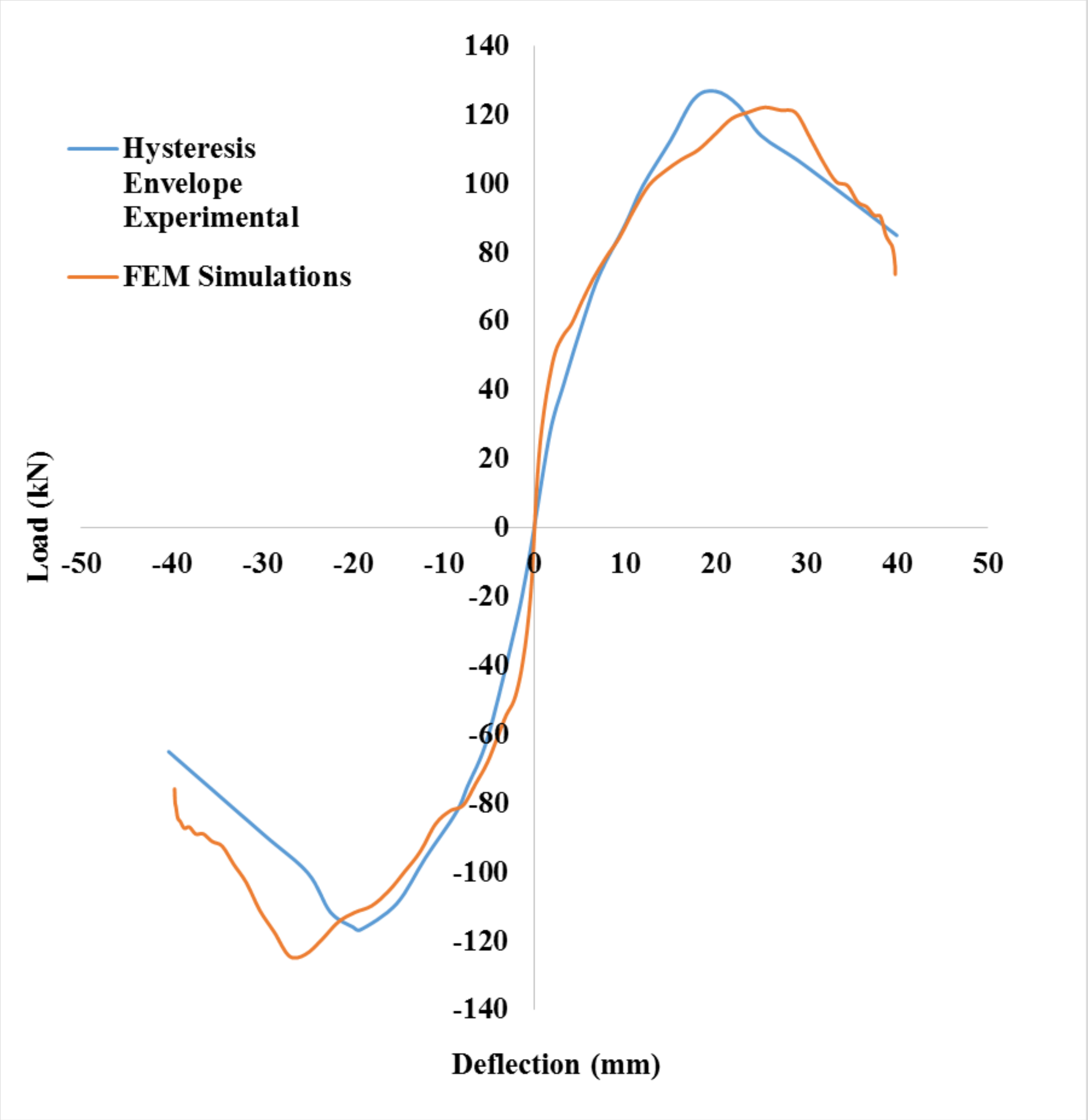

Figure 6.46: Comparison of load-displacement response for BCJ-RC4S

It has been observed that FEM simulations showed good agreement with the experimental results. FEM results were stiffer initially but later on curve matches closely with experimental results. The ultimate load of 122.14 kN and 124.39 kN was achieved at displacement of 25.43 mm and 27.01 mm whereas in case of experimental it was 127.59 kN and 116.9 kN at displacement of 19.86 mm and 18.54 mm in push and pull directions, respectively. The maximum stress in steel at ultimate load corresponding to 25.43 mm displacement in push direction is shown in Figure 6.47 which clearly indicates that there is no yielding of steel and the maximum stresses in steel was 455 MPa which is lesser than the yield stress of steel. The stress S11, S22 and S12 in concrete for push direction are shown in Figure 6.48, Figure 6.49 and Figure 6.50 at ultimate load.

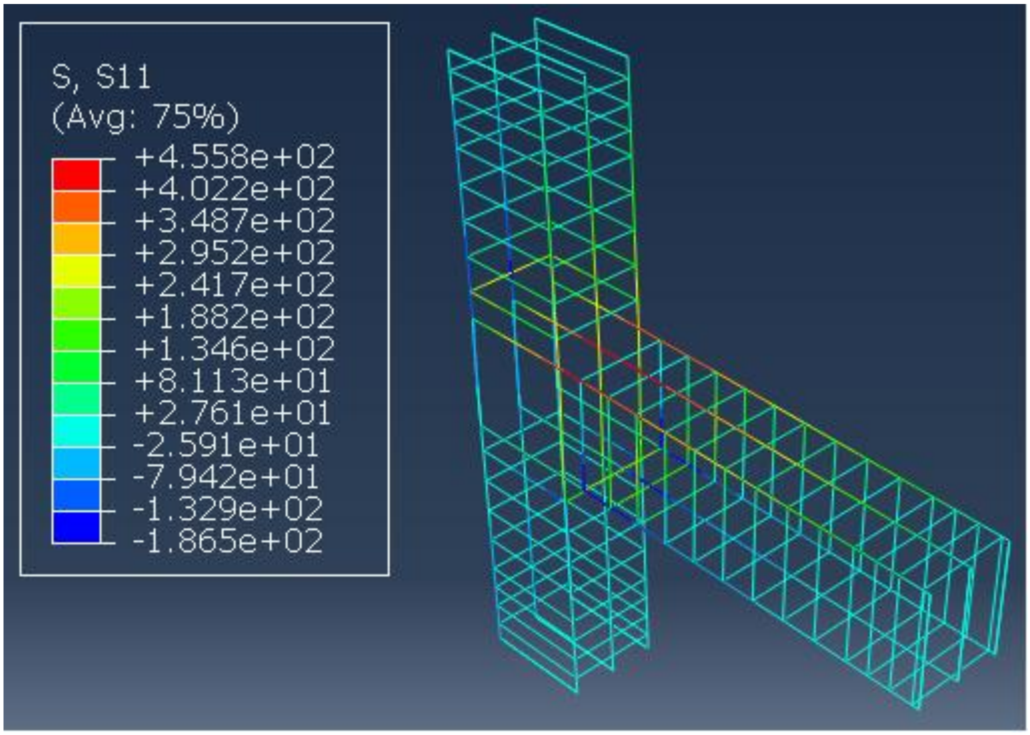

Figure 6.47: Steel stresses at the ultimate load corresponding to 25.43 mm displacement for BCJ-RC4S in push direction

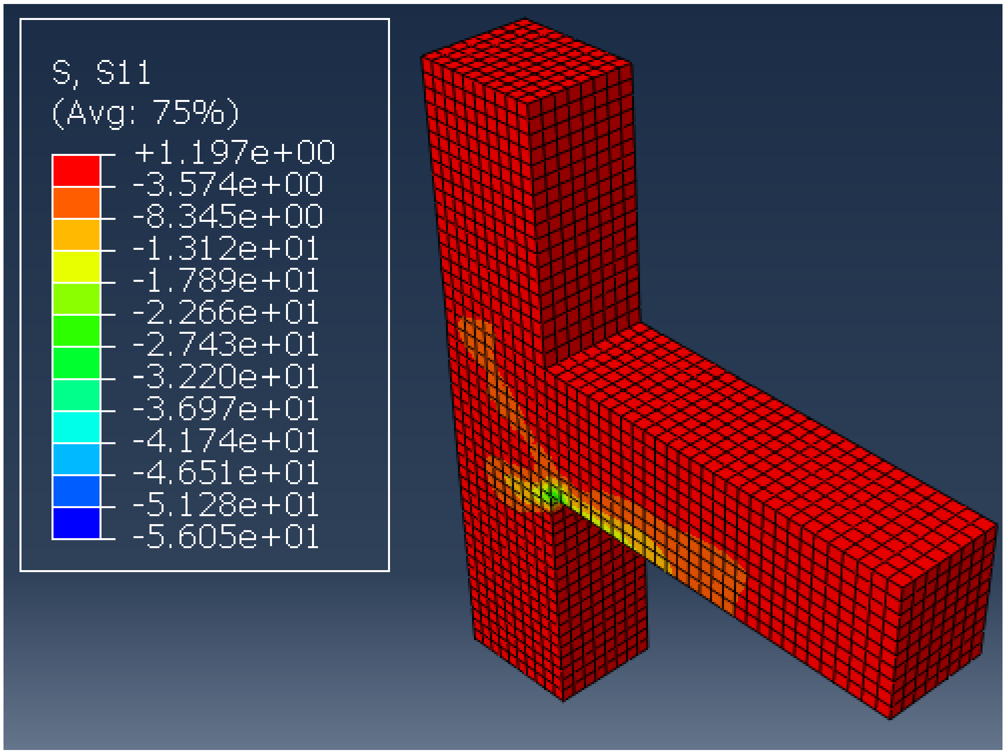

Figure 6.48: Stress S11 in concrete at the ultimate load corresponding to 25.43 mm displacement for BCJ-RC4S in push direction

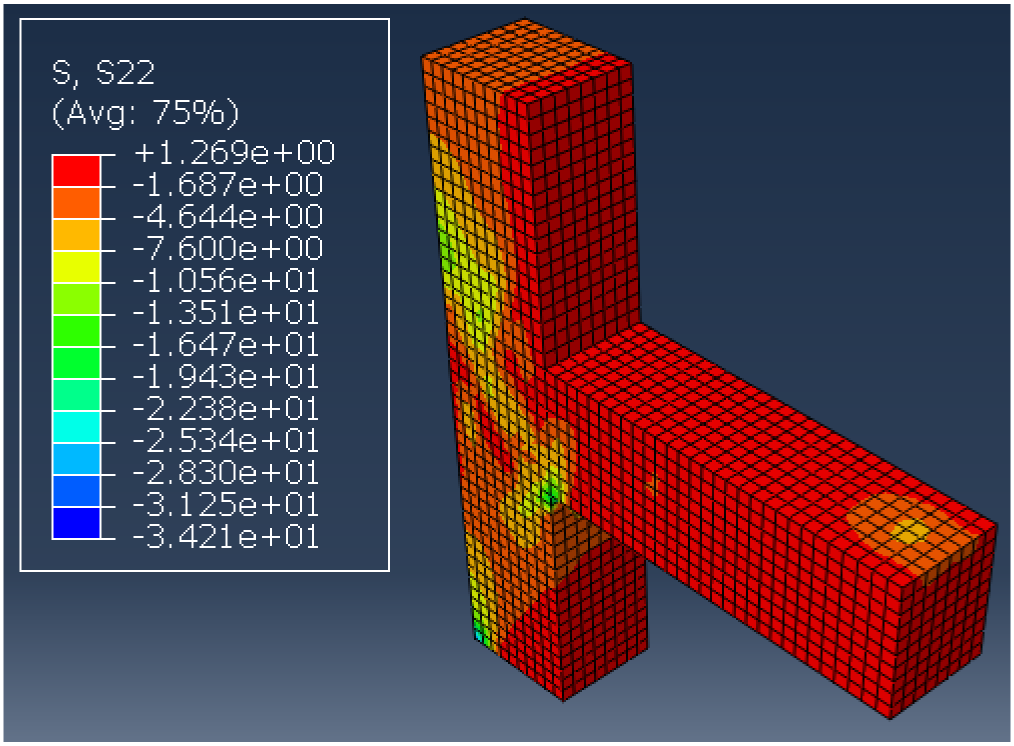

Figure 6.49: Stress S22 in concrete at the ultimate load corresponding to 25.43 mm displacement for BCJ-RC4S in push direction

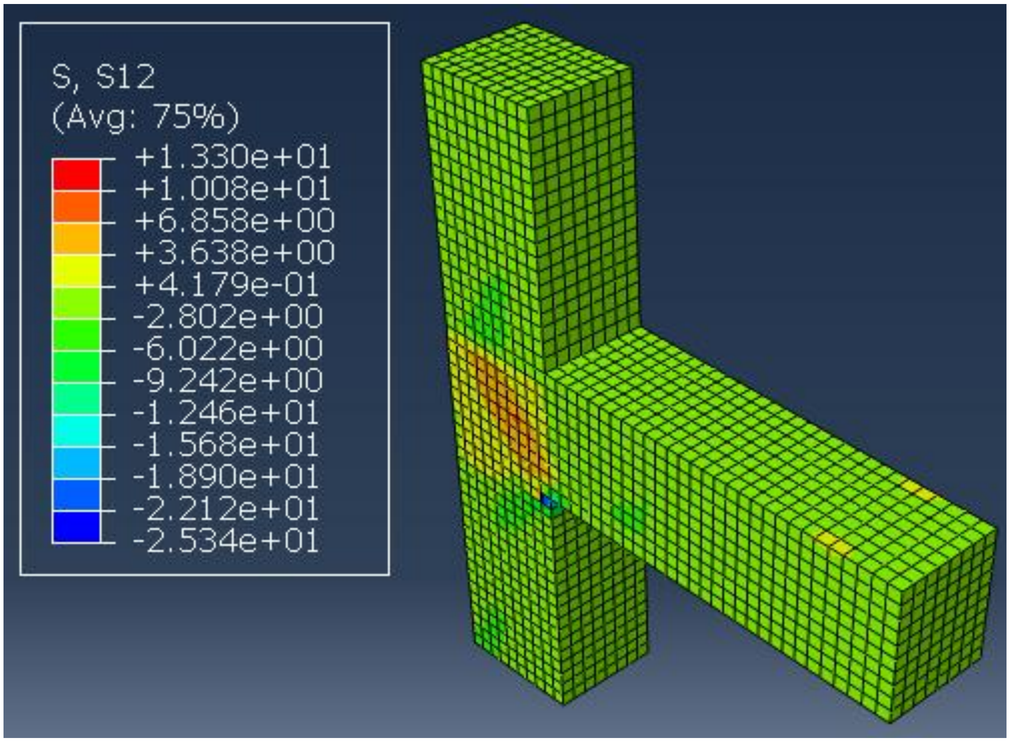

Figure 6.50: Stress S12 in concrete at the ultimate load corresponding to 25.43 mm displacement for BCJ-RC4S in push direction

Figure 6.51 shows the stresses and strains in SMAs sheet at ultimate load which shows that sheets are still in austenite phase. Figure 6.52 shows the damage evolution in concrete at ultimate load in push direction. Figure 6.53 shows the stresses and strains in SMAs sheets corresponding to 40 mm displacement which shows SMAs sheets entered the phase transformation (austenite to martensite). Figure 6.54 shows the comparison of experimental cracks pattern and concrete damage in FEM model for BCJ-RC4S at displacement of 40 mm in push and pull direction which shows good agreement.

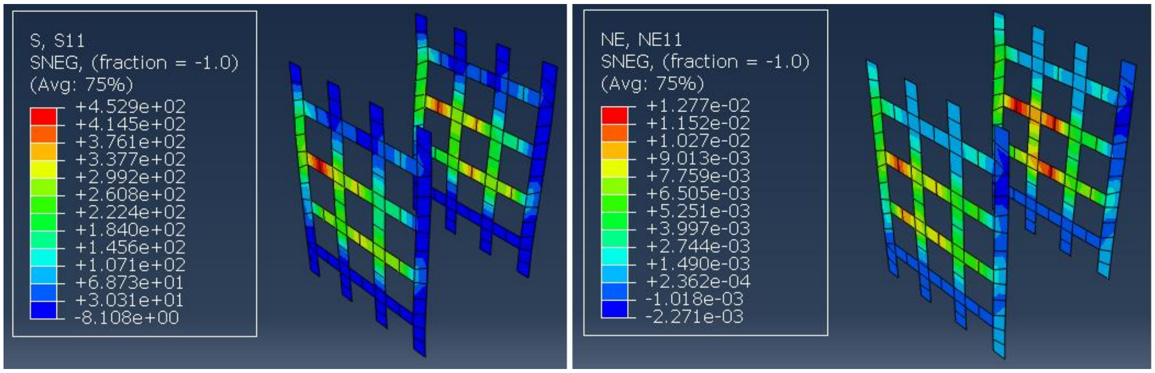

Figure 6.51: Stresses (left) and strains (right) in SMAs Sheets at ultimate load for BCJ-RC4S in push direction

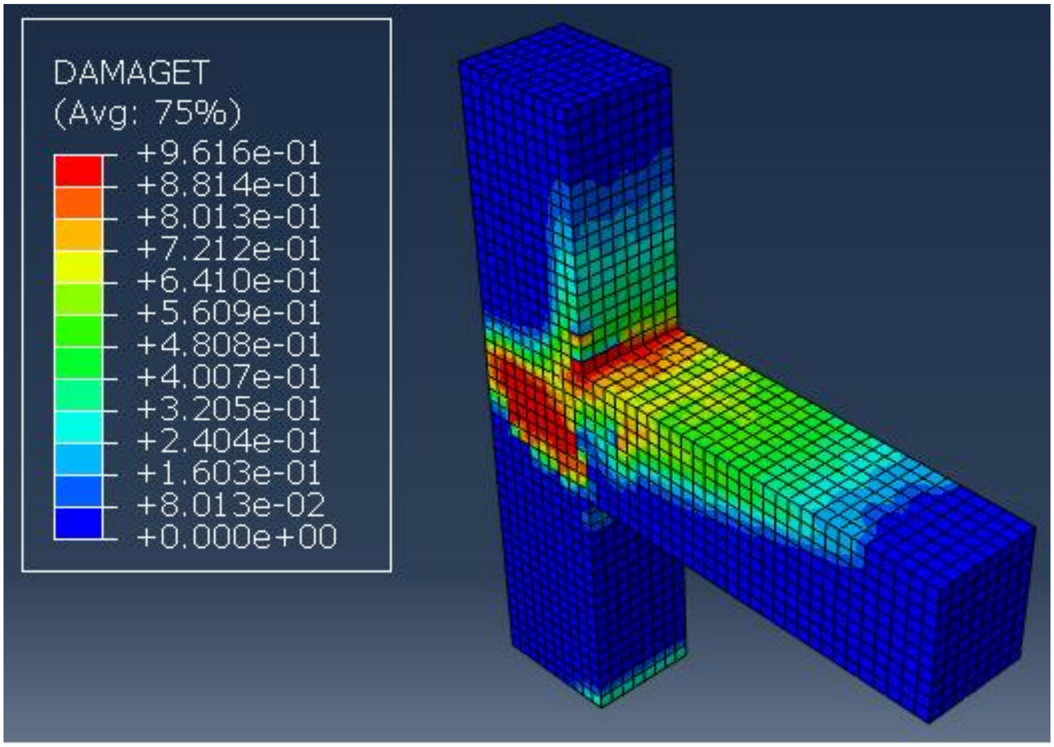

Figure 6.52: Concrete damage at the ultimate load corresponding to 25.43 mm displacement for BCJ-RC4S in push direction

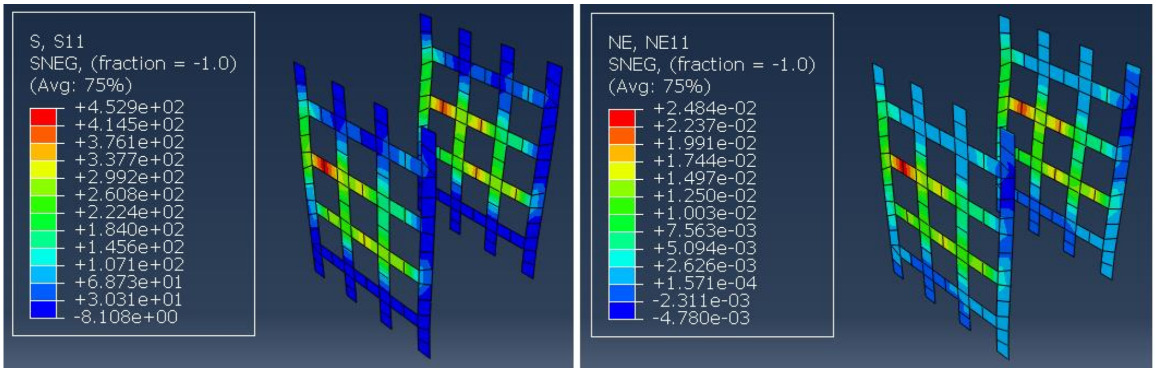

Figure 6.53: Stresses (left) and strains (right) in SMAs Sheets at displacement of 40 mm for BCJ-RC4S in push direction

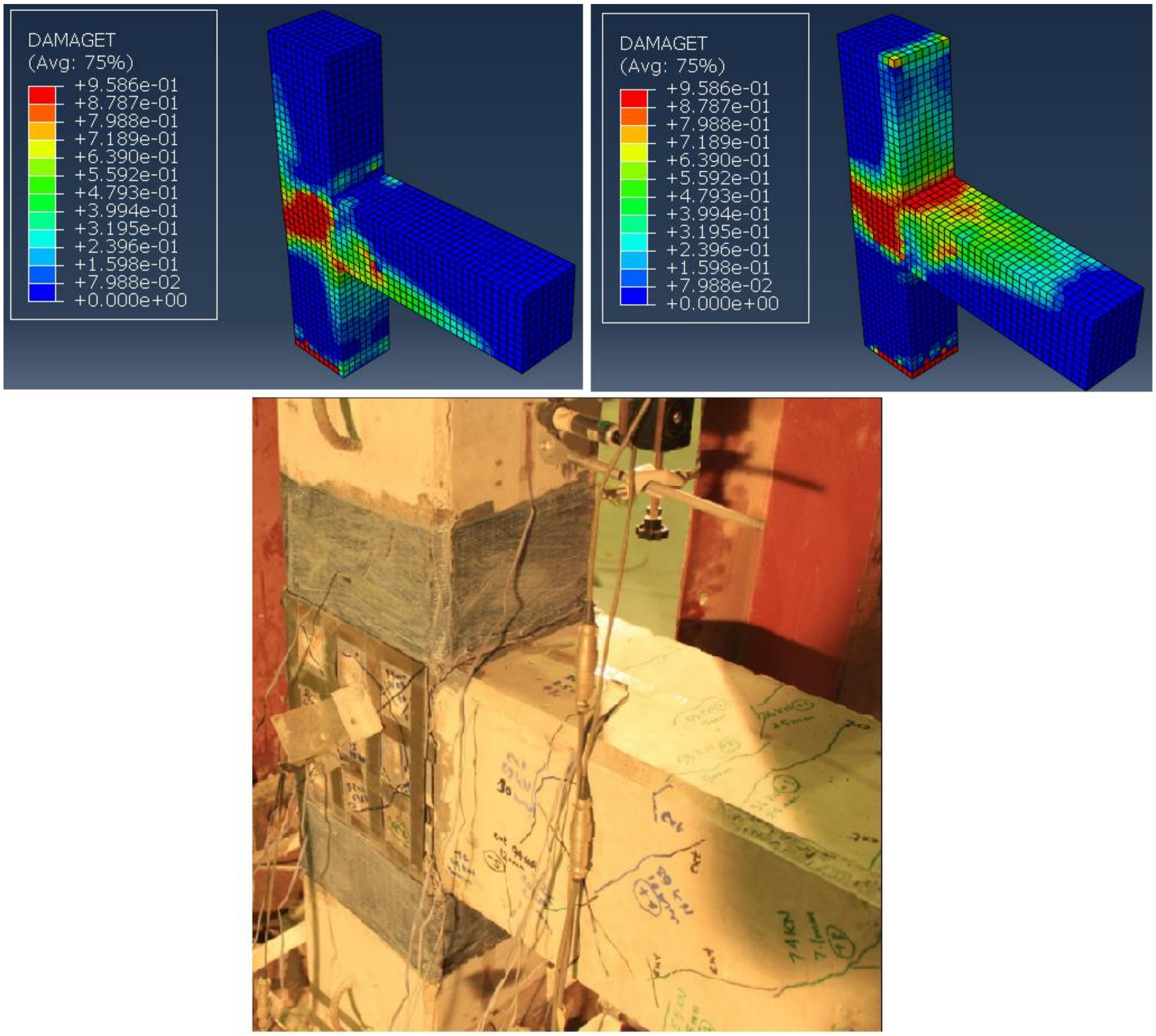

Figure 6.54: Comparison of crack pattern and concrete damage for BCJ-RC4S at displacement of 40 mm in push and pull directions

6.8.2 Numerical Simulations of BCJ-RC2S

It has been reported by many researcher that ABAQUS cannot model pinching hysteresis. To get pinching hysteresis one can use user develop concrete material model and element to get pinching effect. As this study doesn’t focus on the developing of user subroutine for concrete, so hysteresis envelopes were model for all specimens under reverse cyclic loading. The numerical simulation were done up to the failure of specimen. The beam tip was pushed up to the displacement of 40 mm. Figure 6.55 shows the load-deflection response of FEM simulations and experimental results for BCJ-RC2S.

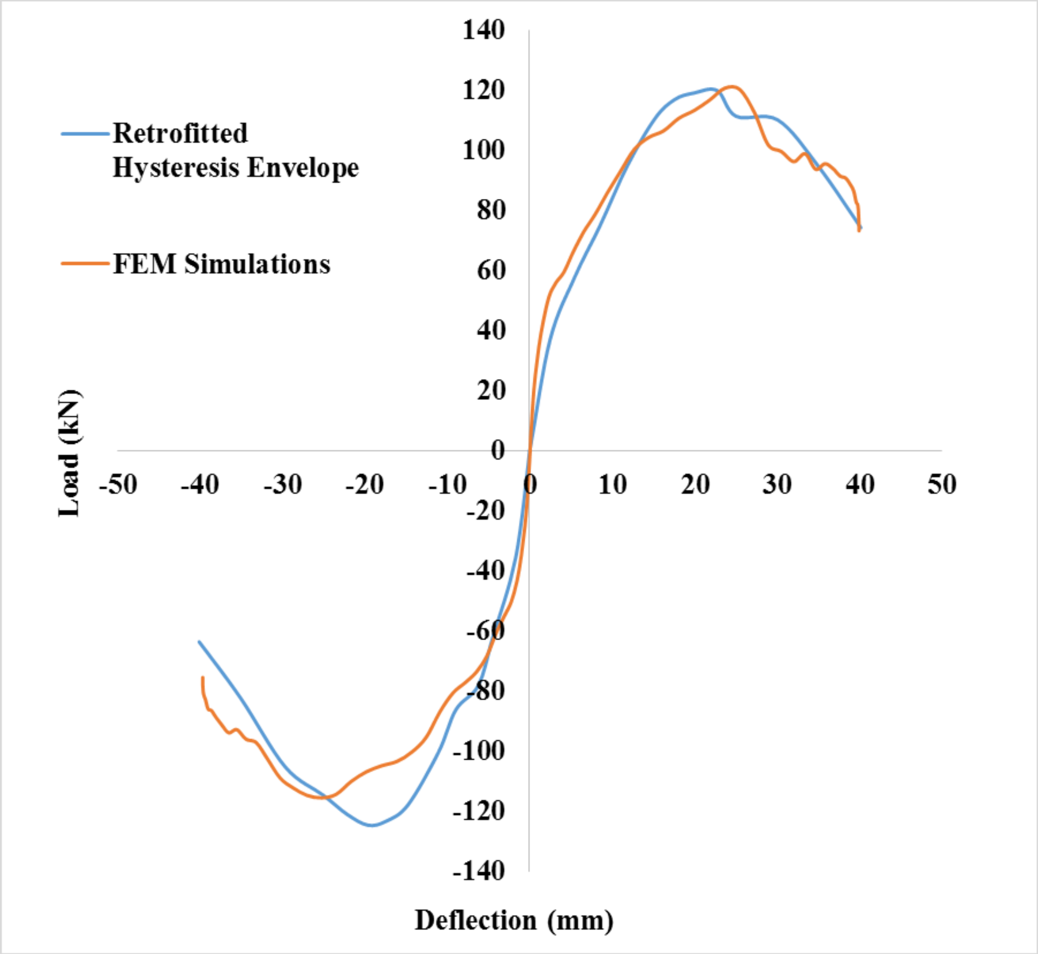

Figure 6.55: Comparison of load-displacement response for BCJ-RC2S

It has been observed that FEM simulations showed good agreement with the experimental results. FEM results were stiffer initially but later on curve matches closely with experimental results. The ultimate load of 120.64 kN and 115.48 kN was achieved at displacement of 23.66 mm and 25.28 mm whereas in case of experimental it was 120.76 kN and 125 kN at displacement of 22.75 mm and 20.06 mm in push and pull directions, respectively. The maximum stress in steel at ultimate load corresponding to 23.66 mm displacement in push direction is shown in Figure 6.56 which clearly indicates that there is no yielding of steel and the maximum stresses in steel was 424 MPa which is lesser than the yield stress of steel. The stress S11, S22 and S12 in concrete for push direction are shown in Figure 6.57, Figure 6.58 and Figure 6.59 at ultimate load.

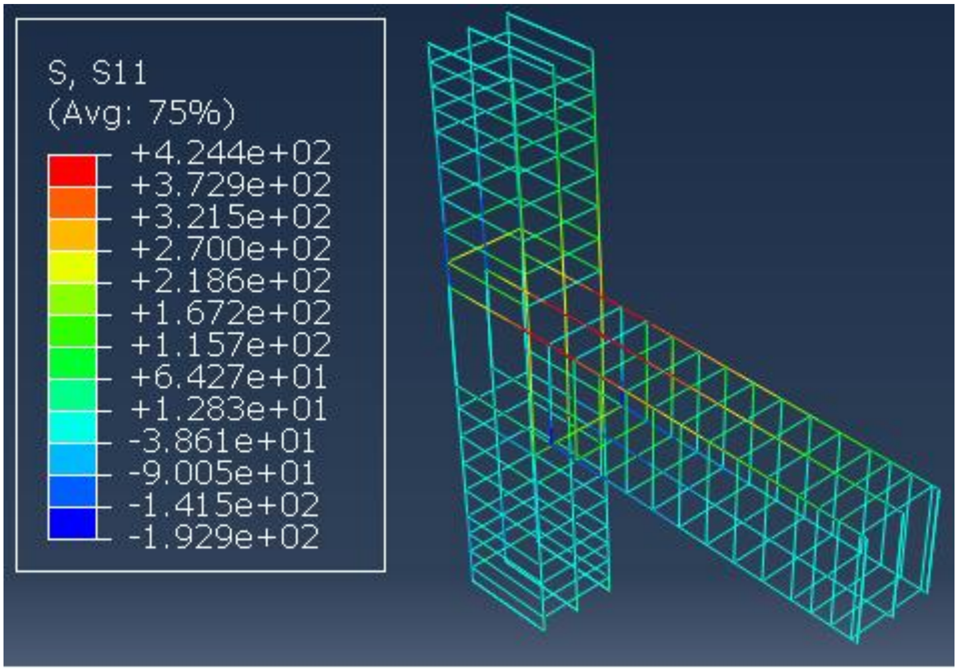

Figure 6.56: Steel stresses at the ultimate load corresponding to 23.66 mm displacement for BCJ-RC2S in push direction

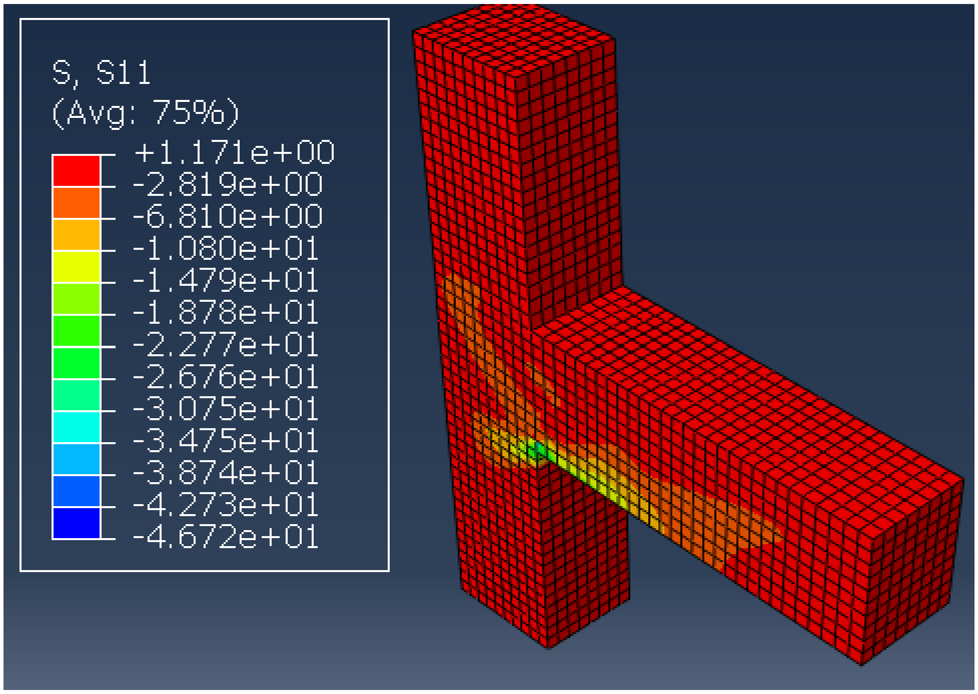

Figure 6.57: Stress S11 in concrete at the ultimate load corresponding to 23.66 mm displacement for BCJ-RC2S in push direction

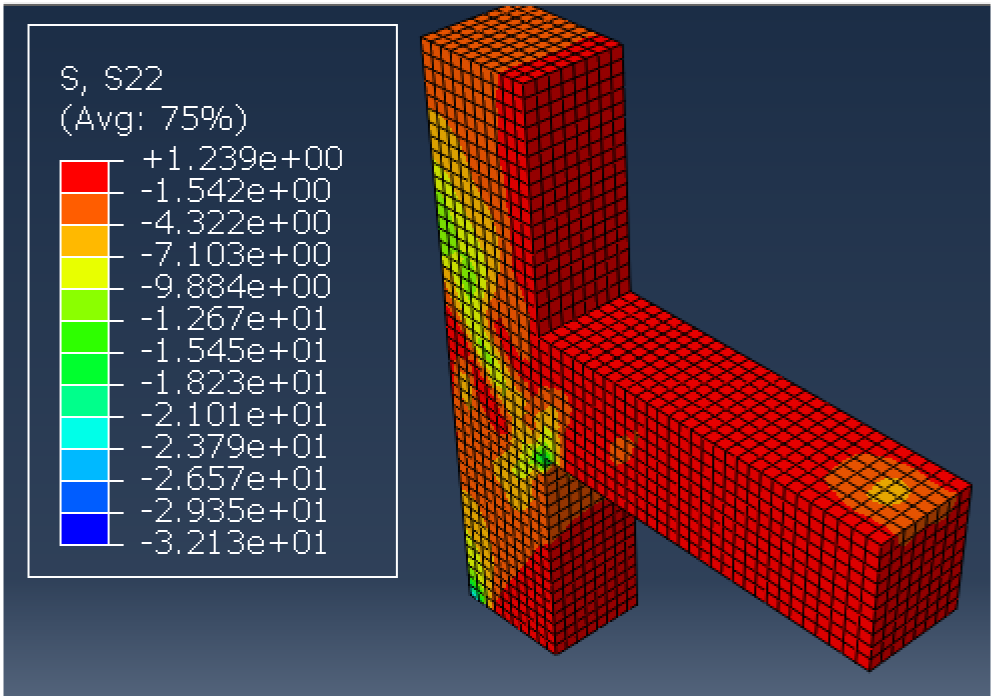

Figure 6.58: Stress S22 in concrete at the ultimate load corresponding to 23.66 mm displacement for BCJ-RC2S in push direction

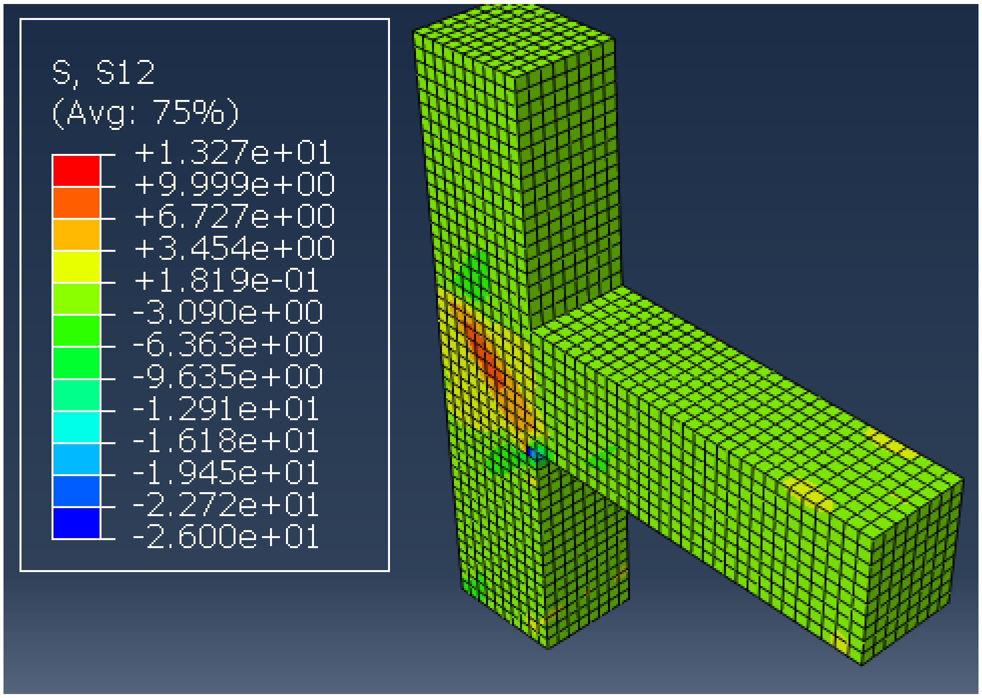

Figure 6.59: Stress S12 in concrete at the ultimate load corresponding to 23.66 mm displacement for BCJ-RC2S in push direction

Figure 6.60 shows the stresses and strains in SMAs sheet at ultimate load which shows that sheets are still in austenite phase. Figure 6.61 shows the damage evolution in concrete at ultimate load in push direction. Figure 6.62 shows the stresses and strains in SMAs sheets corresponding to 40 mm displacement which shows SMAs sheets entered the phase transformation (austenite to martensite). Figure 6.63 shows the comparison of experimental cracks pattern and concrete damage in FEM model for BCJ-RC2S at displacement of 40 mm in push and pull direction which shows good agreement.

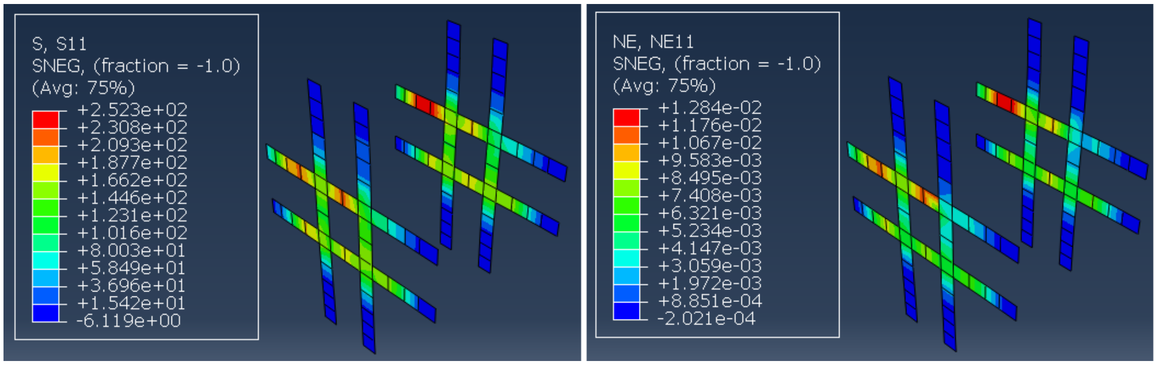

Figure 6.60: Stresses (left) and strains (right) in SMAs Sheets at ultimate load for BCJ-RC2S in push direction

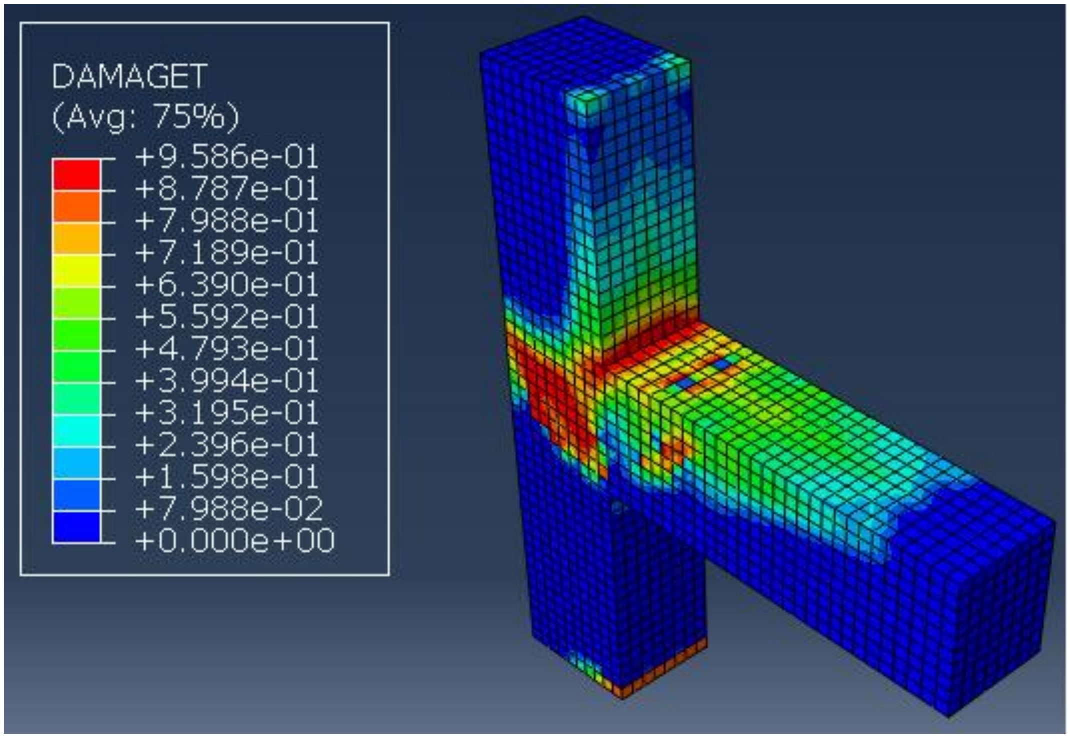

Figure 6.61: Concrete damage at the ultimate load corresponding to 23.66 mm displacement for BCJ-RC2S in push direction

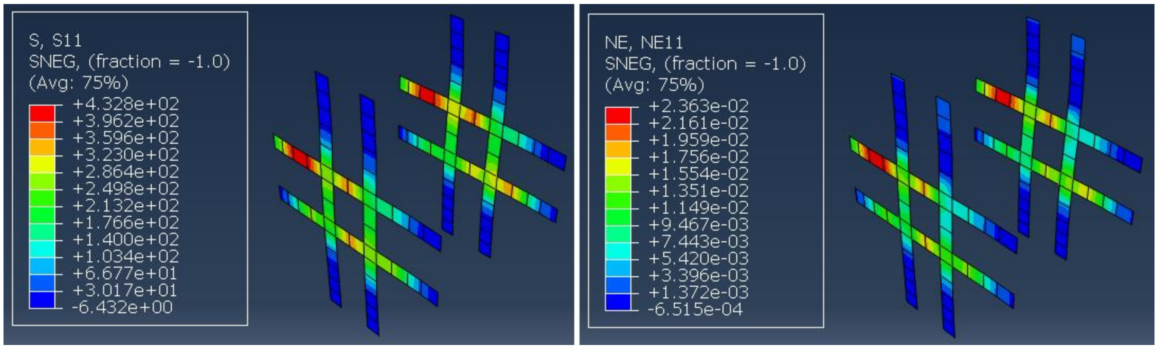

Figure 6.62: Stresses (left) and strains (right) in SMAs Sheets at displacement of 40 mm for BCJ-RC2S in push direction

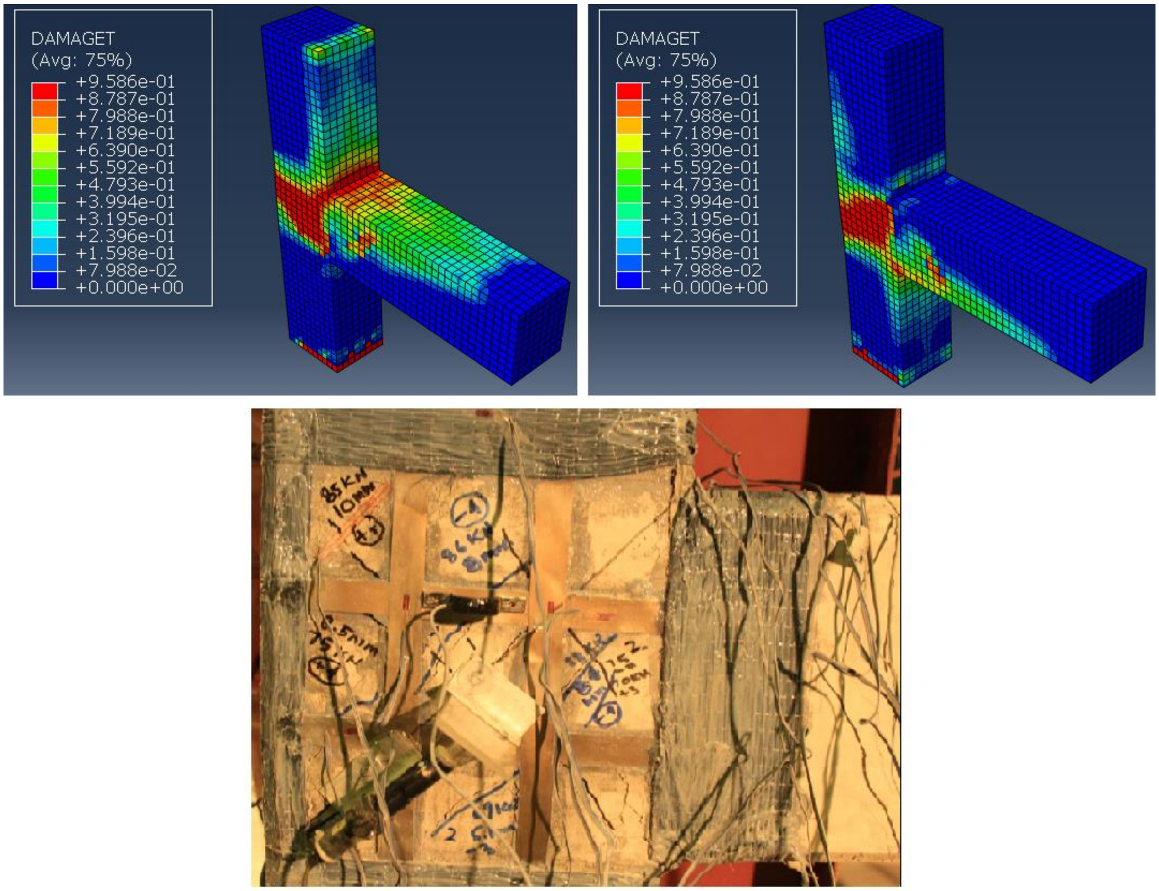

Figure 6.63: Comparison of crack pattern and concrete damage for BCJ-RC2S at displacement of 40 mm in push and pull directions

6.8.3 Numerical Simulations of BCJ-RCXS

It has been reported by many researcher that ABAQUS cannot model pinching hysteresis. To get pinching hysteresis one can use user develop concrete material model and element to get pinching effect. As this study doesn’t focus on the developing of user subroutine for concrete, so hysteresis envelopes were model for all specimens under reverse cyclic loading. The numerical simulation were done up to the failure of specimen. The beam tip was pushed up to the displacement of 40 mm. Figure 6.64 shows the load-deflection response of FEM simulations and experimental results for BCJ-RCXS.

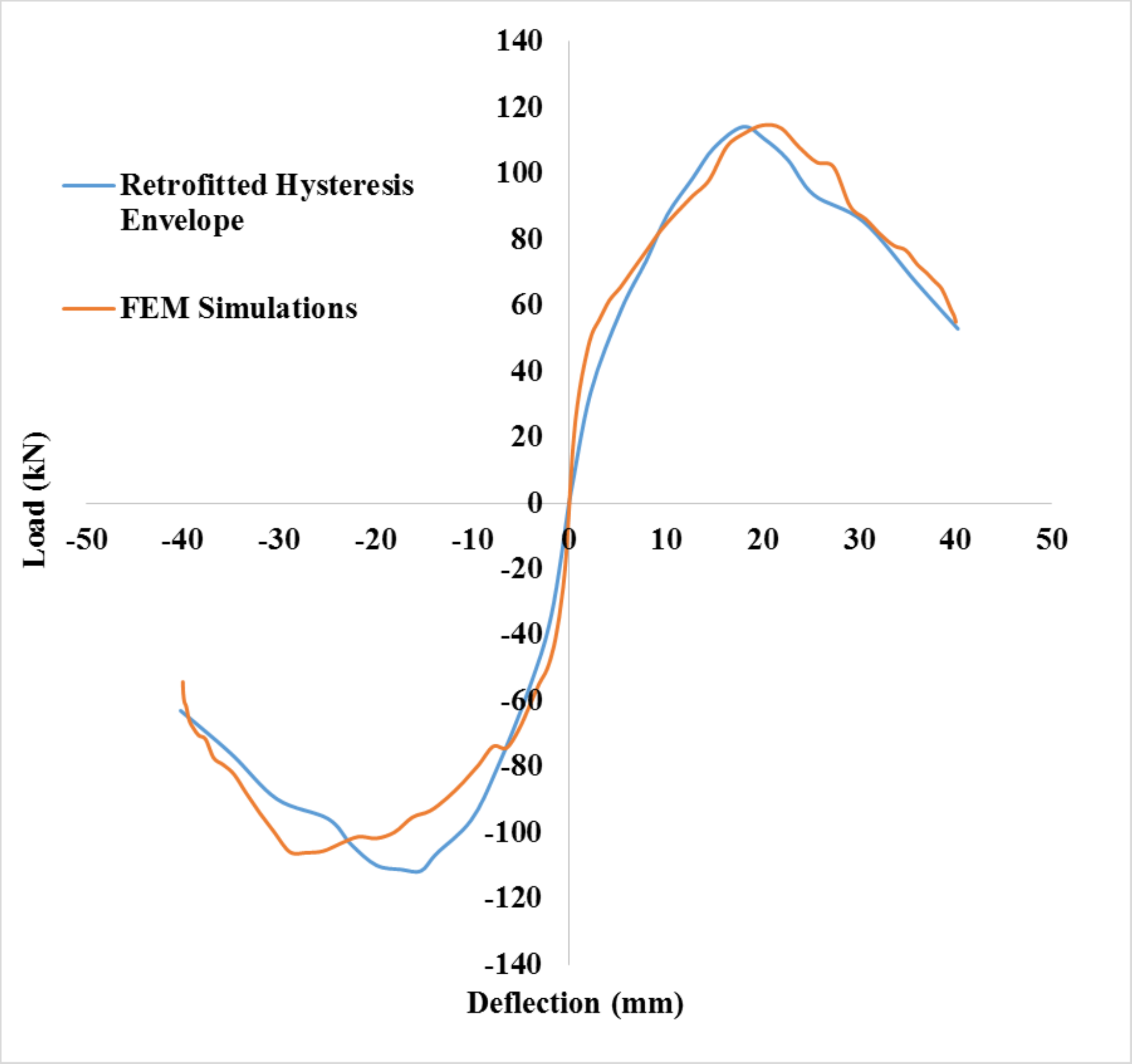

Figure 6.64: Comparison of load-displacement response for BCJ-RCXS

It has been observed that FEM simulations showed good agreement with the experimental results. FEM results were stiffer initially but later on curve matches closely with experimental results. The ultimate load of 114.64 kN and 106.1 kN was achieved at displacement of 20.07 mm and 27.21 mm whereas in case of experimental it was 114.32 kN and 111.6 kN at displacement of 18.01 mm and 15.32 mm in push and pull directions, respectively. The maximum stress in steel at ultimate load corresponding to 20.07 mm displacement in push direction is shown in Figure 6.65 which clearly indicates that there is no yielding of steel and the maximum stresses in steel was 401 MPa which is lesser than the yield stress of steel. The stress S11, S22 and S12 in concrete for push direction are shown in Figure 6.66, Figure 6.67 and Figure 6.68 at ultimate load.

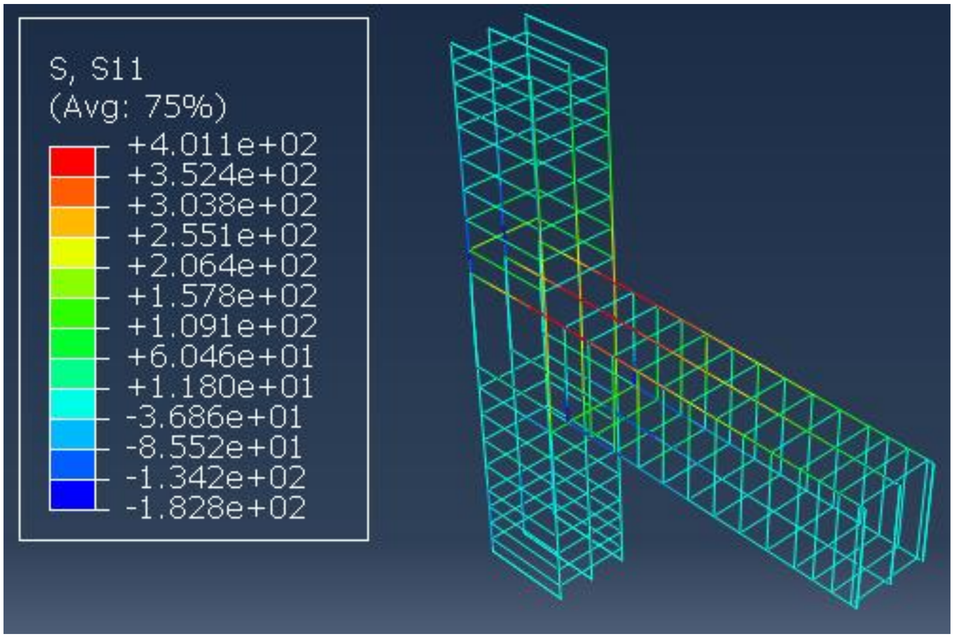

Figure 6.65: Steel stresses at the ultimate load corresponding to 20.07 mm displacement for BCJ-RCXS in push direction

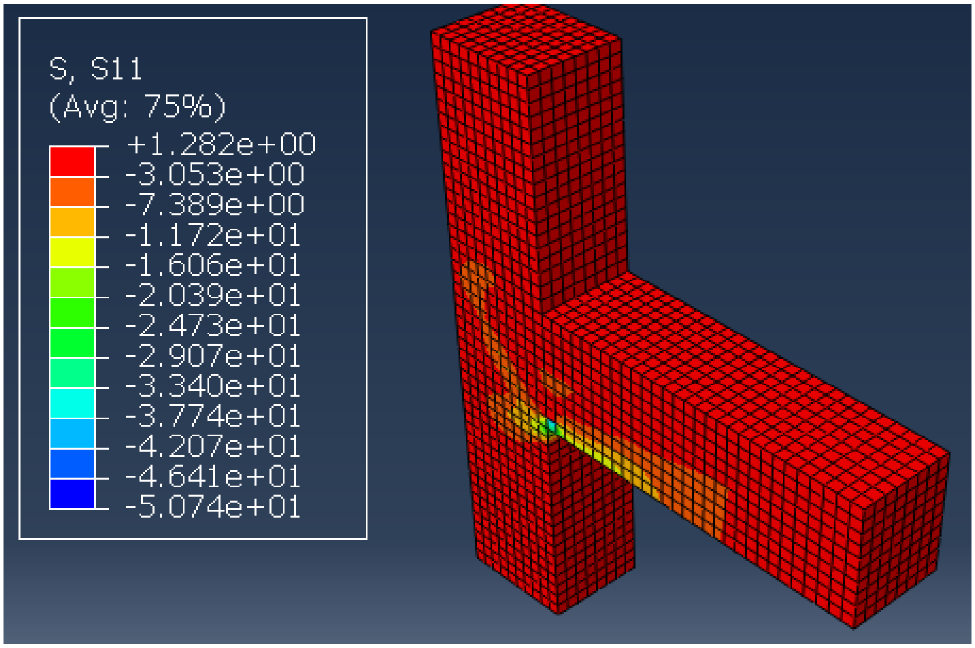

Figure 6.66 : Stress S11 in concrete at the ultimate load corresponding to 20.07 mm displacement for BCJ-RCXS in push direction

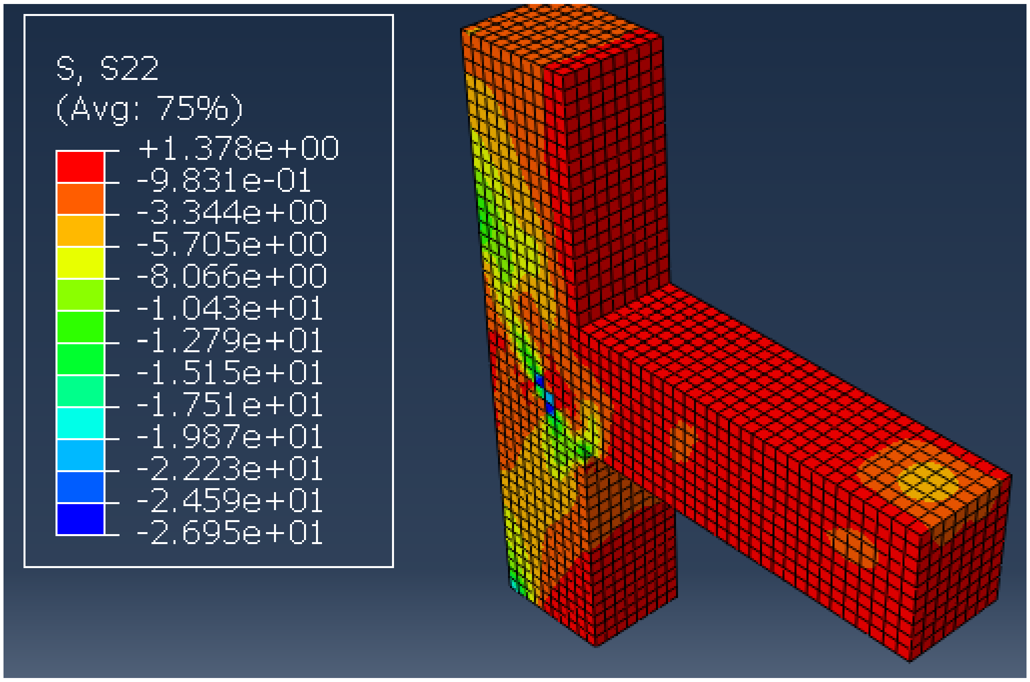

Figure 6.67: Stress S22 in concrete at the ultimate load corresponding to 20.07 mm displacement for BCJ-RCXS in push direction

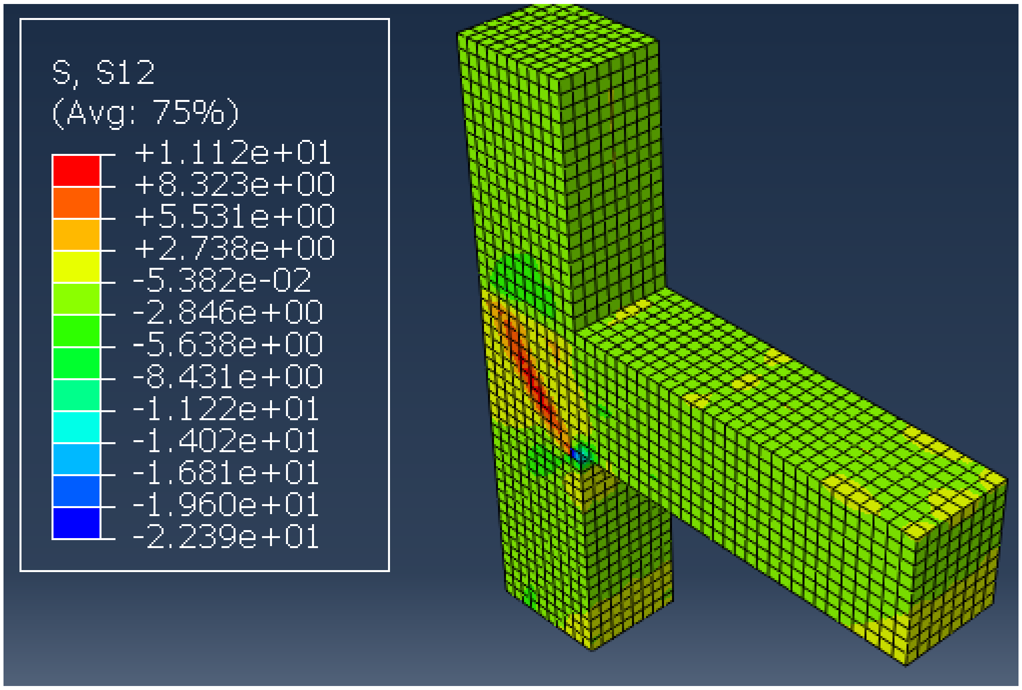

Figure 6.68: Stress S12 in concrete at the ultimate load corresponding to 20.07 mm displacement for BCJ-RCXS in push direction

Figure 6.69 shows the stresses and strains in SMAs sheet at ultimate load which shows that sheets are still in austenite phase. Figure 6.70 shows the damage evolution in concrete at ultimate load in push direction. Figure 6.71 shows the stresses and strains in SMAs sheets corresponding to 40 mm displacement which shows SMAs sheets entered the phase transformation (austenite to martensite). Figure 6.72 shows the comparison of experimental cracks pattern and concrete damage in FEM model for BCJ-RCXS at displacement of 40 mm in push and pull direction which shows good agreement.

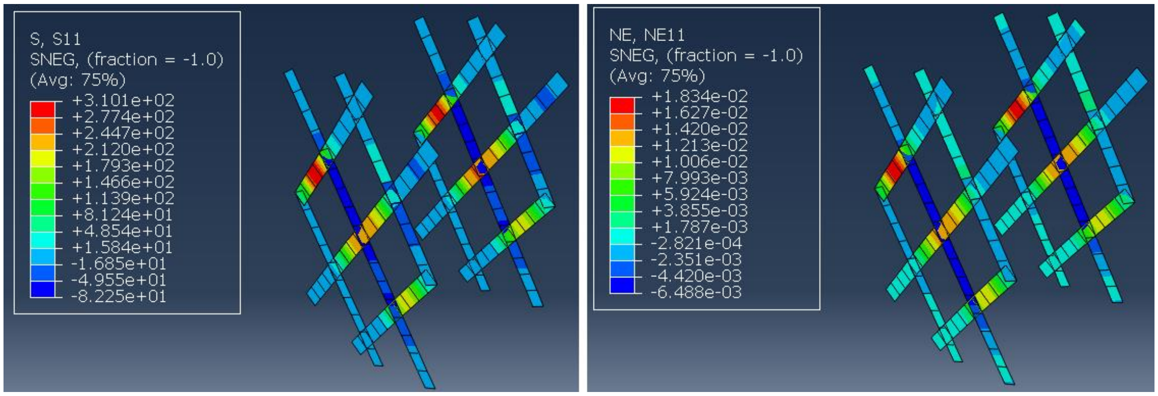

Figure 6.69: Stresses (left) and strains (right) in SMAs Sheets at ultimate load for BCJ-RCXS in push direction

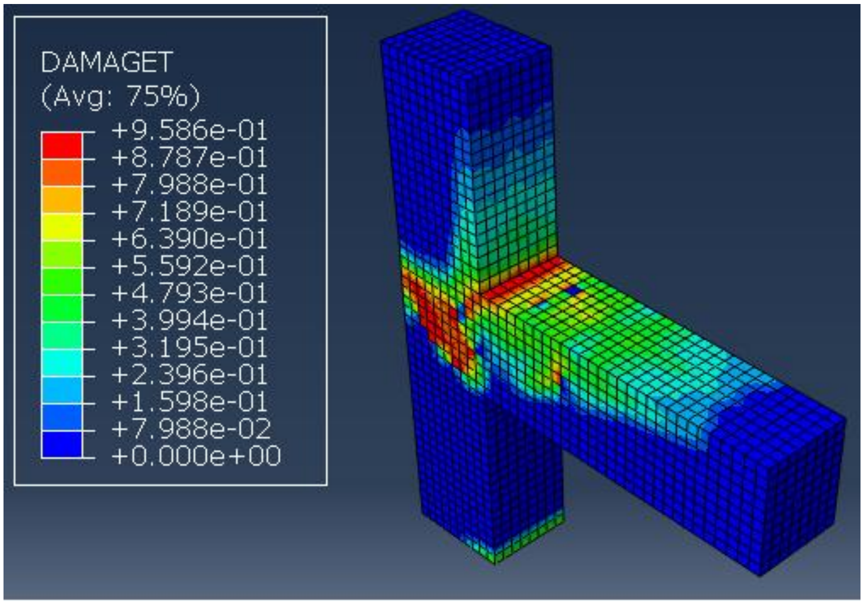

Figure 6.70: Concrete damage at the ultimate load corresponding to 20.07 mm displacement for BCJ-RCXS in push direction

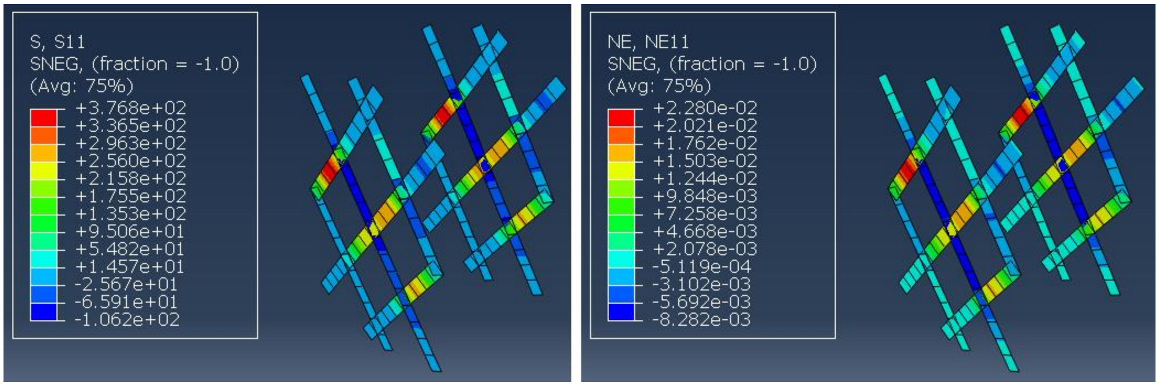

Figure 6.71: Stresses (left) and strains (right) in SMAs Sheets at displacement of 40 mm for BCJ-RCXS in push direction

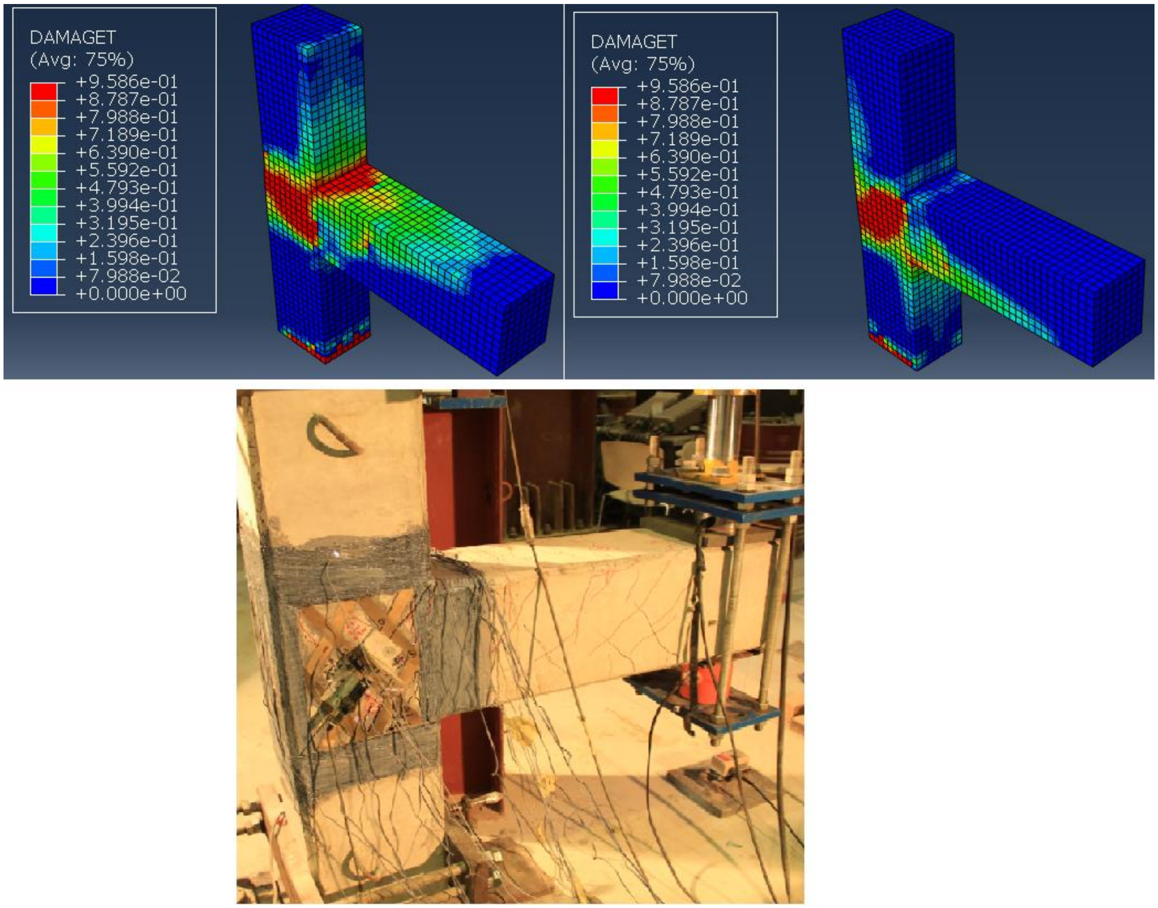

Figure 6.72: Comparison of crack pattern and concrete damage for BCJ-RCXS at displacement of 40 mm in push and pull directions

6.8.4 Numerical Simulations of BCJ-CLIS

It has been reported by many researcher that ABAQUS cannot model pinching hysteresis. To get pinching hysteresis one can use user develop concrete material model and element to get pinching effect. As this study doesn't focus on the developing of user subroutine for concrete, so hysteresis envelopes were model for all specimens under reverse cyclic loading. The numerical simulation were done up to the failure of specimen. The beam tip was pushed up to the displacement of 40 mm. Figure 6.73 shows the load-deflection response of FEM simulations and experimental results for BCJ-CLIS.

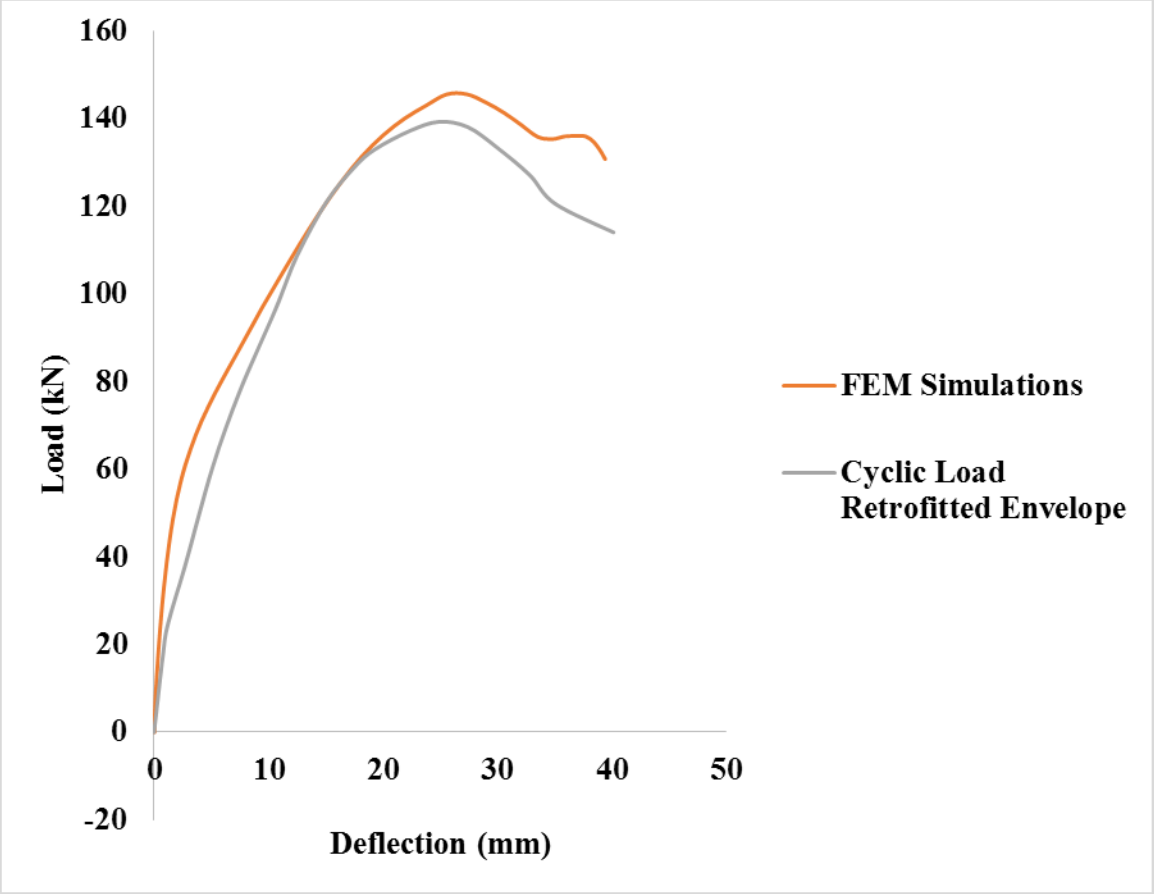

Figure 6.73: Comparison of load-displacement response for BCJ-CLIS

It has been observed that FEM simulations showed good agreement with the experimental results. FEM results were stiffer initially but later on curve matches closely with experimental results. The ultimate load of 145.5 kN at displacement of 25.5 mm whereas in case of experimental it was 139.23 kN at displacement of 24.87 mm, respectively. The maximum stress in steel at ultimate load corresponding to 25.5 mm displacement in push direction is shown in Figure 6.74 which clearly indicates that there is no yielding of steel and the maximum stresses in steel was 507 MPa which is lesser than the yield stress of steel. The stress S11, S22 and S12 in concrete shown in Figure 6.75, Figure 6.76 and Figure 6.77 at ultimate load.

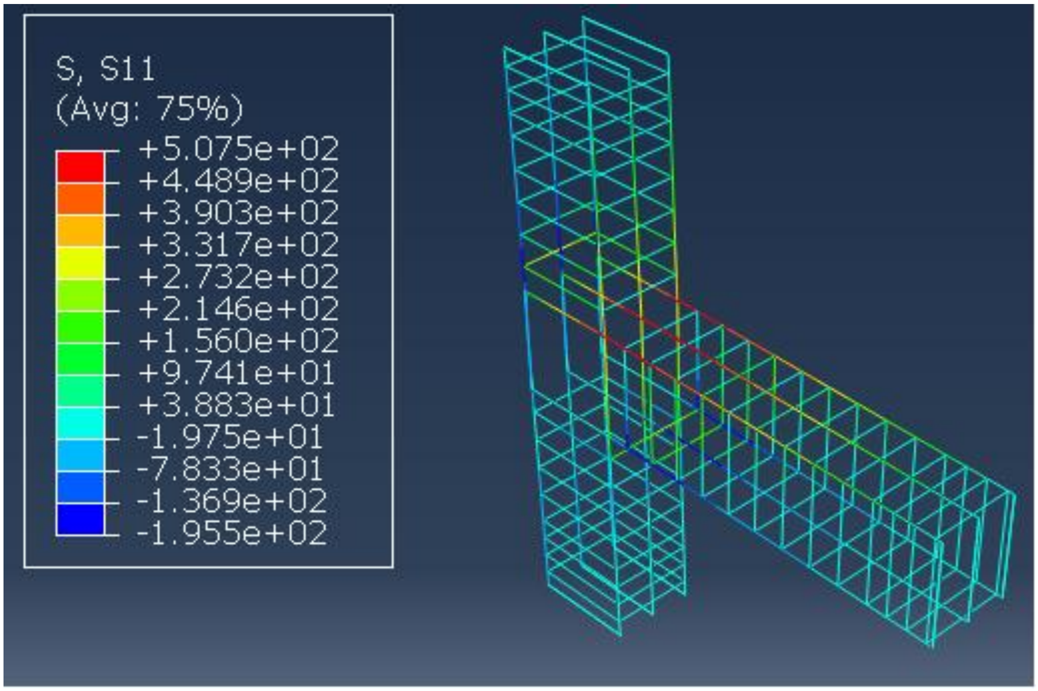

Figure 6.74: Steel stresses at the ultimate load corresponding to 25.5 mm displacement for BCJ-CLIS

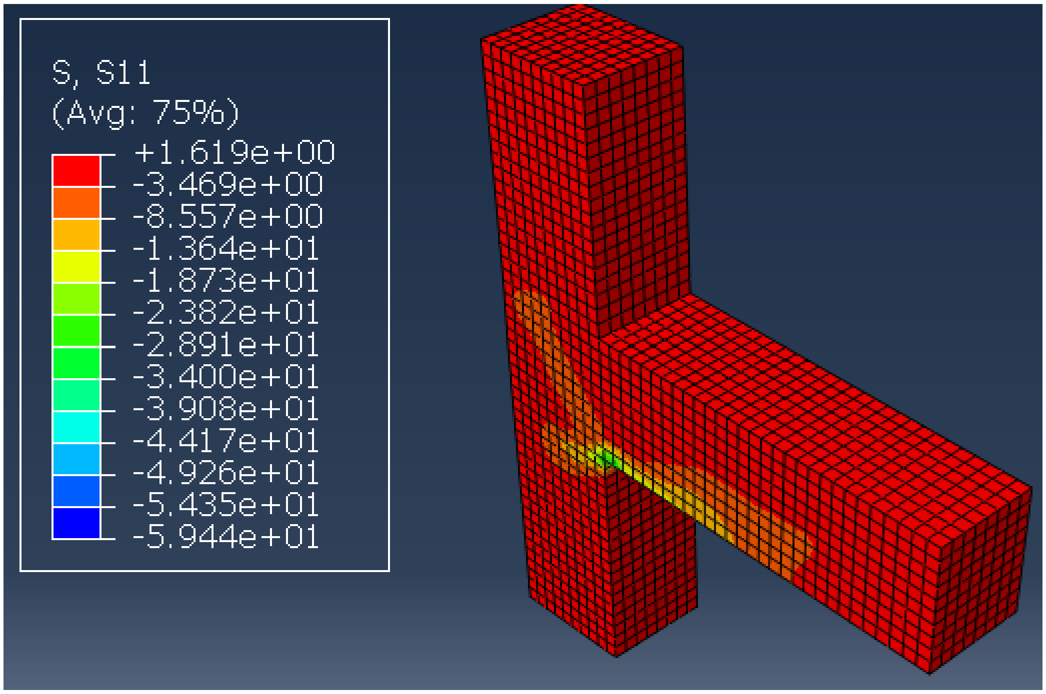

Figure 6.75: Stress S11 in concrete at the ultimate load corresponding to 25.5 mm displacement for BCJ-CLIS

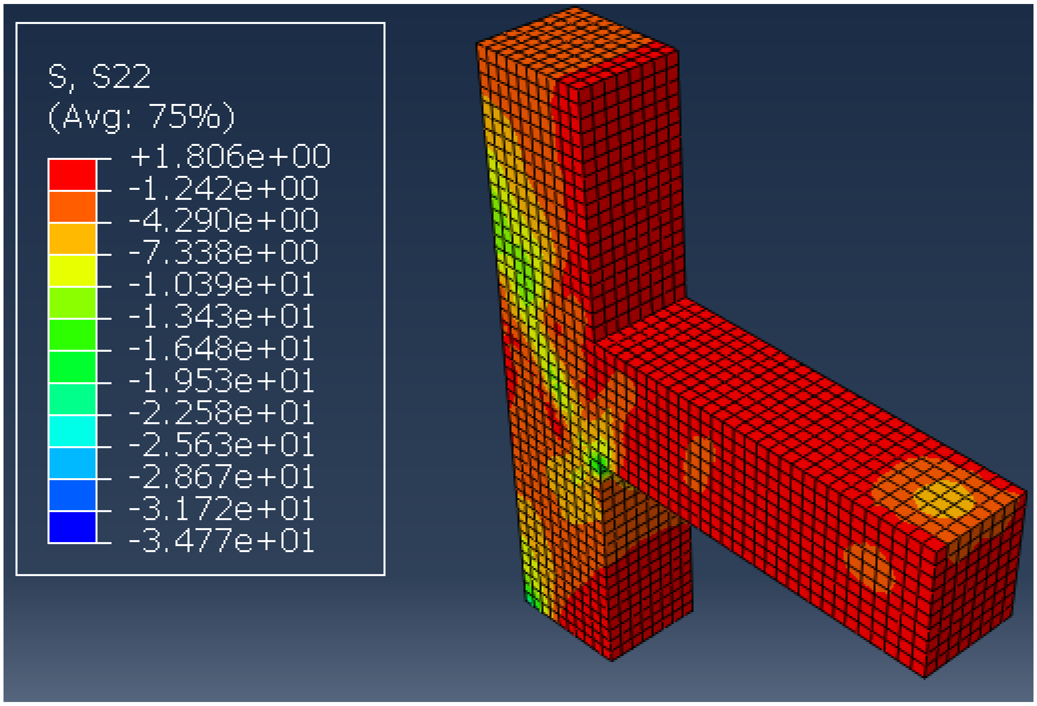

Figure 6.76: Stress S22 in concrete at the ultimate load corresponding to 25.5 mm displacement for BCJ-CLIS

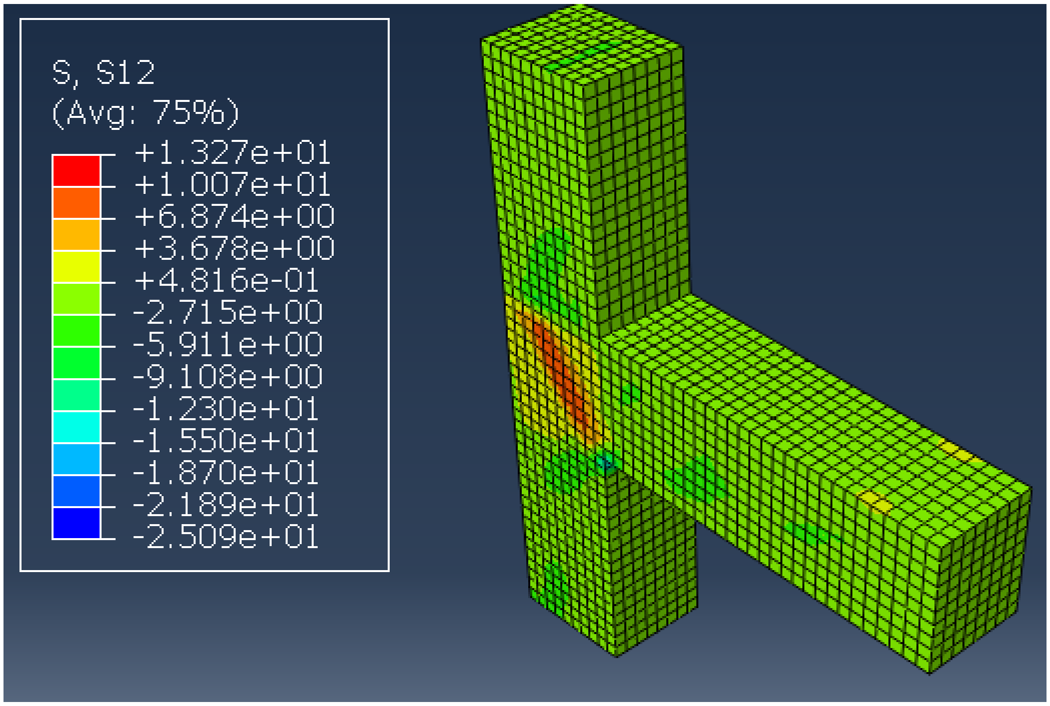

Figure 6.77: Stress S12 in concrete at the ultimate load corresponding to 25.5 mm displacement for BCJ-CLIS

Figure 6.78 shows the stresses and strains in SMAs sheet at ultimate load which shows that sheets enters into the phase transformation. Figure 6.79 shows the damage evolution in concrete at ultimate load. Figure 6.80 shows the stresses and strains in SMAs sheets corresponding to 40 mm displacement which shows SMAs sheets entered the phase transformation (austenite to martensite). Figure 6.81 shows the comparison of experimental cracks pattern and concrete damage in FEM model for BCJ-RCXS at displacement of 40 mm which shows good agreement.

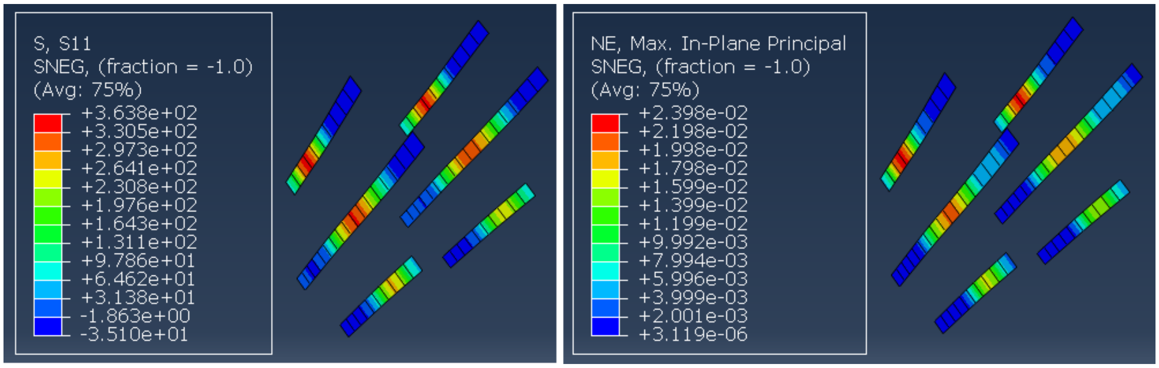

Figure 6.78: Stresses (left) and strains (right) in SMAs Sheets at ultimate load for BCJ-CLIS

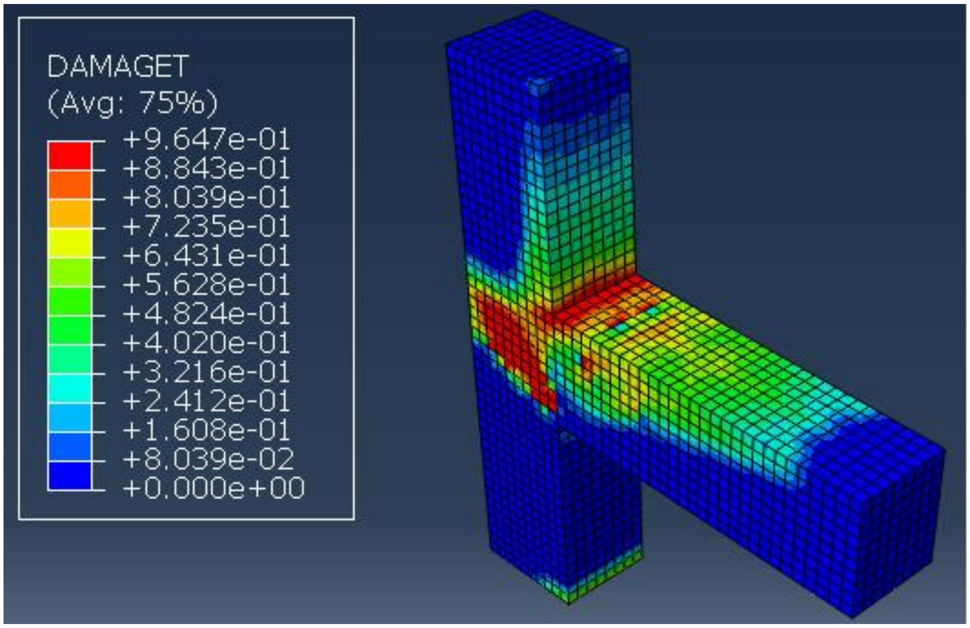

Figure 6.79: Concrete damage at the ultimate load corresponding to 20.07 mm displacement for BCJ-CLIS

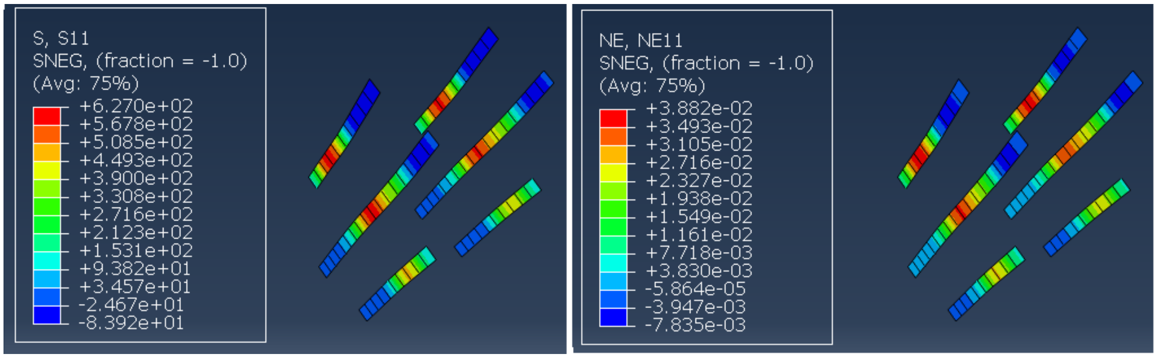

Figure 6.80: Stresses (left) and strains (right) in SMAs Sheets at displacement of 40 mm for BCJ-CLIS

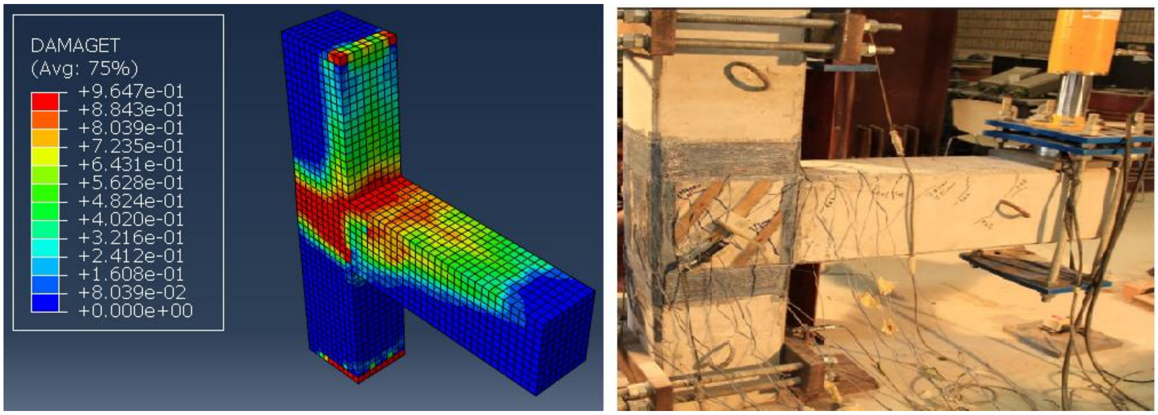

Figure 6.81: Comparison of crack pattern and concrete damage for BCJ-CLIS at displacement of 40 mm

6.9 Comparison of ultimate loads and joint shear capacity from FEM

The ultimate load obtained from FEM simulations showed good agreement with the experimental ultimate load. Table 12 shows the difference in ultimate loads obtained from FEM simulations and experimental study. Table 13 shows the joint shear capacity obtained from FEM for the specimens.

Table 12: Comparison of ultimate load for experimental and FEM Simulations

Specimen	Experimental				FEM simulations				Load Difference %	
	Ultimate load kN		Displacement mm		Ultimate load kN		Displacement mm			
	Push	Pull	Push	Pull	Push	Pull	Push	Pull	Push	Pull
BCJ-M	122.46	104.2	20.46	20.28	121.41	-	18.11	-	0.87	-
BCJ-CL	111.25	-	21.93	-	111.33	-	18.10	-	0.07	
BCJ-RC	105.82	103.9	14.98	16.25	104.72	115.48	16.24	19.24	1.04	11.15
BCJ-CLIS	139.23	-	24.88	-	145	-	25.5		4.14	-
BCJ-RC4S	127.59	116.9	19.86	18.54	122.14	124.39	25.43	27.01	4.27	6.41
BCJ-RC2S	120.76	125	22.75	20.05	120.64	115.48	23.66	25.28	0.09	7.62
BCJ-RCXS	114.32	111.6	18.02	15.32	114.64	106.1	20.07	27.21	0.27	4.92

Table 13: Comparison of joint shear capacity obtained from experiments, mechanistic model and FEM Simulations

Specimens	V_{test}	$V_{Mechanistic}$	V_{FEM}	V_{test}	$V_{predicted}$	V_{FEM}	$\frac{V_{predicted}}{V_{test}}$	$\frac{V_{FEM}}{V_{test}}$
	kN	kN	kN	MPa	MPa	MPa		
BCJ-M	379.3	392.3	383.2	4.21	4.36	4.26	1.0	1.0
BCJ-RC	317.9	392.3	357.2	3.53	4.36	3.96	1.2	1.1
BCJ-CL	296.6	392.3	360.3	3.29	4.36	4.0	1.3	1.2
BCJ-RC4S	377.4	397.8	410.3	4.19	4.42	4.55	1.1	1.1
BCJ-RC2S	351.9	397.0	376.3	3.91	4.41	4.18	1.1	1.1
BCJ-RCXS	386	395.5	356.3	4.28	4.39	3.96	0.9	0.9
BCJ-CLIS	461.6	398.5	451.1	5.12	4.43	5.01	0.9	1

CHAPTER 7

CONCLUSIONS AND RECOMMENDATIONS

7.1 Conclusions

In this study, beam-column joints with lack of seismic detailing have been studied experimentally and numerically using ABAQUS FEM software. Seven specimens were tested which includes 3 control specimens and 4 retrofitted specimens using shape memory alloys (SMAs) sheets under monotonic, cyclic and reverse cyclic loading. Based on experimental and FEM simulations following conclusions have been drawn.

- SMA sheets can undergo large deformation during loading and can recover large deformation with no permanent residual strain or slightly residual strain but less than 0.5 %. The maximum strain at which sheets were failed was 29 % and the mode of failure of sheets at 29 % strain was rupture. The maximum recovery of strain was observed when sheets were loaded up to 8 % strain. The sheets showed pseudoelasticity behavior and flag type stress-strain curve was obtained.
- The SMA Sheets showed enhancement in the shear strength of the joint as well as reduces the crack width upon unloading which will be good sign of post-earthquake self-rehabilitation. It has been observed during testing of BCJs that with usage of SMA sheets as a retrofitting material control cracking appeared and the number of cracks at the joint region were less than the control specimens.

- It has been observed that majority of SMAs during the testing of retrofitted specimens were in austenite phase except BCJ-RC2S where sheets went to forward phase transformation during last cycles of loading and upon unloading maximum recovery of strain was observed i.e. 44 % recovery of strain.

- It has been noticed that the load-deflection response of control and retrofitted specimens showed pinching effect which is due to the sudden loss of joint stiffness due to the damage of concrete prior to the yielding of rebars. The mode of failure did not change in control and retrofitted specimens and all specimens failed completely in shear without yielding of rebars.

- The specimen BCJ-CFRP showed that CFRP wrap and vertical strips used at the side of column doesn't contribute in the shear strength enhancement of the joint and CFRP only contributed in holding the ends of SMAs sheets only.

- It has been noticed that the SMAs sheets were debonded from some location during the test.

- For the Specimen BCJ-CLIS the SMAs sheets enhanced the joint shear capacity by 26 % as compared to the control specimen BCJ-CL and improved the hysteresis behavior i.e. more energy dissipation was observed.

- For the Specimen BCJ-RC4S the SMAs sheets enhanced the joint shear capacity by 20.58 % and 12.5 % in pull and push directions as compared to the control specimen BCJ-RC. The reason of less enhancement of shear strength in pull direction was due to debonding of SMAs sheets caused by cyclic loads. It has been also observed that the hysteresis behavior of BCJ-RC4S improved as compared to the control specimen BCJ-RC which helped in dissipation of more energy.

- For the Specimen BCJ-RC2S the SMAs sheets enhanced the joint shear capacity by 14.12 % and 20.31 % in pull and push directions as compared to the control specimen BCJ-RC. The reason of less enhancement of shear strength in push direction was due to debonding of SMAs sheets and wider cracks caused by cyclic loads. It has been also observed that the hysteresis behavior of BCJ-RC2S improved as compared to the control specimen BCJ-RC which helped in dissipation of more energy.

- For the Specimen BCJ-RCXS the SMAs sheets enhanced the joint shear capacity by 8.03 % and 7.41 % in pull and push directions as compared to the control specimen BCJ-RC. The reason of less enhancement in joint shear strength is due to the configuration of SMAs sheets as sheets were applied in inclined direction and we know that the horizontal component of force contributes in enhancement of shear strength of the joint which was less as compared to the BCJ-4S and BCJ-2S. The hysteresis behavior of BCJ-RCXS were also improved as compared to the control specimen BCJ-RC and dissipated more energy.

- The load- deflection response of BCJ-RC4S and BCJ-2S were almost similar which indicates that the sheets used at the interface of joint in horizontal and vertical direction in BCJ-RC4S contributed less.

- It has been noticed that all retrofitted specimens have more residual load in softening zone as compared to the control specimens.
- The maximum crack opening in BCJ-RC was 8 mm and 5 mm during pull and push cycles and upon unloading only 12.5 % and 10 % was recovered whereas in case of BCJ-RC4S it was 1.3 mm and 1.3 mm during pull and push cycles upon unloading 38.45 % and 53.85 % was recovered which shows the unique property of SMAs.
- The maximum crack opening in BCJ-RC was 8 mm and 5 mm during pull and push cycles upon unloading only 12.5 % and 10 % was recovered whereas in case of BCJ-RC2S it was 2.5 mm and 3 mm during pull and push cycles and upon unloading 64 % and 50 % was recovered which shows the unique property of SMAs.
- The maximum crack opening in BCJ-CL was 2.5 during push cycle upon unloading only 30 % was recovered whereas in case of BCJ-CLIS it was 1.75 mm push cycle upon unloading 60 % was recovered which shows the unique property of SMAs.
- Mechanistic model developed showed good agreement of shear capacity with experimental results.
- It has been noticed that Concrete plastic damage (CPD) model was unable to predict the pinching effect due to which hysteresis envelopes were calibrated.

- The CPD and SMAs model predict closed experiment load when envelopes were calibrated. Also CPD model predicts the softening mode of failure of joint due to shear which is not usually captured by other concrete models.

- The FEM scalar damage prediction showed diagonal profile damage through the joint region at ultimate loads which closely matched with experimental study.

- Concrete damage contours pattern during FEM simulations behaves realistic that was observed during experiments.

- Cohesive contact used for SMAs sheets resulted in close simulations of retrofitted specimens in term of ultimate load and failure of retrofitted BCJs.

- The ultimate load for BCJ-M obtained from FEM simulations was 121.4 kN which shows 0.87 % difference as compared to the experimental load.

- The ultimate load for BCJ-CL obtained from FEM simulations was 121.4 kN which shows 0.87 % difference as compared to the experimental load.

- The ultimate load for BCJ-RC obtained from FEM simulations was 104.72 kN and 115.48 kN in push and pull direction which shows 1.04 % and 11.15 % difference as compared to the experimental load.

- The ultimate load for BCJ-RC4S obtained from FEM simulations was 122.14 kN and 124.39 kN in push and pull direction which shows 4.27 % and 6.41 % difference as compared to the experimental load.

- The ultimate load for BCJ-RC2S obtained from FEM simulations was 120.64 kN and 115.48 kN in push and pull direction which shows 0.09 % and 7.62 % difference as compared to the experimental load.

- The ultimate load for BCJ-RCXS obtained from FEM simulations was 114.64 kN and 106.1 kN in push and pull direction which shows 0.27 % and 4.92 % difference as compared to the experimental load.

- SMAs strain obtained from FEM simulations were between 2 % to 3.5 % which clearly showed that SMAs sheets were in between the austenite phase to forward transformation phase which were also observed in experimental study.

- It was also observed that CFRP strains in FEM simulations were very low which were also predict in experimental study and CFRP wraps and vertical strips were acting as anchorage system for SMAs sheets ends.

7.2 Future Recommendations

It can be seen from this study that SMAs can be used as retrofitting material or as reinforcing material in reinforced concrete structure. Following recommendations are useful for future studies.

1. This study just focus on the shear enhancement capacity of joints. This study can be extended to the flexural members for enhancing the flexural capacity.
2. This study was done on exterior beam-column joints neglecting the slab effect. This can be extended to the all type of joint including the slab which will help in better understanding the behavior SMAs material.
3. This study doesn’t focus on the interface failure of SMAs sheets and concrete which could be another area for study.
4. This study can be extended to the damage beam-column joints to see the response of SMAs sheets after repairing and rehabilitation of joints with SMA sheets.
5. Looking at CDP model which is deficient in predicting the pinching effect, so this study can be extended to different concrete models to predict the pinching effect.

REFERENCES

[1] Y. A. Al-Salloum; S.H. Alsayed; T.H. Almusallam and N. A. Siddiqui “Seismic behavior of FRP upgrade exterior RC beam-column joints”, Concrete Repair, Rehabilitation and Retrofitting II, London, 2009

[2] K. Le-Trung; K. Lee; J. Lee; D.H. Lee; S. Woo, “Experimental study of RC beam–column joints strengthened using CFRP composite”, *Composites: Part B*, pp. 76-85, 2010

[3] S. Sasmal; K. Ramanjaneyulu; B. Novák; V. Srinivas; K. S. Kumar; C. Korkowski; C. Roehm; N. Lakshmanan; N. R. Iyer, “Seismic retrofitting of non-ductile beam-column sub-assemblage using FRP wrapping and steel plate jacketing”, Construction and Building Materials, pp. 175-1782, 2011

[4] M. D. Ludovico; A. Balsamo; A. Prota; G.M. Verderame; M. Dolce; G. Manfredi, “Experimental behavior of non-conforming full scale RC beam-column joints retrofitted with FRP”, International Workshop: Role of research infrastructures in seismic rehabilitation, Feb., 2012

[5] Garcia, R.; Jemaa Y.; Helal, Y.; Guadagnini, M.; Pilakoutas, K., “Seismic strengthening of severely damaged beam-column RC joints using CFRP”, Journal of Composites for Construction, 18 (2). ISSN 1090-0268, 2013

[6] R. Realfonzo; A. Napoli; J.G. R. Pinilla, “Cyclic behavior of RC beam-column joints strengthened with FRP systems”, Construction and Building Materials, pp. 282-297, 2014

[7] M. N. S. Hadi; T. M. Tran, “Seismic rehabilitation of reinforced concrete beam–column joints by bonding with concrete covers and wrapping with FRP composites”, Materials and Structures, Jan. 2015

[8] R. DesRoches; J. McCormick; M. Delemont, “Cyclic Properties of Superelastic Shape Memory Alloy Wires and Bars”, Journal of Structural Engineering, ASCE, pp.38-46, Jan. 2004

[9] H.N. Li; D. Cui; G. Song; Y.L. Mo, “Experimental Investigation on Self-rehabilitation of Intelligent Concrete Beams Reinforced with Superelastic Shape Memory Alloys”, Conference of earth and space, ASCE, 2006

[10] M.S. Saiidi; M. S. Zadeh; C. Ayoub; A. Itani, “Pilot Study of Behavior of Concrete Beams Reinforced with Shape Memory Alloys”, Journal of material in Civil engineering, ASCE, June 2007

[11] M. Nehdi; M. S. Alam, M.A.Youssef, “Development of corrosion-free concrete beam-column joint with adequate seismic energy dissipation”, Engineering Structures, pp. 2518-2528, 2010

[12] M. Nehdi; M. S. Alam, M.A.Youssef, “Seismic behavior of repaired superelastic shape memory alloy reinforced concrete beam-column joint”, Smart Structures and Systems, pp. 329-348, 2011

[13] A. Abdulridha; D. Palermo; S. Foo; F. J. Vecchio, “Behavior and modeling of superelastic shape memory alloy reinforced concrete beams”, Engineering Structures, pp. 893-905, 2013

[14] A. Zafar; B. Andrawes, “Experimental flexural behavior of SMA-FRP reinforced concrete beam”, Frontiers of Structural and Civil Engineering, pp. 341-355, 2013

[15] S. Pampanin; G.M. Calvi; M. Moratti, “Seismic behaviour of R.C. beam-column joints designed for gravity loads”, 12th European Conference on Earthquake Engineering, 2002

[16] J. Lee; G. L. Fenves, “Plastic-Damage model for cyclic loading of concrete structures”, Journal of engineering mechanics, pp. 892-900, 1998

[17] J. Lubliner; J. Oliver; S. Oller; E. Oñate, “A plastic-damage model for concrete”, International Journal of Solids and Structures, pp. 299-326, 1989

[18] D. Ahmed, “Retrofitting of exterior beam-column joints using CFRP”, M.S. Thesis, King Fahd University of Petroleum and Minerals, 2012

[19] SBC 301, “Saudi Building Code for Load and Forces Requirements”, SBC-301, Saudi Arabia, 2007

[20] F. Auricchio; R. L. Taylor, “Shape-memory alloys: modeling and numerical simulations of the finite-strain superelastic behavior,” Computer Methods in Applied Mechanics and Engineering, vol. 143, pp. 175-194, 1997

[21] F. Auricchio; R. L. Taylor; J. Lubliner., "Shape-memory alloys: macromodeling and numerical simulations of the superelastic behavior," Computer Methods in Applied Mechanics and Engineering, vol. 146, pp. 281-312, 1997

[22] CEB-FIP Model Code, “Comité euro-international du béton”, Thomas Telford Ltd., 1990

[23] W. Tsai, “Uniaxial Compressional Stress-Strain Relation of Concrete”, Journal of Structural Engineering, pp. 2133-2136, 1988

[24] P. G. Bakir; H. M. Bodurogulu, “A new design equation for predicting the joint shear strength of monotonically loaded exterior beam-column joints”, Engineering Structures, pp. 1105-1117, 2002

[25] A. Khatib; M. Al-Osta; M. Baluch; A. K. Azad; M. K. Rahman, “Performance of hybrid beam-column joint cast with high strength concrete”, (Under Review)

APPENDIX A

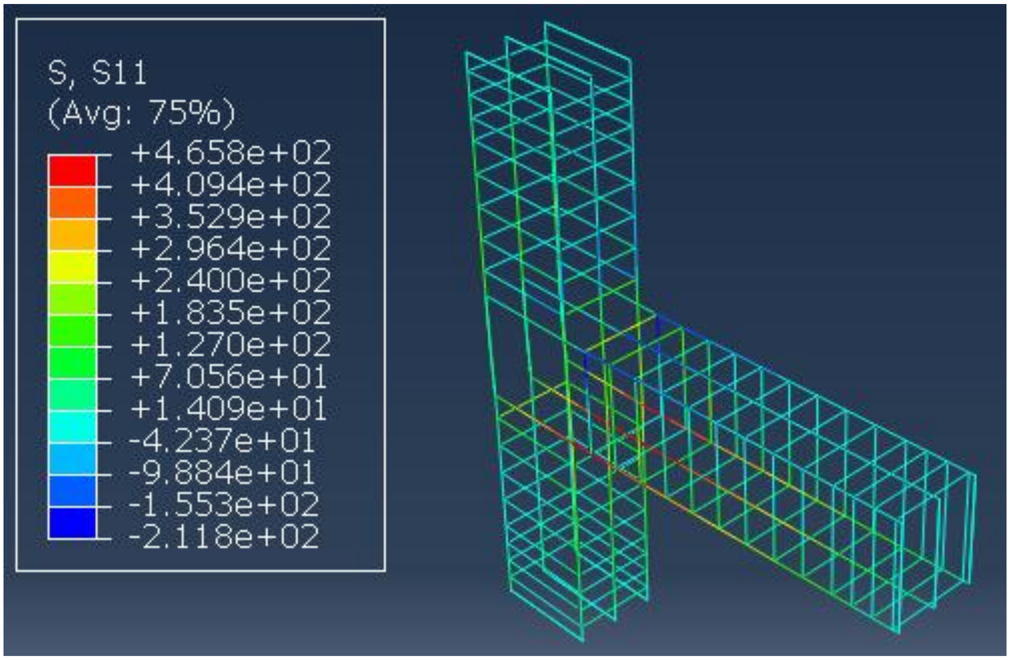

Figure A.1: Steel stresses at the ultimate load corresponding to 27.01 mm displacement for BCJ-RC4S in pull direction

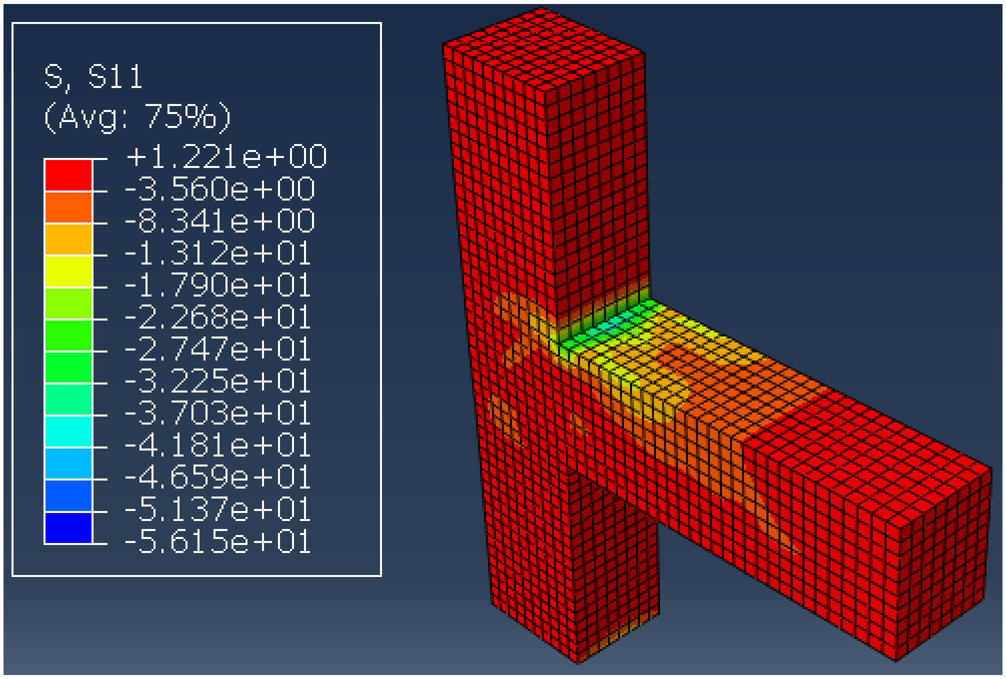

Figure A.2: Stress S11 in concrete at the ultimate load corresponding to 27.01 mm displacement for BCJ-RC4S in pull direction

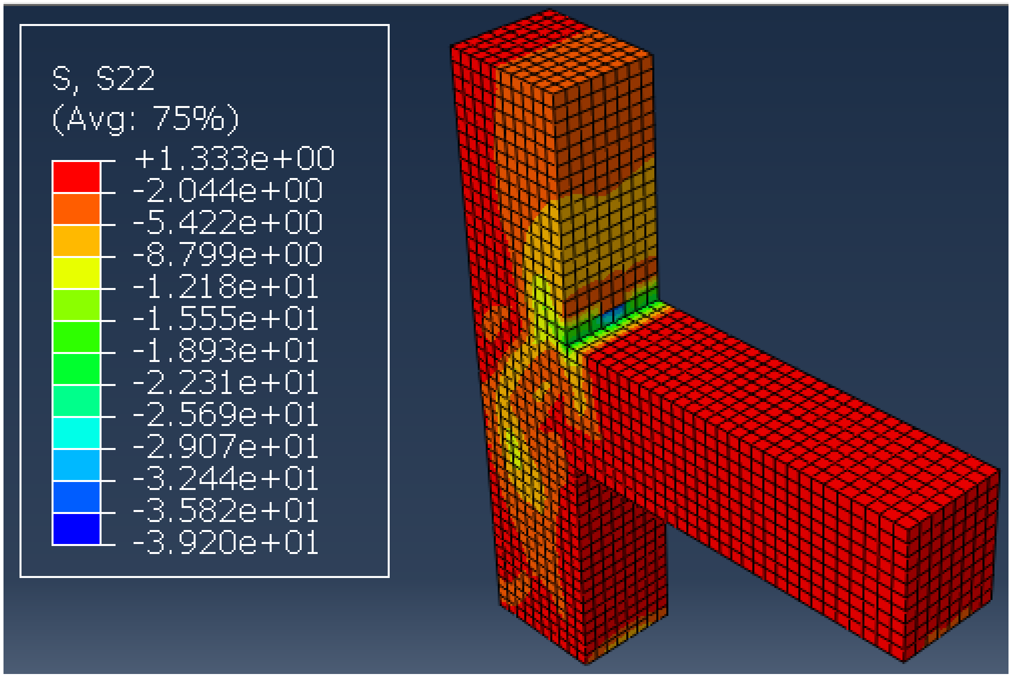

Figure A.3: Stress S22 in concrete at the ultimate load corresponding to 27.01 mm displacement for BCJ-RC4S in pull direction

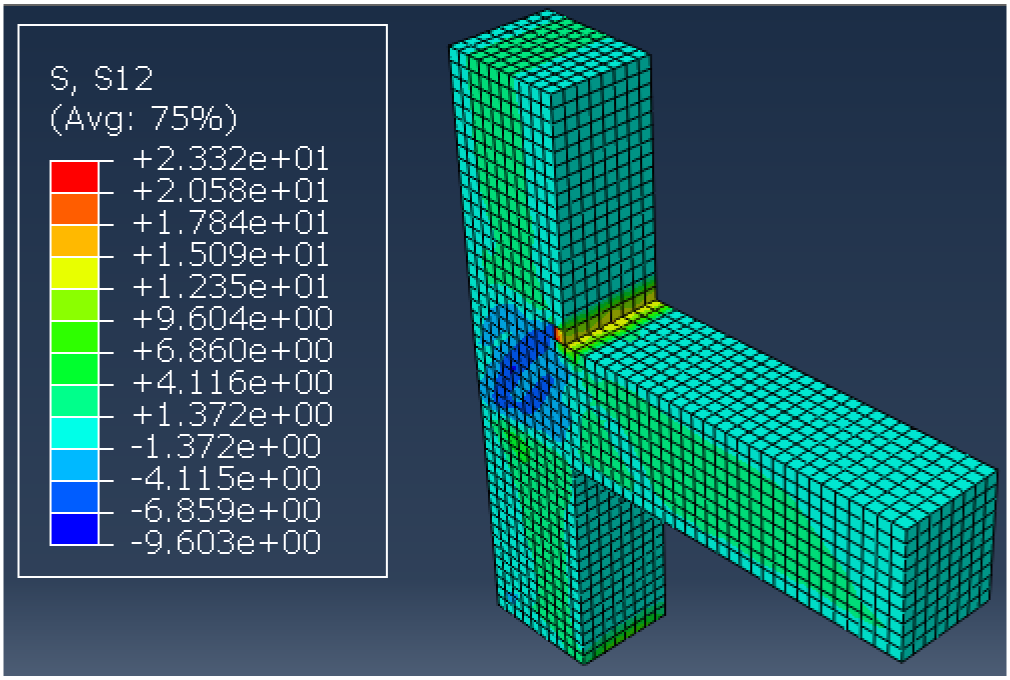

Figure A.4: Stress S12 in concrete at the ultimate load corresponding to 27.01 mm displacement for BCJ-RC4S in pull direction

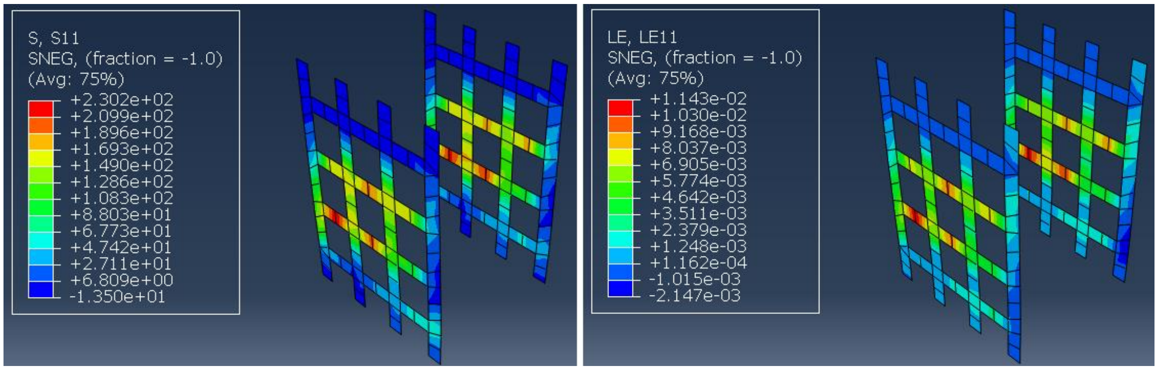

Figure A.5: Stresses (left) and strains (right) in SMAs Sheets at ultimate load for BCJ-RC4S in pull direction

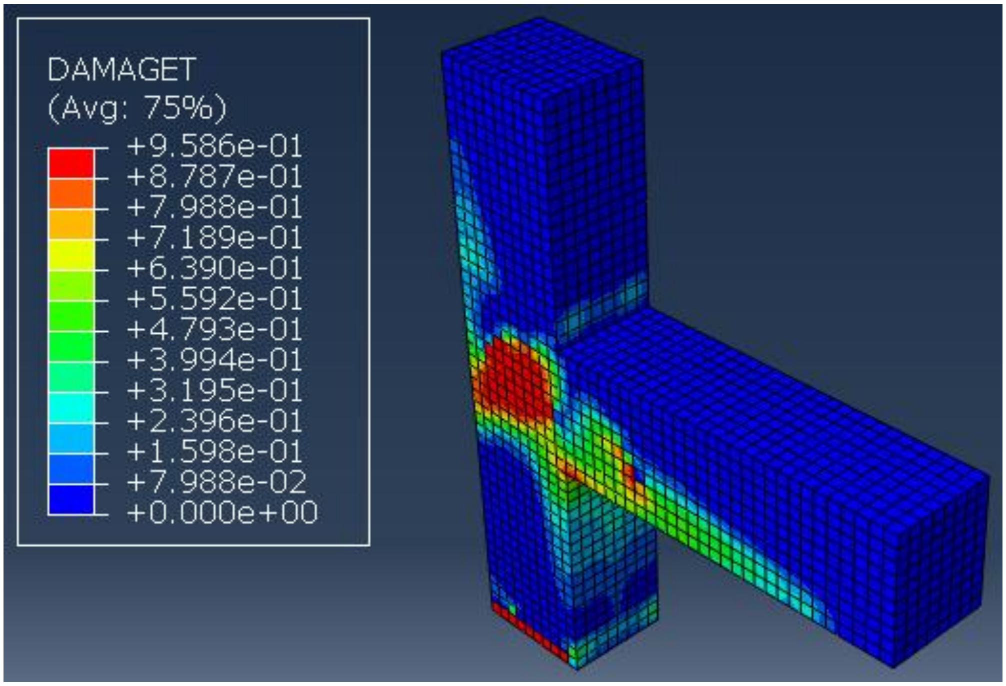

Figure A.6: Concrete damage at the ultimate load corresponding to 27.01 mm displacement for BCJ-RC4S in pull direction

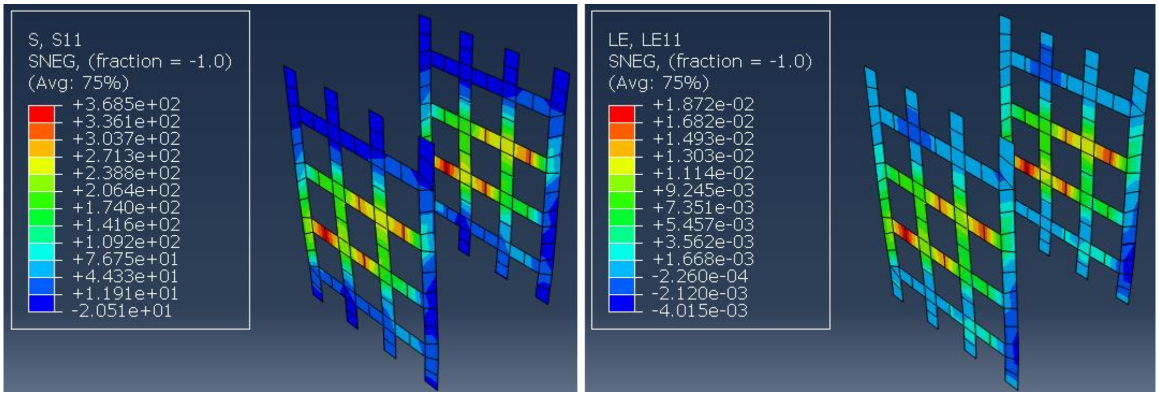

Figure A.7: Stresses (left) and strains (right) in SMAs Sheets at displacement of 40 mm for BCJ-RC4S in pull direction

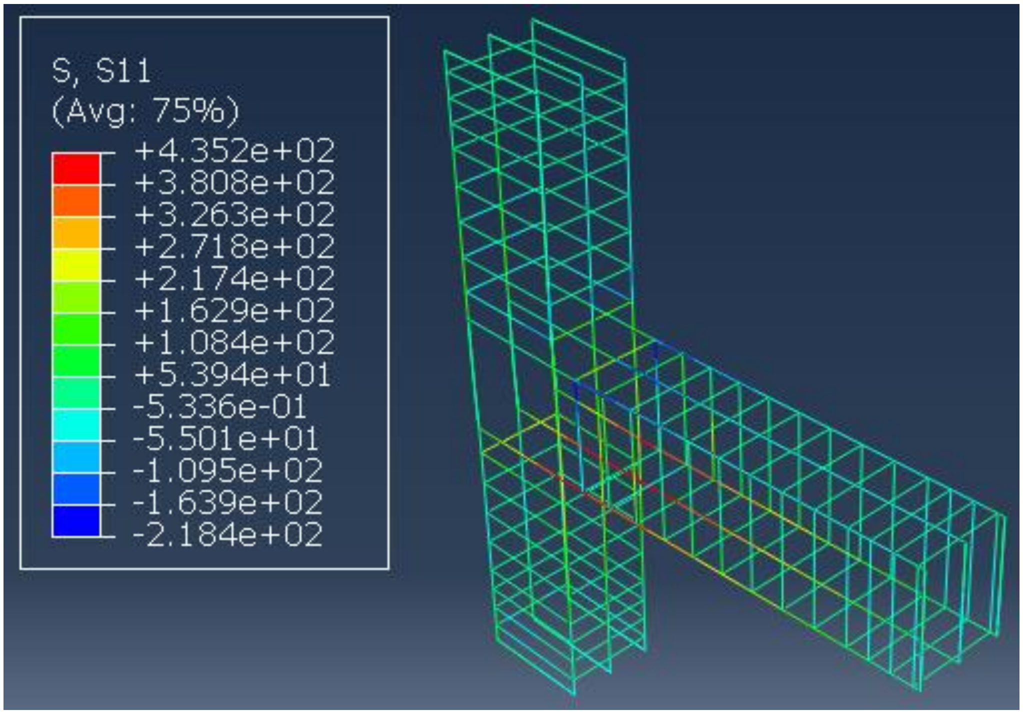

Figure A.8: Steel stresses at the ultimate load corresponding to 25.28 mm displacement for BCJ-RC2S in pull direction

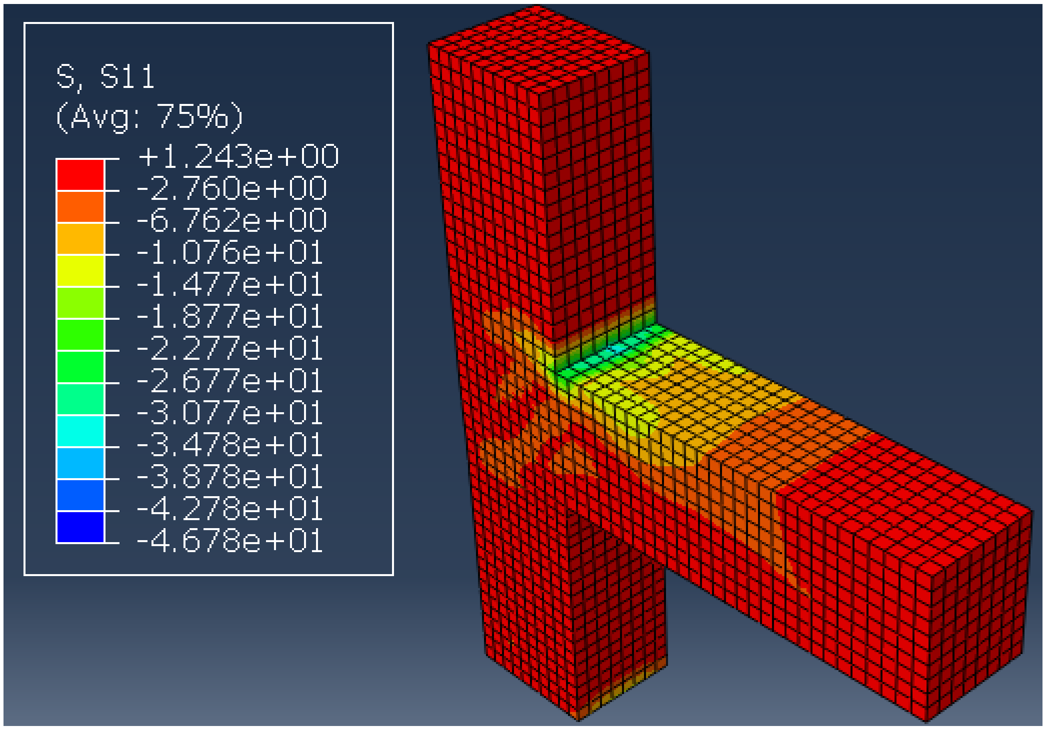

Figure A.9: Stress S11 in concrete at the ultimate load corresponding to 25.28 mm displacement for BCJ-RC2S in pull direction

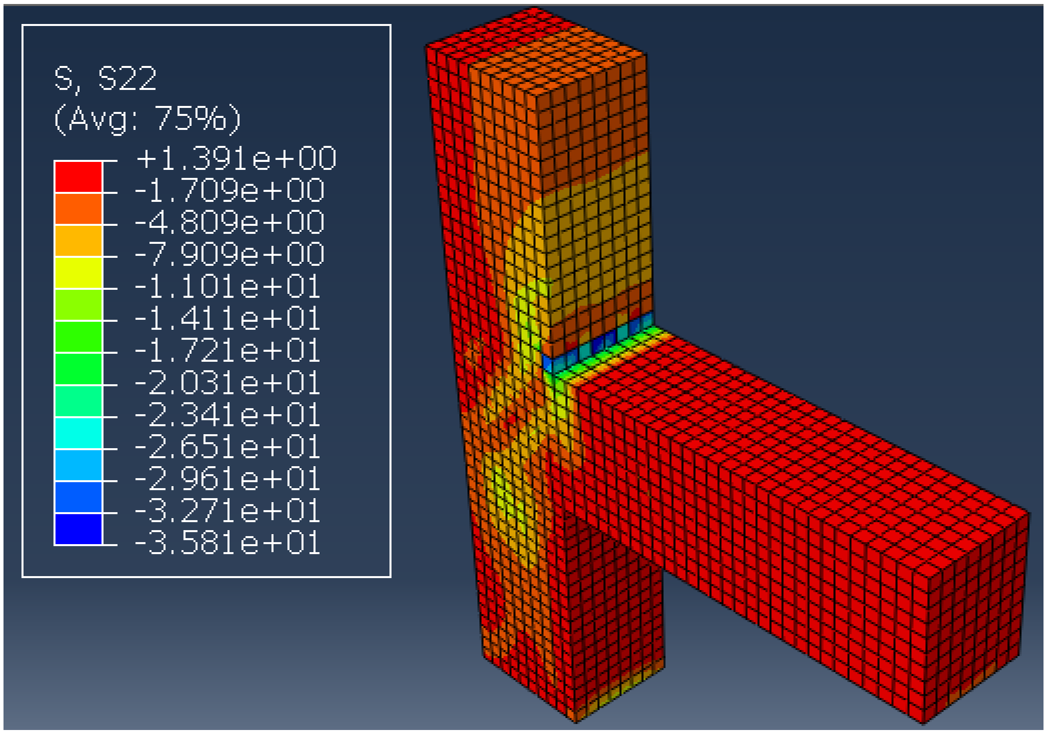

Figure A.10: Stress S22 in concrete at the ultimate load corresponding to 25.28 mm displacement for BCJ-RC2S in pull direction

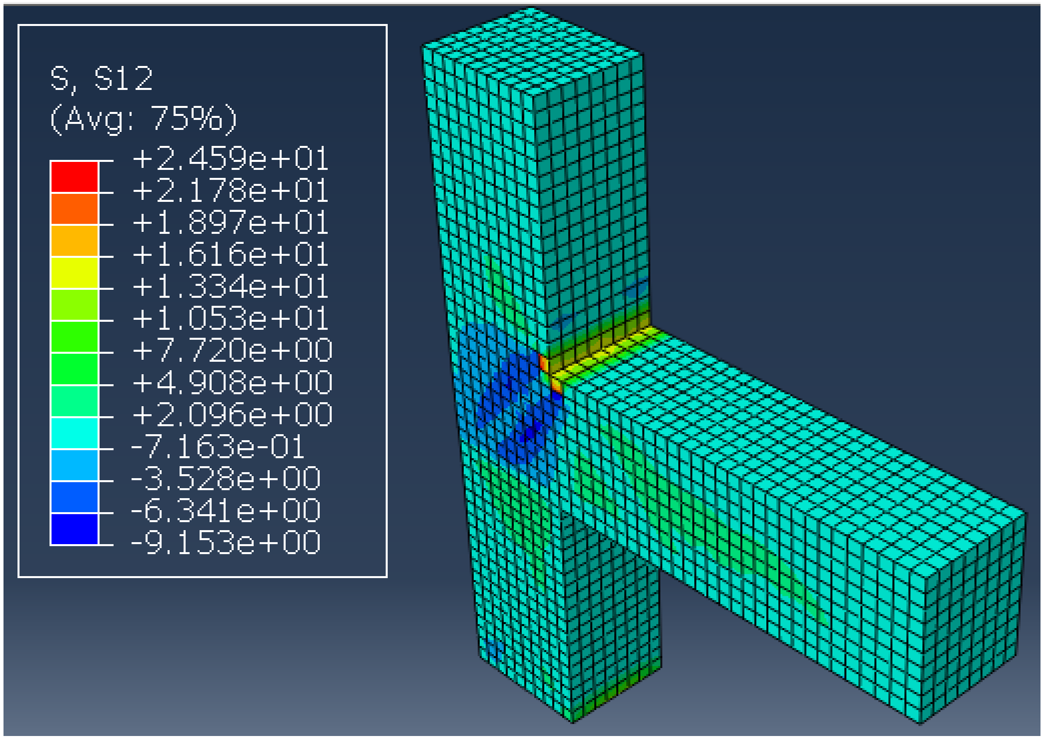

Figure A.11: Stress S12 in concrete at the ultimate load corresponding to 25.28 mm displacement for BCJ-RC2S in pull direction

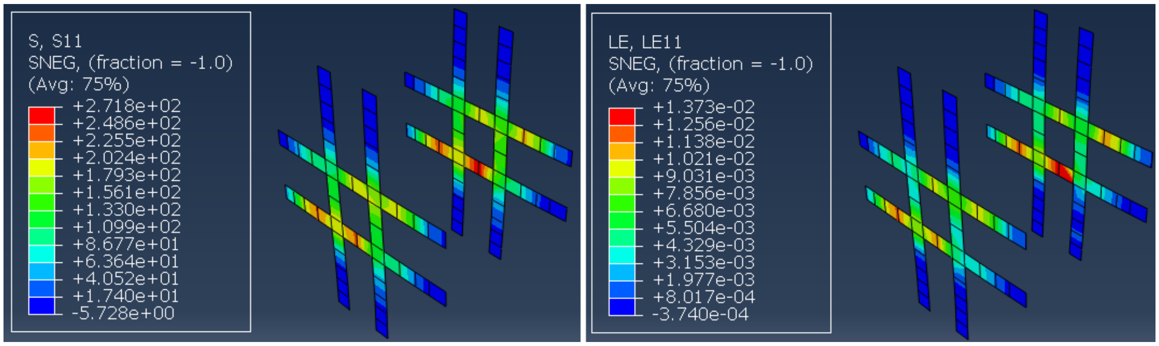

Figure A.12: Stresses (left) and strains (right) in SMAs Sheets at ultimate load for BCJ-RC2S in pull direction

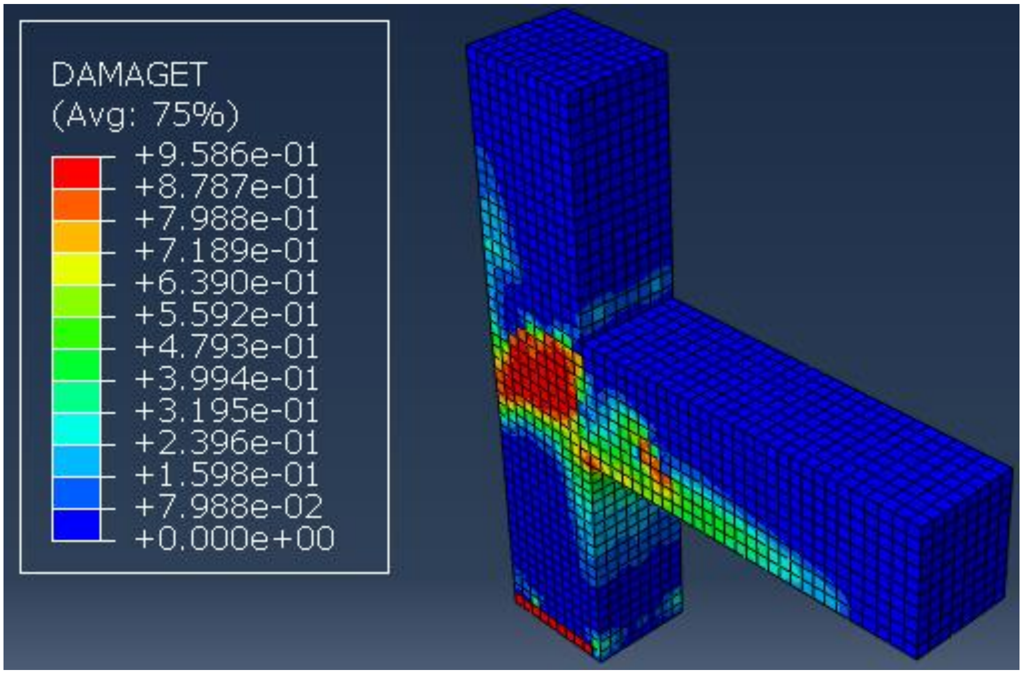

Figure A.13: Concrete damage at the ultimate load corresponding to 25.28 mm displacement for BCJ-RC2S in pull direction

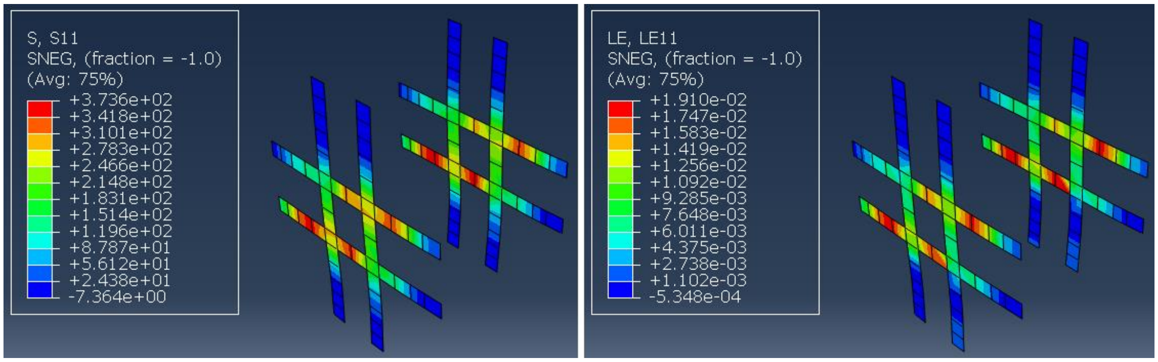

Figure A.14: Stresses (left) and strains (right) in SMAs Sheets at displacement of 40 mm for BCJ-RC2S in pull direction

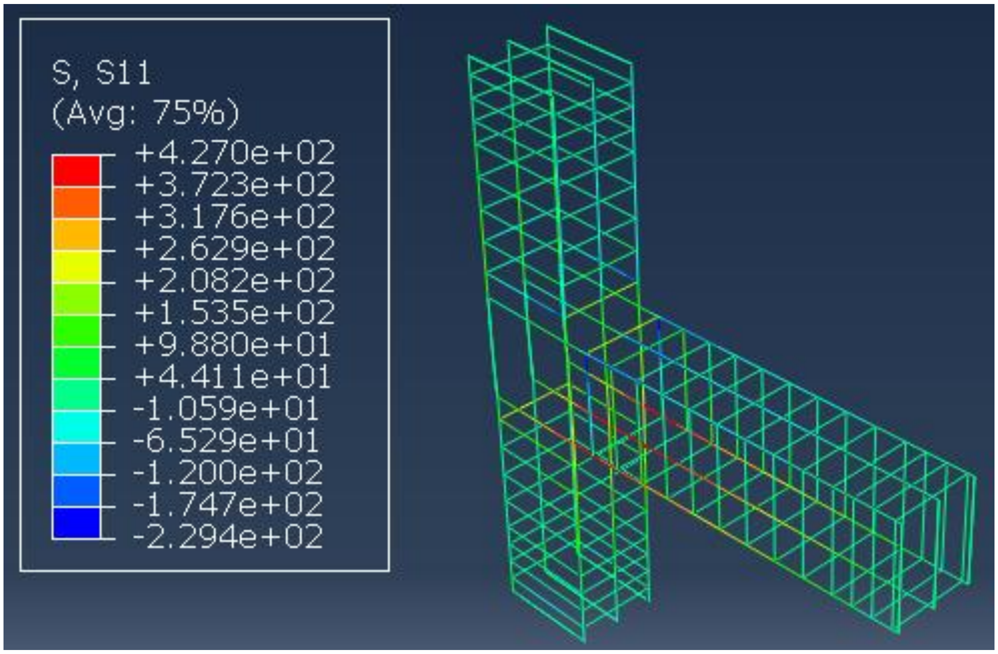

Figure A.15: Steel stresses at the ultimate load corresponding to 207.21 mm displacement for BCJ-RCXS in pull direction

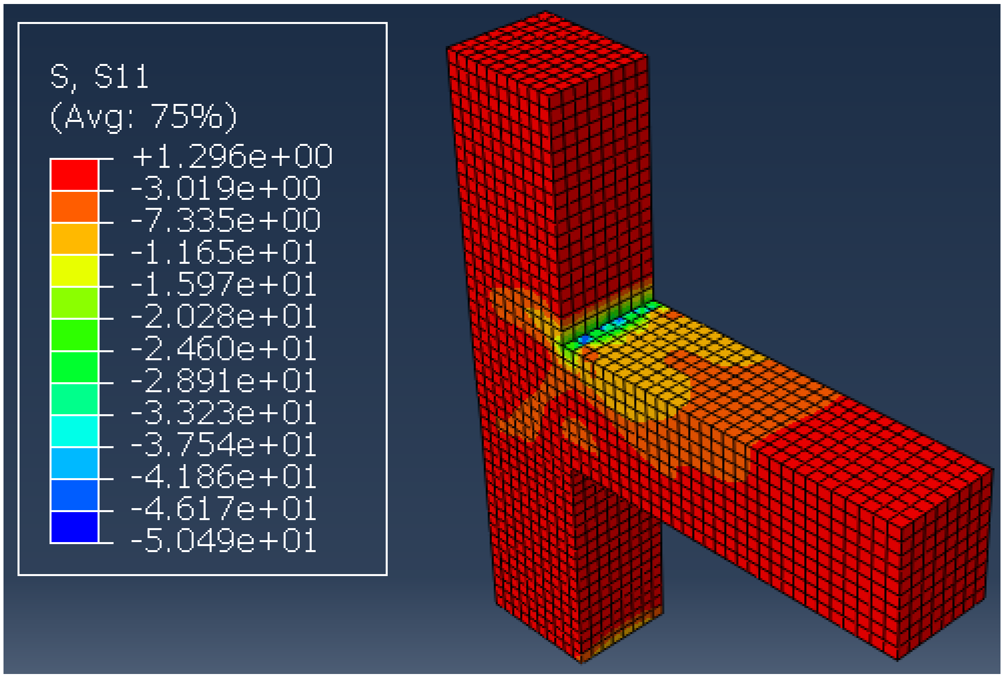

Figure A.16: Stress S11 in concrete at the ultimate load corresponding to 27.21 mm displacement for BCJ-RCXS in pull direction

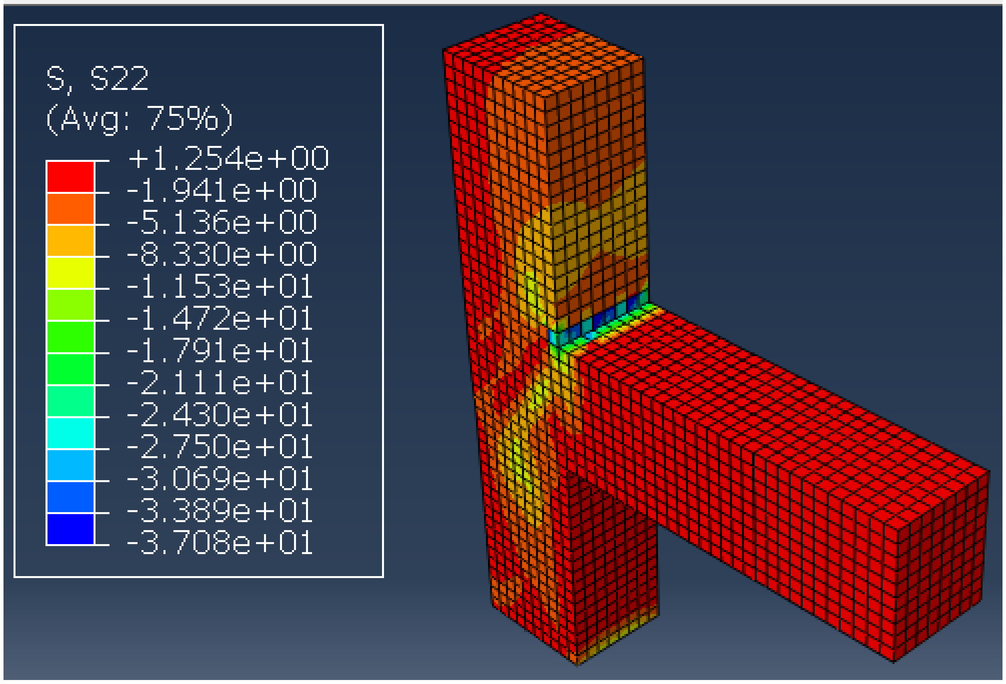

Figure A.17: Stress S22 in concrete at the ultimate load corresponding to 27.21 mm displacement for BCJ-RCXS in pull direction

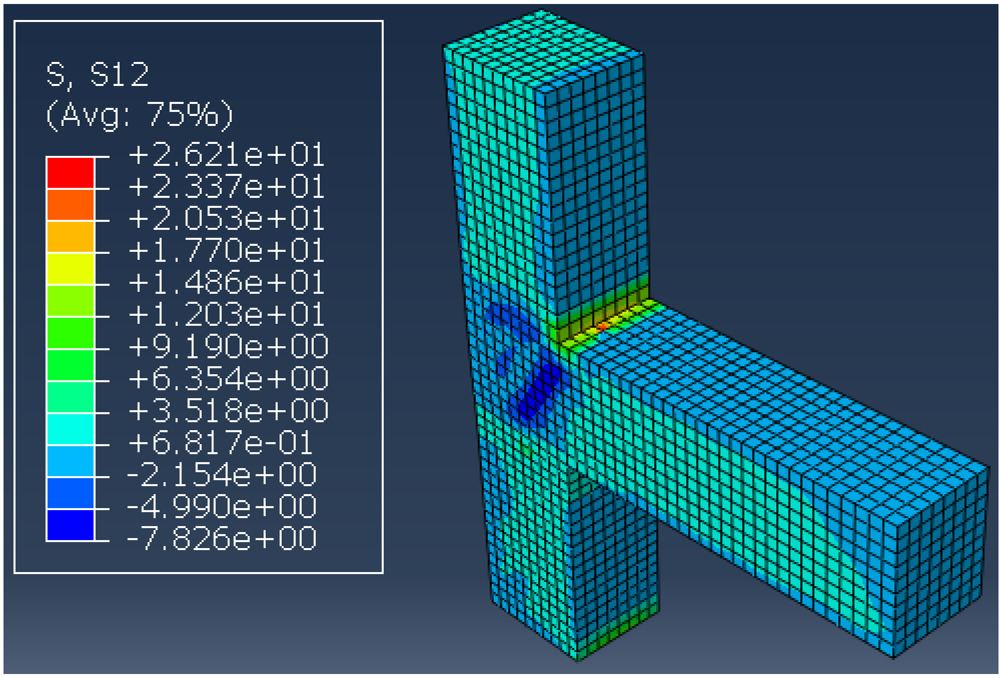

Figure A.18: Stress S12 in concrete at the ultimate load corresponding to 27.21 mm displacement for BCJ-RCXS in pull direction

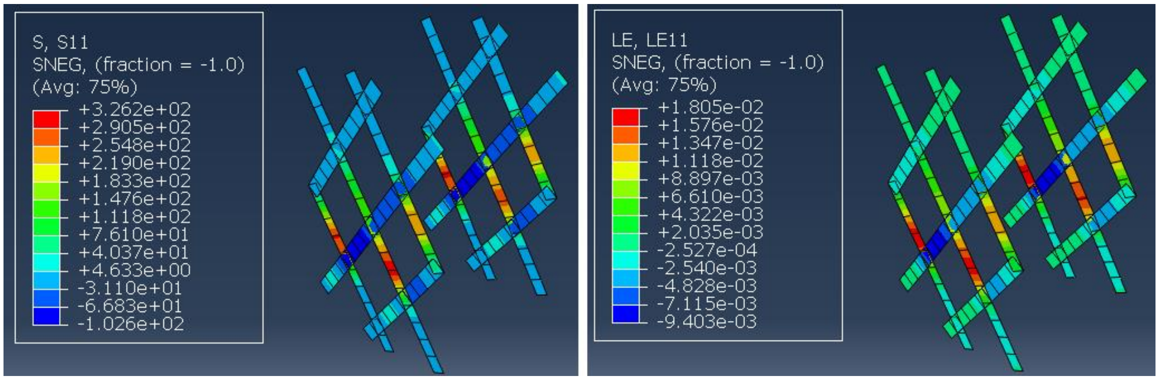

Figure A.19: Stresses (left) and strains (right) in SMAs Sheets at ultimate load for BCJ-RCXS in pull direction

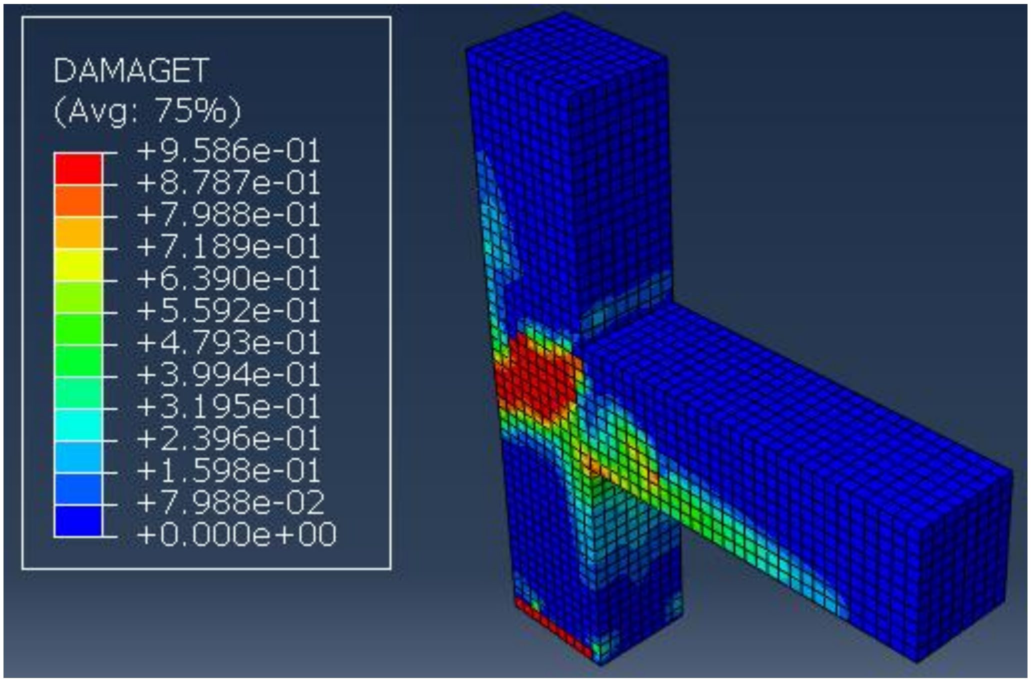

Figure A.20: Concrete damage at the ultimate load corresponding to 27.21 mm displacement for BCJ-RCXS in pull direction

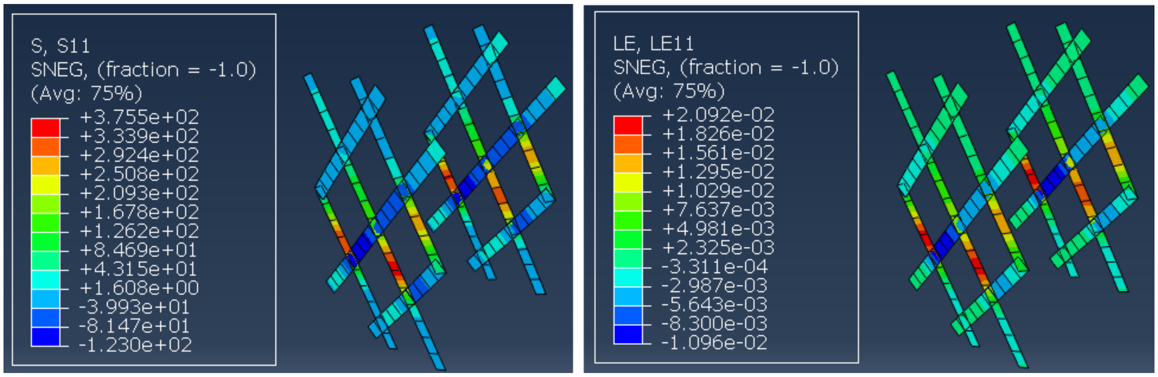

Figure A.21: Stresses (left) and strains (right) in SMAs Sheets at displacement of 40 mm for BCJ-RCXS in pull direction

Vitae

Name : Muhammad Ajmal

Nationality : Pakistani

Date of Birth : 06/06/1985

Email : majmal11@hotmail.com

Current Address : P. O. Box 172, 31411 Dammam Saudi Arabia.

Address : HNo.8 St. # 2-A Fateh Garh Near Ghani Steel Mill
Mughal Pura Lahore, Pakistan.

Academic Background : Bachelor of Engineering Science, Major Civil Engineering, University Engineering and Technology Lahore, Pakistan, 2009.

: Master of Science, Major Structural Engineering, King Fahd University of Petroleum & Minerals, Dhahran, Saudi Arabia, 2012.

: Doctor of Philosophy, Major Structural Engineering, King Fahd University of Petroleum & Minerals, Dhahran, Saudi Arabia, 2016.